UNIVERSITY OF Southampton

University of Southampton Research Repository
ePrints Soton

Copyright © and Moral Rights for this thesis are retained by the author and/or other copyright owners. A copy can be downloaded for personal non-commercial research or study, without prior permission or charge. This thesis cannot be reproduced or quoted extensively from without first obtaining permission in writing from the copyright holder/s. The content must not be changed in any way or sold commercially in any format or medium without the formal permission of the copyright holders.

When referring to this work, full bibliographic details including the author, title, awarding institution and date of the thesis must be given e.g.

AUTHOR (year of submission) "Full thesis title", University of Southampton, name of the University School or Department, PhD Thesis, pagination

http://eprints.soton.ac.uk

UNIVERSITY OF SOUTHAMPTON

Faculty of Engineering, Science and Mathematics

Optoelectronics Research Centre

Modelling and optimisation of microfluidic devices for bioanalysis applications

by Daniel Friedrich

A thesis submitted in partial fulfilment for the degree of Doctor of Philosophy

November 2009

UNIVERSITY OF SOUTHAMPTON

ABSTRACT

FACULTY OF ENGINEERING, SCIENCE AND MATHEMATICS
OPTOELECTRONICS RESEARCH CENTRE

Doctor of Philosophy

MODELLING AND OPTIMISATION OF MICROFLUIDIC DEVICES FOR BIOANALYSIS APPLICATIONS

by Daniel Friedrich

The small size of integrated microfluidic systems offers many advantages such as cost, speed and portability for bioanalysis applications. However, due to the small scale the careful consideration of the transport of analytes in the bulk of the integrated microfluidic system and the interaction of analytes with surface immobilised analyte recognition molecules (receptors) is crucial for an efficient device operation. This thesis is concerned with the mathematical analysis and optimisation of the convective and diffusive transport of analytes and the analyte-receptor interaction in integrated microfluidic affinity systems with the aim of creating design guidelines for more efficient bioanalysis systems.

The first part of this thesis considers device configurations where every analyte molecule can reach the surface immobilised receptors. In this case, which is important for sensing and separation applications, the transport-reaction model is solved analytically. This analytical solution is analysed for two bioanalytical applications: (i) affinity separation and (ii) affinity sensing. For fast analyte-receptor interactions, which are essential for affinity separation systems, the analysis of the analytical solution reveals simple expressions for the retention and the dispersion of the analyte due to the interaction with the receptors. With these expressions, which depend only on global device parameters, a framework for the design of multiplexed separation systems for the separation of proteins from complex sample mixtures is developed. Subsequently, the analytical solution of the transport-reaction model is used in the derivation of improved design strategies for microfluidic affinity sensors for the detection of analytes from small sample plugs. Three design strategies, which achieve a high capture fraction and a significantly increased uniformity of the bound analyte concentration over the sensor surface, are presented. The first two strategies rely on the variation of one device parameter, i.e. the flow velocity or the surface immobilised receptor concentration, as the analyte plug is flowed through the channel. The third approach is based on non-rectangular devices where the analyte plug is replenished by a narrowing of the flow channel. This third design strategy is applied to the redesign of a biosensor for the detection of low cytokine levels from small sample volumes.

In the second part a novel microfluidic system for the generation of concentration gradients across microfluidic channels is developed. In this design the analytes are transported by surface groove induced secondary flow from the source to the sink stream. Numerical optimisations over the shape and size of the surface groove result in gradient generators which yield a well-defined linear or exponential concentration gradient across the width of the microfluidic channel. The resulting gradient generators have a much smaller footprint than conventional gradient generators and are thus more suitable for highly integrated lab-on-a-chip systems.

Contents

List of Figures

List of Tables

List of Symbols

a	Flow modification parameter
a	Concentration variation parameter
a_{ij}	Length of separation patch j in lane i
a_{max}	Maximal patch length
a_{min}	Minimal patch length
A	Analyte concentration
A_0	Inlet analyte concentration
A_b	Velocity averaged analyte concentration
A_i	Surface immobilised analyte concentration
A_{i0}	Initial surface immobilised analyte concentration
A_s	Simulated analyte concentration
A_w	Analyte concentration near the active channel wall
b	Concentration modification parameter
B	Bound analyte concentration
B_{avg}	Average bound analyte concentration
B_{eq}	Equilibrium bound analyte concentration
B^f	Concentration of bound fluorescent ligand
c_i	Average analyte concentration in outlet i
C_{dye}	Dye concentration
C_m	Mobile phase concentration
C_s	Stationary phase concentration
δ	Dirac delta function
δ_s	Diffusion boundary layer thickness
d_{ik}	Detection spot k in lane i
d_d	Dual-patch peak separation distance
$d_{s,max}$	Maximal single-patch peak separation distance
$d_{s,min}$	Minimal single-patch peak separation distance
D	Diffusion coefficient
D_{eff}	Effective diffusion coefficient
Da	Damköhler number
Da_E	Damköhler number in the 'entrance region'
E_e	Relative error exponential concentration gradient
E_l	Absolute error linear concentration gradient
f	Analyte input function
F	Capture fraction
g	Gravitational body force

$g(x)$	Active area boundary
Gz	Graetz number
H	Channel height
H_e	Effective channel height
H_g	Groove depth
$\hat{\mathrm{H}}$	Heaviside step function
I_0, I_1	Modified Bessel function of first kind
J_D	Diffusive flux
J_R	Reactive flux
κ	Adsorption capacity
k	Column capacity
k_a	Association rate constant
k_d	Dissociation rate constant
k_m	Plug dispersion in open-tubular systems
$\mathrm{K_d}$	Dissociation constant
$\bar{\mathrm{K}}_\mathrm{d}$	Nondimensional dissociation constant
K_{jk}	Dissociation constant for analyte k with receptor j
λ	Input time of the analyte plug
λ_i	Eigenvalues
λ_w	Wavelength
L	Channel length
L_a	Groove offset
L_d	Detection area length
L_f	Groove length far side
L_i	Initial plug length
L_m	Groove length at the midpoint
L_n	Groove length near side
L_o	Outlet channel length
L_p	Minimal receptor patch length
L_{plug}	Plug length
μ	Dynamic viscosity
ν	Kinematic viscosity
$\mathbf{n}$	Inward pointing normal vector
N	Number of detection spots
ω	Coefficient of exponential decay
p, p_1, p_2	Pressure
Pe	Peclet number
Q	Flow rate
ρ	Density
r	Separation ratio
R	Ligand concentration
Re	Reynolds number
σ^2	Variance
s	Laplace variable
S	Active surface area
S_{ikl}	Plug separation of analytes k and l on lane i
Sh	Sherwood number

τ_w	Shear stress
t	Time variable
t_{assay}	Assay time
t_C	Convection time scale
t_d	Minimal retention time
t_D	Diffusion time scale
t_{eq}	Equilibrium time scale
t_{eq}^{dl}	'Diffusion limited' equilibrium time scale
t_{ex}	Exposure time
t_{ik}	Retention time of analyte k on lane i
t_{off}	Offset
T_g	Glass transition temperature
$\mathbf{u} = (u, v, w)$	Flow velocity
u_p	Analyte plug velocity
$u(t)$	Temporal variation of the flow velocity
U	Mean flow velocity
U_{band}	Band velocity
V	Volume
V_m	Mobile phase volume
V_s	Stationary phase volume
w_{ik}	Plug width of analyte k on lane i
W	Channel width
W_i	Sample inlet width
W_l	Lane width
W_m	Groove midpoint
$W(x)$	Channel wall position
ξ	Channel capacity
ξ_{max}	Maximal channel capacity
ξ_{min}	Minimal channel capacity
x, y, z	Spatial variables
x_d	Cross lane diffusion distance
X	Receptor concentration
X_0	Initial receptor concentration
X_b	Bound analyte-receptor complex concentration
$X_a(x), X_s(x)$	Spatial variation of the surface immobilised receptor concentration
υ	Uniformity
ζ	Reaction/convection number

List of Abbreviations

2D-DIGE	2D differential gel electrophoresis
2D-PAGE	2D polyacrylamide gel electrophoresis
CCD	Charge-coupled device
CE	Capillary electrophoresis
COC	Cycle-olefine copolymer
DNA	Deoxyribonucleic acid
DRIE	Deep reactive ion etching
ELISA	Enzyme-linked immunosorbent assay
EOF	Electroosmotic flow
ESI	Electrospray ionisation
FEM	Finite element method
FWHM	Full width at half maximum
GUI	Graphical user interface
HPLC	High performance liquid chromatography
IBE	Ion beam etching
LIF	Laser induced fluorescence
LIGA	Lithography, electroplating and molding
LOD	Limit of detection
MALDI	Matrix assisted laser desorption ionisation
mRNA	Messenger ribonucleic acid
MS	Mass spectrometry
MSI	Mass spectrometry imaging
ODE	Ordinary differential equations
PC	Polycarbonate
PCR	Polymerase chain reaction
PDMS	Poly(dimethylsiloxane)
PEEK	Polyetheretherketone
PMMA	Polymethylmethacrylate
POC	Point-of-care
RCA	Rolling-circle amplification
SHM	Staggered herringbone mixer
SPR	Surface plasmon resonance

Declaration of authorship

I, Daniel Friedrich

declare that the thesis entitled

Modelling and optimisation of microfluidic devices for bioanalysis applications

and the work presented in the thesis are both my own, and have been generated by me as the result of my own original research. I confirm that:

- this work was done wholly or mainly while in candidature for a research degree at this University;
- where any part of this thesis has previously been submitted for a degree or any other qualification at this University or any other institution, this has been clearly stated;
- where I have consulted the published work of others, this is always clearly attributed;
- where I have quoted from the work of others, the source is always given. With the exception of such quotations, this thesis is entirely my own work;
- I have acknowledged all main sources of help;
- where the thesis is based on work done by myself jointly with others, I have made clear exactly what was done by others and what I have contributed myself;
- parts of this work have been published as in Publications, Appendix E.

Signed:.....

Date: November 25, 2009

Acknowledgements

I would like to thank my supervisors Dr. Tracy Melvin and Prof. Colin Please for their guidance and support throughout my research. I would also like to thank Prof. James Wilkinson and Dr. Ping Hua for their continuous help and support in the application of the theoretical models to the multisensor. I am grateful for the help from Dr. Lucy Braddick, Dr. Patrick Garland, Dr. Matt Praeger and Dr. Nicolas Perney with the practical aspects of lab-on-a-chip systems.

A thank you goes to my colleagues and friends in the ORC and ECS: Tim, Chris, Hamish, Lucy, Matt, Nic, Chien, Mukhzeer, Katrin, Patrick and Julian. You have all made my time in Southampton more enjoyable.

A special thanks goes to my family. They have always encouraged me to find and pursue my own goals and have supported my decisions without questions.

Finally, I would like to thank Simone. Thank you for always believing in me.

Chapter 1

Introduction

1.1 Overview

This thesis is concerned with the efficient transport of analytes in integrated microfluidic affinity systems. Analytical and numerical models are used to evaluate and optimise the transport of analytes in the bulk of the microfluidic channel and the analyte mass transfer to the active surface. First, the transport to the active surface in microfluidic affinity systems for the separation and detection of analytes from small sample quantities is considered. The second part considers analyte transport in microfluidic channels with surface groove induced secondary flow. Whilst the models are motivated specifically from the requirements for the analysis of low copy number analytes, it is likely that they are applicable for other bioanalytical applications.

Integrated systems within microfluidic structures are becoming more routinely used for environmental monitoring and in the life sciences [1]. An integrated microfluidic system, a so called lab-on-a-chip, has several advantages over conventional laboratory-scale systems. Besides the more obvious effects of the small size of microfluidic devices, such as low sample consumption, rapid analysis and high portability, integrated microfluidic devices offer a highly controlled microenvironment. The precise control of the environmental parameters such as the flow rate or nutrient concentration on length scales in the low micrometre range allows applications which are not feasible in the macro

regime [2]. Furthermore, the precise control increases the repeatability and reliability of quantitative bioanalysis studies [3].

Lab-on-a-chip systems are expected to have a large impact on the study of the human proteome, i.e. the study of proteins and their interactions [4]. The study of proteins, which are the active components of an organism, and their interactions offers many possibilities for the diagnosis, understanding and treatment of diseases [5]. For example, it is suggested that elevated cytokine levels may contribute to the progression of chronic neurodegenerative diseases such as Alzheimer's and Multiple Sclerosis [6]. However, a high level of automation and integration, which is difficult to achieve in macro-scale systems, is required for the analysis of the human proteome because a human cell contains many thousand proteins whose concentrations range over $6-8$ orders of magnitude [7]. Furthermore, the available sample quantities, for example from single cells or small cell cultures, are limited so that efficient ways for the sample handling are required. Microfluidic lab-on-a-chip systems offer the possibilities to fulfil many of these requirements. One of the main strengths of integrated microfluidic systems is the incorporation of several functions, such as sample preparation, separation and detection, into one system which facilitates the automatic and parallel analysis of small samples with many thousand proteins [4].

One of the most promising types of integrated microfluidic systems for the analysis of the proteome is based on the specific affinity interaction of proteins with antibodies [8]. These microfluidic affinity systems consist of a fluidic channel with one or more functionalised surfaces. The configuration of microfluidic affinity systems is illustrated in figure 1.1. The characteristic dimension of the flow channel is in the micrometre range

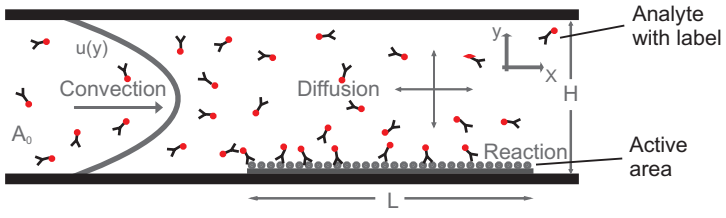

Figure 1.1: Schematic side view of a microfluidic affinity system. The analyte molecules are transported by convection and diffusion and bind to the receptor molecules on the active sensor area.

which ensures a stable, turbulence-free flow profile [3]. This stable, laminar flow provides a highly controllable fluidic environment. One or more of the surfaces are functionalised by conjugating receptor molecules to them. Analyte molecules from the bulk of the microfluidic channel are transported to the functionalised surface and interact with the surface immobilised receptor molecules in a recognition-binding event where the analyte molecule binds to the matched receptor molecule. The analyte-receptor pairs are often an antibody-antigen pair such as the cytokine IL-6 and the IL-6 antibody [9]. These interactions between the analytes and the surface immobilised receptors can be used for affinity separations, i.e. affinity chromatography and affinity electrophoresis [10], as well as for analyte-sensing assays [11]. The specificity of the recognition-binding event between proteins and the matching protein antibody can be utilised in the design of analytical systems with high specificity. These microfluidic affinity systems are uniquely suited for the study of proteins and especially post-translational modifications of proteins which often change the binding properties of the proteins [12; 13].

There has been much effort focused on the reduction of the channel dimensions to reduce the sample consumption [14], on the improvement of the transducer to achieve more sensitive sensors [15] and on the integration of affinity systems into sensor arrays [16; 17]. Far less attention has been placed on the improvement of the microfluidic elements and especially the analyte transport to the active surface. However, the decreasing size of the microfluidic system and the decreasing analyte volume can lead to depletion effects which negate the advantages achieved in sensor sensitivity and miniaturisation. The first depletion effect is due to the stable laminar flow in microfluidic channels where the transport of analytes to the functionalised surface is dominated by transverse molecular diffusion [18]. For many device configurations the diffusion of analytes to the active surface is slower than the affinity reaction. This leads to the formation of a depleted diffusion boundary layer and consequently to mass transport limitations as well as to a non-uniform distribution of bound analyte along the length of the functionalised surface. The second depletion effect is due to the limited sample volume in microfluidic systems [19]. Here the analyte concentration in the sample plug depletes as it moves along the channel due to the interaction with the surface immobilised receptors. This also leads to a non-uniform distribution of bound analyte along the length of the

functionalised surface. Strategies which compensate the analyte depletion and ensure a more uniform distribution of bound analyte along the functionalised surface are needed for the design of sensitive microfluidic biosensors.

The design of optimised microfluidic systems is benefited by mathematical models and theoretical analysis. Mathematical models are valuable tools for the analysis of existing devices but more importantly can give invaluable insight into the device behaviour which can be used in the design of future devices. In this thesis the transport and reaction of analytes in microfluidic systems is modelled through a set of differential equations with suitable boundary conditions. The resulting mathematical model is evaluated for two different physical regimes of the microfluidic system. These regimes are characterised by the nondimensional Graetz number Gz which is the ratio of the diffusion time to the residence time. In the 'fully developed' regime ($\mathrm{Gz} \ll 1$) every analyte molecule can diffuse to the functionalised surface while in the 'entrance region' ($\mathrm{Gz} \gg 1$) some analyte molecules flow through the channel before they can diffuse to the functionalised surface.

In the first part of this thesis integrated microfluidic affinity systems which are operated in the 'fully developed' regime ($\mathrm{Gz} \ll 1$) are analysed. This regime is especially suited for the separation and detection of analyte molecules from complex samples because every analyte molecule can reach and interact with the receptor molecules at the active surface. Several microfluidic separation systems, which operate in this regime, have been reported in the literature [20]. However, a thorough theoretical investigation describing the separation process as a function of the interaction of the solution phase analyte with the surface immobilised receptor has not been previously reported. Here the governing equations for the microfluidic affinity system are analysed and simple, analytical expressions for the analyte retention time and dispersion are derived. These analytical expressions are then used to derive a design framework for multiplexed microfluidic separation systems for the separation of proteins. The integration of parallel and serial separation in one multiplexed separation system offers the possibility of efficient and automated analysis of complex biological samples from small sample volumes. Conventionally, such a design would require either many iterative trial and error steps or computationally expensive numerical simulations of the nonlinear governing equations.

The second application of integrated microfluidic systems in the 'fully developed' regime is the sensitive detection of low concentrations of proteins from minute sample quantities. Here it is important to design the integrated microfluidic system so that a significant fraction of the analyte molecules bind to the surface immobilised receptor molecules. However, for these systems most of the analyte association will happen near the beginning of the active sensor region and the analyte concentration in the main part of the flow will be significantly depleted [19]. Little design consideration has previously been given to strategies which provide uniform analyte mass transfer to the active surface and subsequent association over the whole sensor patch. After showing the shortcomings of standard rectangular biosensors with constant device parameters, design guidelines and assay protocols which increase the uniformity of the surface bound analyte along the channel length are presented. The increased uniformity of the associated analyte along the sensor surface will provide a more robust and potentially more sensitive integrated microfluidic affinity sensor. The derived design guidelines are used to redesign the flow cell of the optical waveguide sensor of Hua et al. [21] for the detection of low levels of cytokines from small sample volumes. The redesigned flow cell has the potential to reach a similar limit of detection ($\sim 1\,\mathrm{ng\,l^{-1}}$) while reducing the sample consumption from the millilitre to the low microlitre range. This reduction in sample consumption is important for the continuous monitoring of cytokine levels, so that as little blood as possible is needed from the patient, and for the analysis of samples which are only available in limited quantities, e.g. the blood of neonates or cerebrospinal fluid [22].

The second part of this thesis considers microfluidic systems which are operated in the 'entrance region', i.e. $\mathrm{Gz} \gg 1$. In this regime, where the residence time is much shorter than the diffusion time, the mixing of two parallel flowing analyte streams is negligible; thus the mixing of two analyte streams poses a significant challenge. One possibility to increase the analyte transport from a source to a sink stream is the incorporation of a micromixer into the microfluidic channel [23]. Micromixers which use surface groove induced secondary flow are considered to be the 'gold standard' of passive micromixers [24]. The surface grooves induce a secondary flow with components perpendicular to the main flow direction. This secondary flow has been used to increase the mixing of two analyte streams or to improve the transport of analytes to the active

surface in microfluidic affinity sensors [25]. Here the secondary flow is used to transport analyte molecules in a controlled manner from the source stream to the sink stream and thus creating a controlled concentration gradient across the width of the microfluidic channel. These concentration gradients have many applications: microfluidic grey-scale masks [26] and the study of chemotaxis [27] to name only two.

It has been shown that the secondary flow depends on the shape and size of the surface grooves [28; 29]; thus the secondary flow can be manipulated by a change in the groove shape and size. Here numerical optimisations, over the groove shape and size, are performed with the aim of matching the concentration profile at the channel exit to a predefined concentration profile. The resulting grooved gradient generator requires less chip real estate compared to conventional gradient generators which rely on diffusion [30] alone.

1.2 Methods

This thesis focuses on the use of mathematical methods for the evaluation and improvement of analyte transport in integrated microfluidic systems. The mathematical models for the analyte transport in integrated microfluidic systems are analysed by analytical and numerical methods. The resulting solutions are used to interpret the behaviour of existing device but more important to predict the behaviour of microfluidic devices with different geometries or operational parameters.

The aim in this work is not to create a highly specialised mathematical model of a specific analyte system, but rather to create approaches that contain the main elements of the physical system and that can be easily exploited to evaluate and improve the behaviour of integrated microfluidic affinity systems. The used methodology starts by analysing the governing equations through nondimensionalisation. This reveals the relationship between different physical effects in the system, e.g. the Graetz number links diffusion and convection, and is a valuable tool in the understanding of the physical system. In the next step the governing equations are analysed in the asymptotic limits of the nondimensional numbers. The resulting approximate solutions are limiting cases for

the device behaviour and thus provide insight into the scope of the analysed system. The last step is the numerical simulation of the system for specific parameter values. These simulations can provide accurate solutions of the full system for one set of parameter values but give no insight into the general device behaviour or the relationship between the physical effects.

The use of both analytical and numerical methods combines their advantages and strengths and allows the circumvention of the weaknesses of each approach. Together they provide a more complete and reliable picture of the device behaviour.

1.3 Thesis structure

Chapter 2 introduces microfluidic lab-on-a-chip systems and their bioanalysis applications. The characteristic attributes, advantages and disadvantages, as well as the relevance of microfluidic affinity systems, i.e. affinity sensors and affinity separation devices, for bioanalytical applications are detailed. The microfabrication methods and device operation of lab-on-a-chip systems including device assembly and detection methods are described next. Due to the wide range of applications this chapter details only generic properties and applications of microfluidic affinity systems. More specific background reviews are given at the beginning of the relevant chapters.

Chapter 3 describes the mathematical modelling of microfluidic systems with affinity interactions between analytes and surface immobilised receptor molecules. The governing equations for the fluid flow and the transport-reaction problem are introduced. These equations are nondimensionalised to identify the important nondimensional numbers whose values give insight into the device behaviour. At the end of the chapter a review of the previous work on the governing equations is presented: general solutions, approximate solutions in the asymptotic limits of the nondimensional numbers and numerical solutions are given.

Chapter 4 is concerned with the modelling and application of microfluidic devices for the separation of proteins. The mathematical model developed in chapter 3 is simplified for systems with fast diffusion across the channel height and high adsorption capacity.

By solving the reduced problem analytically two simple, analytical expressions, that describe the retention time and dispersion of sample plugs in open microfluidic affinity separation systems, are revealed. Together these expressions describe the behaviour of sample plugs in microfluidic separation systems. The remainder of the chapter details the application of the two analytical expressions for the design of multiplexed separation systems for the parallel and sequential separation of proteins from complex samples.

Chapter 5 presents new design strategies to improve the analyte mass transfer to the active surface and subsequent association to surface immobilised receptor molecules. The simplified model from chapter 4 is used to design microfluidic systems which optimise the analyte capture fraction and the uniformity of the distribution of bound analytes along the sensor surface simultaneously. Analytical and numerical optimisation techniques are used to evaluate the effect of (i) a variation of the analyte flow velocity over the affinity sensor, (ii) a non-uniform distribution of surface immobilised receptor molecules along the active area and (iii) non-rectangular device geometries. Subsequent numerical simulations with the full transport-reaction model are employed to verify the predicted high capture fraction and uniform bound analyte distribution over the sensor surface of the modified systems.

In chapter 6 the theoretical approaches from chapter 5 are applied to the redesign of a microfluidic affinity sensor for the detection of low levels of cytokine from small samples. The microfluidic flow cell of the waveguide sensor from Hua et al. [21] is replaced by a flow cell with tapered channels and 'boat-shaped' sensor patches. This redesigned flow cell reduces the sample consumption while retaining the excellent limit of detection. The fabrication and alignment, which are crucial for the efficient device operation, of the biosensor are described. The limit of detection of the assembled device is established with bulk dye experiments.

Chapter 7 details the use of surface groove induced secondary flow for the generation of concentration gradients across microfluidic channels. The shape of the surface groove, which controls the secondary flow profile, is varied with the aim of matching a predefined concentration gradient across the outlet of the microfluidic channel. Numerical optimisation over the shape and dimensions of the surface groove is used to achieve the

desired linear or exponential concentration gradient profiles.

Chapter 8 summarises the achievements and results obtained in this thesis and suggests directions for further work.

Chapter 2

Background - Lab-on-a-chip systems

2.1 Introduction

The lab-on-a-chip concept was introduced in the early nineties by Manz and coworkers [31] and has since then received much attention. The idea behind the lab-on-a-chip concept is the integration of several laboratory functions, which are normally performed in specialised laboratories by trained staff, on a single microfluidic chip. These lab-on-a-chip systems have many advantages compared to laboratory scale systems. The small size of the microfluidic channels in these devices leads to fast analysis times, a large reduction in the required sample volume and highly portable devices [32]. Reducing the sample volume from the millilitre to the micro- or even nanolitre range reduces the reagent and disposal costs and perhaps more important makes the sample collection less invasive [33]. This is especially vital for chronic conditions where a patient has to be monitored continuously or at least frequently. Further advantages are the improved control of the microenvironment and the potential for the integration of multiple analysis steps in one microfluidic lab-on-a-chip system. For example, the stable, laminar flow in microfluidic channels can be used to precisely control the chemical and mechanical environment and thus to mimic the *in vivo* microenvironment [34]. Finally, the integration of several laboratory functions such as sample preparation, separation and detection into one microfluidic device creates a more robust analysis system and facilitates the automation of the analysis [4].

While this thesis is mainly concerned with the modelling of microfluidic lab-on-a-chip systems it is important to understand the applications of these devices as well as the limitations in device fabrication and operation. In this chapter an overview of the practical aspects of lab-on-a-chip systems is presented. First, the application of lab-on-a-chip systems for the study of proteins is described. Next the major microfabrication methods for lab-on-a-chip systems are reviewed: both the traditional methods in silicon and glass as well as the methods for polymer fabrication are covered. In the last sections an overview of the device assembly and operation is given; this includes the sample introduction, surface modification of the channel walls and the main detection methods.

2.2 Applications

The lab-on-a-chip concept has been applied to numerous bioanalysis and chemical analysis systems ranging from river water monitoring [21] over cell and tissue analysis [35] to immunoassays [8]. Immunoassays are biological assays which are used to detect or quantify an analyte (antibody or antigen) based on a recognition-binding event between antibodies and antigens [36]. The formation of the antibody-antigen complex is translated into a detectable signal (section 2.5) which is related to the concentration of the target analyte. Immunoassays are very sensitive and specific due to the very specific antibody-antigen interaction.

The integration of immunoassays into lab-on-a-chip systems has great potential for the analysis of proteins and their interactions [4]. Proteins are the active components of the organism and knowledge of their quantities and interactions is crucial for a complete understanding of biological systems [5]. Furthermore, proteins can act as biomarkers and targets for drugs which makes them important for the diagnosis, understanding and treatment of diseases [37]. Lab-on-a-chip systems for the analysis of proteins are developed for two distinct application scenarios [33]. The first scenario requires portable and autonomous devices for the diagnosis at the bedside or in areas without access to conventional laboratories. These point-of-care (POC) devices should be easy to use and independent of external instrumentation [38]. The second scenario requires the high-throughput and large-scale analysis of all proteins in an organism. These systems have

to be highly integrated, automated and parallelised [4]. Both scenarios require analysis systems which are very sensitive and operate on small sample volumes. Microfluidic lab-on-a-chip systems have the potential to fulfil the requirements in both application scenarios. While the research presented in this thesis is more applicable to the second scenario of large-scale analysis systems, there is no fundamental reason why the results can't be applied to POC devices.

The systematic and large-scale analysis of all proteins expressed by the genome is called proteomics [5]. This includes characterising and quantifying the proteins, their interactions and modifications. While the genome of an organism remains almost constant, the proteome of an organism is highly dynamic. The proteome varies for different cell types and changes over time due to different internal and external stimuli such as gene mutation and effects of diet or illness [4]. The well established techniques for the analysis of the genome can be used to gain information about the composition and abundance of proteins because the protein compositions are encoded in the genes and the abundance is related to the levels of mRNA which are translated into proteins [5]. However, the genome provides no information about post-translational modifications, localisation of the gene products and protein-protein interactions [37]. Furthermore, the levels of mRNA which are linked to the protein expression are not necessarily equal to the protein expression levels [39]. Thus the direct analysis of proteins is necessary to gain a complete understanding of the proteome.

The direct analysis of the proteome requires sophisticated methods for the preparation, separation and detection of the constituent proteins because the concentrations of the ~ 20000 proteins in a human cell range over $6 - 8$ orders of magnitude [7]. The difficulties associated with the large concentration range of proteins, i.e. sub-picomolar to micromolar, are increased by the absence of amplification methods in contrast to the analysis of the genome which has polymerase chain reaction (PCR), which can amplify a single DNA molecule by several orders of magnitude, for the amplification of minute concentrations [40]. A further difficulty lays in the limited sample volumes. For example, for the study of the proteins of a small number of cells the available sample volume is in the picolitre range. To sum up, the large number of proteins, the large dynamic range and the limited sample volumes pose significant challenges on the sensitivity, selectivity

and dynamic range of the analysis tools.

The analysis of the proteome in a conventional laboratory is a slow and labour-intensive process. Commonly the proteins are extracted from cells, separated by gel electrophoresis (see section 4.2) and analysed by mass spectrometry (MS) [5]. Integrating these or similar steps in a lab-on-a-chip device could reduce the analysis time and complexity considerably. Furthermore, the small, highly controllable microenvironment and the possible automation of integrated devices facilitates the analysis of the proteome from complex biological samples which are only available in small quantities. Typical sample sizes in microfluidic systems range from the high picolitre to low microlitre range [32]. These small sample sizes are useful for the analysis of small cell populations or even single cells.

In summary, microfluidic lab-on-a-chip systems have the potential for the automated and parallel analysis of proteins from small samples which would allow the systematic and organism-wide analysis of the proteome. However, while most of the required steps for the analysis of the proteome have been achieved in microfluidic systems, e.g. electrophoretic protein separation [41] and sensitive detection [42], a complete, fully integrated device for the automated protein analysis is still missing.

2.3 Fabrication

In the early days of microfluidic devices the fabrication techniques were mainly adapted from the well developed techniques used for the fabrication of microelectronic devices and were thus focused on silicon as a substrate material [43]. As the field developed different techniques and substrate materials were used as an alternative to silicon fabrication [44], notably fabrication in glass and polymers. This section gives an overview of the main fabrication methods and materials. It starts with silicon and glass fabrication and moves on to polymer fabrication which is becoming widely used as a substrate material for lab-on-a-chip devices [45]. All fabrication methods in this section create 2D structures in the plane of the substrate surface unless otherwise specified.

2.3.1 Silicon fabrication

Silicon was used for the early microfluidic systems for bioanalytical applications [43]. However, in recent years the fabrication of microfluidic systems has shifted away from silicon which is mainly due to the high cost of silicon fabrication and the optical and electrical properties of silicon, i.e. silicon is opaque in the visible light spectrum and not ideal for capillary electrophoresis.

Etching techniques are the most widely used microfabrication techniques for the fabrication of microfluidic structures in silicon substrates [43]. All etch techniques start with the deposition of a masking layer which protects the substrate material and leaves only parts of the substrate exposed to the etchant. This masking step is mainly performed by photolithography which is described in figure 2.1. Briefly, a photoresist is spin-coated onto the substrate material. The photoresist coated substrate is prebaked and then illuminated through a photomask. After this exposure a post-exposure bake is performed and finally the photoresist coated substrate is developed which reveals the intended pattern. After the photolithographic patterning the exposed areas of the substrate are etched. The etchant which can be a liquid (wet etching) or an ionised gas (reactive ion etching) chemically or physically removes layers of the exposed substrate. A schematic of the etch process of silicon is shown in figure 2.1. The removal of the substrate material can be either isotropic where the etching is equally fast in every direction or anisotropic. The figure shows the resulting shapes for an isotropic wet etch in (8a) and for an anisotropic wet etch in (8b) and (8c). The shapes of the anisotropic wet etch are defined by the crystallographic planes of the silicon. Wet etching in silicon is a relatively simple fabrication method which has been used to fabricate channels with sub-micrometre depth [46]. The lateral feature size is defined by the photolithographic masking step, which can achieve sub-micrometre features, and by the required etch depth, i.e. in the isotropic etch the substrate is etched in every direction so that the etch depth and the feature size are linked.

An alternative to wet etching is deep reactive ion etching (DRIE) where the etchant is an ionised gas [47]. Here the substrate material is removed by a combination of a physical and chemical etching component. Ions are accelerated by an electric field

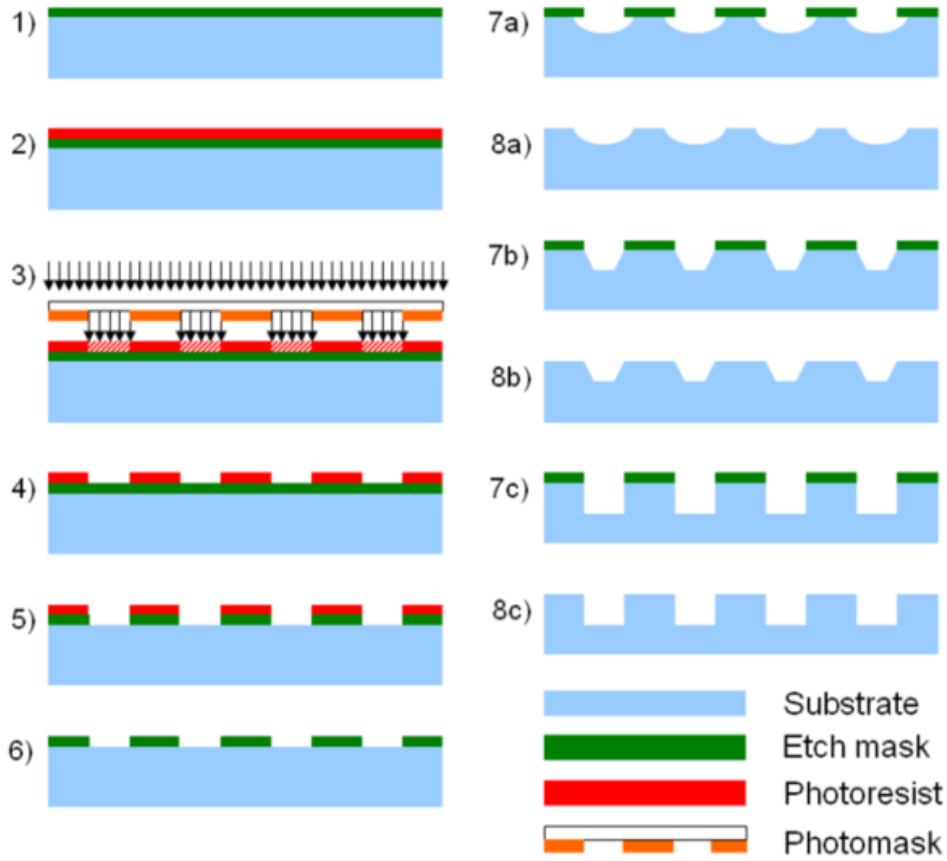

Figure 2.1: Schematic of the photolithographic patterning and of the silicon wet etch process: (1) the material to protect the bulk material is deposited, (2) a photoresist is coated on the protection material, (3) the photoresist is illuminated through a photomask, (4) the photoresist is developed which removes the exposed areas in the case of positive photoresist as shown or removes the unexposed areas in the case of negative photoresist, (5) the protection material is etched which leaves parts of the bulk material open, (6) the remaining photoresist is removed, (7) the actual etching step is performed and (8) finally the remaining protective material is removed. (7a) and (8a) show the resulting profile for isotropic etch with HF-HNO_3, (7b) and (8b) show the anisotropic KOH etch in silicon $\langle 100 \rangle$ and (7c) and (8c) show the anisotropic KOH etch in silicon $\langle 110 \rangle$.

towards the silicon substrate which produces a relatively slow but anisotropic etch. The chemical component results from the reaction between radicals, e.g. SF_6 or CBr_4, and the silicon substrate. This chemical component is much faster than the physical component but is isotropic. An anisotropic etch is achieved by alternating this etching step with a passivation step. The process starts with an isotropic etch which creates a small, initial trench. After this the passivation step, in which a protective layer is deposited on the whole substrate, and the etching step alternate. In the etching step the anisotropic physical etch removes the protective layer only from the bottom of the trench which is then etched isotropically. DRIE has high etch rates and most important an anisotropic etch profile which allows near vertical side walls. The resulting structures are independent of the orientation of the crystal and aspect ratios of up to 50 : 1 are possible. The feature size is only limited by the photolithographic masking step.

2.3.2 Glass fabrication

Glass has been used in biological and chemical experiments for hundreds of years so it is an obvious choice for the development of a lab-on-a-chip device. Besides the chemical stability glass has some advantages compared to silicon. Glass is transparent in the visible light spectrum so that optical methods can be used for the observation and monitoring of the device behaviour. Furthermore, glass has better electrical properties, e.g. glass is an insulator, than silicon which allows its use for electrophoresis applications [22].

Wet etching is the most widely used microfabrication technology for glass microfluidic devices [48]. The process is comparable to the process for silicon wet etching shown in figure 2.1 and the resulting structures are similar to the trenches in figure 2.1 (8a). Wet etching in glass which is performed with various concentrations of hydrofluoric acid has achieved etch depths of 500 μm with etch rates up to 8 $\mu\mathrm{m\,min}^{-1}$. Similar to the isotropic wet etch of silicon the feature size is limited by the masking step and the required etch depth.

Deep reactive ion etching (DRIE) for glass has been shown to achieve high aspect ratio ($> 10 : 1$) channels with nearly vertical and smooth side walls [49]. In contrast to DRIE of silicon the anisotropic etching is achieved by an increase of the physical

component through an increase of the applied bias voltage. However, the etch rates which depend strongly on the glass composition [50] are below $1\,\mu\mathrm{m\,min^{-1}}$ which is much slower than the wet etch of glass or DRIE of silicon. Ion beam etching (IBE) is a dry etch process which relies solely on the physical component [43]. The substrate is bombarded with inert ions which remove layers of the substrate material. IBE can achieve high resolution features ($< 10\,\mathrm{nm}$) but the etch rates are even slower than for DRIE of glass.

2.3.3 Polymer fabrication

In recent years microfluidic devices made from polymers have received much attention in the microfluidics community [51]. There are many reasons for the shift away from silicon and glass fabrication. The main advantages of polymer devices are the relative low cost of the substrate material and fabrication methods compared to silicon and glass [45]. The lower fabrication costs are mainly due to the existence of replication methods such as hot embossing, injection moulding and casting which are not available for silicon or glass substrates. Furthermore, many of the polymer fabrication methods are relatively simple and do not require expensive or aggressive chemicals. An overview of the achievable structures with the different polymer fabrication methods is given in table 2.1.

Technique	Thickness	Min. structure widths	Aspect ratios max	Normal aspect ratios
Contact UV lithography	Up to mm	1 μm	100:1	10:1
X-ray lithography	Up to few mm	1 μm	1000:1	20:1
Electron beam lithography	Few μm	10 nm	2:1	1:1
Laser ablation	Up to ~100 μm	<1 μm	2:1	1:1
Polymer etching	Up to ~100 μm	few μm	20:1	1:1
Casting	Up to mm	10 nm	10:1	2:1
Hot embossing	Up to mm	10 nm	10:1	2:1
Injection molding	Up to mm	1 μm	2:1	1:1

Table 2.1: Overview over microfabrication methods. Reproduced from [52] with permission from the author.

A further advantage of polymer fabrication is the large diversity of the different

polymers [45; 53]. The mechanical properties, temperature stabilities, optical properties and resistances against acids and bases of different polymers vary over a considerable range. For example, Polyetheretherketone (PEEK) is stable for temperatures up to 250°C and Cycle-olefine copolymer (COC) and Polymethylmethacrylate (PMMA) have a high transparency and are resistant against many acids and bases.

Polymers have some disadvantages for microfluidic applications compared to silicon and glass [53]. The resistance to chemicals in general is lower and polymer materials deteriorate with time. Furthermore, polymer materials generally have a lower mechanical stability and UV radiation increases the aging. A further drawback is the increased autofluorescence compared to glass [54]. For shorter wavelengths ($\lambda_w < 400\,\mathrm{nm}$) many polymers exhibit up to 4 times higher absorbance and up to 10 times higher autofluorescence. This can prove problematic for devices with optical detection and special attention has to be paid to the choice of polymer material with respect to the excitation and detection wavelength.

From a fabrication point of view polymers can be divided into three main classes which are mainly defined by the glass transition temperature T_g and the interaction of the polymer chains:

1. Thermoplastic polymers: unlinked or weakly linked chain molecules. If the polymer is heated above the glass transition temperature it can be moulded by replication methods such as hot embossing or injection moulding. Examples: PMMA, COC, polycarbonate (PC)

2. Elastomeric polymers: weakly linked chains. The polymer molecules return to their original state after stressing and relaxing. Example: poly(dimethylsiloxane) (PDMS)

3. Duroplastic polymers: chain molecules cross-link if subjected to enough heat, pressure or radiation. The curing is an irreversible chemical reaction so that the duroplastic polymers can only be shaped once. Examples: SU-8, polyimide

Direct mastering

Direct mastering of polymer devices refers to the fabrication of a system without the need for a master [45]. The most widely used direct mastering method is based on photolithography which was introduced in section 2.3.1. Conventional photoresists, which are used for the patterning of masks for etch processes, can only provide a layer thickness of a few micrometres. However, the arrival of thick photoresists which allow the patterning of hundreds of micrometre thick layers increased the interest in photoresists as structural materials [55; 56]. Especially the negative photoresist SU-8 is becoming more important in the microfabrication of microfluidic systems [44; 45]. A layer thickness of several hundred micrometres can be achieved in one spin-coating step of SU-8 [55]. This thick SU-8 layer is processed by conventional photolithography. However, the optimisation of the fabrication protocol for thick SU-8 layers is more crucial than for conventional photoresists; pre- and post-exposure bake times, as well as the exposure dose have to be considered more carefully to achieve high quality and crack-free structures [57; 58]. SU-8 processed by photolithography can be used to create channels which have near vertical side walls, high aspect ratios (100 : 1) and sub-micrometre features [55]. Sequential processing of multiple SU-8 layers allows the fabrication of channels with a limited 3D structure [55].

A fully processed SU-8 structure has good mechanical strength and is chemically resistant against many acids and bases [45]. Furthermore, SU-8 has good optical properties with a transmittance of more than 92% for a 250 μm thick layer at a wavelength of 488 nm [59]. A drawback is the autofluorescence of SU-8 which is higher than the autofluorescence for glass. Excitation with a 488 nm wavelength laser induces a broad autofluorescence spectrum with wavelength in the 520 nm to 650 nm range. While several studies have shown that SU-8 is biocompatible [60; 61], the water contact angle of $\sim 90^\circ$ makes the surface prone to biofouling, i.e. proteins attach nonspecifically to the SU-8 surface. Oxygen plasma treatment or surface modification with cericammoniumnitrate and ethanolamine can lower the contact angle and thus the hydrophobicity so that the surface is more resistant to biofouling [62; 63].

Further direct mastering methods include micro-stereolithography [64] and laser ab-

lation [65; 66]. The former is a true 3D microfabrication technique which can create arbitrary 3D structures with micrometre features by scanning a focused laser beam through a photocurable liquid monomer. In the latter method, laser ablation, the substrate material is ablated by focusing a high energy laser beam onto the surface of the substrate. This can results in channels with near vertical side walls and micrometre-sized features [67]. Laser ablation is suitable for generating structures with a limited 3D component in almost any material; the structures can have an arbitrary shape in the plane of the substrate surface and can vary in depth across the substrate. However, the resulting surface roughness is usually much higher than for the unablated substrates. Laser ablation has been used to fabricate channels in a wide variety of polymers such as PC, PDMS, PMMA and polystyrene as well as in glass. The flexibility of these two methods, micro-stereolithography and laser ablation, is offset by the long process time which can reach several hours for complex designs.

Replication methods

The existence of replication methods for polymers is one of the main reasons for the increased interest in polymers as substrate material for microfluidic lab-on-a-chip devices [45]. Replication methods work by moulding the intended device structure from a master which is fabricated as the inverse of the intended structure. This allows the fast and inexpensive fabrication of multiple devices with cycle times between a few seconds (injection moulding) and a few hours (casting of PDMS). This opens opportunities for inexpensive and disposable lab-on-a-chip systems.

The fabrication of the mould master is a crucial step in every replication method because the resolution and surface roughness of the replicated structure can only be as good as the resolution and surface roughness of the master. Table 2.2 gives an overview of the different master fabrication techniques and their properties. The required thermal and mechanical stability of the master depends on the requirements of the replication method and the size of the replication series, i.e. injection moulding has higher requirements than hot embossing and casting.

The most widely used mastering method in academia is photoresist mastering with

Microfabrication technology	Choice of geometry	Min. feature size	Height	Total surface area	Aspect ratio	Lifetime	Cost	Commercial availability
Wet silicon etching	-	+	0	++	-	+	+	++
Dry silicon etching	+	++	+	++	+	-	0	+
Photoresist	+	++	+	++	++	-	+	0
Polymer casting (elastomer)	+	++	0	++	-	-	++	-
Optical lithography & electroforming	+	++	+	++	0	+	0	0
Laser ablation & electroforming	++	+	+	-	+	+	-	-
LIGA	+	++	++	-	++	+	-	-
(Ultra) precision micromachining	+	0	+	+	0	++	-	-
μ-EDM	-	0	+	-	+	++	-	-

Table 2.2: Properties of master fabrication methods. With kind permission from Springer Science+Business Media: table 3 from [45]

the thick photoresist SU-8 [68; 69]. The fabrication of SU-8 masters by photolithography is fast and inexpensive compared to other mastering methods. Hard-baked SU-8 which has good mechanical stability and low surface roughness is mainly used as master for the casting of PDMS. Casting is the process where an elastomeric polymer is poured onto a master and then cured [70]. This process is especially widespread in the academic world due to its simple process and low tooling costs. The general concept is shown in figure 2.2: (1) a master is fabricated, (2) the elastomer is poured onto the master and cured either thermally or optically, (3) the cured structure can be peeled from the master. The cycle times of casting are long compared to the other replication methods

Figure 2.2: Casting of PDMS. (1) fabrication of the master (black), (2) pouring and curing of the elastomeric polymer (grey), (3) removal of the cured structure from the master.

so that casting is only feasible for small series of devices. The quality of the replicated channels is initially very good but deteriorates quickly so that the SU-8 master can only

be used for a small series of devices (< 50).

Casting is almost exclusively performed with PDMS. Depending on the quality of the master casting PDMS can reliably produce sub-micrometre features with very low surface roughness and aspect ratios up to $10 : 1$. Furthermore, depending on the master casting PDMS can create structures with an arbitrary shape in the plane of the substrate and varying depth across the substrate. Besides the easy fabrication PDMS also has good properties for microfluidic affinity systems [71]: it is optically transparent down to a wavelength of 300 nm, electrically insulating and chemically inert. However, for optical detection some attention has to be given to the choice of the wavelength due to the higher autofluorescence of PDMS compared to glass [72]. With the right choice of fluorophore the detection limit of laser-induced fluorescence detection (section 2.5) in PDMS channels can be similar to the detection limit in glass devices [73].

Due to the elasticity of PDMS, it has good sticking properties to many surfaces and it is easily handled. PDMS sticks to glass, silicon and other polymers and this can be used as a reversible seal for low pressure applications [70]. For applications requiring higher pressures, an irreversible bond can be achieved by oxygen plasma treatment, i.e. exposure of the PDMS surface to an oxygen plasma in a reactive ion etching system, of the PDMS substrate [68]. On the other hand the elasticity can lead to deformations of microchannels and the collapse of suspended structures [74]. The surface of PDMS channels is hydrophobic which means that the surface is prone to biofouling. Oxygen plasma treatment or the grafting of proteins can make the surface more hydrophilic which reduces the nonspecific attachment of proteins to the PDMS surface [75; 76]. The oxygen plasma treatment reduces the contact angle the greatest but the surface is only stable for a few hours while the surface grafted polymers can be stable for several days. A further problem with PDMS is the shrinkage of the system during curing which increases with the curing temperature and can reach up to 2% [77].

While the casting of PDMS is widely used in the academic world it is unsuitable for the large-scale fabrication of microfluidic lab-on-a-chip systems. However, the other two replication methods, injection moulding and hot embossing, allow the fast and inexpensive fabrication of thousands of devices [78]. The injection moulding process for

microfabrication, which is adapted from the widely used process in the macro world, is shown schematically in figure 2.3. Injection moulding can produce structures which can have any 2D shape and a limited 3D component with micrometre-size features and aspect ratios of 2 : 1. The process can be fully automated and is capable of fabricating thousands of devices with cycle times on the order of seconds. It is therefore mainly used in industrial settings for large batches of devices.

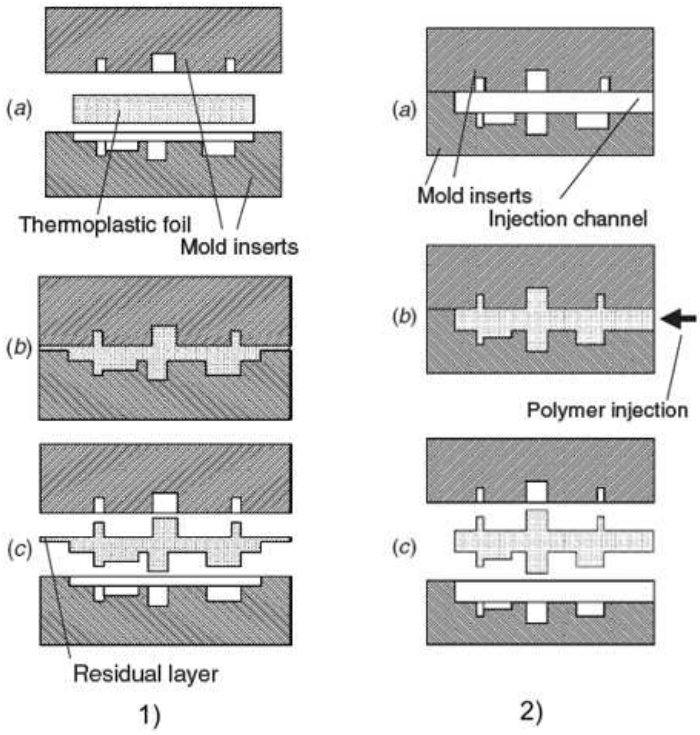

Figure 2.3: Schematic diagram of (1) hot embossing and (2) injection moulding. Reproduced from [78] with permission from the author and IOP Publishing Ltd.

The hot embossing process which is shown schematically in figure 2.3 can repeatedly create complex 2D structures with very small feature sizes (10 nm) and high aspect ratios (10 : 1) [78]. The higher resolution compared to injection moulding is due to the shorter distance the polymer has to flow. This also leads to lower stress in the polymer which is important for optics applications. The relatively simple process can be adapted easily from one polymer to another without changing the setup of the machine. The main costs of hot embossing are the master fabrication, for example by LIGA, and the mounting of the polymer substrate which is not easily automated. This manual mounting leads to relatively long cycle times of hot embossing compared to injection

moulding. Thus hot embossing is mainly used for small to medium batches of devices.

A drawback of injection moulding and hot embossing are the higher tooling costs compared to casting and the higher requirements on the master due to the employed temperatures and pressures. One of the main master fabrication methods for these replication methods is 'Lithografie, Galvanik und Abformung' (LIGA) which is German and means 'lithography, electroplating and molding' [79]. In the LIGA process a metal mould is grown electrolytically in a PMMA mould which is defined through x-ray lithography. The resulting master has very high precision and very low surface roughness but the process is complex and expensive. Due to the good properties of the electroformed master a variety of other methods besides PMMA x-ray lithography have been used as a mould for electroforming. The thick photoresist SU-8 [80] and laser ablation [81] have been used to define the mould for electroforming in processes called UV-LIGA and Laser-LIGA, respectively. The results are almost as good as for the more expensive LIGA process except for a reduced aspect ratio and feature height. Further master fabrication methods are etching in silicon and glass substrates and laser ablation [82].

2.4 Device operation

2.4.1 Surface modification

The large surface to volume ratios of microfluidic channels, which are 100 times higher than in microtiter plates, make them interesting for heterogeneous, surface based bioanalysis systems where the interactions between analytes in solution and surface immobilised receptors are studied (see section 3.3). The large surface to volume ratio ensures that the ratio of surface immobilised receptors to analyte molecules is higher than in microtiter plates which improves the sensitivity of the bioanalysis system. These heterogeneous bioanalysis systems require the immobilisation of receptor molecules to one or more of the channel walls in a controlled pattern [83].

In the easiest, but also least controllable, way to pattern the surface: a droplet of the solution containing the target receptor molecules is pipetted onto the surface. After a

sufficient incubation time, during which the receptors associate to the substrate surface, the remaining solution is washed off. This method offers almost no control over the size of the receptor patch and is therefore not suitable for highly integrated microarray or microfluidic systems. A widely used method to improve the spatial accuracy and repeatability of this method is ink-jet patterning [84]. This methods adapts commercial ink-jet printers to directly print small droplets of protein containing solutions onto the substrate surface. Multiple, different receptor molecules can be printed and the spot size is on the order of 100 μm. A further method which improves the accuracy of the pattern is microfluidic patterning [85], see figure 2.4. Here a microfluidic network is placed over

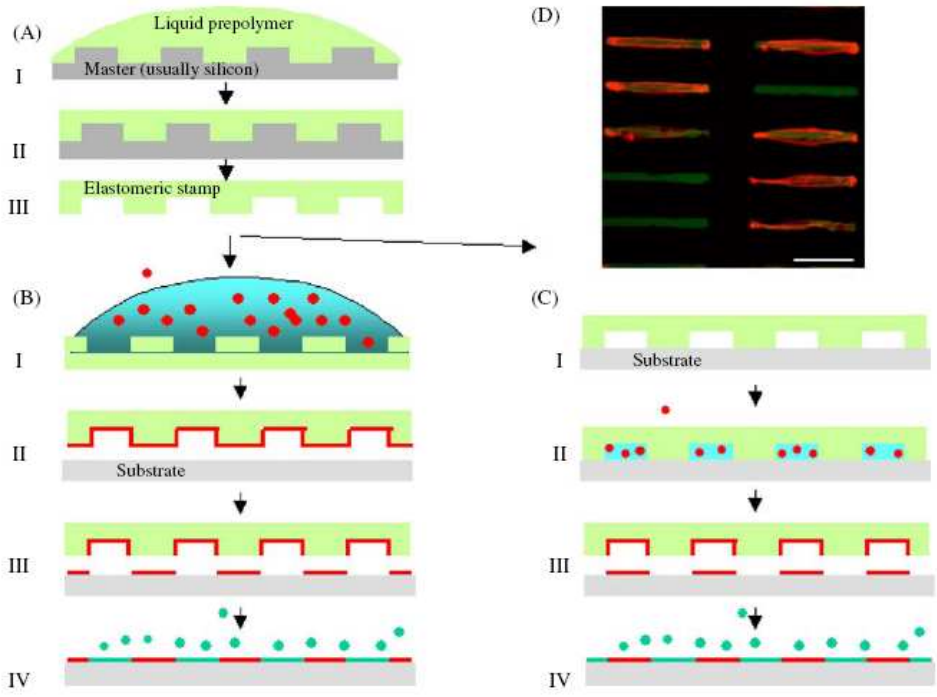

Figure 2.4: Schematic diagram of (B) microcontact printing and (C) microfluidic patterning. (B) In microcontact printing the target receptor molecules (red) are incubated on the stamp (green) which is then pressed against the substrate. (C) In microfluidic patterning the target receptor molecules (red) are flowed through a microfluidic network (green) which is placed onto the substrate. Reprinted from [83] with permission from Elsevier.

the substrate surface and a solution containing the target receptor molecules is flowed through these channels. The patterning of different receptors on one surface is straight forward by using different receptors in different channels. While this method offers good

control over the surface concentration, the achievable patterns are restricted to fluidic networks.

Microcontact printing is one of the most widely used surface patterning methods [83]. In this method, which is shown schematically in figure 2.4, an elastomeric stamp which is created by casting (see section 2.3.3) is incubated with a solution containing the receptor molecules. The incubated stamp is then pressed against the substrate to transfer the receptor molecules to the substrate. This method has been used with a wide range of receptor molecules such as avidin and protein A and substrates ranging from glass to metal and polymer surfaces. The surface concentration of the immobilised receptor molecules can be modified by changing the concentration of the incubation solution. Patterns with sub-micrometre features have been achieved with PDMS stamps [86]. Furthermore, microcontact printing can be used to create patterns of different receptors either in a sequential or a parallel way. The first way requires the repeated aligning and stamping of the substrate [87; 88] while the latter requires the incubation of one stamp with different receptors [89]. Limitations of this technique are variations in the receptor concentration across large stamps and between different experiments.

A further patterning method is photoimmobilisation patterning [90]. Here the receptor molecules are immobilised on the substrate surface by a linker molecule which is activated by UV light. The shape of the pattern is either defined by a photolithographic mask (section 2.3.1) or by scanning a laser across the substrate. The immobilisation yield is correlated to the exposure dose which allows the creation of gradients in the concentration of surface immobilised receptor molecules. The feature size of photoimmobilisation patterning depends on the patterning method; photolithographic patterning can achieve sub-micrometre features and the feature size of the second patterning method, i.e. scanning a laser across the substrate, depends on the spot size of the laser beam.

2.4.2 Device assembly

The microfabrication methods described in section 2.3 create only the building blocks of functioning lab-on-a-chip systems. These building blocks have to be assembled, bonded

and connected to the macro world. These back-end processes are crucial for the fabrication of efficient microfluidic lab-on-a-chip systems; advantages gained by microfabrication, e.g. low volume and accurate fabrication, can easily be countervailed by misalignment of the separate building blocks or connectors with large dead volumes.

The microfabrication methods presented in section 2.3 create open structures which have to be bonded to another substrate to create closed microfluidic channels. This assembling of the device frequently requires the alignment of the two substrates, i.e. the structures in one substrate have to be aligned to the structures in the second substrate. The alignment is usually performed in a mask or bond aligner where fiducial marks on the substrates are aligned under a microscope [43]. These allow alignment accuracy down to 0.1 μm. After the alignment step the substrates have to be bonded to create a closed microfluidic channel.

The bonding step which is crucial in the device fabrication of most microfluidic systems differs for different substrate materials. For silicon and glass substrates bonding methods exist which can create high strength molecular bonds [43]. However, these techniques require high temperatures and pressures which can pose problems for lab-on-a-chip systems where biological molecules are immobilised at the channel walls. An alternative method is adhesive bonding which is used for the bonding of silicon and glass to almost any material at low temperatures [91]. Adhesive bonding can be performed at room temperature which leads to low stress bonds. However, the bond strength is lower than for the other bonding techniques. Furthermore, the introduction of an adhesive can have undesired effects, such as clogging of channels or interaction between the analytes and the adhesive. Advantages of adhesive bonding are the ability to bond almost any two materials and the low requirements on the surface topography.

The bonding of polymer microfluidic devices is often simpler than the bonding for glass or silicon devices [45]. As described above in section 2.3, elastomeric polymers like PDMS stick to most flat surfaces which makes PDMS an ideal material for prototype devices. This reversible bond can withstand pressures up to 34 kPa [71]. Irreversible and stronger bonding with bond strength up to 400 kPa can be achieved through oxygen plasma treatment of PDMS [92].

Adhesive bonding is a common technique for the sealing of polymer microfluidic channels [45]. The choice of adhesive material depends on the possible activation method which can be UV light, heat or pressure as well as on the required parameters of the device. The glue has to be resistant to the used sample fluid to prevent contamination of the sample. Furthermore, care has to be taken to prevent the glue from flowing into the channel which can lead to an impediment or total blocking of the fluid flow. A variant of adhesive bonding which is only applicable to polymer substrates is solvent bonding [93]. A thin layer of solvent is applied to one of the polymer substrates before they are brought into contact. The solvent dissolves the polymers at the interface. After the evaporation of the solvent the polymers solidify again which combines the two parts. The solvent has to be applied carefully to avoid dissolving the channel structures.

Thermal bonding, where the wafers are heated above the glass transition temperature and pressed together, is a widely used bonding technique for thermoplastic polymers [94]. It achieves the best results if the two wafers have different glass transition temperatures so that only one of them is reached. However, the required temperatures can make thermal bonding unsuitable for lab-on-a-chip systems with biological surface functionalisations. Welding methods, for example ultrasonic [95] and laser welding [96], are variations of thermal bonding. These methods have the advantage that the polymer substrates are heated locally at the interface which reduces the thermal effects on the polymer substrate and the surface functionalisations.

2.4.3 Fluidic connections

The aligned and bonded microfluidic chip has to be connected to the macro world which poses a considerable challenge in the fabrication of microfluidic systems. Microfluidic connectors should have low dead volume, high reliability and ease of use and fabrication. Microfluidic connections can be divided into reversible and irreversible connections. Reversible connections have, in general, a lower connection strength but are beneficial for prototypes where different microsystems and configurations have to be tested. A further division can be made between connections from the top and connections from the side of the device. Connections from the top require the fabrication of holes in one

of the two substrates [97].

Most microfluidic devices have the fluidic connections in the cover plate which separates the microfabrication of the device from the drilling of the hole. The holes in the cover plate can be fabricated by mechanical drilling, ultrasonic drilling, laser ablation or deep etch techniques [43; 97]. If holes in the substrate layer are required the hole fabrication has to be integrated into the substrate layer fabrication or the hole has to be drilled after the substrate layer fabrication. Both methods can be employed for PDMS devices; the hole can be made during the casting of PDMS through capillaries, which are glued to the master, or by punching through the cured PDMS with a syringe needle [98; 99]. Fabricating the holes during casting produces holes with a higher quality and a better reproducibility but adds the extra step of glueing a capillary to the master.

Capillaries can be reversibly connected to PDMS channels due to the elasticity of PDMS. The capillary, which has to be slightly larger than the hole, is simply pushed into the hole in the PDMS. Due to the size difference between the capillary and the hole a tight seal is produced [71]. Depending on the thickness of the PDMS and the size difference between the capillary and hole these connectors can withstand pressures up to 0.6 MPa and tens of insertion and removal cycles [98]. The excellent sealing properties of PDMS with many materials can be utilised to create reversible connectors for microfluidic devices made of silicon, glass or other hard polymers. A connector chip which contains a PDMS slab with holes matching the inlet holes of the microfluidic chip is used to easily and reversibly connect capillaries to a microfluidic chip made of silicon [100]. Capillaries are inserted into the holes and the assembly is pressed onto the cover plate of the microfluidic chip. This setup can withstand pressures up to 0.2 MPa. A similar setup sandwiches a PDMS device between a microscope slide and a PMMA cover [99]. The PMMA cover houses all fluidic connectors and is used to press the PDMS and glass layers together to achieve a good seal.

Commercial connectors are available for the connection of capillaries with outer diameters down to 360 μm to devices with rigid cover plates (Upchurch Scientific, Oak Harbor, USA). These connectors can withstand pressures up to 10 MPa. A drawback of these connectors is the relatively large size of these connectors which limits the con-

nector density in microfluidic systems. A variety of alternative approaches exists which achieve the required connection strengths and often have a smaller footprint. Most of these methods are based on gluing capillaries to the holes with a suitable adhesive [97]. Glued connectors can withstand pressures up to 0.2 MPa. However, glued connections have similar drawbacks to adhesive bonding: namely, clogging of the channel as well as contamination of the sample. Designs which use a sealing element such as an O-ring circumvent the problem of clogging present in adhesion connections and achieve connections which withstand pressures up to 0.7 MPa [101].

Fluidic connections from the side of the device have the advantage that no holes in the top plate are needed. However, the microfluidic channels either have to go up to the edge of the substrate or the substrate has to be accurately cleaved. Capillaries are pushed into the fluidic channels from the side of the device and fixed with adhesives [102]. The resulting connectors can withstand pressures up to 1 MPa. To accommodate capillaries which are larger than the microfluidic channels connection holes have to be drilled from the side [103]. This requires high precision drilling and alignment similar to the fabrication of holes for connections from the top.

2.4.4 Sample introduction

In contrast to microtiter plates microfluidic lab-on-a-chip systems rely on the flow of the sample through the system. The main methods to induce the flow are electroosmotic flow (EOF) and pressure driven flow [3]. Electroosmotic flow relies on the formation of an electrical double layer at the channel walls. Many channel surfaces are negatively charged so that cations migrate to the wall forming an electrical double layer. By applying an electrical potential along the length of the channel the cations are attracted towards the cathode. The movement of the cations at the channel wall drags the bulk of the liquid along which induces a flat flow profile. EOF is easy to integrate into lab-on-a-chip systems but requires exact control of the wall surface charge and chemistry as well as sample ionic strength and pH. The required large voltages reduce the portability of the device and the electrochemical reactions at the electrodes can have undesired effects such as water electrolysis.

Pressure driven flow is controlled by mechanical pumps. These can be either integrated onto the chip or external [3]. Integrated pumps have the advantage of low dead volume while external pumps are robust and easy to control. The flow rates in pressure driven flow are independent of the channel wall and sample properties but depend on the size of the channels. The resulting flow profile in microfluidic channels is parabolic. This work is mainly concerned with pressure driven flow but most of the models are easily adapted to electroosmotic flow.

The sample introduction in lab-on-a-chip systems is crucial to achieve the desired device performance [104]. The main requirements are low dead volume, easy and repeatable operation and robustness. Sample introduction schemes can be split into two groups: off-chip and on-chip schemes. The main off-chip sample injectors are six-port valves which consist of a sample loop with a fixed volume. This loop is filled with the sample while the buffer is flowed through a parallel channel from the pump to the valve outlet. Once the sample loop is filled the valve is switched and the buffer is rerouted through the sample loop thus injecting the sample into the buffer stream. Sample loops ranging from hundreds of microlitres to tens of nanolitres are commercially available (IDEX Corporation, Benton Harbor, USA). Advantages of off-chip systems are the ease-of-use, robustness and repeatability of the sample injection. A further advantage is the option to replace the sample loop to change the injection volume. However, the fact that the components are not integrated into the chip is a drawback by itself but it also increases the dead volume through the connection between the valve and the chip. A further effect of the connection tubing is the increased plug dispersion and the positional uncertainty of the sample plug due to variations in the tubing length and diameter.

On-chip sample injection methods can be classed according to the flow actuation: hydrodynamic injection and electrokinetic injection. The latter requires fast and precise voltage control and is biased by the migrational behaviour of the sample [104]. Hydrodynamic injection on the other hand is independent of the sample and often easier to implement [105]. The injection methods presented here are based on a microfluidic channel crossing as shown in figure 2.5. The sample injection is achieved by opening and closing the different inlets and outlets of the crossing in a specific sequence. In the simplest form the sample solution is flowed across the crossing, i.e. from (C) to (A)

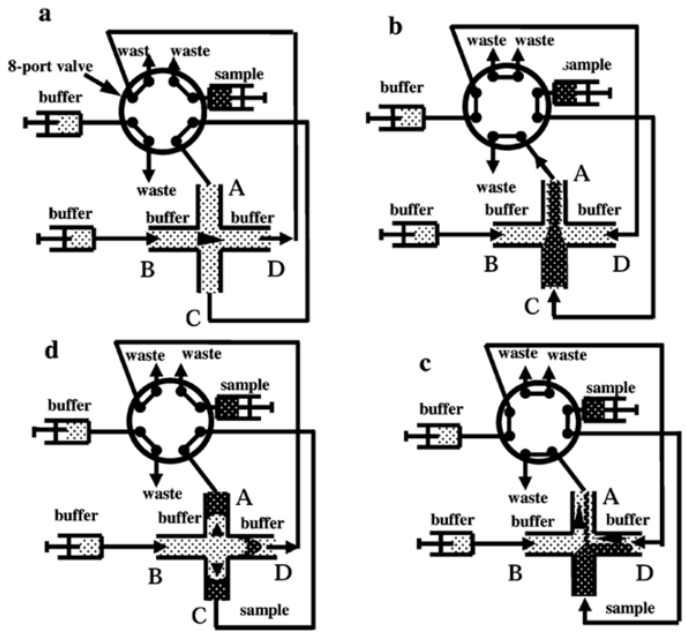

Figure 2.5: Schematic diagram of pinched on-chip sample injection from [106] - Reproduced by permission of The Royal Society of Chemistry. The arms of the crossing are connected to (A) the sample waste, (B) the buffer inlet, (C) sample inlet and (D) the analysis channel. (b) The sample solution is flowed across the channel and pinched from both sides to prevent sample leakage.

in figure 2.5, while the buffer flow (B) is stopped. Switching from the sample (C) to the buffer flow (B) and blocking the sample waste (A) injects a sample plug into the analysis channel (D). The sample size is defined by the geometry of the cross section. A problem for this injection method is leakage of the sample during the sample loading stage. This can be reduced by using pinched injection [106] shown in figure 2.5 or by using a double-T cross section [107] shown in figure 2.6. The former method uses slow flow from the buffer inlet and the analysis channel to focus the sample stream in the middle of the crossing. These methods have a low dead volume and can repeatable inject sample volumes from the picolitre to the low nanolitre range. The main drawback is the fixed sample volume which is defined by the design of the microfluidic crossing.

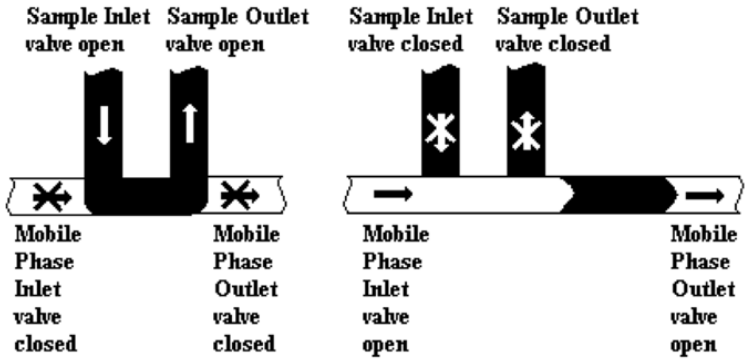

Figure 2.6: Schematic of a double-T on-chip sample injector. Reprinted from [107] with permission from Elsevier.

2.5 Detection methods

Microfluidic lab-on-a-chip systems for the study of proteins and their interactions require sophisticated and sensitive detection methods due to the large concentration range of proteins in a human cell and the limited sample volumes [11]. Various detection methods which employ different strategies and properties (e.g. optical, mass) have been employed in lab-on-a-chip systems [42; 108; 109]. These detection methods can be split into two groups: detection requiring a label and label-free detection. The first group of detection methods requires the attachment of a label which is often a fluorophore to the analyte of interest. The label changes the physical properties, e.g. fluorescence, of the analyte which can be detected by a suitable detector. The label-free methods directly detect the presence of analytes due to changes in the physical properties, e.g. refractive index, of the system. Label-free detection methods have the obvious advantage that no labelling molecule which can alter the system behaviour has to be used. This reduces the complexity of the assay format and improves the reliability of the system but often leads to a reduced sensitivity compared to detection methods which use labels [110]. A further distinction of the detection methods can be made between bulk and surface detection methods. The former measure the analyte concentration in the bulk of the system while the latter measure the surface concentration of analyte associated at the active sensor surface. The main criteria for efficient detection systems are the specificity, sensitivity and dynamic range of the detection. The sensitivity is given by the limit of detection (LOD) which is the lowest analyte concentration which can be distinguished

from the blank sample.

Fluorescence detection is the most common detection method in lab-on-a-chip systems [111]. Briefly, a fluorophore which is attached to the analyte is excited by a light source, e.g. waveguide or laser, and the emitted light is detected by a photodiode or charge-coupled device (CCD) camera. Two forms of excitation light source are especially suited for integration into lab-on-a-chip systems: laser-induced fluorescence (LIF) and optical waveguides [112]. The advantage of these excitation methods is that the excitation is localised to a small volume in the microfluidic channel. In LIF the laser beam can be focused into a micrometre-sized detection area thus reducing the background noise and increasing the detection sensitivity to the sub-picomolar level [113]. In optical waveguide sensors the fluorophores from any labelled analytes associated to the sensor surface are excited by the evanescent field of the waveguide. This evanescent field is an exponential decaying electromagnetic standing wave which extends about 100 nm from the waveguide surface into the microfluidic channel. Thus the optical excitation is localised to the waveguide-channel interface. A typical setup is shown in figure 2.7. This

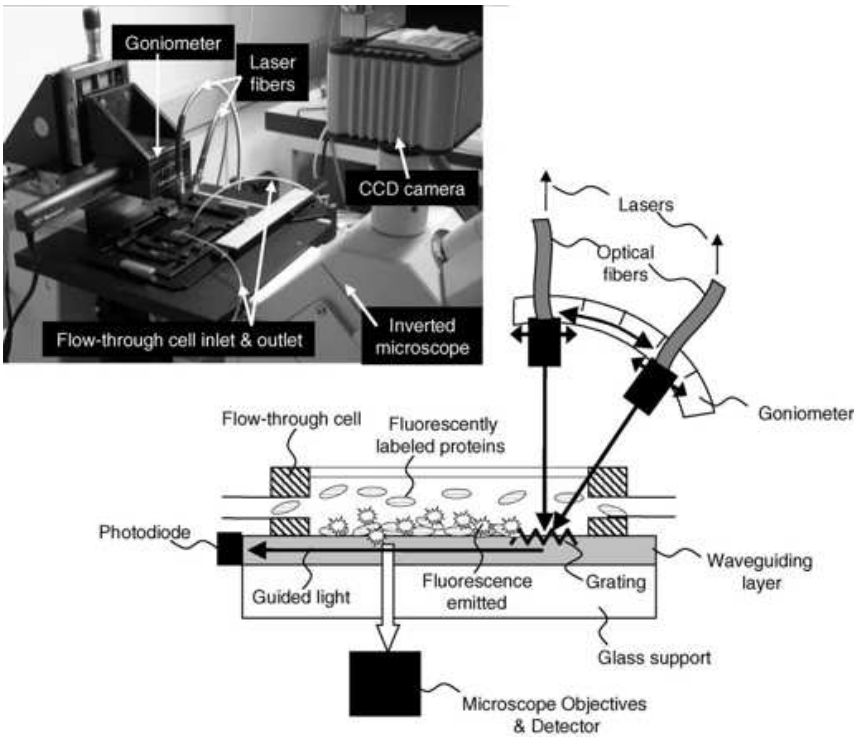

Figure 2.7: Schematic of a waveguide sensor. Reprinted from [114] with permission from Elsevier.

localisation of the excitation leads to a detector which is very specific to surface-based interactions. Waveguide sensors have reached a limit of detection of $0.25\,\mathrm{pmol\,m^{-2}}$ [42]. A further advantage of waveguide sensors is the ease of integration and the possibility for simultaneous detection of multiple analytes [21]. The success of fluorescence detection, both LIF and waveguide sensors, is due to its very high sensitivity and selectivity. A drawback of fluorescence detection is the need to attach a fluorescent label which might alter the behaviour of the analyte molecules. This label is necessary because most analytes are non-fluorescent. However, this attachment of fluorescent labels offers the possibility of signal amplification. By attaching multiple fluorophores per analyte molecule the signal can be increased. For example, the waveguide sensor of Pawlak et al. [42] achieves the high sensitivity with a dye to protein ratio of 5.

Surface plasmon resonance (SPR) detection is a widely used optical, label-free detection method for lab-on-a-chip systems [108]; a schematic of SPR is shown in figure 2.8. SPR sensors use surface plasmons, which are electromagnetic waves that propagate

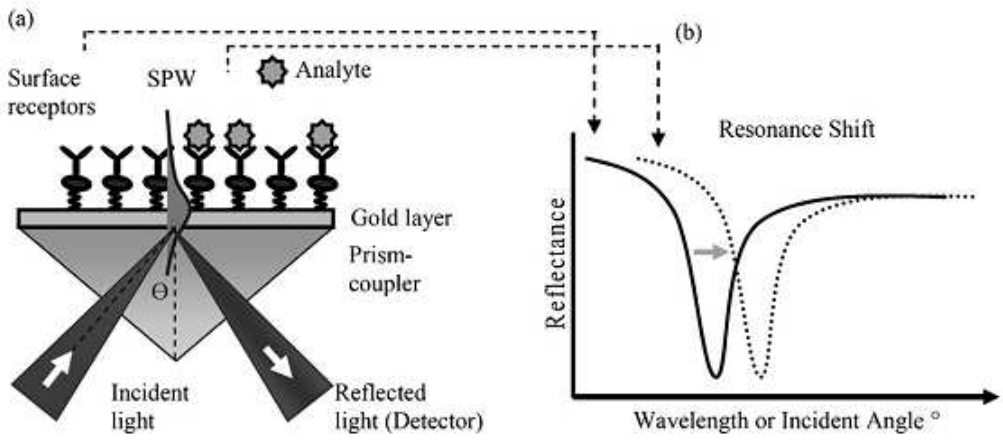

Figure 2.8: Schematic of a SPR sensor. Reprinted from [115] with permission from Elsevier.

along the interface between a metal and a dielectric, to probe interactions close to this interface. When analytes associate to the substrate the refractive index changes and thus the properties of the surface plasmons. SPR sensor can detect mass changes down to $\sim 0.3\,\mathrm{ng\,cm^{-2}}$. These changes can be measured in real-time and related back to the concentration of the analyte attached to the surface. Much of the work on affinity and kinetic measurements has been made with the commercial Biacore systems (Biacore, GE

Healthcare, USA). A drawback of label-free methods is that they have to rely on surface immobilised receptors to measure specific events, i.e. a specific recognition-binding event is required to distinguish between two different analytes.

Mass spectrometry (MS) is an analytical method which is used to analyse the components of a sample [116]. The general principle is as follows: (1) the sample is ionised, (2) the ionised particles are accelerated by an electromagnetic field according to their mass-to-charge ratio (m/z), (3) the separated ions are detected by a detector, e.g. photomultiplier tube or electron multiplier. Two ionisation methods for the ionisation of biological molecules are shown in figure 2.9: electrospray ionisation (ESI) and matrix-assisted laser desorption/ionisation (MALDI) [116]. These ionisation methods are so

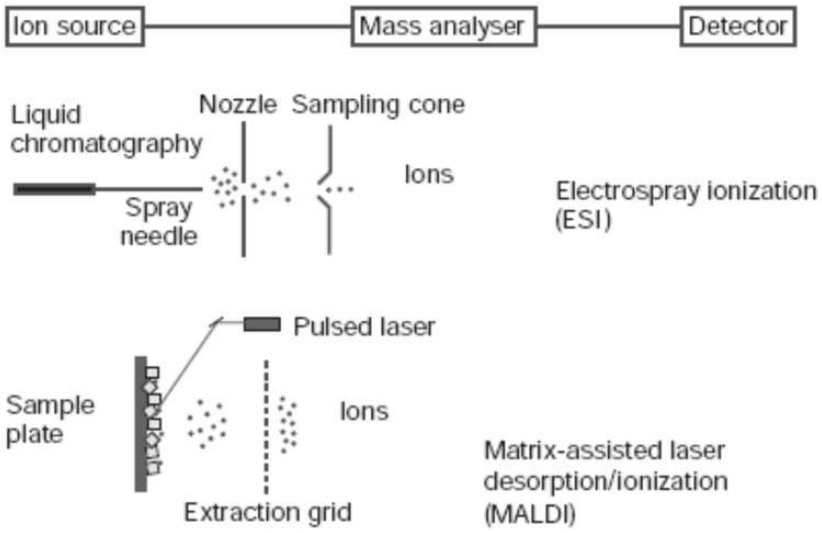

Figure 2.9: Schematic of (top) ESI and (bottom) MALDI. Adapted by permission from Macmillan Publishers Ltd: Nature [116], copyright 2003.

called soft ionisation methods which leave the biological molecules intact. In ESI the sample is flowed through an electrospray nozzle where it is ionised and transported into the mass spectrometer by a strong electric field [117]. ESI-MS can be incorporated directly into microfluidic devices and can reach a LOD of less than 10 nM [118]. In MALDI the sample is mixed with a highly absorbing matrix and spotted onto a substrate. This spot is excited by a laser and the highly absorbing matrix transforms the laser energy into excitation energy for the sample thus improving the energy transfer efficiency and

preventing damaging of the biomolecules. This method can achieve a LOD of 35 ng cm^{-2} [119]. Mass spectrometry imaging (MSI) is an extension to MALDI where the excitation laser is scanned across the sample. This generates profiles and two-dimensional density maps of peptides and proteins with a spatial resolution down to 50 μm [120]. Drawbacks of mass spectrometry compared to fluorescence detection are the lower sensitivity and the complex apparatus.

Method	LOD	Label	Bulk/Surface	Reference
LIF	< 1 pM	label	bulk	[113]
Waveguide sensor	< 0.25 pmol m^{-2}	label	surface	[42]
SPR	< 0.5 ng cm^{-2}	label-free	surface	[108]
ESI	< 10 nM	label-free	bulk	[118]
MALDI	< 35 ng cm^{-2}	label-free	surface	[119]

Table 2.3: Comparison of the characteristics of various detection methods

2.6 Summary

Practical aspects of microfluidic affinity systems were described in this chapter; this includes the application areas as well as the fabrication and device operation. It was shown that microfluidic affinity systems offer interesting opportunities and possibilities for the analysis of proteins and for the integration of several laboratory functions into a so called lab-on-a-chip system. However, this high level of integration requires sophisticated methods for the fabrication and functionalisation of microfluidic structures. While there has been significant progress in recent years, the fabrication and instrumentation of microfluidic lab-on-a-chip systems is still very limited. For example, it is difficult and expensive to fabricate microfluidic channels with arbitrary cross section or non-uniform depth along the length of the channel. Thus these limitations of the device fabrication and operation have to be taken into consideration for the subsequent design studies.

Chapter 3

Background - Modelling of microfluidic affinity systems

3.1 Introduction

Mathematical modelling is an important tool in the development and operation of microfluidic affinity systems. Mathematical models can be used in two different application scenarios: (i) analysis of the device behaviour [121] and (ii) predicting the behaviour of future devices [122]. While the analysis aspect is important for the running of the device, the predictive aspect of mathematical models is invaluable for the design and optimisation of microfluidic affinity systems. Mathematical models of the device behaviour give insight into the different physical effects, e.g. diffusion and convection, which can be used to optimise the device performance without many iterative prototype devices. This allows faster and cheaper product cycles and more importantly, more rigorous optimisation of the device; a prototype device explores only one device geometry while mathematical models allow the extensive optimisation over the complete parameter space. However, it has to be kept in mind that every mathematical model is based on assumptions and simplifications and thus describes only certain aspects of the full, physical system. The validation of the assumptions and simplifications as well as the model results is an important step in mathematical modelling.

In this chapter the fundamental mathematical models governing the behaviour of integrated microfluidic affinity systems are presented. The modelling of microfluidic affinity systems is split into two parts: (i) the modelling of the fluid flow in microfluidic channels (section 3.2) and (ii) the modelling of the transport of analyte molecules in the bulk of the channel as well as the analyte mass transfer to the active surface and subsequent association with surface immobilised receptor molecules (section 3.3). Both sections (3.2 and 3.3) introduce the mathematical model as well as the conventions used throughout this thesis. The applicability and the limitations of the models and the asymptotic limits relevant for microfluidic systems are explored. The last part of the chapter gives an overview of the prior modelling work relevant for the description of microfluidic affinity systems.

The modelling of microfluidic affinity systems in this thesis uses the conventions shown in figure 3.1. The flow is assumed to be in the positive x direction which is from

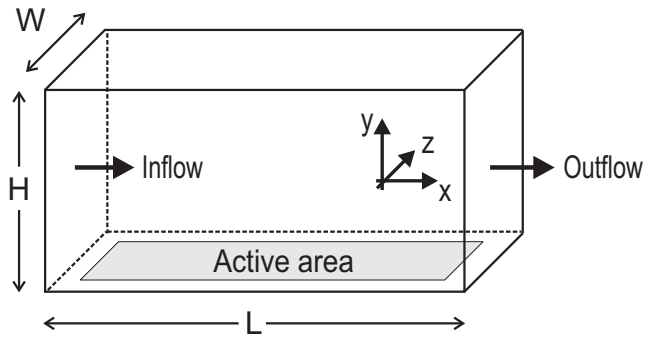

Figure 3.1: Schematic diagram of a microfluidic affinity system with the corresponding coordinates and dimensions used in this thesis.

left to right in all figures in this thesis. The active surface, i.e. the area with surface immobilised receptor molecules, in these affinity systems is always located in the base of the microfluidic channel. The main variables used in the modelling including their units and range are given in table 3.1. The variables A, B and X refer to the bulk analyte concentration, surface bound analyte concentration and free surface immobilised receptor concentration, respectively. The subscript 0 is used to indicate the initial concentration for the bulk analyte and surface immobilised receptor concentrations.

Symbol	Description	Size	Units
k_a	Association rate constant	$10^5 - 10^6$	$\mathrm{M^{-1}\,s^{-1}}$
k_d	Dissociation rate constant	$10^{-3} - 1$	$\mathrm{s^{-1}}$
H	Channel height	$\leq 10^{-5}$	m
W	Channel width	$10^{-5} - 10^{-3}$	m
L	Channel length	$10^{-3} - 10^{-1}$	m
U	Mean flow velocity	$10^{-5} - 10^{-3}$	$\mathrm{m\,s^{-1}}$
A	Bulk analyte concentration	$\leq 10^{-8}$	M
B	Bound analyte concentration	$10^{-8} - 10^{-7}$	$\mathrm{mol\,m^{-2}}$
X	Free receptor concentration	$10^{-8} - 10^{-7}$	$\mathrm{mol\,m^{-2}}$
D	Diffusion coefficient	$10^{-11} - 10^{-10}$	$\mathrm{m^2\,s^{-1}}$

Table 3.1: Variables used in the modelling of lab-on-a-chip systems

3.2 Microfluidics

Microfluidics is the theory of fluids, liquids and gases, in devices with at least one characteristic dimension between 100 nm and 1 mm [3]. For the movement of liquids through these microfluidic channels the continuum approach is applicable which means that the movement can be described through a system of partial differential equation. For an incompressible Newtonian liquid with constant density ρ and constant kinematic viscosity ν the flow through a channel can be described by the Navier-Stokes equations. These equations can be derived from the principles of conservation of mass and momentum and are given by

$$\frac{\partial \mathbf{u}}{\partial t} + (\mathbf{u} \cdot \bigtriangledown)\mathbf{u} = -\frac{1}{\rho} \bigtriangledown p + \nu \bigtriangledown^2 \mathbf{u} + g \tag{3.1}$$

$$\bigtriangledown \cdot \mathbf{u} = 0 \tag{3.2}$$

where p is the pressure and g is the gravitational body force [123]. The vector $\mathbf{u} = (u, v, w)$ describes the flow in the x, y and z direction. For a complete description of the flow in microfluidic channels suitable boundary conditions are required. At the channel entrance and exit the pressure is set to a constant value, i.e. p_1 and p_2, respectively, and it is required that the viscous stress is zero. This leads to a pressure driven flow. At

the channel side walls the no-slip boundary condition is applied. This condition implies that the fluid velocity at the side walls is zero relative to the side walls.

The behaviour of the fluid in the channel is dependent on the ratio of the inertia term $(\mathbf{u} \cdot \bigtriangledown)\mathbf{u}$ and the viscous term $\nu \bigtriangledown^2 \mathbf{u}$ in the Navier-Stokes equations [123]. When the inertia term dominates the viscous term the fluid flow can become turbulent and vortices can develop spontaneously. On the other hand, when the viscous term dominates the inertia term the fluid flow is laminar and the streamlines are locally parallel. The influence of the inertia and viscous forces is characterised by the nondimensional Reynolds number

$$\mathrm{Re} = \frac{\rho U H}{\mu} = \frac{U H}{\nu} = \frac{\text{inertia forces}}{\text{viscous forces}} \tag{3.3}$$

where U is the characteristic velocity, μ is the dynamic viscosity coefficient and H is the characteristic length. The characteristic velocity and length of the system are the velocity and channel dimension which dictate the device behaviour. In the cases considered here the characteristic velocity of the system is given by the axial velocity and the characteristic length is the channel height. The Reynolds number can be derived by analysing the inertia and viscous terms in the Navier-Stokes equations. The first derivatives such as $\partial u/\partial x$ are of order U/H and the second derivatives are of order U/H^2 so that the inertia and viscous terms of the Navier-Stokes equations can be approximated through

1. inertia term: $|(\mathbf{u} \cdot \bigtriangledown)\mathbf{u}| = \mathcal{O}(U^2/H)$
2. viscous term: $|\nu \bigtriangledown^2 \mathbf{u}| = \mathcal{O}(\nu U/H^2)$

The ratio between the inertia and the viscous terms is of the same order as the Reynolds number Re. This shows that for large values of the Reynolds number the inertia term dominates the fluid behaviour while for small values of the Reynolds number the viscous term dominates. The Reynolds number in the macro regime, i.e. $H > 1\,\mathrm{cm}$, is large for aqueous solutions which leads to a strong influence of the inertia term and possibly turbulent flow. In contrast to this the Reynolds number in microfluidic channels is at most of the order $\mathcal{O}(1)$ which indicates a larger influence of the viscous forces and laminar flow. Most microfluidic systems have a Reynolds number which is much smaller than

1 [3]. In this case the inertia terms on the left side of equation 3.1 can be neglected. This reduces the nonlinear Navier-Stokes equations 3.1-3.2 to the linear Stokes equations [124]

$$\frac{\partial \mathbf{u}}{\partial t} = -\frac{1}{\rho} \bigtriangledown (p + \rho\chi) + \nu \bigtriangledown^2 \mathbf{u} \tag{3.4}$$

$$\bigtriangledown \cdot \mathbf{u} = 0 \tag{3.5}$$

where the gravitational body force g was written as the gradient of a potential $g = -\bigtriangledown\chi$.

Gravity modifies the pressure field in the y direction and thus has little effect on the flow in the x direction [123]. Neglecting the gravitational body force g and considering steady flow in a long, rectangular microfluidic channel the Stokes equations can be simplified even further. In this case the pressure depends only on x while the flow depends only on y and z thus simplifying the Stokes equations to

$$p_x = \mu(u_{yy} + u_{zz}) \tag{3.6}$$

In a long, rectangular channel with a high aspect ratio ($H \ll W \ll L$) the flow profile is uniform over most of the width of the microfluidic channel and is given by the analytical solution for the flow between two parallel plates

$$u(y) = 6U\frac{y(H-y)}{H^2} \tag{3.7}$$

where U is the mean velocity. This equation describes a stable, parabolic flow profile. In this configuration the shear stress at the top and bottom wall of the channel can be evaluated by Newton's law of viscosity

$$\tau_w = 6\mu\frac{U}{H} \tag{3.8}$$

and the pressure drop from the channel entrance to the channel exit can be approximated by

$$\Delta p = \frac{12\mu L}{WH^3}Q \tag{3.9}$$

where the flow rate is given by $Q = UHW$ [124].

Due to the stable laminar flow condition, analytes in microfluidic channels are mixed only by diffusion. The basic mechanism of diffusion is described by Fick's law which links the diffusive flux J_D to the local change in analyte concentration

$$J_D = -D\frac{\partial A}{\partial x} \tag{3.10}$$

where A is the analyte concentration and D is the diffusion coefficient. For dilute solutions the diffusion coefficient is independent of the analyte concentration and is inversely proportional to the diameter of the molecule [125]. Diffusion coefficients for proteins in aqueous solution range from 10^{-11} to $10^{-10}\,\mathrm{m^2\,s^{-1}}$ [126] which is about two orders of magnitude smaller than the self-diffusion coefficients of the majority of liquids.

The dispersion of analyte molecules in microfluidic channels depends on the relative importance of convection and diffusion due to the purely diffusive mixing in the stable flow regime. For a constant diffusion coefficient D the required time for analytes to diffuse across the height H of the channel is proportional to the square of the channel height and inversely proportional to the diffusion coefficient, i.e. $t_D \sim H^2/D$. During the diffusion time t_D the analyte is convected a distance $x_C \sim t_D U$ along the channel. The ratio of the convection distance x_C and the diffusion distance H indicates the relative importance of convection and diffusion and gives the nondimensional Péclet number

$$\mathrm{Pe} = \frac{UH}{D} = \frac{\text{convection distance}}{\text{diffusion distance}} \tag{3.11}$$

where U is the average flow velocity and H is the characteristic length of the device perpendicular to the flow direction. For a microfluidic channel with characteristic length $10\,\mu\mathrm{m}$ and flow speed of $10^{-3}\,\mathrm{m\,s^{-1}}$ the Péclet number for large molecules is about 100 which would result in a mixing length of about 1 mm. The long mixing length is beneficial in applications where mixing is not desired such as solute analysers and filtration devices [2]. On the other hand the slow mixing is impairing the integration of chemical and biological processes in microfluidic devices. To alleviate this problem a broad range of micromixers using many different techniques are used [23].

The small size of microfluidic systems leads to a large surface area to volume ratio which is inversely proportional to the characteristic length of the system [3]. The consequence of this is a larger influence of surface effects compared to macro-scale systems which is beneficial for heterogeneous affinity systems (see section 3.3) and can also be facilitated for the movement of liquids through EOF (see section 2.4).

3.3 Transport and reaction equations

The behaviour of microfluidic affinity systems is defined by the convective and diffusive transport of analyte molecules and the interaction of analyte molecules with receptor molecules. Microfluidic affinity systems are grouped according to the location of the analyte-receptor interaction into homogeneous and heterogeneous systems. In homogeneous systems the analytes interact with the receptor molecules in the bulk of the microfluidic channel, while in heterogeneous systems the receptor molecules are immobilised at the channel walls so that the interactions between the analyte and receptor molecules take place only at these active surfaces [8]. Homogeneous systems have the advantage that no receptor immobilisation steps are required and that nonspecific binding at the channel walls has a negligible effect on the device performance (see section 2.4.1). However, the sensitivity and selectivity of homogeneous systems are generally lower than for heterogeneous systems. In this thesis only heterogeneous affinity system are considered because they offer the sensitivity required for the analysis of low-abundance proteins. A schematic side view of an heterogeneous affinity system indicating the convective and diffusive transport as well as the recognition-binding event at the active surface in the bottom of the channel is shown in figure 3.2.

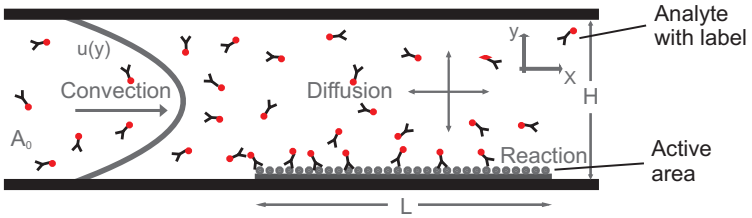

Figure 3.2: Schematic side view of a microfluidic affinity system. The analyte molecules are transported by convection and diffusion and bind to the receptor molecules on the active sensor area.

The convective and diffusive transport of the analyte molecules in the bulk of the microfluidic channel can be described by the following differential equation [127]

$$\frac{\partial A}{\partial t} + (\mathbf{u} \cdot \bigtriangledown) A = D \bigtriangledown^2 A \tag{3.12}$$

where A is the analyte concentration in the bulk, D is the diffusion coefficient and

$\mathbf{u} = (u, v, w)$ is the flow velocity. This is a convection-diffusion equation where the left side describes the convective transport of analytes along with the flow, while the right side describes the motion of analytes due to molecular diffusion. The flow velocity is governed by the Navier-Stokes equations 3.1 and 3.2 which yield a stable, parabolic flow profile for pressure driven actuation in long and shallow microfluidic channels.

The kinetics of the binding of the analyte molecules with the free surface immobilised receptor molecules at the active surface are described by the following formula

$$A_w + X \underset{k_d}{\overset{k_a}{\rightleftharpoons}} B \tag{3.13}$$

where A_w is the analyte concentration near the active channel wall, X is the free surface immobilised receptor concentration, B is the bound analyte concentration and k_a and k_d are the association and dissociation rate constants of the bimolecular reaction. This equation 3.13 describes the simplest, $1:1$ analyte-receptor association.

It is assumed that the Langmuir isotherm is fulfilled, i.e. monolayer coverage, receptor site equivalence and independence [128]. By the law of mass action, the analyte-receptor association at the active surface can be reformulated into the following differential equation

$$\frac{\partial B}{\partial t} = k_a A^i X^j - k_d B^l \tag{3.14}$$

The parameters i, j and l denote the order with which each reactant enters the reaction and the sum $i + j$ gives the order of the forward reaction. This work considers only second order kinetics where $i, j, l = 1$. This restriction is reasonable because many antibody-antigen interactions can be accurately described by second order kinetics [128]. It is further assumed that the reaction rates k_a and k_d are independent of the analyte concentration which is reasonable for the here studied aqueous solutions.

The differential equation 3.14 which describes the analyte-receptor association at the active surface has to be coupled to the differential equation 3.12 which describes the analyte mass transfer in the microfluidic channel. For this it is assumed that, (i) the laws of mass conservation apply, (ii) the transfer of analyte from the bulk solution to the active surface is purely by diffusion and convection, (iii) there is no initial surface concentration of analyte associated on the active area of the channel and (iv) the transfer

of analyte from the fluid is balanced by the rate of analyte association on the active area, i.e. every analyte molecule associated at the active surface occupies exactly one surface immobilised receptor molecule. It is further assumed that the receptor molecules are either free or occupied by an analyte molecule so that

$$B + X = X_0 \tag{3.15}$$

where X_0 is the total concentration of surface immobilised receptor molecules. Hence at the active surface of the sensor

$$D\frac{\partial A}{\partial \mathbf{n}} = \frac{\partial B}{\partial t} = k_a A(X_0 - B) - k_d B \tag{3.16}$$

where $\mathbf{n}$ is a vector perpendicular to the active surface and inward pointing. This equation forms the boundary condition for the differential equation 3.12 at the active surface. In the case considered here, see figure 3.1, the vector $\mathbf{n}$ is equal to the coordinate y.

In contrast to much of the published work [129; 130] this thesis is mainly concerned with a small analyte plug of input time λ

$$A(0, y, z, t) = A_0 \,\hat{\mathrm{H}}(t)\,\hat{\mathrm{H}}(\lambda - t) \tag{3.17}$$

where A_0 is the initial concentration of the analyte and $\hat{\mathrm{H}}$ is the Heaviside function. For a short plug in relation to the channel length it is required that $\lambda U \ll L$. A short analyte plug reduces the sample and reagent requirements which is beneficial for expensive and rare analytes, e.g. samples from neonates or animal models. However, the analysis of the resulting system is more complex because the movement of the analyte plug through the system has to be taken into account while systems with a continuous analyte input often reach a quasi-steady state [131].

The boundary conditions for the convection-diffusion equation 3.12 at the non-active channel walls are given by no flux across these channel walls, i.e. with the conventions from figure 3.1 the boundary conditions are given by $A_y = 0$ at the top of the channel and $A_z = 0$ at the side walls. Here the short form $A_n = \partial A/\partial n$ was introduced. These conditions ensure that no analyte is 'lost' or 'gained' at the non-active channel walls. At the channel exit the boundary condition is given by no diffusive flux, i.e. $A_x = 0$. This

is a simplification of the real situation where the analytes are leaving the channel by convection and diffusion. However, the Péclet number is usually high (Pe $\gg 1$) so that diffusion plays only a small role compared to convection. To further reduce the effect of this simplification, the numerical simulations are performed on channels which have a non-active area before and after the active area, i.e. the start and end of the active area do not coincide with the channel entrance and exit, respectively. Initially no analyte molecules are in the channel ($A = 0$) and all surface immobilised receptor molecules are free ($X = X_0$). The coupled differential equations 3.12 and 3.16 together with the other boundary and initial conditions fully describe the behaviour of the transport-reaction problem.

To gain insight into the relevance of the physical effects, the governing equations and boundary conditions are nondimensionalised with the following variables: $x = L\tilde{x}$, $y = H\tilde{y}$, $z = W\tilde{z}$, $\mathbf{u} = \left(U, \frac{UH}{L}, \frac{UW}{L}\right)\tilde{\mathbf{u}}$, $A = A_0\tilde{A}$, $X = X_0\tilde{X}$, $B = X_0\tilde{B}$, $t = \frac{L}{U}\tilde{t}$ and $\lambda = \frac{L}{U}\tilde{\lambda}$. Here the tilde indicates the nondimensional variables. Other nondimensionalisations are possible and have been applied for different analysis goals [131; 132]. In this case the resulting nondimensional system is

$$\tilde{A}_{\tilde{t}} + \tilde{\mathbf{u}} \cdot \nabla \tilde{A} = \frac{LD}{H^2U}\left(\frac{H^2}{L^2}\tilde{A}_{\tilde{x}\tilde{x}} + \tilde{A}_{\tilde{y}\tilde{y}} + \frac{H^2}{W^2}\tilde{A}_{\tilde{z}\tilde{z}}\right) \qquad , x, y, z \in [0,1] \tag{3.18}$$

$$\tilde{A}_{\tilde{y}} = \frac{k_a H X_0}{D}\left(\tilde{A}(1-\tilde{B}) - \frac{k_d}{k_a A_0}\tilde{B}\right) \qquad , x, z \in [0,1], y = 0 \tag{3.19}$$

$$\tilde{B}_{\tilde{t}} = \frac{LD}{H^2U}\frac{A_0 H}{X_0}\tilde{A}_{\tilde{y}} \qquad , x, z \in [0,1], y = 0 \tag{3.20}$$

For the ease of readability the tilde atop the nondimensional variables is neglected from now on. The nondimensionalisation reveals four nondimensional numbers which define the device behaviour: the Graetz number Gz, the Damköhler number Da, the nondimensional dissociation constant $\bar{\mathrm{K}}_\mathrm{d}$ and the adsorption capacity κ. These are given by

$$\mathrm{Gz} = \frac{H^2U}{LD} = \frac{\text{diffusion time}}{\text{convection time}} \tag{3.21}$$

$$\mathrm{Da} = \frac{k_a H X_0}{D} = \frac{\text{association rate}}{\text{diffusion rate}} \tag{3.22}$$

$$\bar{\mathrm{K}}_\mathrm{d} = \frac{k_d}{k_a A_0} = \frac{\text{dissociation constant}}{\text{analyte concentration}} \tag{3.23}$$

$$\kappa = \frac{X_0}{A_0 H} = \frac{\text{receptor concentration}}{\text{analyte concentration}} \tag{3.24}$$

The Graetz number Gz is a measure of the relative importance of diffusion and convection. For $Gz \ll 1$ all analyte molecules have enough time to diffuse to the recognition molecules attached on the surface of the sensor and the concentration profile is 'fully developed', while for $Gz \gg 1$ many analyte molecules flow through the device without encountering the recognition molecules on the sensor surface and the channel is said to be in the 'entrance region'. The Damköhler number Da relates the rate of diffusion of the analyte molecules toward the active surface to the rate of association between the analyte and surface immobilised receptor molecules at the active surface. For $Da \ll 1$ the rate of association is much slower than diffusion and the system is said to be 'binding limited', while for $Da \gg 1$ the diffusion is much slower than the rate of association and the system is 'diffusion limited'. The nondimensional dissociation constant $\bar{K}_d$ is the dissociation constant $K_d = k_d/k_a$ scaled with the analyte concentration. For $\bar{K}_d \ll 1$ the receptor patch saturates, i.e. every receptor molecule is occupied by an analyte molecule, in equilibrium while for $\bar{K}_d \gg 1$ only a small fraction of the surface immobilised receptor molecules are occupied. The adsorption capacity κ is a measure for the relation between the surface immobilised receptor concentration and the bulk analyte concentration. A small adsorption capacity results in fast saturation of the surface immobilised receptor molecules while a large adsorption capacity leads to long saturation times.

3.4 Literature review - transport and reaction equation

The transport-reaction problem 3.18-3.20 has no complete, analytical solution due to the nonlinear surface reaction. On the other hand, for different regimes of the nondimensional numbers Gz, Da, $\bar{K}_d$ and κ the problem can be simplified so that analytical solutions for these special cases can be found. These analytical solutions give valuable insight into the behaviour of the transport-reaction problem in the asymptotic limits and are applicable for various physical systems. Especially the case of small Graetz number Gz and large adsorption capacities κ so that every analyte molecule can reach the active surface and finds an almost constant surface immobilised receptor concen-

tration is important for sensing and separation applications [131] (see chapters 4 and 5).

3.4.1 Stagnant and well-mixed systems

The simplest case of the transport-reaction model is given for stagnant and well-mixed systems. Here the channel is filled with the sample and then the flow is stopped so that $\mathrm{Gz} = 0$. Furthermore, the system is considered to be well-mixed which is equivalent to a 'binding limited' system, i.e. $\mathrm{Da} \ll 1$. In this case the transport-reaction model given by equations 3.12 and 3.16 reduces to just a reaction model [128]. In this closed system the concentrations of bound analyte molecules and free analyte molecules are linked by the principle of conservation of mass so that for the analyte concentration the following expression holds

$$A = A_0 - \frac{B}{H} \tag{3.25}$$

where the bound analyte concentration B had to be transformed into a volume concentration by division with the channel height H. With this expression the equilibrium solution of equation 3.16 is given by

$$B_{eq} = \frac{1}{2}(H(\mathrm{K_d} + A_0) + X_0) \pm \sqrt{\frac{1}{4}(H(\mathrm{K_d} + A_0) + X_0)^2 - HA_0X_0} \tag{3.26}$$

The plus sign in equation 3.26 can be ruled out because the bound analyte concentration B has to be smaller than the initial surface immobilised receptor concentration X_0.

If the concentration of analyte molecules stays constant the general solution of equation 3.16 is given by

$$B(t) = \frac{X_0}{1 + \mathrm{K_d}/A_0}\left(1 - e^{-(k_a A_0 + k_d)t}\right) \tag{3.27}$$

This solution is a good approximation for $A \approx A_0$ which is true if the number of analyte molecules is much larger than the number of receptor molecules. When the ratio of analyte molecules to receptor molecules drops below 10 depletion of the analyte concentration becomes significant and equation 3.27 is not valid anymore [128]. In the case of constant analyte concentration the fraction of occupied surface immobilised receptor molecules in equilibrium is only dependent on the ratio of the dissociation constant $\mathrm{K_d}$ and the initial analyte concentration A_0. If the initial analyte concentration

is much smaller than the dissociation constant ($A_0 \ll \mathrm{K_d}$) only a small fraction of the available surface immobilised receptor molecules will be occupied

$$B_{eq} \approx X_0 A_0 / \mathrm{K_d} \ll X_0 \tag{3.28}$$

If the initial analyte concentration on the other hand is much larger than the dissociation constant ($A_0 \gg \mathrm{K_d}$) the surface immobilised receptor sites are saturated $B_{eq} \approx X_0$. An approximation for the equilibrium time can be gained from equation 3.27

$$t_{eq} \sim (k_a A_0 + k_d)^{-1} = k_d^{-1} \left(1 + \frac{A_0}{\mathrm{K_d}}\right)^{-1} \tag{3.29}$$

This relationship shows that for low initial analyte concentrations ($A_0 \ll \mathrm{K_d}$) the equilibrium time scale depends mainly on the dissociation rate constant k_d while for high initial analyte concentrations ($A_0 \gg \mathrm{K_d}$) mainly the association rate constant k_a governs the equilibrium time scale.

Instead of systems with an almost constant analyte concentration A this thesis is mainly concerned with systems with an almost constant surface immobilised receptor concentration $X \approx X_0$. For this case which is important for sensor and separation applications a result analogous to equation 3.27 is obtained

$$A(t) = \frac{A_0}{1 + \frac{X_0}{\mathrm{K_d}\, H}} \left(1 - e^{-(k_a X_0 / H + k_d) t}\right) \tag{3.30}$$

as well as an analogous result for the equilibrium time

$$t_{eq} \sim (k_a X_0 / H + k_d)^{-1} \tag{3.31}$$

3.4.2 Models with full transport

For non-stagnant systems ($\mathbf{u} \neq 0$) the full transport-reaction model has to be considered. This complicates the problem and there is no analytical solution for this problem. However, for different regimes of the nondimensional parameters the system of equations can be simplified so that analytical solutions can be found [131; 133]. The solutions presented here consider a continuous input of analytes ($\lambda = \infty$), which might not be appropriate for rare and expensive analytes, and systems with a high adsorption capacity ($\kappa \gg 1$). Furthermore, the 3D model is reduced to a 2D model in the $x - y$ plane.

This simplification is appropriate for systems with a high aspect ratio ($H \ll W$). In this case the flow profile for pressure driven flow is parabolic and given by equation 3.7. The presentation follows the publications of Gervais and Jensen [131] and Squires et al. [133].

For the case of high adsorption capacity ($\kappa \gg 1$) the nonlinearity at the boundary 3.19 can be removed. This is the case because the surface immobilised receptor concentration is much higher than the analyte concentration which reaches a quasi-steady state while the receptor concentration stays almost constant. Taking the analyte concentration to be in steady state, neglecting axial diffusion and the dissociation of bound analyte molecules the full problem given by equation 3.12 reduces to the Graetz problem

$$u(y)\frac{\partial A(x,y)}{\partial x} = D\frac{\partial^2 A(x,y)}{\partial y^2} \qquad ,x,y \in [0,1] \tag{3.32}$$

with the linear boundary condition

$$D\frac{\partial A}{\partial y} = k_a A X_0 \qquad ,x \in [0,1], y = 0 \tag{3.33}$$

This problem can be solved through an eigenfunction expansion [134]. However, this eigenfunction expansion converges only slowly so that further approximate solutions are warranted.

The approximate solutions are grouped according to the Graetz number which defines two regimes with different behaviour. First, the 'entrance region' with $\mathrm{Gz} \gg 1$ where only a small fraction of the analyte molecules can reach the active surface. Second, the 'fully developed' region with $\mathrm{Gz} \ll 1$ where all analyte molecules can take part in the reaction. The following solutions all consider the Graetz problem given by equations 3.32 and 3.33.

'Entrance region': $\mathrm{Gz} \gg 1$

In the 'entrance region' not all analyte molecules have enough time to diffuse to the active surface and to associate with surface immobilised receptor molecules. This leads to the formation of a diffusion boundary layer. Analyte molecules which are in this

diffusion boundary layer can diffuse to the active surface while analyte molecules outside the diffusion boundary layer can not reach the active surface. The thickness δ_s of this diffusion boundary layer can be estimated by finding the maximal distance from the active surface so that the time required to convect past the active surface is equal to the time required to diffuse to the active surface. The diffusion time across the diffusion boundary layer is $t_D \sim \frac{\delta_s^2}{D}$ while the convection time past the active surface is $t_C \sim \frac{L}{u(\delta_s)}$. If the diffusion layer thickness is much smaller than the channel height ($\delta_s \ll H$) the flow velocity can be approximated as $u(\delta_s) \approx \frac{6U}{H}\delta_s$. Equating the two time scales gives a relationship for the diffusion boundary layer thickness

$$\frac{\delta_s}{H} \sim \left(\frac{LD}{6H^2U}\right)^{1/3} = 6^{-1/3}\,\mathrm{Gz}^{-1/3} \tag{3.34}$$

The analyte mass transport through this diffusion boundary layer is given by the diffusive flux

$$J_D \sim \frac{D(A_0 - A_w)}{\delta_s} \tag{3.35}$$

which has to balance the reactive flux

$$J_R \sim k_a A_w X_0 \tag{3.36}$$

so that the analyte concentration at the active surface is

$$\frac{A_w}{A_0} \sim \frac{1}{1 + k_a X_0 \delta_s / D} \tag{3.37}$$

where the second term in the denominator is the Damköhler number Da_E for the 'entrance region'. For this Damköhler number the channel height is replaced with the height of the diffusion boundary layer so that $\mathrm{Da}_E \sim \mathrm{Da}\,\mathrm{Gz}^{-1/3}$.

For the 'binding limited' case ($\mathrm{Da}_E \ll 1$) the association rate is much slower than the diffusion so that the analyte-receptor association is effectively decoupled from the transport of analytes to the active surface. In this case the equilibrium time scale is given by equation 3.29 because the reaction is the limiting step. Commercial systems such as Biacore which are mainly used to measure reaction rate constants operate in this regime. The bound analyte concentration is only dependent on the association rate constant k_a which can be obtained from a plot of the signal strength over input analyte concentration [135]. The dissociation rate constant k_d is obtained from the

dissociation phase, i.e. the bulk analyte concentration is zero, where the bound analyte concentration is assumed to decay exponentially [135].

In practical applications it is not always possible for the Damköhler number Da_E to approach zero. In this case where $\mathrm{Da}_E < 1$ but does not approach zero ($\mathrm{Da}_E \not\ll 1$) the system is not completely 'binding limited', i.e. the analyte mass transfer has a slight influence on the system response. For these systems the two-compartment model which takes transport effects into account is a simple and widely used numerical model [121]. The two-compartment model, which is schematically shown in figure 3.3, treats the

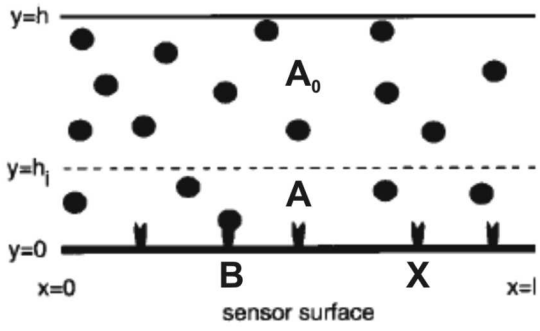

Figure 3.3: Schematic of the two-compartment model. Here h_i is the height of the diffusion boundary layer. Adapted from [127] with permission from Elsevier.

analyte concentration above the diffusion boundary layer as constant and equal to the input analyte concentration. The analyte concentration in the diffusion boundary layer is uniform in space, i.e. the analyte concentration A in figure 3.3 is uniform along the sensor length, but may change in time. This change in time is described by an ordinary differential equation (ODE) which takes the analyte-receptor association rate constant and the transport between the two compartments into account. It was shown that the two-compartment model is able to recover the original rate constants and the transport coefficient with a relative error of 1% in the case of transport influenced binding kinetics [127]. The two-compartment model with uniform analyte concentration in space is applicable for low initial analyte concentrations where the spatial gradients are small and for higher analyte concentrations near the equilibrium where the initial spatial inhomogeneities are dispersed [136]. Extensions of the original two-compartment model incorporate the dissociation term into the solution [137]. On the other hand, even

the two-compartment model is only valid for the 'binding limited' case with $\mathrm{Da}_E < 1$. Asymptotic and perturbation methods have been used to analyse the analyte mass transfer to the active surface and subsequent association to surface immobilised receptors when reaction and diffusion are balanced $\mathrm{Da}_E = \mathcal{O}(1)$ [132; 138]. The resulting integral equations can be used to calculate the binding kinetics from Biacore raw data and the results are consistent with numerical experiments [139].

For the 'diffusion limited' case ($\mathrm{Da}_E \gg 1$) every analyte molecule associates almost immediately with a surface immobilised receptor molecule when it reaches the active surface so that $A_w \to 0$. With $A_w = 0$ the Sherwood number, a nondimensional mass transfer coefficient, is given by

$$\mathrm{Sh} = 0.978 \left(\frac{x}{\mathrm{Gz}}\right)^{-1/3} = \frac{\text{convective mass transfer}}{\text{diffusive mass transfer}} \tag{3.38}$$

The bulk analyte concentration can be calculated by inserting the Sherwood number into the mass transfer equation

$$\frac{\partial A_b(x,t)}{\partial x} = -\,\mathrm{Sh}(A_b(x,t) - A_w(x,t)) \tag{3.39}$$

where A_b is the velocity averaged bulk analyte concentration. Solving equation 3.39 gives the velocity averaged bulk analyte concentration along the channel

$$A_b(x) = \exp\left(-1.467 \left(\frac{x}{\mathrm{Gz}}\right)^{2/3}\right) \tag{3.40}$$

In this case the time scale to reach equilibrium is dependent on the Graetz and Damköhler numbers and given by

$$t_{eq}^{dl} \sim \frac{k_a X_0 H}{(k_a A_0 + k_d) D}\,\mathrm{Gz}^{-1/3} \sim t_{eq}\,\mathrm{Da}_E \tag{3.41}$$

where Da_E is the Damköhler number for the 'entrance region' from equation 3.37.

'Fully developed' region: $\mathrm{Gz} \ll 1$

In the 'fully developed' region ($\mathrm{Gz} \ll 1$) every analyte molecule can diffuse to the active surface and no diffusion boundary layer develops. For 'diffusion limited' binding ($\mathrm{Da} \gg 1$) an analytical expression for the Sherwood number can be found

$$\mathrm{Sh} = \frac{\lambda_1^2}{6} \approx 2.4304 \tag{3.42}$$

where λ_1 is the first eigenvalue of the eigenfunction expansion of the Graetz problem given by equations 3.32 and 3.33. Integrating the mass transfer equation 3.39 with the Sherwood number 3.42 gives the velocity averaged bulk analyte concentration along the channel

$$A_b(x) = \exp\left(-2.4304\frac{x}{\mathrm{Gz}}\right) \tag{3.43}$$

Gervais and Jensen [131] calculated the critical value of $\frac{x}{\mathrm{Gz}}$ at which the solution for the 'entrance region' given by equation 3.40 and the solution for the 'fully developed' region given by equation 3.43 give the same error compared to the numerical simulation to be 0.22. By using equation 3.43 for $x \geq 0.22\,\mathrm{Gz}$ and equation 3.40 for $x < 0.22\,\mathrm{Gz}$ the velocity averaged bulk analyte concentration can be approximated for all x with a maximal absolute error of 6 %.

In the 'reaction limited' case ($\mathrm{Da} \ll 1$) the Sherwood number is given as a combination of the analyte mass transfer rate to the active surface and the association rate

$$\mathrm{Sh}(\mathrm{Da}) = \left(\frac{6}{\lambda_1^2(\mathrm{Da})} + \frac{1}{\mathrm{Da}}\right)^{-1} \tag{3.44}$$

This Sherwood number approaches zero for $\mathrm{Da} \to 0$. Integrating the mass transfer equation 3.39 with the Sherwood number 3.44 gives the velocity averaged bulk analyte concentration along the channel

$$A_b(x) = \exp\left(-\frac{\lambda_1^2(\mathrm{Da})}{6\,\mathrm{Gz}}x\right) \tag{3.45}$$

In contrast to the 'diffusion limited' case, the analyte mass transfer to the active surface and subsequent association depends on the transport conditions as well as on the association rate. If the Damköhler number approaches zero ($\mathrm{Da} \to 0$) the analyte mass transfer to the active surface and subsequent association is limited by the association rate and the velocity averaged bulk analyte concentration is given by

$$A_b(x) = \exp\left(-\frac{\mathrm{Da}}{\mathrm{Gz}}x\right) \tag{3.46}$$

For the 'fully developed' region every analyte molecule can diffuse to the active surface and thus the boundary depletion layer stretches across the whole channel height. In this case the equilibrium time depends on the nondimensional reaction/convection number ζ defined by

$$\zeta = \frac{\mathrm{Da}}{\mathrm{Gz}} = \frac{k_a L X_0}{HU} = \frac{\text{reaction rate}}{\text{convection rate}} \tag{3.47}$$

For $\zeta < 1$ the binding is strongly reaction-limited and the equilibrium time is given by equation 3.29. For larger values of ζ the binding is 'convection limited' and the equilibrium time depends on the adsorption capacity and the nonlinear dissociation constant.

As well as the semi-analytical methods, several full numerical approaches have been used to solve the transport-reaction model. A finite volume computational fluid dynamics solver combined with a least-square fitting algorithm has been used to derive rate constants from Biacore data [140]. The advantage of this approach is an implicit inclusion of the transport effects; both the intrinsic as well as the mass transport independent rate constants can be determined. A drawback compared to the semi-analytical methods is the high computational cost. On the other hand, numerical methods are easily adapted to consider more complex binding models than the simple, $1:1$ analyte-receptor interaction 3.13. For example, the fitting of Biacore data to extended binding models which incorporate multiple, different surface immobilised receptor molecules [141] or two competing analytes [142] can improve the accuracy of the fit. While full numeric approaches are excellent for the investigation of specific points in the parameter space of the system, they are of limited use for the prediction of the device behaviour in different parts of the parameter space.

The presented asymptotic and numerical solutions give a framework for the analysis of microfluidic affinity sensors with different configurations. However, all the models consider analyte plugs which are long compared to the sensor surface ($\lambda \gg 1$). Thus there is a need for models which describe the device behaviour for short analyte plugs.

3.5 Different assay types

So far only the direct binding of an analyte to surface immobilised receptors has been described. This direct assay is useful for label-free detection methods, e.g. SPR or MS (section 2.5). Other detection methods, e.g. fluorescence, often require different assay types [8; 11]. One of the reasons for this is that most analytes are not fluorescent and thus a further labelling step is required. Schematics of the direct assay, the direct and

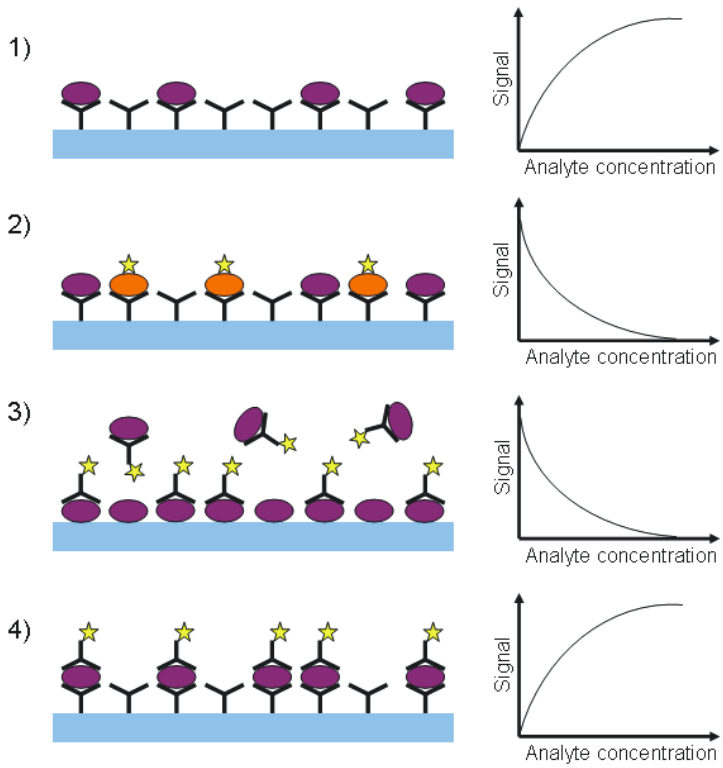

Figure 3.4: Schematic of the different assay types. (1) Direct assay: the association of the analytes (purple circle) with the surface immobilised receptor (**Y**) molecules is directly detected. (2) Direct competitive assay: the analyte molecules directly compete with labelled ligands (orange circle) for the surface immobilised receptor molecules. (3) Indirect competitive assay: the analyte molecules are incubated with labelled receptor molecules in solution; the receptor molecules which are not associated to the analyte molecules in the solution can bind to the surface immobilised analyte molecules. (4) Sandwich assay: the analyte molecules associate to surface immobilised receptor molecules; labelled detection antibodies bind to the analyte molecules which are associated with the surface immobilised receptor molecules.

indirect competitive assay and the sandwich assay are shown in figure 3.4.

An alternative to the direct assay are competitive assays. Here the sensor response is indirectly proportional to the analyte concentration, i.e. a high analyte concentration gives a low signal while a low analyte concentration gives a large signal. In the direct competitive assay a labelled ligand R competes with the unlabelled analyte A for the surface immobilised receptors X. The direct competitive assay is described by the

following formula

$$A + X \underset{k_d}{\overset{k_a}{\rightleftharpoons}} B \tag{3.48}$$

$$R + X \underset{k'_d}{\overset{k'_a}{\rightleftharpoons}} B^f \tag{3.49}$$

where B^f is the concentration of the bound fluorescent ligand. In the indirect competitive assay the analyte is incubated with a labelled receptor in solution. The mixture of the analyte, remaining unbound receptor and analyte-receptor complex is introduced into the sensor. The remaining unbound receptors associate with the surface immobilised analyte molecules. The assay is described by the formula

$$A + X \underset{k_d}{\overset{k_a}{\rightleftharpoons}} X_b \tag{3.50}$$

$$X + A_i \underset{k'_d}{\overset{k'_a}{\rightleftharpoons}} B \tag{3.51}$$

where X_b is the bound analyte-ligand complex in solution and A_i is the surface immobilised analyte concentration. The assay time for the indirect competitive assay is longer compared to the direct competitive assay due to the required incubation step. The decision which competitive assay is used often depends on the available immobilisation protocols.

The sandwich assay is a two step process. In the first step, the analyte associates to the surface immobilised receptors. In the second step, a labelled detector antibody R binds to the surface bound analyte. The assay protocol is given by

$$A + X \underset{k_d}{\overset{k_a}{\rightleftharpoons}} B \tag{3.52}$$

$$R + B \underset{k'_d}{\overset{k'_a}{\rightleftharpoons}} B^f \tag{3.53}$$

where B^f is the labelled detector antibody-surface bound analyte complex. The sandwich assay has the highest selectivity due to the two binding steps. On the other hand, the sandwich assay is only possible for analytes which are able to bind to two receptors simultaneously [8].

The choice of the assay format mainly depends on the target analyte and the employed detection method. For label-free detection or analytes with intrinsic fluorescence the direct assay is preferred due to its simplicity. For label-based detection methods

the other assays have to be used. For large molecules with two binding sites, for which receptors are available, the sandwich assay is preferred due to its high specificity while competitive assays have to be used for small analytes which have only one binding site. A comparison of the different binding assays with a fluorescence-based biosensor showed that the direct assay has the best limit of detection but the smallest dynamic range [143]. The competitive assay offered a slightly reduced limit of detection but a much wider dynamic range. Combining competitive and direct assays which have an opposed sensor response (see figure 3.4) can increase the dynamic range of immunoassays [144].

3.6 Summary

In this chapter background information and theory on the modelling of microfluidic affinity systems was presented; this includes the mathematical models and conventions used in this thesis. The modelling of microfluidic affinity systems is split into two parts: (i) a model for the flow profile and (ii) a model describing the transport and interaction of the analytes. The flow in microfluidic channels is stable, laminar flow which is described by the Stokes equations. The transport of the analyte molecules in the microfluidic channel is described by the convection-diffusion equation with a suitable boundary condition which describes the interaction with surface immobilised receptors. These equations are linked by nondimensional numbers which define the device behaviour; especially the Graetz number Gz and the Damköhler number Da, which can vary considerably for different devices, characterise different operational regimes of the microfluidic affinity systems. While no analytical solution to the full problem exists, approximate solutions in the limits of these nondimensional numbers have been described in some detail. The last section introduces the different assay types which are employed in microfluidic affinity sensors.

Chapter 4

Modelling of microfluidic devices for the separation of proteins

4.1 Introduction

The analysis of the human proteome has enormous potential for the understanding, identification and treatment of diseases (section 2.2). However, the fulfilment of this potential requires sophisticated methods for the preparation, separation and detection of the constituent proteins due to the large number and large concentration range of the proteins expressed by a human cell, see section 2.2. While there are laboratory-scale methods for the sensitive analysis of protein samples, e.g. capillary electrophoresis coupled with mass spectrometry [145], there is no analysis platform which is suitable for the large-scale analysis of the proteome from limited sample volumes. However, microfluidic affinity separation systems have the potential to fill this gap and offer a method for the sensitive and multiplexed analysis of the proteome from small sample volumes [4].

One of the most important steps in the analysis of the proteome is the separation of the complex sample, which contains hundreds or even thousands of different proteins, into simpler subsets [4]. This reduces the complexity of the sample and facilitates the subsequent identification and quantification of the proteins in the individual sub-

sets. However, the most common separation methods, gel electrophoresis, capillary electrophoresis and column chromatography, have limitations in the separation resolution and sample size requirements as well as in the automation and parallelisation which is required for the analysis of the proteome [146]. These limitations might be partly overcome by moving the separation from columns or gels into integrated microfluidic separation systems. The controlled environment and small size of microfluidic separation systems can offer high resolution from limited sample volumes and allows the integration of different analysis steps in one device [4]. One of the main advantages of chip-based separation systems compared to their column-based counterparts is the possibility to integrate many parallel analysis channels which each contain many sequential steps such as enzymatic digestion, multiple separation steps and on-line detection methods [20; 147]. This integration increases the reproducibility and high-throughput potential of the device compared to the conventional separation methods.

One of the most promising separation methods for proteins is based on the affinity interaction between proteins and surface immobilised receptor molecules [10]. In these affinity based separation systems the retention time of the proteins in the separation channel depends on the strength of the affinity interaction between the proteins and the surface immobilised receptors as illustrated in figure 4.1. Compared to other separation

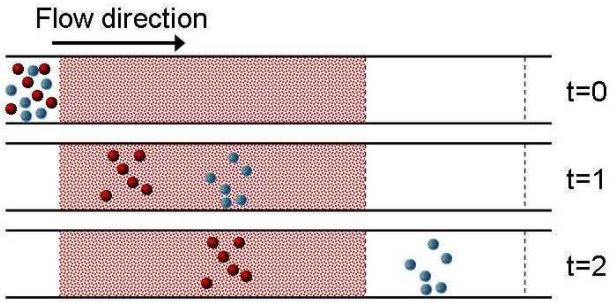

Figure 4.1: Top view of a separation device for three different times. The receptors (red hatching) specifically interact with the red analytes while they have no affinity for the blue analytes. This results in different retention times for the two analytes.

methods, affinity based systems have very high specificity and sensitivity which is due to the specific recognition-binding event between proteins and protein antibodies.

While affinity based separation has been employed in several microfluidic separation systems [20; 148; 149; 150] the theoretical modelling of these systems has received only limited attention. However, such models would be beneficial for the analysis of existing systems and for the development of multiplexed, microfluidic affinity separation systems. Here the applicability and limitations of the reaction-dispersive model, which is well established for column chromatography [151], for the description of the separation process in open microfluidic affinity separation systems are investigated. The model is derived from the governing equations for the transport of analytes in the bulk of the microfluidic channel and the recognition-binding event of the analyte molecules with surface immobilised receptor molecules at the active surface which were introduced in chapter 3. These equations are simplified, by making the assumptions that there is a large adsorption capacity and fast diffusion across the height of the channel, i.e. $\kappa \gg 1$ and $\mathrm{Gz} \ll 1$. These assumptions are feasible for an increasing number of microfluidic affinity systems. For example, the microchannel resonator from Burg et al. [152] is operated at Graetz numbers much smaller than 1 and with large adsorption capacities ($\kappa > 1000$).

The simplified model is solved analytically with the Laplace transform method. The subsequent analysis of the solutions in the case of fast association of the analyte molecules with the surface immobilised receptor molecules, which is essential for separation applications, reveals two simple, analytical expressions for the analyte retention time and the plug dispersion. These expressions depend only on global device parameters and define the behaviour of a sample plug in microfluidic affinity separation systems. By comparing the analytical solution with numerical simulations the simplifications are validated and the limits of applicability of the analytical expressions for the retention time and plug dispersion are explored.

In the second part of the chapter a theoretical framework for the design of multiplexed separation systems based on these analytical expressions is developed. The theoretical framework describes the separation and dispersion of analyte plugs in microfluidic affinity separation systems; a task which usually requires the numerical simulation of the full problem. The simplicity of the calculation of the separation performance allows the design of complex, multiplexed separation systems; these separation systems consist

of parallel separation channels which each contain multiple, sequential receptor patches. These multiplexed systems offer the possibility to separate a large number of analytes with a wide range of affinities.

4.2 Literature review - separation methods

4.2.1 Column chromatography and electrophoresis

The two main separation techniques for bioanalysis applications are column chromatography and electrophoresis which are both well established in the industry [153; 154]. Chromatography is the general term for separation techniques based on the interaction of analyte molecules with a mobile and stationary phase [153]. Briefly, the analyte molecules are dissolved in the mobile phase and then forced through an immobile stationary phase by pressure driven flow. Differences in the interaction with the stationary phase for different molecules result in different retention times; analytes which have a stronger interaction with the stationary phase will stay longer on the stationary phase and therefore longer in the separation column. Under the umbrella of chromatography many different operational modes for the separation according to different properties exist, e.g. reverse phase, size exclusion, affinity.

Electrophoresis is the directed movement of charged molecules relative to a conductive medium, usually a gel or aqueous buffer, under an applied electric field [154]. The molecules are loaded onto a separation column and then subjected to an electric field. Positively charged molecules move towards the negative electrode while negatively charged molecules move to the positive electrode. The migration velocity is proportional to the charge to size ratio of the molecules. The most common electrophoresis method for protein analysis is 2D polyacrylamide gel electrophoresis (2D-PAGE) [155]. In 2D-PAGE proteins are first separated by their isoelectric point, i.e. the pH value at which the molecule carries no electrical charge, and then by mass. The second dimension increases the probability to separate two proteins because it is less likely that two molecules have similar values in two distinct properties. After the separation step the protein spots can be visualised by staining with dyes, mostly coomassie, silver or

fluorophores. The visualised protein spots are excised from the gel and analysed with either MALDI-MS or ESI-MS [116] (section 2.5). This process is shown schematically in figure 4.2. This combined approach can lower the detection limit of 2D-PAGE to the

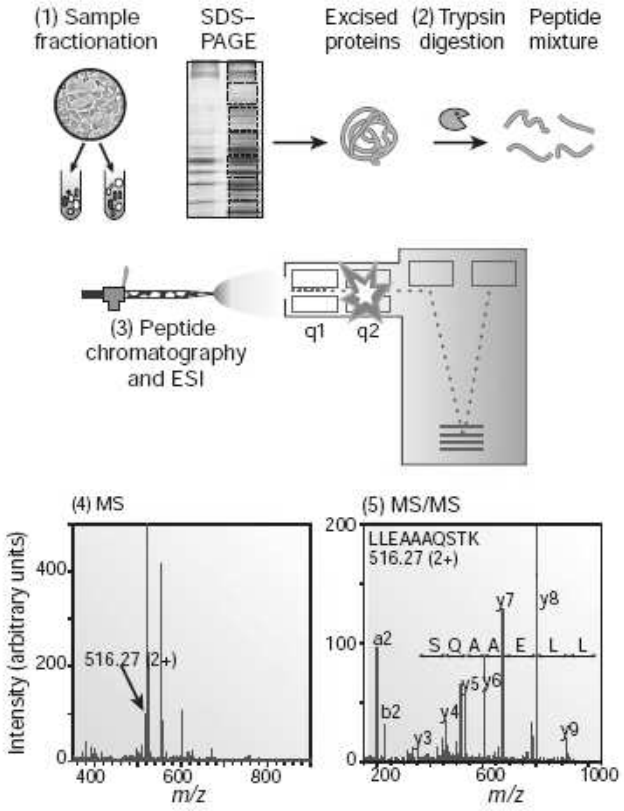

Figure 4.2: Schematic of the combined 2D-PAGE/ESI-MS protein analysis. Reprinted by permission from Macmillan Publishers Ltd: Nature [116], copyright 2003.

low nanomolar regime [156].

2D-PAGE is routinely used to separate and visualise hundreds or even thousands of proteins [157]. However, the low-abundance proteins which form $50\% - 75\%$ of the proteome and range in copy-numbers from 10 to 10000 in a single cell are not detected due to masking by the high-abundance proteins and due to the low dynamic range of the detection methods. Also membrane proteins and proteins with extreme isoelectric points or molecular masses can not be resolved. A further problem of 2D gel electrophoresis is the poor quantification of the analytes which is in part due to the difficulty in aligning the gel plate for the sample and the control which are loaded onto two different plates [158]. 2D differential gel electrophoresis (2D-DIGE) is an improvement of the

original technique which allows the separation and visualisation of three different samples in one gel plate [159]. The three samples are labelled with different fluorescent dyes which have distinct excitation and emission spectra so that differences in the abundance levels between the three samples can be readily compared.

The remaining limitations of gel electrophoresis, namely limited dynamic range, low sensitivity, low proteome coverage and not easy to automate, necessitate the application of more sophisticated methods [146]. One of the more sophisticated and sensitive methods is capillary electrophoresis (CE) [154] where the electrophoretic separation is performed in small capillaries with diameters below $100\,\mu$m. This reduces the sample size to the sub-microlitre range and allows the application of much higher electric fields which increases the sensitivity, selectivity and speed compared to 2D gel electrophoresis; the assay time can be reduced from minutes or even hours for 2D-PAGE to seconds for CE. Capillary electrophoresis can separate proteins which differ by only one amino acid and achieves sensitivities in the femtomolar range [160]. However, the high electric fields ($\sim$ kV) can lead to adverse effects such as water electrolysis, metallic ion injection, excessive heat generation and bubble formation [3].

A separation method which has similar sensitivity and sample requirements than CE but avoids the use of high electric fields is high performance liquid chromatography (HPLC) [153]. HPLC is a further development of conventional column chromatography [153] where the mobile phase is forced through the column under high pressures up to 100 MPa. The increased flow rate decreases the retention time and diffusion of the analyte plug which leads to much higher resolution and shorter run-times (minutes) compared to conventional column chromatography. For capillaries with diameters between $10\,\mu$m and $100\,\mu$m liquid chromatography is called nanoLC [161]. This reduction in the size of the capillary reduces the solvent and sample consumption and thus the costs for the reagents as well as for the waste disposal. Typical sample volumes for nanoLC range from the low nanolitre to the high microlitre range. Due to these small sample volumes nanoLC requires efficient detectors which are usually laser-induced fluorescence or mass spectrometry which were described in section 2.5. For example, nanoLC coupled to MS, which is shown schematically in figure 4.3, achieved protein identification from 0.5 pg of protein digests with a dynamic range of $5-6$ orders of magnitude [162]. This translates

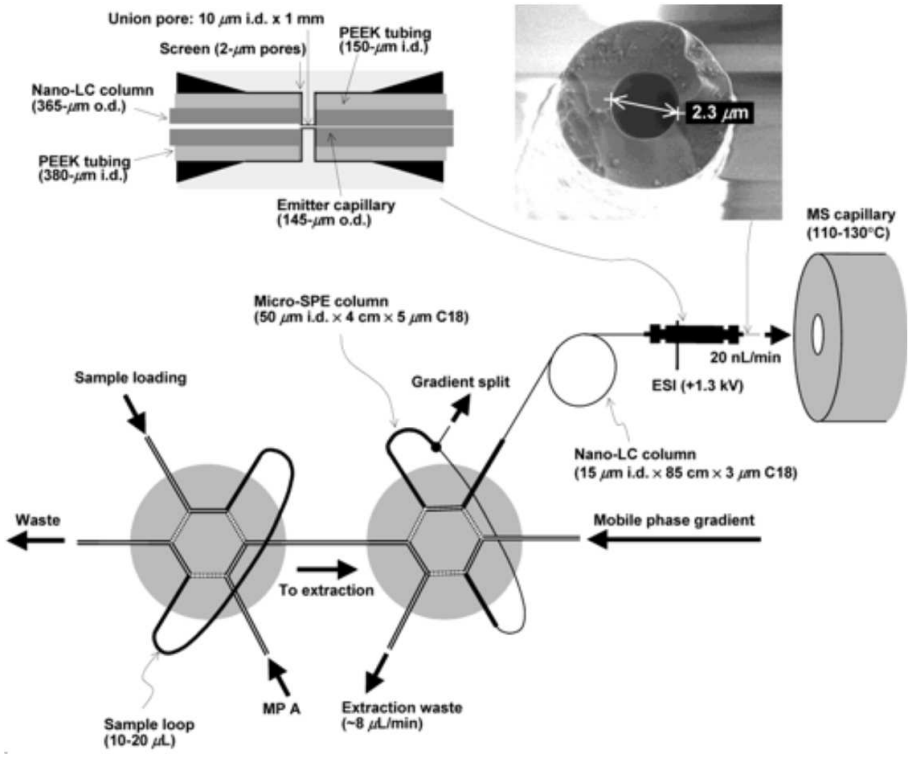

Figure 4.3: Schematic diagram of nanoLC coupled to ESI-MS. Reprinted with permission from [162]. Copyright 2004 American Chemical Society.

to a sensitivity in the femtomolar range.

Both CE and nanoLC are widely used in the analysis of protein samples [145]. Combined with MS or LIF detection both methods are able to separate and detect sub-nanomolar analyte concentrations from small samples ($\sim \mu$l). Furthermore, the operation of the separation device can be automated which increases the throughput and the reliability because errors due to human involvement are reduced. However, the integration of CE or nanoLC into a complete device with sample preparation, multiple separation stages and on-line detection requires complex instrumentation and many connections. The former makes such a system unsuitable for portable applications, while the latter increases the dead volume and the probability of leaks. Moving the separation from capillaries onto integrated microfluidic chips, where the protein preparation, separation and detection are performed in one device, has the potential to overcome these limitations of integration while retaining the benefits of CE and nanoLC [10].

4.2.2 Affinity based separation

Affinity based separations use the specific interactions between analytes and receptor antibodies to change the retention time of the analytes in the separation channel. In affinity chromatography the interaction between the immobilised receptor and the analyte moves the analyte from the mobile into the stationary phase which increases the retention time of the analyte molecule [163]. The separation in affinity electrophoresis is based on the different charge to size ratio of the analyte and the analyte-receptor complex [164]. Affinity separations, both affinity chromatography and affinity electrophoresis, can be classified into three principal configurations [12; 165]. The first is affinity depletion where a group of proteins is removed from the sample mixture. For the removal of high-abundance proteins often immunoglobulin G-based affinity columns are used. These columns can efficiently and selectively remove over 98% of the high-abundance proteins from human serum samples [166]. IgG-based systems show minimal nonspecific binding so that not-targeted, low-abundance proteins are not removed from the serum. High-abundance protein depletion is often performed to reduce the complexity of the protein sample before further steps such as 2D-PAGE are performed [12].

In the second configuration a target molecule is extracted from a sample mixture. In this case the target analyte interacts specifically with the receptor molecules in the column while the other constituents of the sample plug have no affinity for the receptor molecules. After the other molecules are eluted from the column, the target analyte has to be eluted. In the case of a weak or moderately strong interaction ($K_d > 1\,\mu M$) between the target analyte and the receptor the elution can be performed with the sample buffer [167]. For stronger interactions between the target analyte and the receptor, special elution conditions are required to accelerate the elution of the target analyte. These elution conditions can be photolytic elution [168], different but often harsh (pH, ionic strength) elution buffers, electrical [169] or thermal elution [170]. With the right choice of elution conditions the target analytes are released faster than they were captured and are thus released in a higher concentration [171]. This can be utilised to preconcentrate the analyte plug. In the third configuration a complex sample is fractionated into several subsets of reduced complexity [172]. These subsets contain a smaller number of different proteins compared to the original sample and thus the subsequent analysis of

the sample subsets has a greater chance to detect low-abundance proteins.

4.2.3 Microfluidic separation systems

Much work has been published on performing protein separations in microfluidic channels instead of gels or capillaries [10]. The properties of microfluidics as described in section 3.2 and the lab-on-a-chip approach (section 2.2) make microfluidic systems interesting for protein separations. The high surface-to-volume ratio, fast kinetics and low sample consumption of microfluidic assays are particularly beneficial for on-chip separations of proteins from small samples [150; 173]. However, the major benefit of chip-based approaches is the ability to integrate different analysis steps in one device [4; 174]. The integration of sample injectors, multiple separation steps and sample detection in one separation chip significantly decreases the dead volume and band spreading compared to conventional CE and nanoLC devices [118; 175]. Furthermore, the automation and reduced complexity of the instrumentation increases the repeatability and portability of the separation device. However, the reduced size of the microfluidic channel also creates problems which are not as important for larger columns. The high surface-to-volume ratios in microfluidic channels increases the need for specialised wall coatings. These wall coatings are needed to prevent nonspecific analyte adsorption and to tune the EOF in electrophoresis devices [176]. Furthermore, microfluidic affinity separation systems have a low sample loading capacity and thus require very sensitive and selective detectors such as LIF and MS [177] (section 2.5). This is especially true for liquid chromatography in open microfluidic channels. The height of these channels has to be below 10 μm so that sophisticated injection methods, pumps and detection methods are required to handle and detect the sub-nanolitre sample volumes [178].

Many operational modes of chromatography and electrophoresis, for example size exclusion electrophoresis [41] and reverse-phase chromatography [175], have been successfully adapted to microfluidic devices. Furthermore, the three configurations for affinity separations described in section 4.2.2 have also been transferred to microfluidic chips; microfluidic affinity depletion has been mainly applied to the removal of cells from serum samples [179] while analyte extraction [173] and preconcentration [150] were ap-

plied to protein mixtures. Combining affinity separation with reverse-phase capillary electrochromatography shows the applicability of microfluidic affinity separation systems for the prefractionation of the sample as well as for integrated multidimensional separation [20; 147]. These microfluidic separation systems work on sample sizes in the sub-nanolitre to microlitre range and achieve sensitivities in the nanomolar range.

Despite these examples both microchip affinity chromatography and microchip affinity electrophoresis are still less common than their capillary counterparts. This is partly due to the difficulties in the fabrication and integration of microchip separation systems. A further problem which is addressed in this chapter is the lack of theoretical models describing the separation in multiplexed, chip-based separation systems. A framework describing the protein separation in microfluidic systems with multiple parallel and sequential separation steps would be a valuable tool in the design and optimisation of microfluidic separation systems.

4.3 Modelling of microfluidic affinity separation systems for small Graetz numbers

The transport of an analyte plug in a microfluidic channel and the interaction between the analyte molecules and surface immobilised receptors can be described by the transport-reaction equations 3.18-3.20 which were introduced in section 3.3. Here these equations are simplified in the asymptotic limit of fast diffusion across the height of the microfluidic channel ($\mathrm{Gz} \ll 1$) and high adsorption capacity ($\kappa \gg 1$). The simplified model is then solved using the Laplace transform method. The resulting analytical solution describes the behaviour of an analyte plug in microfluidic affinity separation systems.

4.3.1 Analytical model

The governing equations 3.18-3.20 (section 3.3) are repeated here in their nondimensional form

$$A_t + \mathbf{u} \cdot \nabla A = \mathrm{Gz}^{-1} \left(\frac{H^2}{L^2} A_{xx} + A_{yy} + \frac{H^2}{W^2} A_{zz} \right) \qquad , x, y, z \in [0,1] \qquad (4.1)$$

$$A_y = \mathrm{Da} \ \left(A(1-B) - \bar{\mathrm{K}}_\mathrm{d} \, B \right) \qquad , x, z \in [0,1], y = 0 \qquad (4.2)$$

$$B_t = \mathrm{Gz}^{-1} \, \kappa^{-1} \, A_y \qquad , x, z \in [0,1], y = 0 \qquad (4.3)$$

where A is the analyte concentration in the bulk of the channel and B is the bound analyte concentration, i.e. the concentration of analyte associated to the surface immobilised receptor molecules. The remaining boundary conditions are given by no diffusive flux across the outlet, no flux across channel walls and sample injection at the channel inlet

$$A_x(1, y, z, t) = 0 \qquad , y \in [0,1], z \in [0,1], t \geq 0 \qquad (4.4)$$

$$A_y(x, 1, z, t) = 0 \qquad , x \in [0,1], z \in [0,1], t \geq 0 \qquad (4.5)$$

$$A_z(x, y, 0, t) = 0 \qquad , x \in [0,1], y \in [0,1], t \geq 0 \qquad (4.6)$$

$$A_z(x, y, 1, t) = 0 \qquad , x \in [0,1], y \in [0,1], t \geq 0 \qquad (4.7)$$

$$A(0, y, z, t) = f(t) \qquad , y \in [0,1], z \in [0,1], t \geq 0 \qquad (4.8)$$

where f is any specified function. In this thesis only sample injections with a short input time λ, i.e. the inlet analyte concentration is zero except for a short period of time, are considered (see section 3.3). Initially no analyte is in the microfluidic channel ($A = 0$) and all surface immobilised receptor molecules are free ($B = 0$). The four nondimensional numbers

$$\mathrm{Gz} = \frac{H^2 U}{L D} \qquad \mathrm{Da} = \frac{k_a H X_0}{D}$$

$$\bar{\mathrm{K}}_\mathrm{d} = \frac{k_d}{k_a A_0} \qquad \kappa = \frac{X_0}{A_0 H}$$

which link the physical effects in equations 4.1-4.3 were introduced in section 3.3.

From now on, only shallow and wide rectangular microfluidic channels are considered. This assumption is fulfilled for many integrated microfluidic systems [175]. In these

channels the diffusion term in the x and z direction in equation 4.1 can be neglected because the channel height is much smaller than the channel width and length so that $H/W \to 0$ and $H/L \to 0$. A further effect of the large aspect ratio of the channel is that the flow profile for most of the channel width (except close to the side walls) is parabolic over the height of the channel so that $\mathbf{u} = (u(y), 0, 0)$ where $u(y)$ is given by

$$u(y) = 6y(1-y) \tag{4.9}$$

With these simplifications the governing equation 4.1 in the bulk of the channel reduces to

$$A_t + u(y)A_x = \mathrm{Gz}^{-1} A_{yy} \tag{4.10}$$

From now on, only systems in the asymptotic limit $\mathrm{Gz} \ll 1$, where all analyte molecules can diffuse to the active surface and interact with the surface immobilised receptor molecules, are considered. This condition is necessary for separation systems because otherwise some analyte molecules would not interact with the surface immobilised receptors and thus are not retained. For values of the Graetz number much smaller than 1 the analyte plug concentration can be considered constant across the height of the channel. Thus the analyte concentration A depends only on the distance along the channel x and time t. For a mathematically more rigorous derivation see appendix A. In this case the theory of Taylor dispersion [180] states that the analyte plug moves along the channel with the average flow velocity. With these simplifications equation 4.10 can be integrated over the height of the channel and reduced to a 1D equation which describes the convection of the analyte plug and the reaction between the analyte molecules and surface immobilised receptor molecules. The reduced equations are given by

$$\frac{\partial A}{\partial t} + \frac{\partial A}{\partial x} = -\zeta(A(1-B) - \bar{\mathrm{K}}_\mathrm{d}\, B) \tag{4.11}$$

$$\frac{\partial B}{\partial t} = \frac{\zeta}{\kappa}(A(1-B) - \bar{\mathrm{K}}_\mathrm{d}\, B) \tag{4.12}$$

where ζ is the nondimensional reaction/convection number

$$\zeta = \frac{\mathrm{Da}}{\mathrm{Gz}} = \frac{k_a L X_0}{HU} = \frac{\text{reaction rate}}{\text{convection rate}} \tag{4.13}$$

The boundary and initial conditions for the differential equations 4.11 and 4.12 are given

by

$$A(x,0) = 0 \qquad , x \in [0,1] \tag{4.14}$$

$$B(x,0) = 0 \qquad , x \in [0,1] \tag{4.15}$$

$$A(0,t) = f(t) \qquad , t \geq 0 \tag{4.16}$$

where f is any specified function. The reaction/convection number ζ is the ratio between the reaction rate and the convection rate. For a small reaction/convection number ($\zeta \ll 1$) the transport is 'reaction limited' and most of the analyte molecules are convected through the system before they can associate with the receptors at the active surface. For a large reaction/convection number ($\zeta \gg 1$) the system becomes 'convection limited' and most of the analyte molecules bind at the beginning of the active surface.

The equations 4.11 and 4.12 define a mass balance between the bulk and the surface of the microfluidic channel similar to the one used in the reaction-dispersive model of column chromatography [151]. Under the assumption that the adsorption capacity is much larger than the reaction/convection number, i.e. $\kappa \gg \zeta > 0$, the governing equations 4.11 and 4.12 can be further simplified: the bound analyte concentration is expanded in powers of κ^{-1}

$$B = B^{(0)} + \frac{1}{\kappa} B^{(1)} + \frac{1}{\kappa^2} B^{(2)} + \mathcal{O}\left(\kappa^{-3}\right) \tag{4.17}$$

and inserted into equation 4.12 to get

$$B_t^{(0)} = 0 \tag{4.18}$$

From this it follows that $B_t = 0$ in first order and that the nondimensional bound concentration B is staying close to the initial value of 0, i.e. $B = \mathcal{O}\left(\kappa^{-1}\right)$. This suggests that the bound concentration B can be removed from the right side of equations 4.11 and 4.12. However, when the analyte plug has passed a point on the active surface, i.e. the unbound analyte concentration above that point is zero, or when there is a local equilibrium between the unbound and bound analyte concentration, the dissociation term can not be ignored. In the case of a local equilibrium between the unbound and bound analyte concentration the association and dissociation terms in equations 4.11

and 4.12 are equal and thus

$$A(1-B) = \bar{\mathrm{K}}_\mathrm{d}\, B \tag{4.19}$$

$$\Rightarrow \quad A = \bar{\mathrm{K}}_\mathrm{d}\, \frac{B}{1-B} = \bar{\mathrm{K}}_\mathrm{d}\, \mathcal{O}\left(\kappa^{-1}\right) \tag{4.20}$$

From this it follows that

$$A(1-B) - \bar{\mathrm{K}}_\mathrm{d}\, B = \bar{\mathrm{K}}_\mathrm{d}\left(\mathcal{O}\left(\kappa^{-1}\right) - \mathcal{O}\left(\kappa^{-2}\right)\right) - \bar{\mathrm{K}}_\mathrm{d}\, \mathcal{O}\left(\kappa^{-1}\right) \tag{4.21}$$

which shows that the nondimensional bound concentration B can only be removed from the association term in equation 4.11 and 4.12 and not from the dissociation term. This step which is in line with much of the previous publications reviewed in section 3.4 transforms the second order kinetics into first order kinetics. This removes the nonlinearity from the system of governing equations and the resulting linear differential equations can be solved analytically. Briefly, the Laplace transform reduces the partial differential equation 4.11 to an ordinary differential equation which can be solved analytically. The inverse Laplace transform of this analytical solution generates the solution to the original equation.

The Laplace transform [181] of the equations 4.11 and 4.12 gives

$$s\tilde{A} + \tilde{A}_x = -\zeta(\tilde{A} - \bar{\mathrm{K}}_\mathrm{d}\, \tilde{B}) \tag{4.22}$$

$$s\tilde{B} = \frac{\zeta}{\kappa}(\tilde{A} - \bar{\mathrm{K}}_\mathrm{d}\, \tilde{B}) \tag{4.23}$$

where $\tilde{A}(x,s)$ and $\tilde{B}(x,s)$ are the Laplace transforms of $A(x,t)$ and $B(x,t)$, respectively. Extending the derivation from Orszaghova [182] for an adsorption capacity $\kappa \neq 1$ the two equations are combined to get an ordinary differential equation for $\tilde{A}$

$$\tilde{A}_x = \tilde{A}\left(-\zeta - s + \frac{\zeta^2\, \bar{\mathrm{K}}_\mathrm{d}}{s\kappa + \zeta\, \bar{\mathrm{K}}_\mathrm{d}}\right) \tag{4.24}$$

Integrating this equation directly gives

$$\tilde{A} = \tilde{f} \exp\left(-\zeta x - sx + \frac{\zeta^2\, \bar{\mathrm{K}}_\mathrm{d}\, x}{\kappa s + \zeta\, \bar{\mathrm{K}}_\mathrm{d}}\right) \tag{4.25}$$

where $\tilde{f}$ is the Laplace transform of the boundary condition 4.16. Applying the convolution theorem and the second shift theorem the inverse Laplace transform of $\tilde{A}$ is given

by

$$A = e^{-\zeta x} \int_0^t e^{\frac{-\zeta \bar{\mathrm{K}}_\mathrm{d}\, r}{\kappa}} f(t-x-r)\, \hat{\mathrm{H}}(t-x-r) \tag{4.26}$$

$$\left(\delta(r) + \sqrt{\frac{\zeta^2\, \bar{\mathrm{K}}_\mathrm{d}\, x}{\kappa r}} I_1\left(2\sqrt{\frac{\zeta^2\, \bar{\mathrm{K}}_\mathrm{d}\, xr}{\kappa}}\right)\right) dr \tag{4.27}$$

where I_1 is the modified Bessel function of the first kind and $\hat{\mathrm{H}}$ the Heaviside step function. By replacing the arbitrary sample injection f with a short sample impulse defined by the Dirac delta function δ the integral can be solved analytically

$$A(x,t) = e^{-\zeta x}\, \hat{\mathrm{H}}(t-x)\delta(x-t) \tag{4.28}$$

$$+ e^{-\zeta x - \frac{\zeta \bar{\mathrm{K}}_\mathrm{d}}{\kappa}(t-x)} \sqrt{\frac{\zeta^2\, \bar{\mathrm{K}}_\mathrm{d}\, x}{\kappa(t-x)}} I_1(2\sqrt{\zeta^2\, \bar{\mathrm{K}}_\mathrm{d}\, x(t-x)/\kappa})(1-\hat{\mathrm{H}}(x-t)).$$

The first summand describes how the initial analyte plug travels down the channel and associates with the surface immobilised receptors. The second term of the sum describes a secondary plug which develops for $t > x$. This analyte plug consists of analyte which was already bound to the surface and dissociated. Figure 4.4 shows the distribution of unbound analyte along the channel for different values of ζ and at different times t. The plot shows that the analyte plug moves slower than the buffer flow velocity

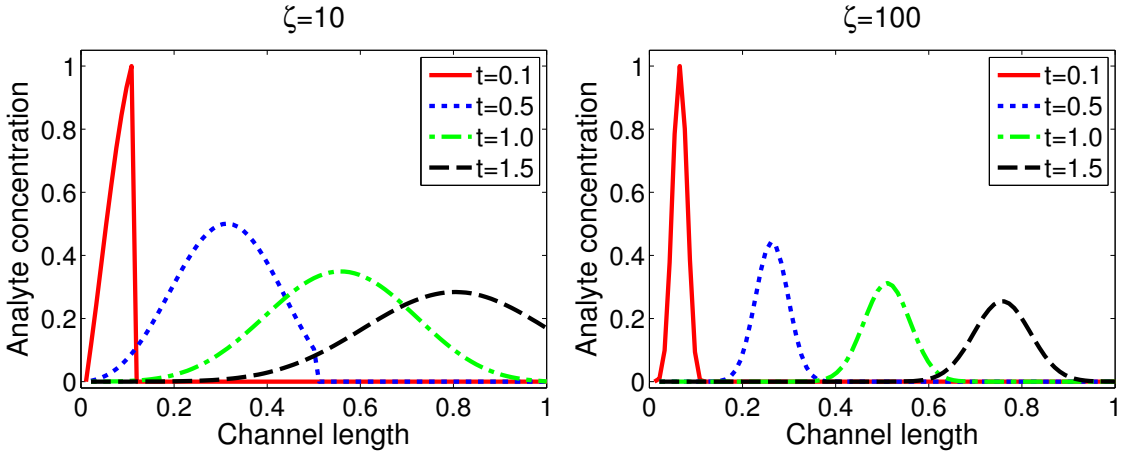

Figure 4.4: Plot of the unbound analyte concentration A calculated from equation 4.28 along the length of the channel for various times t. The plots are normalised with the maximal analyte concentration for $t = 0.1$. Parameters: (left) $\zeta = 10$, $\kappa = 10$, $\bar{\mathrm{K}}_\mathrm{d} = 10$, (right) $\zeta = 100$, $\kappa = 10$, $\bar{\mathrm{K}}_\mathrm{d} = 10$

($u = 1$). It can also be seen that the plug disperses. This dispersion is entirely due to

the adsorption/desorption of analyte at the active surface because axial diffusion was neglected in the governing equations. The dispersion in the left plot of figure 4.4 is much larger than in the right plot which is due to the lower reaction/convection number ζ compared to the right-hand side plot. The two effects of a lower reaction/convection number are the longer existence of the initial plug and the slower rebinding of the secondary plug. Both mechanisms lead to a larger dispersion of the analyte plug. The drop in analyte concentration observed for $t = 0.1$ in the left-hand side plot is an artifact due to the omission of axial diffusion in the calculations.

The Laplace transform for the analyte concentration given by equation 4.25 is inserted into the equation for the bound analyte concentration 4.23 which can be rearranged to

$$\tilde{B} = \frac{\zeta}{\kappa s + \zeta \bar{\mathrm{K}}_\mathrm{d}} \tilde{A}. \tag{4.29}$$

Following similar steps to those for the analyte A the Laplace transform can be inverted to get

$$B = \frac{\zeta}{\kappa} e^{-\zeta x} \int_0^t e^{-\zeta \bar{\mathrm{K}}_\mathrm{d} r/\kappa} I_0(2\sqrt{\zeta^2 \bar{\mathrm{K}}_\mathrm{d} xr/\kappa}) f(t-x-r)\, \hat{\mathrm{H}}(t-x-r) dr \tag{4.30}$$

where I_0 is the modified Bessel function of first kind and $\hat{\mathrm{H}}$ the Heaviside step function. By replacing the analyte input f with the Dirac delta δ the integral can be evaluated to get the explicit solution

$$B(x,t) = \frac{\zeta}{\kappa} e^{-\zeta x} e^{-\zeta \bar{\mathrm{K}}_\mathrm{d}(t-x)/\kappa} I_0(2\sqrt{\zeta^2 \bar{\mathrm{K}}_\mathrm{d}\, x(t-x)/\kappa})(1 - \hat{\mathrm{H}}(x-t)). \tag{4.31}$$

Figure 4.5 shows a plot of the bound analyte concentration for different values of ζ and at different times t. This plot shows that the bound analyte concentration B behaves similar to the unbound analyte concentration A. A slight difference can be seen in the left-hand side plot where the peak of the bound analyte concentration for $t = 0.1$ is less advanced than the peak of the corresponding analyte concentration also shown in figure 4.5. This slight lag of the peak of the bound analyte concentration is again due to the lower value of the reaction/convection number, i.e. the peak of the analyte concentration in figure 4.4 is given by the initial analyte plug while the peak in the bound analyte concentration in figure 4.5 corresponds to the position of the peak in the secondary analyte plug.

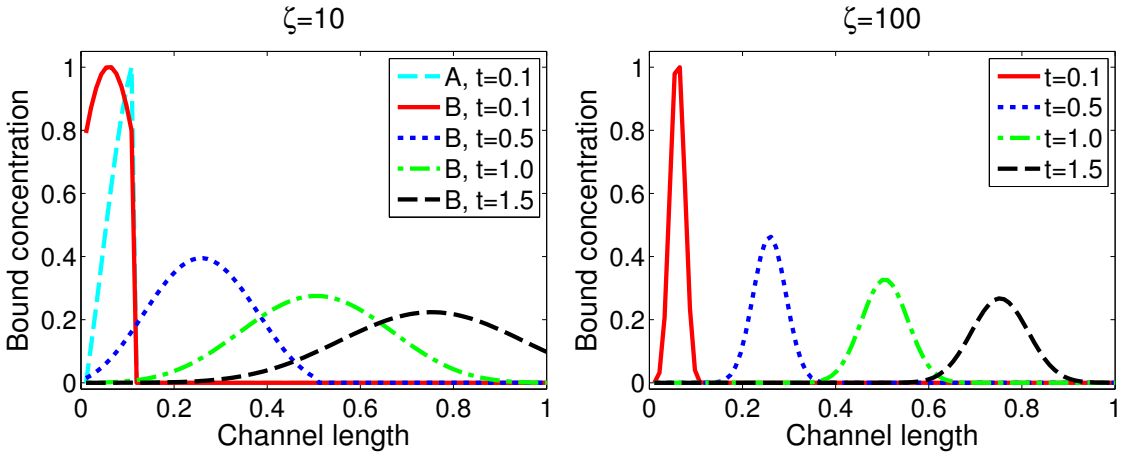

Figure 4.5: Plot of the bound analyte concentration B calculated from equation 4.31 along the length of the channel for various times t. The left plot shows also the normalised unbound analyte concentration A at $t = 0.1$. The plots are normalised with the maximal bound concentration for $t = 0.1$. Parameters: (left) $\zeta = 10$, $\kappa = 10$, $\bar{\mathrm{K}}_\mathrm{d} = 10$, (right) $\zeta = 100$, $\kappa = 10$, $\bar{\mathrm{K}}_\mathrm{d} = 10$

4.3.2 Verification of the simplifications

The simplification of the governing equations 4.1 - 4.3 are based on the assumptions that the analyte concentration is constant over the height of the microfluidic channel for a small enough Graetz number ($\mathrm{Gz} \ll 1$) and that the concentration of free receptor molecules is constant for a large adsorption capacity ($\kappa \gg 1$). Here, numerical simulations are performed to verify the simplifications and to find limits for the sufficient values of the Graetz number and the adsorption capacity. The numerical simulations provide the solution of the full problem given by equations 4.1-4.3 which includes second order kinetics, the parabolic flow profile and diffusion. For details about the implementation of the numerical simulations see appendix B.

The required Graetz number for which the analyte concentration is uniform across the height of the microfluidic channel depends on the value of the Damköhler number. For a Damköhler number much larger than 1 the systems is 'diffusion limited' (see section 3.4) and a depleted boundary layer develops. For the assumption of a uniform analyte concentration to be accurate the Damköhler number has to be smaller or at least not much larger than 1. The left plot of figure 4.6 shows the relative error of

the bound concentration for the Graetz number Gz = 0.05 and various values of the reaction/convection number. It can be seen that this value of the Graetz number is sufficient to keep the relative error in the bound concentration below 0.1 for most of the channel. The right plot of figure 4.6 shows that for a Graetz number Gz = 0.05 and a

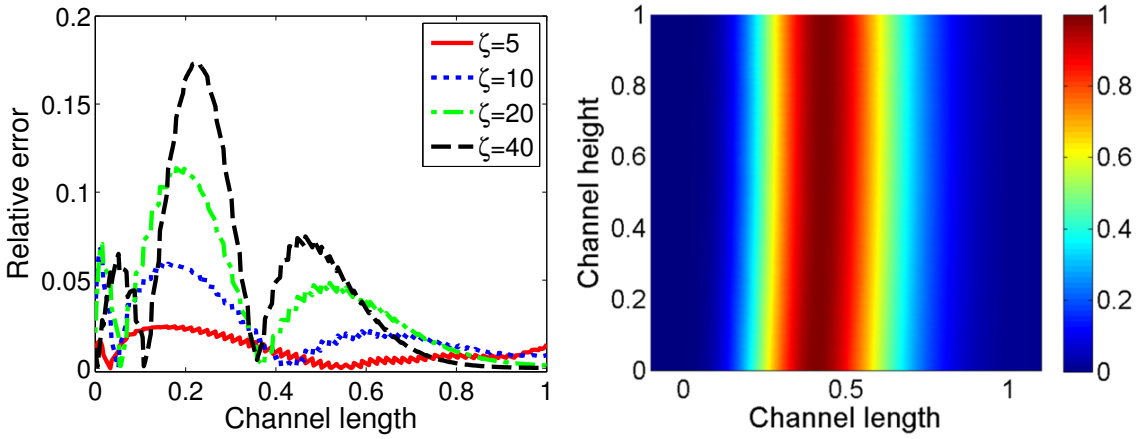

Figure 4.6: (left) Plot of the relative error between the analytical solution of the bound analyte concentration given by equation 4.31 and numerical simulations of the full problem for different values of the reaction/convection number ζ, (right) 2D plot of the simulated bulk concentration A_s for $\mathrm{Da} = \zeta\,\mathrm{Gz} = 2$. Parameters: (left) $\mathrm{Gz} = 0.05$, $\kappa = 100$, $\bar{\mathrm{K}}_\mathrm{d} = 20$, $\lambda = 1$, $t = 2$, (right) $\mathrm{Gz} = 0.05$, $\kappa = 100$, $\bar{\mathrm{K}}_\mathrm{d} = 20$, $\lambda = 1$, $t = 3$, $\zeta = 40$

Damköhler number Da = 2 the concentration of the analyte plug is almost uniform over the height of the channel. If the Graetz number is increased the relative error increases and the analyte plug moves much faster at the top of the channel compared to the bottom. A further point worth noticing is that the width of the analyte plug is reduced from the original width $\lambda = 1$ to a width less than 0.5. This is due to the reduced plug velocity over the active receptor patch and will be explored in section 4.5.2.

For the adsorption capacity the stationary case ($u = 0$) and nonstationary case ($u \neq 0$) are considered. In the stationary case which corresponds to Gz = 0 the adsorption capacity κ is the inverse of the maximal bound fraction of the receptor molecules which is only reached for systems with no detachment ($\bar{\mathrm{K}}_\mathrm{d} = 0$). This means that for $\kappa = 100$ maximal 1% of the surface immobilised receptor molecules are occupied. For flow through systems the situation becomes more complicated and the analyte plug length λ has to be taken into account. For analyte plugs which are shorter than the

active surface the requirement of a large adsorption capacity ($\kappa \gg \zeta > 0$) is sufficient to ensure first order kinetics. However, for analyte plugs which are long compared to the active surface ($\lambda \gg 1$) the requirement of a large adsorption capacity is not sufficient. The additional requirement that the analyte concentration is much smaller than the dissociation constant K_d ($\bar{K}_d \gg 1$), in which case equation 3.28 shows that $B_{eq} \ll X_0$, is needed. Figure 4.7 shows the relative error between a simulation based on the linear, first order binding kinetics and a simulation based on the nonlinear, second order kinetics for different values of κ. Both plots are for a plug length equal to the

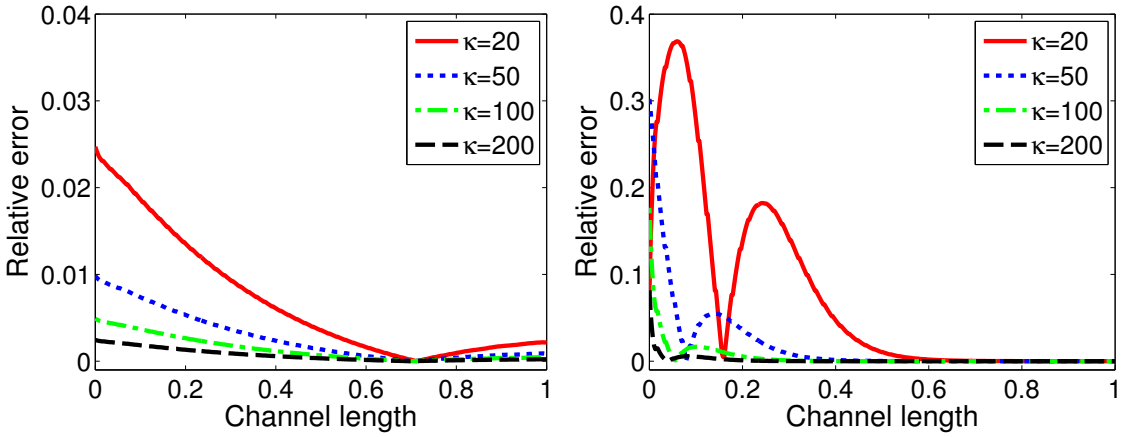

Figure 4.7: Plot of the relative error between the simulated bound analyte concentration for second order and first order kinetics for different values of the adsorption capacity κ. Parameters: (left) $Gz = 0.05$, $\bar{K}_d = 0.1$, $\lambda = 1$, $t = 3$, $\zeta = 1$, (right) $Gz = 0.05$, $\bar{K}_d = 1$, $\lambda = 1$, $t = 3$, $\zeta = 50$

length of the active surface but have different values of the reaction/convection number ζ and the nondimensional dissociation constant $\bar{K}_d$. The right plot of figure 4.7 shows that even for $\bar{K}_d = 1$ and $\zeta = 50$ an adsorption capacity of ~ 200 is sufficient to keep the relative error below 1% for most of the active surface. Furthermore, the plot suggests that the strong requirement on the relationship between the adsorption capacity and the reaction/convection number, i.e. $\kappa \gg \zeta$, can be relaxed. For separation applications the plug length would be much smaller than the length of the active receptor patch so that $\kappa = 200$ is sufficient to ensure that the first order binding kinetics are applicable.

4.4 Derivation of expressions for the analyte plug velocity and plug dispersion

Plots of the unbound analyte concentration like the one in figure 4.4 showed that for large values of ζ the analyte plug moves more slowly than the fluid velocity. The resulting retention of the analyte plug can be exploited to produce a separation device. For the design of such a separation device it would be beneficial to translate the analyte concentration distribution which is given by equation 4.28 into expressions for the plug velocity and plug dispersion.

4.4.1 Derivation

To find a simple, analytical expression for the plug velocity the unwieldy equation 4.28 for the unbound analyte concentration A has to be simplified. Under the prerequisite of fast adsorption the first summand of equation 4.28 quickly goes to zero and only the second summand which is zero for $t < x$ has to be considered. For $t > x$ the bulk analyte concentration A reduces to

$$A = e^{-\zeta x+\zeta \bar{\mathrm{K}}_\mathrm{d}(x-t)/\kappa}\sqrt{\frac{\zeta^2\,\bar{\mathrm{K}}_\mathrm{d}\,x}{\kappa(t-x)}}I_1\left(2\sqrt{\zeta^2\,\bar{\mathrm{K}}_\mathrm{d}\,x(t-x)/\kappa}\right) \tag{4.32}$$

For $w = 2\sqrt{\zeta^2\,\bar{\mathrm{K}}_\mathrm{d}\,x(t-x)/\kappa} \gg 1$ the Bessel function can be approximated in first order through $I_1(w) \approx \frac{e^w}{\sqrt{2\pi w}}$ [183]. Inserting this into equation 4.32 gives the following approximation

$$\begin{aligned} A &\approx \sqrt{\frac{\zeta^2\,\bar{\mathrm{K}}_\mathrm{d}\,x}{\kappa(t-x)}}\frac{e^{2\sqrt{\zeta^2\,\bar{\mathrm{K}}_\mathrm{d}\,x(t-x)/\kappa}-\zeta x+\zeta\,\bar{\mathrm{K}}_\mathrm{d}(x-t)/\kappa}}{\sqrt{2\pi 2\sqrt{\zeta^2\,\bar{\mathrm{K}}_\mathrm{d}\,x(t-x)/\kappa}}} \\ &= \sqrt{\frac{\zeta\sqrt{\bar{\mathrm{K}}_\mathrm{d}}}{4\pi\sqrt{\kappa}}}\sqrt{\frac{\sqrt{x}}{(t-x)^{3/2}}}e^{2\sqrt{\zeta^2\,\bar{\mathrm{K}}_\mathrm{d}\,x(t-x)/\kappa}-\zeta x+\zeta\,\bar{\mathrm{K}}_\mathrm{d}(x-t)/\kappa} \end{aligned} \tag{4.33}$$

which is justified for fast binding and for $t > x$. In the following analysis the first and the second factor are neglected because the first is constant and the second is monotonic increasing in x with a small gradient. The exponential factor $E(x,t) = e^{2\sqrt{\zeta^2\,\bar{\mathrm{K}}_\mathrm{d}\,x(t-x)/\kappa}-\zeta x+\zeta\,\bar{\mathrm{K}}_\mathrm{d}(x-t)/\kappa}$ on the other hand is the governing factor for the analyte concentration distribution along the channel length.

The position of the maximum of equation 4.33 should travel with the speed of the analyte plug. Thus finding the maximum position over time will allow the calculation of the plug velocity. The necessary condition for the position of the maximum is that the first derivative is zero. Differentiating the exponential factor E with respect to x and equating to zero produces an algebraic equation for the position of the peak analyte concentration

$$0 = E(x,t)\left(\zeta(\bar{\mathrm{K}}_\mathrm{d}/\kappa - 1) + \sqrt{\zeta^2\,\bar{\mathrm{K}}_\mathrm{d}/\kappa}\frac{t-2x}{\sqrt{x(t-x)}}\right) \tag{4.34}$$

$$\Rightarrow \quad 0 = x^2 - xt + \frac{t^2}{2+\bar{\mathrm{K}}_\mathrm{d}/\kappa + \kappa/\bar{\mathrm{K}}_\mathrm{d}} = \left(x - \frac{t}{1+\kappa/\bar{\mathrm{K}}_\mathrm{d}}\right)\left(x - \frac{t}{1+\bar{\mathrm{K}}_\mathrm{d}/\kappa}\right) \tag{4.35}$$

Solving this equation gives two different analyte plug velocities

$$u_p = \frac{x}{t} = \frac{1}{1+\kappa/\bar{\mathrm{K}}_\mathrm{d}} = \frac{1}{1+\frac{k_a X_0}{k_d H}} \tag{4.36}$$

$$\tilde{u}_p = \frac{x}{t} = \frac{1}{1+\bar{\mathrm{K}}_\mathrm{d}/\kappa} = \frac{1}{1+\frac{k_d H}{k_a X_0}} \tag{4.37}$$

The plots of the unbound analyte concentration A in figure 4.4 show that the analyte plug is travelling with one discrete velocity. Therefore only one of the two velocities 4.36 and 4.37 describes the plug movement while the second velocity was introduced through squaring of equation 4.34. By inserting the two velocities, i.e. the two relationships between x and t, into equation 4.34 the second velocity 4.37 can be ruled out through the following sign argument

$$\zeta(1-\bar{\mathrm{K}}_\mathrm{d}/\kappa)\sqrt{x(t-x)} = (t-2x)\sqrt{\zeta^2\,\bar{\mathrm{K}}_\mathrm{d}/\kappa} \tag{4.38}$$

$$\Rightarrow \qquad \mathrm{sign}\left(1-\bar{\mathrm{K}}_\mathrm{d}/\kappa\right) = \mathrm{sign}\,(t-2x) \tag{4.39}$$

From equation 4.39 it follows that

$$\frac{x}{t} > 0.5 \quad \Rightarrow \quad \bar{\mathrm{K}}_\mathrm{d} > \kappa \quad \Rightarrow \quad u_p = \frac{x}{t} > 0.5, \tilde{u}_p = \frac{x}{t} < 0.5 \tag{4.40}$$

$$\frac{x}{t} < 0.5 \quad \Rightarrow \quad \bar{\mathrm{K}}_\mathrm{d} < \kappa \quad \Rightarrow \quad u_p = \frac{x}{t} < 0.5, \tilde{u}_p = \frac{x}{t} > 0.5 \tag{4.41}$$

This clearly shows a contradiction for the second velocity 4.37 and thus only the expression 4.36 describes the velocity of the peak concentration of the analyte plug.

The simple approximation 4.36 for the velocity depends only on the channel height, surface immobilised receptor concentration and the dissociation constant. Figure 4.8

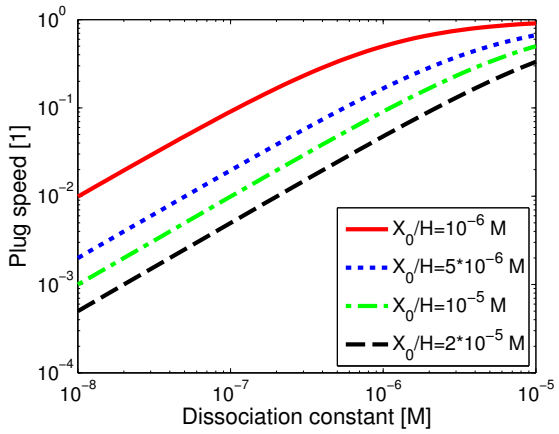

Figure 4.8: Plot of the plug velocity u_p calculated from equation 4.36. The plotted ratios X_0/H cover the range of possible surface immobilised receptor concentrations and channel heights.

shows the resulting plug velocity for a feasible range of parameters. The figure shows that the dissociation constant of the analyte-receptor pair should be in the range $10^{-5} - 10^{-8}$ M. For weaker interactions the retention of the analyte is not sufficient for the separation of proteins while for stronger interactions it is difficult to elute the analyte from the separation channel. Analyte-receptor pairs with a dissociation constant in this range have been employed in so called weak affinity chromatography [167].

The ratio of the adsorption capacity κ and the nondimensional dissociation constant $\bar{\mathrm{K}}_\mathrm{d}$ defines the nondimensional channel capacity

$$\xi = \frac{\kappa}{\bar{\mathrm{K}}_\mathrm{d}} = \frac{k_a X_0}{k_d H} \tag{4.42}$$

The channel capacity is a measure for the retention of an analyte plug in microfluidic affinity separation systems. For $\xi \ll 1$ the analyte plug is only weakly retained and the plug velocity approaches the buffer velocity. For $\xi \gg 1$ the analyte plug is strongly retained and the plug velocity goes to zero.

Figure 4.4 shows that the analyte plug broadens as it moves along the channel. The original analyte impulse develops into a Gaussian function with increasing variance σ^2. This is expected because the Dirac delta function can be seen as the limit $\sigma \to 0$ of the Gaussian function. A common quantification for the width of an impulse is the full width at half maximum (FWHM) which is the distance between the two points where

the impulse has half its maximal value. For the Gaussian function this width is related to the variance and given by FWHM $= 2\sqrt{2\log 2}\sigma$. To get a measure for the width of the slowed analyte plug the second derivative of equation 4.33 is calculated and analysed at the position of the maximum because the variance σ^2 of the Gaussian function is proportional to the second derivative. The second derivative of the exponential function E from equation 4.33 is given by

$$E''(x,t) = e^{2\sqrt{\zeta^2\,\bar{\mathrm{K}}_\mathrm{d}\,x(t-x)/\kappa}-\zeta x+\zeta\,\bar{\mathrm{K}}_\mathrm{d}(x-t)/\kappa}\left(-\zeta+\zeta\,\bar{\mathrm{K}}_\mathrm{d}/\kappa+\frac{\zeta^2\,\bar{\mathrm{K}}_\mathrm{d}(t-x)-\zeta^2\,\bar{\mathrm{K}}_\mathrm{d}}{\sqrt{\zeta^2\,\bar{\mathrm{K}}_\mathrm{d}\,\kappa x(t-x)}}\right.$$
$$\left.-\frac{(\zeta^2\,\bar{\mathrm{K}}_\mathrm{d}(t-x)/\kappa-\zeta^2\,\bar{\mathrm{K}}_\mathrm{d}\,x/\kappa)^2}{2(\zeta^2\,\bar{\mathrm{K}}_\mathrm{d}\,x(t-x)/\kappa)^{3/2}}-\frac{2\zeta^2\,\bar{\mathrm{K}}_\mathrm{d}}{\sqrt{\zeta^2\,\bar{\mathrm{K}}_\mathrm{d}\,xt-x)\kappa}}\right) \tag{4.43}$$

where the exponential factor which is equal to 1 at the peak of the analyte plug is scaled by the subsequent terms. The first three terms represent the first derivative of the exponential term E which is zero at the peak of the analyte plug. Therefore only the last two terms of the sum which will give a measure of the standard deviation σ have to be analysed. At the location of the peak which is given by equation 4.36 the last two terms reduce to the variance

$$E''(x,(1+\xi)x) = \sigma^2 = t\frac{2\xi^2}{\zeta(1+\xi)^3} = x\frac{2\xi^2}{\zeta(1+\xi)^2} \tag{4.44}$$

This shows that the standard deviation σ and therefore the plug dispersion is dependent on $\sqrt{t}$ and the nondimensional device parameters ξ and ζ.

4.4.2 Numerical verification of the simplifications

In the last section a simplified model of the transport and reaction of an analyte plug in a microfluidic channel with surface immobilised receptors was developed. Several simplifying assumptions have been used to reach the analytical solution. In this section the model predictions are compared with numerical simulations. The numerical simulations will use the full 2D model including diffusion and second order kinetics. All plots of the simulated analyte concentration A_s in this chapter show the simulated analyte concentration at half the channel height, i.e. $y = 0.5$. For the implementation and validation of the numerical simulations see appendix B.

First the minimal value for the reaction/convection number ζ so that the simplification of equation 4.28 is justified has to be found. The approximation of the Bessel function is not the limiting factor because the approximation shows for $w > 1$ the same qualitative behaviour and only a small quantitative deviation from the Bessel function. The limiting factor for this simplification is the fast binding of the initial analyte plug so that the first summand in equation 4.28 can be neglected. Figure 4.9 shows the unbound analyte concentration for various values of the reaction/convection number. It can be seen in the left plot of figure 4.9 that the concentration distribution changes

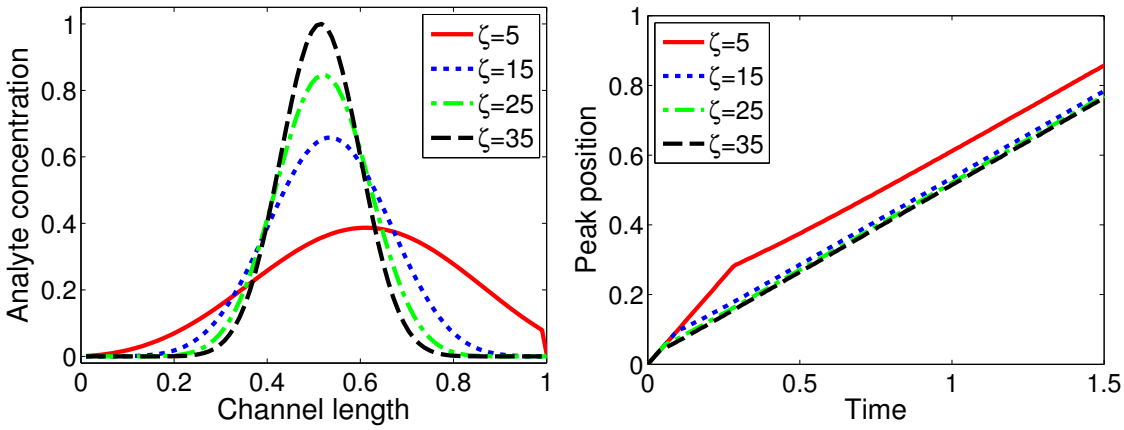

Figure 4.9: (left) Plot of the unbound analyte concentration A calculated from equation 4.28 along the length of the channel for various values of ζ. The plot is normalised with the maximal analyte concentration. (right) Peak position of the analyte plug for different values of ζ. Parameters: (left) $t = 1$, $\xi = 1$, (right) $\xi = 1$

considerably from $\zeta = 5$ to $\zeta = 15$ while the peak position is fairly constant for $\zeta \geq 15$. For $\zeta = 20$ about 86% of the analyte binds in the first 10% of the channel length. Values in this range are possible for antigen-antibody interactions in shallow microfluidic channels. The right plot of figure 4.9 shows the peak position over time. The resulting plot converges to the linear slope given by equation 4.36 for increasing ζ. The 'kink' in the right plot is due to the first summand in equation 4.28. For low values of the reaction/convection number ζ the interaction at the active surface is not fast enough and thus the first summand in equation 4.28 which represents the initial analyte plug does not go to zero quick enough. This initial analyte plug moves through the channel with the buffer velocity which is 1 in this nondimensional plot. At the 'kink' the value

of the initial analyte plug is equal to the value of the secondary analyte plug which after this point dominates the device behaviour. For larger values of ζ the 'kink' moves closer to the origin. The figure indicates that the interaction between the analyte and surface immobilised receptors is fast enough and thus the analysis from the last section valid for $\zeta > 15$. In the remainder of this section the slightly higher value of $\zeta = 25$ is used. Feasible values for the Graetz number Gz and the adsorption capacity κ so that the approximations are valid were discussed in section 4.3.2. In the subsequent simulations $\mathrm{Gz} = 0.05$ and $\kappa = 250$ which fulfil the prerequisites are used.

The derivation of the solution is based on an analyte impulse given through the Dirac delta function δ. This is clearly not physically possible because every analyte plug would have nonzero width and finite concentration. However, the simulations are performed with an analyte plug whose length λ is short in comparison to the channel length L. This generalisation is reasonable for the linearised system with high adsorption capacity as shown in the left-hand plot of figure 4.10. The position of the analyte

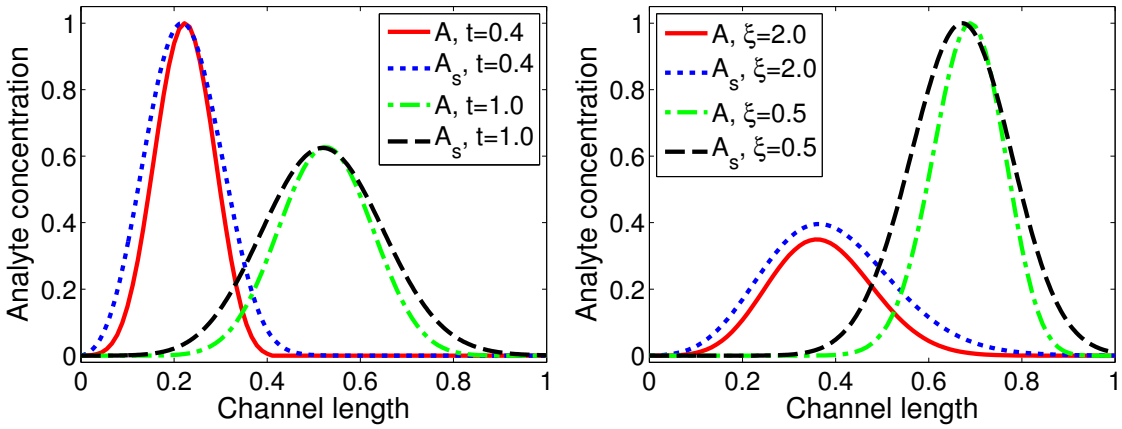

Figure 4.10: Plot of the analytical analyte concentration A given by equation 4.28 and the simulated analyte concentration A_s for different system configurations. The numerical simulations for the simulated analyte concentration A_s were performed with equations 4.1-4.3. (left) Comparison for different times and (right) comparison for different values of ξ. The plots are normalised with the maximal analyte concentration. Parameters: (left) $\mathrm{Gz} = 0.05$, $\kappa = 250$, $\lambda = 0.05$, $\xi = 1$, $\zeta = 25$, (right) $\mathrm{Gz} = 0.05$, $\kappa = 250$, $\lambda = 0.05$, $\zeta = 25$, $t = 1$

plug is almost identical for the analytical solution A of the simplified problem and the numerical solution A_s of the full problem which indicates that the model is applicable to

starting plugs with nonzero width. For details of the implementation in COMSOL Multiphysics 3.4 (COMSOL AB, Stockholm, Sweden) see appendix B. Furthermore, once the analytical and numerical solutions are normalised at one time point the solutions at other time points have the same amplitude. The subsequent simulations are carried out with a starting plug width of $\lambda = 0.05$. A further reduction in the starting plug width λ would increase the numerical complexity without providing additional information. The right-hand side of figure 4.10 shows a plot of the unbound analyte concentration for fixed values of ζ and t but for two values of the channel capacity ξ. The peak position of the analytical and the simulated analyte plug agree with the predicted peak positions from the analytical expression for the plug velocity 4.36. Similar plots for values of ξ between 0.05 and 100 (data not shown) also confirm the analytical plug velocity.

The larger width of the analyte plug given by the numerical simulations is due to the nonzero starting plug width compared to the Dirac impulse for the analytical model and the axial diffusion which is neglected in the analytical model. However, it has been shown that for linear binding kinetics and fast reactions the effects of axial diffusion and mass transfer resistance are additive [184]. The two dispersive effects both lead to a Gaussian distribution in the concentration. For fast reaction and diffusion these effects are independent and the variance of the resulting Gaussian is the sum of the variance for the axial diffusion and the mass transfer resistance. This is used in section 4.5 to calculate the total width of the analyte plug.

The analytical expression for the plug width 4.44 is now compared with the FWHM of the analytical solution 4.28 and the FWHM of the numerical simulation. Figure 4.11 shows the peak width of the analyte plug for different values of the two governing nondimensional parameters ζ and ξ. The development of the plug dispersion over time in figure 4.11 correlates with equation 4.44. The dispersion is inversely proportional to the square root of the reaction/convection number ζ as shown in the left plot of figure 4.11. From this it is clear that fast adsorption is crucial to keep the plug dispersion as small as possible. The right plot of figure 4.11 shows that the dispersion is maximal for $\xi = 2$ which is the maximum of $\xi^2(1+\xi)^{-3}$ and that the dispersion is proportional to the square root of $\xi^2(1+\xi)^{-3}$. Furthermore the FWHM matches with good accuracy the FWHM of the Gaussian function stated earlier. The 'kinks' in the plot are again

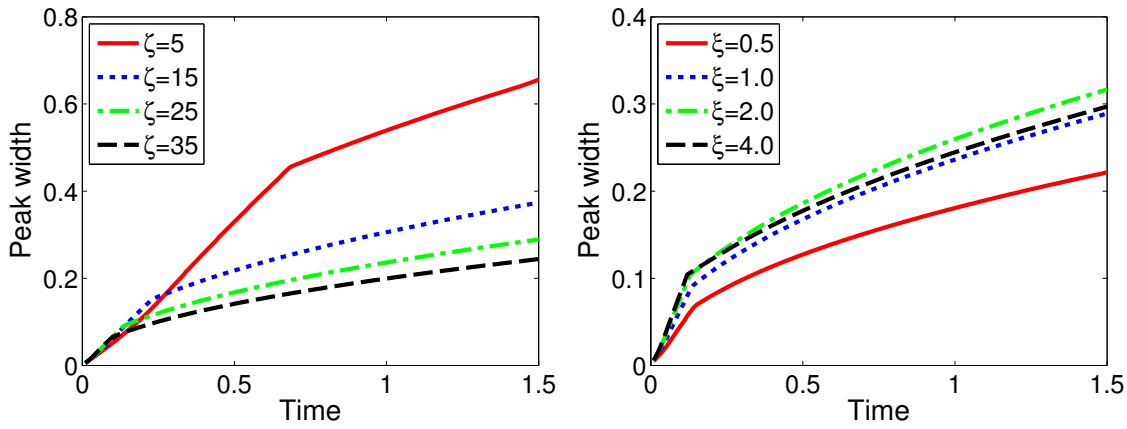

Figure 4.11: Plots of the FWHM of the unbound analyte plug calculated from equation 4.28 for (left) different values of the reaction/convection number ζ and (right) different values of the channel capacity ξ . Parameters: (left) $\xi = 1$, (right) $\zeta = 25$

due to the limited value of the reaction/convection number ζ (see figure 4.9); briefly, for a small value of ζ the initial analyte plug, which moves with the buffer velocity, does not go to zero quick enough and thus increases the dispersion of the analyte plug.

The comparison of the analytical analyte concentration A and the simulated analyte concentration A_s in figure 4.10 shows that the simulated analyte plug disperses faster than predicted by the analytical solution. This is due to the neglected axial diffusion in the analytical model. Table 4.1 compares the FWHM for a slowed and a non-slowed simulated analyte plug along the length of the channel. The data shows that the width of both the slowed and the non-slowed plug increase proportional to the square root of the distance along the channel. Only the proportionality constant for the slowed plug is larger than the proportionality constant for the non-slowed plug. This shows that the two dispersive effects, adsorption/desorption and axial diffusion, are additive in the here studied case.

4.4.3 Results

The derived analytical expressions for the analyte plug velocity 4.36 and the plug dispersion 4.44 are sufficient to describe the behaviour of analyte plugs in microfluidic affinity separation systems with small Graetz number and large adsorption capacity.

Position	FWHM slowed plug	FWHM non-slowed plug
0.04	0.070	0.065
0.08	0.095	0.085
0.12	0.110	0.100
0.16	0.120	0.105
0.20	0.125	0.110
0.24	0.130	0.115
0.28	0.140	0.120
0.32	0.145	0.125
0.36	0.150	0.125
0.40	0.155	0.125
0.44	0.160	0.130

Table 4.1: Comparison of the FWHM for a slowed and non-slowed pulse at the same position along the channel. The slowed pulse travels down the channel with 20% of the buffer velocity. Parameters: $\mathrm{Gz} = 0.01$, $\kappa = 333$, $\bar{\mathrm{K}}_\mathrm{d} = 83$, $\lambda = 0.005$, $\zeta = 2000$

The ongoing trend of miniaturisation in microfluidic systems leads to ever-decreasing channel heights [152] so that the prerequisites of the presented model can be fulfilled.

The presented results fit in with the established theory for column chromatography [151]. By comparing equation 4.36 with the equation for the band velocity

$$U_{band} = U\frac{1}{1+k} = U\frac{1}{1+\frac{C_s V_s}{C_m V_m}} \tag{4.45}$$

it is clear that the nondimensional channel capacity ξ is related to the column capacity ratio of liquid chromatography

$$k = \frac{C_s V_s}{C_m V_m} \tag{4.46}$$

Here C_s and C_m are the analyte concentration in the stationary and mobile phase and V_s and V_m are the volume of the stationary and mobile phase, respectively. This shows that the term $k_a X_0$ corresponds to the stationary phase while $k_d H$ corresponds to the mobile phase.

The reduction in the analyte plug velocity depends on the ratio of analyte in the bulk and of analyte bound to the active surface, i.e. the higher the percentage of analyte bound at the active surface the slower the analyte plug velocity. This mass balance between the bulk and bound analyte can be seen in the right-hand plot of figure 4.10 where the slower analyte plug has a smaller amplitude. A similar result to equation 4.36 was derived by Gervais and Jensen [131] from a mass balance between the bulk and the active surface

$$u = \frac{x}{t} = \frac{1}{1 + \frac{k_a X_0}{A_0 k_a H + k_d H}} \tag{4.47}$$

This result is valid for a continuous analyte input but can also be applied to the situation of a short analyte plug. An advantage of the derivation presented here is the explicit dependency of the expression for the plug dispersion 4.44 on the channel capacity and reaction/convection number. Furthermore, the expression for the plug dispersion is similar to the expression describing the dispersion due to mass transfer from the mobile to the stationary phase in open-tubular systems

$$k_m = \frac{1}{N} \frac{f_0 + f_1 k + f_2 k^2}{(1+k)^2} \tag{4.48}$$

where f_0, f_1, f_2 and N are constants depending on the device geometry and flow characteristic [185]. This shows that the two analytical expressions 4.36 and 4.44 can be used in the established theory of column chromatography to design and optimise open microfluidic affinity separation systems [186; 187].

4.5 Design of a microfluidic separation system

4.5.1 Design idea and setup

The study of the human proteome requires efficient separation systems for thousands of proteins from limited sample volumes (section 2.2). Ideally the separation system would consist of many parallel separation channels which each contain several sequential separation stages. Such an integrated microfluidic affinity separation system has the potential to fulfil the requirements on sensitivity, sample consumption and high integration. However, the design of multiplexed separation systems requires either many trial

and error steps or extensive numerical simulations. Here an analytical design strategy for the design of such a separation device with multiple separation lanes and multiple, different receptor patches in each lane is presented.

A schematic top view diagram of the proposed separation device is shown in figure 4.12. The separation channel is divided into lanes which are again divided into

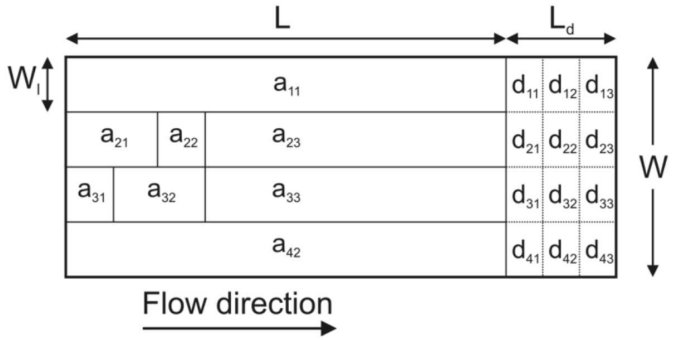

Figure 4.12: Top view of the proposed separation device. Shown are 4 separation lanes with different receptor patches a_{ij} and the detection region L_d. Each lane in the detection region can be split into several detection spots d_{ik}.

patches a_{ij} of varying length and with different surface immobilised receptor molecules. The length of the receptor patches is given through a_{ij} where i is the lane number and j specifies the receptor molecule, i.e. patches with the same value of j have the same type of surface immobilised receptor molecules. The receptor patches have different lengths which are to be determined to achieve an optimal separation of the target analytes. In this optimisation the patch lengths are restricted by the minimal patch length L_p and the maximal patch length L. It will be shown in section 4.5.2 that the ratio of the maximal patch length L to the minimal patch length L_p directly influences the ratio of the smallest to the largest channel capacity the channel can detect. Here the channel capacity refers to the analyte with this channel capacity, i.e. the smallest channel capacity refers to the analyte with the smallest channel capacity. Furthermore, patches with different receptor molecules have different surface immobilised receptor concentrations X_{0j} and different dissociation constants K_{jk} for different analytes A_k. A sample plug is injected from the left and flowed through the separation channel with length L to the detection region of length L_d. Depending on the detection method used each lane

of the detection region can be split into several detection spots d_{ij}. In figure 4.12 each lane is split into 3 detection spots but this number can vary depending on the detection method and fabrication constraints. In the following analysis a_{ij} and d_{ij} specify both the patch as well as the patch length and the meaning is clear from the context.

Once the different analyte molecules are separated they have to be quantified. While most methods developed for chromatography and electrophoresis can be used, laser-induced fluorescence and mass spectrometric detection offer the highest sensitivity and resolution and are therefore most suitable (section 2.5). Laser-induced fluorescence can be performed in an on-line manner where the analytes are analysed when they leave the separation channel. In this case the detection region L_d corresponds to the duration of the detection and the detection spots d_{ij} correspond to different capture frames. Mass Spectrometric Imaging (MSI) a variant of MALDI-MS offers slightly lower sensitivity than LIF but without the need for labelling [119]. Once the analytes are in the detection region the flow is stopped and the substrate is allowed to dry. The MALDI matrix is applied to the dry substrate and the detection is performed in a commercial mass spectrometer. By this technique the detection region is divided into several detection spots whose size is limited by the spatial resolution of the mass spectrometer. The lower limit for the spot size is about $50\,\mu$m and a typical resolution is between $100\,\mu$m and $200\,\mu$m [120]. For both detection methods, LIF and MSI, the detection region is split into N detection spots or detection frames. For a finite number N of detection spots d_{ij} the peak of the analytes with the smallest and largest channel capacities should be in the middle of the last and first detection spot, respectively. This reduces the separation range of the lane and L_d has to be replaced with $\tilde{L}_d = \frac{N-1}{N} L_d$.

Most of the microfabrication methods reviewed in section 2.3 are suitable for the fabrication of microfluidic affinity separation devices because the fluidic structures are fairly simple and have large feature sizes ($> 10\,\mu$m). The main restrictions on the fabrication methods stem from device operation parameters, such as applied pressure, used detection method and receptor immobilisation (see chapter 2). The theoretical framework presented here is independent of the detection and microfabrication methods.

The design of the microfluidic system is constrained by fabrication limitations and

the following three equations

$$\zeta = \frac{k_a L_p X_0}{HU} > 20 \tag{4.49}$$

$$\mathrm{Gz} = \frac{H^2 U}{L_p D} < 1 \tag{4.50}$$

$$x_d \sim \sqrt{\frac{2DL}{U}} < W_l \tag{4.51}$$

The first two equations are the prerequisites for the model from section 4.4 while the third equation controls the cross lane diffusion. The necessary values for the flow velocity U, minimal receptor patch length L_p, separation channel length L and the lane width W_l have to be determined from these equations for a given analyte-receptor system.

The three equations illustrate that both the separation channel length L and the minimal patch length L_p depend directly on the flow velocity U. Therefore the flow velocity has no influence on the separation ratio, i.e. the ratio between the maximal channel capacity and the minimal channel capacity the system can detect, of the device because the ratio between the maximal patch length and the minimal patch length defines the separation ratio (see section 4.5.2). The channel height, on the other hand, influences the minimal patch length and should be chosen as small as possible. For the examples in this section, the flow velocity and channel height are chosen to be $U = 10^{-4}\,\mathrm{m\,s^{-1}}$ and $H = 5\,\mu\mathrm{m}$, respectively. For this channel height, which can be reproducibly fabricated with current microfabrication methods (section2.3), liquid chromatography in open microfluidic channels can achieve higher separation efficiencies than in packed microfluidic channels [188]. With this flow velocity and channel height the minimal patch length can be calculated for a given analyte-receptor pair. For the minimal association rate $k_a = 10^5\,\mathrm{M^{-1}\,s^{-1}}$ and the minimal surface immobilised receptor concentration $X_0 = 10^{-8}\,\mathrm{mol\,m^{-2}}$ the minimal patch length is given by $L_p = 0.01\,\mathrm{m}$.

The maximal separation channel length L is limited by the cross lane diffusion which can be estimated from equation 4.51. Once $x_d \sim W_l$ the cross lane diffusion becomes significant. For a lane width $W_l = 200\,\mu\mathrm{m}$ which corresponds to the resolution of MSI, a diffusion coefficient of $D = 5 \times 10^{-11}\,\mathrm{m^2\,s^{-1}}$ and a flow velocity of $U = 10^{-4}\,\mathrm{m\,s^{-1}}$ the maximal separation channel length is 0.04 m. This configuration gives only a separation ratio of $L/L_p = 4$. If a larger separation ratio is required the cross lane diffusion has

to be restricted. This can be done by increasing the width of the lane or by physically splitting the lanes into separate channels. The latter approach is more feasible because it eliminates the cross lane diffusion completely. A further approach to increase the separation ratio is given by a decrease of the channel height. However, this will increase the requirements on the channel fabrication and reduce the sample loading capacity.

Table 4.2 summarises the variables and parameters for the proposed separation device. The given numerical values are either typical values for antibody-antigen systems

Symbol	Variable	Size	Units
$k_{a,jk}$	Association rate constant	$10^5 - 10^6$	$\mathrm{M^{-1}\,s^{-1}}$
$k_{d,jk}$	Dissociation rate constant	$10^{-2} - 1$	$\mathrm{s^{-1}}$
K_{jk}	Dissociation constant	$10^{-8} - 10^{-5}$	M
H	Channel height	5×10^{-6}	m
L_i	Initial plug length	$\sim 10^{-4}$	m
L_d	Detection area length	$10^{-3} - 10^{-1}$	m
L_p	Minimal patch length	0.01	m
L	Separation channel length	$10^{-2} - 1$	m
W	Channel width	$\sim 10^{-3}$	m
W_l	Lane width	2×10^{-4}	m
U	Mean flow velocity	10^{-4}	$\mathrm{m\,s^{-1}}$
u_p	Reduced plug flow velocity	Predicted	1
X_{0j}	Receptor concentration	$10^{-8} - 10^{-7}$	$\mathrm{mol\,m^{-2}}$
A_k	Analyte concentration	$\leq 10^{-8}$	M
D	Diffusion coefficient	5×10^{-11}	$\mathrm{m^2\,s^{-1}}$

Table 4.2: Variables for the proposed separation device

or given by fabrication and design constraints.

4.5.2 Governing equations for the separation

The design of the separation system is based on the simple, analytical expressions for the plug velocity 4.36 and the plug dispersion 4.44. First the analytical expression for

the plug velocity is used to calculate the separation distance between the peaks of two analytes plugs. After this the analytical expression for the plug dispersion is used to calculate the width of the two analyte plugs. Together this yields a measure for the separation between the two analyte plugs.

The analytical expression of the plug velocity 4.36 yields a measure of how long one analyte plug is retained in the separation channel. The retention time which is the extra time needed to reach the end of the separation channel due to the adsorption/desorption for one patch a_{ij} is given through

$$t_{ik} = \frac{a_{ij}}{u_p} - a_{ij} = a_{ij}(1 + \xi_{jk}) - a_{ij} = a_{ij}\xi_{jk} \tag{4.52}$$

with the channel capacity $\xi_{jk} = \frac{X_{0j}}{K_{jk}H}$. All variables here are nondimensional and derived through the nondimensionalisations: $a_{ij} = \frac{\bar{a}_{ij}}{L}$, $t = \frac{\bar{t}U}{L}$, $u = \frac{\bar{u}}{U}$ and $L_p = \frac{\bar{L}_p}{L}$ where the bar indicates the dimensional variables. Extending this expression for multiple patches, lanes and analytes results in the following matrix description for the retention time

$$\begin{pmatrix} a_{11} & a_{12} & \dots & a_{1m} \\ a_{21} & a_{22} & \dots & a_{2m} \\ \vdots & \vdots & \ddots & \vdots \\ a_{n1} & a_{n2} & \dots & a_{nm} \end{pmatrix} \begin{pmatrix} \xi_{11} & \dots & \xi_{1l} \\ \xi_{21} & \dots & \xi_{2l} \\ \vdots & \ddots & \vdots \\ \xi_{m1} & \dots & \xi_{ml} \end{pmatrix} = \begin{pmatrix} t_{11} & \dots & t_{1l} \\ t_{21} & \dots & t_{2l} \\ \vdots & \ddots & \vdots \\ t_{n1} & \dots & t_{nl} \end{pmatrix} \tag{4.53}$$

where n, m and l are the number of lanes, receptors and analytes, respectively. The nondimensional retention times t_{ij} of analyte j on lane i can be directly related to the separation of two different analyte plugs. For example, the separation between the peaks of the two analytes A_1 and A_2 on lane i can be calculated as

$$d_{i12} = |t_{i1} - t_{i2}| \tag{4.54}$$

The matrix equation 4.53 can be used to calculate the peak separation between different analytes and to design a separation system. The objectives for the separation of multiple analytes in a system with multiple receptor patches in each lane are:

1. Detection event: every analyte A_k has at least one lane i where $t_{ik} \in [t_d, t_d + \tilde{L}_d]$
2. Analyte peaks are separated: for every lane i all $t_{ik} \in [t_d, t_d + \tilde{L}_d]$ are different

3. Maximal separation: for every lane i all $t_{ik} \in [t_d, t_d + \tilde{L}_d]$ have maximal distance from each other

4. Short detection region: keep the detection length $\tilde{L}_d$ as short as possible

5. Short separation region: keep the separation channel length L as short as possible

6. Low patch and lane count: use as few patches and lanes as possible

Here $t_d = \min(t_{ij})$ is the minimal retention time and $[t_d, t_d + \tilde{L}_d]$ is the detection window. The objectives are ordered by importance: the first three objectives ensure the efficient separation of different analytes while the last three objectives reduce the complexity and cost of the separation system.

The separation system can be design for two different cases. In the first case the channel capacities of the sample constituents are known. In this case the system is optimised so that as many analytes as possible are in the detection region. The second case is the separation of analytes with unknown channel capacities. In this case the system is designed so that the widest range of channel capacities falls into the detection region. In this work only the second case is considered which gives the maximal separable range of channel capacities. This case acts as a limiting case for the first case of known channel capacities, i.e. the analytes with known channel capacities are separable if they are in the maximal separable range of channel capacities.

For a one-patch system ($m = 1$, i.e. a system with only one type of receptor molecules) the maximal separable range of the channel capacities can be calculated from the minimal and maximal patch length. The retention time for the analyte with the lowest channel capacity on the lane with the longest patch plus the time needed to reach the end of the detection region has to be equal to the retention time for the analyte with the largest channel capacity on the lane with the shortest possible patch length

$$a_{min}\xi_{max} = a_{max}\xi_{min} + \tilde{L}_d \tag{4.55}$$

$$\xi_{max} = \frac{a_{max}\xi_{min} + \tilde{L}_d}{a_{min}} \tag{4.56}$$

where ξ_{min} and ξ_{max} are the minimal and maximal channel capacities for the system and $a_{min} = L_p$ and $a_{max} = 1$ are the minimal and maximal patch lengths. The length of the detection region is added to the retention time of the analyte with the lowest channel capacity because the maximal separation range is given if the analyte with the lowest channel capacity is at the end of the detection region while the analyte with the largest channel capacity is at the start of the detection region. The equation 4.55 allows the calculation of the separation range for a one-patch system from the separation channel length L, detection length L_d and the shortest possible patch L_p. Furthermore, this equation shows that it would be beneficial to have the smallest channel capacity ξ_{min} as small as possible because then the detection region length $\tilde{L}_d$ has a bigger impact on the maximal channel capacity ξ_{max}. The minimal channel capacity ξ_{min} is reduced by a decrease of the surface receptor concentration X_0 or an increase of the channel height H. Unfortunately both options would reduce the reaction/convection number and might invalidate the requirement 4.49.

Next the number of lanes and the required distribution of receptor patch lengths to cover the whole separation range, i.e. $\xi \in [\xi_{min}, \xi_{max}]$, have to be determined. In the first lane the receptor patch with the maximal possible length, i.e. $a_{11} = 1$, is chosen. The retention time t_d of the analyte with the lowest channel capacity on the longest patch $a_{11} = 1$ is given by

$$t_d = a_{11}\xi^1_{min} \tag{4.57}$$

This can be used to find the maximal channel capacity ξ^1_{max} which can be detected on lane 1 through

$$\xi^1_{max} = \frac{t_d + \tilde{L}_d}{a_{11}} = \xi^1_{min} + \frac{\tilde{L}_d}{a_{11}} \tag{4.58}$$

where ξ^i_{min} and ξ^i_{max} are the minimal and maximal channel capacities of lane i. The maximal channel capacity of lane i has to be equal to the minimal channel capacity of lane $i+1$ to cover the whole range of channel capacities, i.e. $\xi^{i+1}_{min} = \xi^i_{max}$ for all i. With this choice the patch lengths $a_{21}, \ldots, a_{n1}$ can be calculated iteratively. The separation range $\xi^i_{max} - \xi^i_{min}$ of lane i is inversely proportional to the patch length a_{i1} so that the separation range increases with decreasing patch length. This increase of the separation range leads to a decrease in the resolution of the individual detection spots because a larger range of channel capacities is detected in each detection spot d_{ij}.

While the separation range of each lane is inversely proportional to the patch length, the separation ratio

$$r = \xi^i_{max}/\xi^i_{min} = 1 + \frac{\tilde{L}_d}{a_{i1}\xi^i_{min}} \tag{4.59}$$

is constant for every lane because $t_d = a_{i1}\xi^i_{min}$ is constant. The separation ratio allows the formulation of simple expressions for the minimal and maximal channel capacity of lane i as well as for the patch length a_{i1}

$$\xi^i_{min} = r^{i-1}\xi_{min} \tag{4.60}$$

$$\xi^i_{max} = r^i\xi_{min} \tag{4.61}$$

$$a_{i1} = a_{max}r^{1-i} \tag{4.62}$$

The maximal channel capacity increases exponentially while the patch length exponentially decreases. These equations fully define a single patch system with n distinct lanes if the minimum patch length is $a_{min} = a_{max}r^{1-n}$ for one n. If on the other hand $a_{min} \neq a_{max}r^{1-n}$ for all n a lane with the minimal patch length has to be added. The separation range of this lane will overlap with the separation range of the lane with the smallest patch length for which $a_{i1} = a_{max}r^{1-i} > a_{min}$ is fulfilled. This overlap lowers the separation range compared to a non-overlapping system. By adjusting the length of the separation region and the detection region it is possible to design a separation system without overlap. From now on, it is assumed that there is no overlap between separation lanes.

The single-patch system is now extended to a dual-patch system ($m = 2$) with two different receptors. It is assumed that the channel capacities ξ_{ij} for both receptors are between ξ_{min} and ξ_{max} or between ξ_{min} and ξ_{max} for one receptor and zero for the other receptor. Thus dual-patch systems cover the case were not all analytes interact with the same type of receptor molecules. The combined patch length $a_{i1} + a_{i2}$ has to be smaller than 1 and each of them has to be bigger than the minimal patch length. The easiest configuration for this separation device is given by two single-patch lane configurations, one for the first receptor and one for the second receptor. Assuming a single-patch system with n lanes this dual-patch setup would require $2n$ lanes which each have only one receptor patch. However, a true dual-patch configuration, i.e. at least one lane has two receptor patches, offers the potential to reduce the number of necessary lanes.

The determination of the optimal receptor patch configuration in the case of a dual-patch system is more complicated than for the single-patch setup and is derived graphically. For a system with two different receptors the separation range can be plotted in a 2D figure. The two channel capacities are plotted on the x and y axis, respectively, and for each lane the region of channel capacities which is separated by this lane is marked. Figure 4.13 shows one of these plots for a system which requires 4 single-patch lanes to cover the whole channel capacity range of the system. The vertical and horizontal

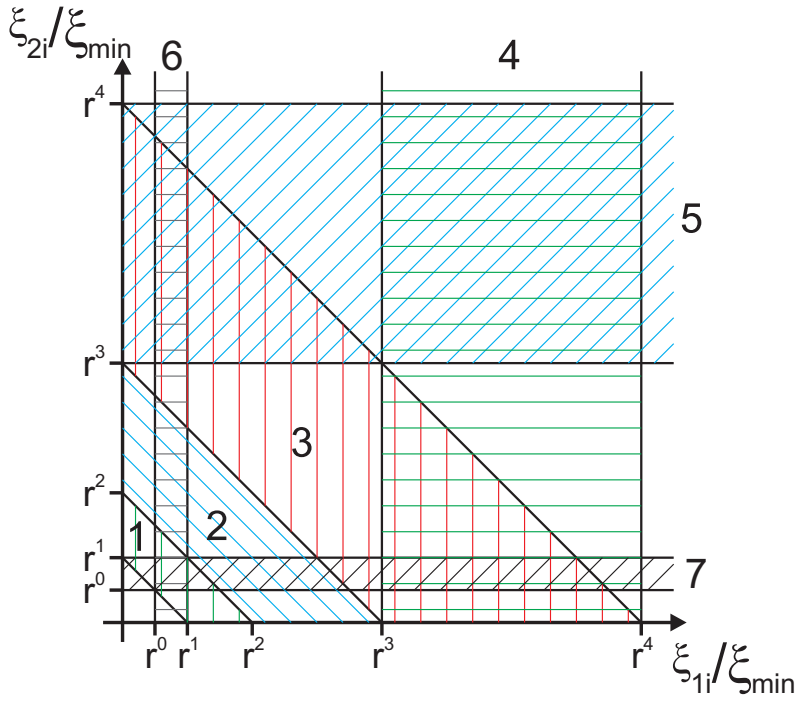

Figure 4.13: Channel capacity coverage of each lane: the shaded area for each lane 1 to 7 indicates the combination of ξ_{1i} and ξ_{2i} which this lane can separate. Parameter: $r = 2$

regions correspond to single-patch lanes for the first and second receptor, respectively. The diagonal areas with an angle of 135° correspond to dual-patch lanes where a_{i1} and a_{i2} have the same length. For $a_{i1} \neq a_{i2}$ the resulting separation range would have an angle between 90° and 135° or between 135° and 180°. Analytes which lay on the same region boundary or on one line parallel to one of the region boundaries have the same retention time and are thus not separated from each other. For example, analytes which lay on the right boundary of region 4 in figure 4.13 are detected in the first detection spot of the detection region.

The patch configuration, which is shown in figure 4.14, was derived in an iterative

manner. By starting with the smallest possible patch length $a_{max}r^{-3}$ it can be seen

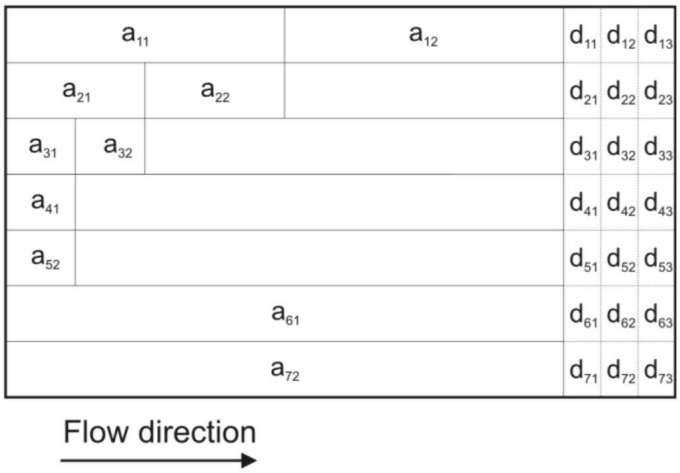

Figure 4.14: Diagram of the lane setup of a dual-patch system. Parameter: $r = 2$

from figure 4.13 that the second patch in this lane should have the smallest possible length as well to achieve the biggest coverage of channel capacities. By iteratively assessing longer patch lengths, it is clear that dual-patch lanes where both patches have the same length give the best coverage of channel capacities per lane. If dual-patch lanes with different length ratios between the first and second patch are used the angles for the separation regions in different lanes will be different which results in gaps or overlap between the different lanes. The areas below lane 1 and above lane 3 in figure 4.13 can not be separated with dual-patch lanes because the maximal and minimal length of the separation patches are restricted. This means that single-patch lanes are necessary to cover the whole range of channel capacities. The separation matrix equation corresponding to figures 4.13 and 4.14 is given by

$$a_{max}\begin{pmatrix} r^{-1} & r^{-1} \\ r^{-2} & r^{-2} \\ r^{-3} & r^{-3} \\ r^{-3} & 0 \\ 0 & r^{-3} \\ r^{0} & 0 \\ 0 & r^{0} \end{pmatrix}\begin{pmatrix} \xi_{11} \\ \xi_{21} \end{pmatrix} = \begin{pmatrix} t_1 \\ t_2 \\ \vdots \\ t_7 \end{pmatrix} \tag{4.63}$$

This matrix gives the optimal dual-patch configuration for a system with $r \geq 2$ and $a_{min} = a_{max}r^{-3}$. In this configuration $n + 3$ lanes (2 single-patch lanes with a_{min}, 2

single-patch lanes with a_{max} and $n-1$ dual-patch lanes) are needed to cover the whole range of possible channel capacities. If the separation ratio r is smaller than 2, every dual-patch lane where $r^{-i} > 0.5$ has to be replaced with two single-patch lanes with patch lengths $a_{max}r^{-i}$ and two additional single-patch lanes with patch length $a_{min}r^{i}$ have to be added. The single-patch lanes with patch lengths $a_{max}r^{-i}$ are necessary because $2r^{-1} > 1$ and the two patches are too large for one lane. The single-patch lanes with patch length $a_{min}r^{i}$ are necessary to cover the whole separation range of the device, e.g. for $r < 2$ the boundaries of the separation regions 3, 4 and 5 in figure 4.13 would not meet in the point (r^3, r^3) which results in a gap in the separation range. This increases the number of lanes needed considerably so that it is beneficial to design the system with $r \geq 2$. The derivation of the optimal patch configuration can be generalised for multi-patch lanes with $m \geq 2$ different patches. For $r \geq m$ the system requires m single-patch lanes with a_{min}, m single-patch lanes with a_{max} and $n-1$ m-patch lanes which results in a total of $n+2m-1$ lanes. For $r < m$ more single-patch lanes have to be added so that the lane count increases considerably and the multi-patch setup is not beneficial compared to the single-patch setup.

The configuration from figure 4.14 and equation 4.63 gives at least one detection event for all analytes which bind to at least one of the two receptors and thus fulfils objective 1. Next the second objective, the separation distance between different analytes, is investigated. Two analytes $A_1 = (\xi_{11}, \xi_{21})$ and $A_2 = (\xi_{12}, \xi_{22})$ which fulfil without loss of generality $\xi_{11} \geq \xi_{12}$ are defined. It is further assumed that the ratios of the channel capacities of these analytes are smaller than r or greater than r^{-1} so that the two analytes are separated in the same lane. First the single-patch system is considered. The difference in retention time between the peaks of two analytes and thus the peak separation is maximised if they get separated by the largest possible receptor patch, which separates both analytes, because in this case the detection region has the highest resolution. The largest patch which separates the two analytes is given when the analyte with the larger channel capacity is on the upper boundary of the separation range. On the other hand, the peak separation is minimised if the analyte with the lower channel capacity is on the lower boundary. For the retention time t_d, given in equation 4.57, the analyte with the larger channel capacity is at the upper boundary

for a patch length

$$a_1 = \frac{t_d + \tilde{L}_d}{\xi_{11}} \tag{4.64}$$

while the analyte with the lower channel capacity is at the lower boundary for a patch length

$$a_2 = \frac{t_d}{\xi_{12}} \tag{4.65}$$

The resulting maximal and minimal peak separation distances for a single-patch system are given by

$$d_{s,max} = (\xi_{11} - \xi_{12})\frac{t_d + \tilde{L}_d}{\xi_{11}} = \left(1 - \frac{\xi_{12}}{\xi_{11}}\right)(t_d + \tilde{L}_d) \tag{4.66}$$

$$d_{s,min} = (\xi_{11} - \xi_{12})\frac{t_d}{\xi_{12}} = \left(\frac{\xi_{11}}{\xi_{12}} - 1\right) t_d \tag{4.67}$$

The peaks of two analytes are separated if the peak separation distance is greater than the detection spot length. Otherwise the two peaks are detected in the same detection spot.

For dual-patch systems the situation becomes a bit more complicated. It is assumed that the boundary of the separation region in the separation region plot, i.e. figure 4.13, is perpendicular to the line between the two analytes as shown in figure 4.15. Due to the

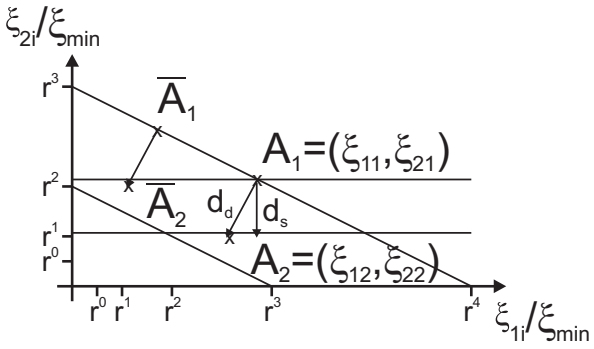

Figure 4.15: Diagram showing the difference in peak separation distance for single-patch and dual-patch setups.

constraint that the patches and channel capacities have to be positive this configuration can only be achieved if $\xi_{11} \geq \xi_{12}$ and $\xi_{21} \geq \xi_{22}$. Thus the channel capacities of the two analytes are linked by

$$\xi_{12} = \xi_{11} - \epsilon_1 \tag{4.68}$$

$$\xi_{22} = \xi_{21} - \epsilon_2 \tag{4.69}$$

where ϵ_1 and ϵ_2 are positive constants. The peak separation distance between A_1 and A_2 is equal to the peak separation distance between $\bar{A}_1$ and $\bar{A}_2$ in the dual-patch lane setup in figure 4.15 which shows that the peak separation distance in this setup is only dependent on ϵ_1 and ϵ_2. The analyte with the larger channel capacity is placed on the upper boundary of the separation region (see figure 4.13) to get the maximal peak separation distance. The two constants ϵ_1 and ϵ_2 define the normal to the separation region boundary and are proportional to the patch widths $a_{11} = c\epsilon_1$ and $a_{12} = c\epsilon_2$ with a positive constant c which can be determined by equating

$$a_{11}\xi_{11} + a_{12}\xi_{21} = c(\epsilon_1\xi_{11} + \epsilon_2\xi_{21}) = t_d + \tilde{L}_d \tag{4.70}$$

With the patch widths a_{11} and a_{12} the maximal peak separation distance can be calculated to be

$$d_d = a_{11}(\xi_{11} - \xi_{12}) + a_{12}(\xi_{21} - \xi_{22}) = c(\epsilon_1^2 + \epsilon_2^2) \tag{4.71}$$

Now the maximal dual-patch peak separation d_d is compared with the maximal single-patch peak separation $d_{s,max}$ which is dependent on the two analytes in the following way

$$d_{s1} = (\xi_{11} - \xi_{12})\frac{t_d + \tilde{L}_d}{\xi_{11}} = \epsilon_1\frac{t_d + \tilde{L}_d}{\xi_{11}}, \qquad \frac{\epsilon_1}{\xi_{11}} \geq \frac{\epsilon_2}{\xi_{21}} \tag{4.72}$$

$$d_{s2} = (\xi_{21} - \xi_{22})\frac{t_d + \tilde{L}_d}{\xi_{21}} = \epsilon_2\frac{t_d + \tilde{L}_d}{\xi_{21}}, \qquad \text{otherwise} \tag{4.73}$$

Assuming $d_d \geq d_{s1}$ it follows that $\frac{\epsilon_1}{\xi_{11}} \leq \frac{\epsilon_2}{\xi_{21}}$. Using this it can be shown that $d_{s1} \leq d_d \leq d_{s2}$ so that the dual-patch peak separation distance can never be greater than the maximal single-patch peak separation distance. This result is shown schematically in figure 4.15. For the single-patch lane the analyte A_1 is detected at the end of the detection region and the analyte A_2 at the beginning while for the dual-patch lane the analyte A_1 is detected at the end of the detection region and the analyte A_2 between the beginning and end of the detection region. By 'rotating' the dual-patch lane anticlockwise the dual-patch lane will approach the single-patch lane and the peak separation distance will approach the peak separation distance of the single-patch lane. This result can be extend to lanes with more patches and will give a similar result, e.g. the peak separation distance in a triple-patch setup is always smaller than the maximal peak separation distance in a single-patch setup.

So far only the separation of the analyte peaks was calculated. To get a useful measure of the separation of two analyte plugs the width of the two plugs has to be taken into account. The plug separation for two analytes A_k and A_l on lane i is given by

$$S_{ikl} = \frac{2|t_{ik} - t_{il}|}{w_{ik} + w_{il}} \tag{4.74}$$

where w_{ik} and w_{il} are measures for the width of the analyte plugs. Here it is assumed that the analyte plugs are symmetric which agrees with the results from section 4.4.2 where the analyte plug could be described by a Gaussian distribution. The width of the Gaussian distribution is related to the variance σ^2. The variance of the analyte plug A_k over the patch a_{ij} due to the adsorption/desorption is given by the analytical expression for the plug dispersion 4.44 which is repeated here

$$\sigma^2_{ijk} = a_{ij} \frac{2\xi^2_{jk}}{\zeta_{jk}(1 + \xi_{jk})^2} \tag{4.75}$$

For a linear system the total variance of the analyte plug over the patch a_{ij} is the sum of the variance due to adsorption/desorption and due to axial dispersion [184]. The axial dispersion in pressure driven flow is described by the theory of Taylor dispersion [180] and the effective diffusion coefficient is given by

$$D_{eff} = D + \frac{U^2 H^2}{210 D} f(H/W) \tag{4.76}$$

where $f(H/W)$ depends on the aspect ratio of the rectangular microfluidic channel [189]. A further modification of the total variance is given by the change of plug width as the plug moves from one sensor patch to the next. This was shown in figure 4.6 where the analyte plug moved from the channel inlet into the first receptor patch: the plug velocity is reduced from 1 to 1/6 and the plug width is reduced from 1 to less than 0.5. The change in plug width depends on the change in plug velocities over different receptor patches so that the plug width is either compressed or extended depending on the ratio of the plug velocities. In the ideal case without axial diffusion and dispersion due to adsorption/desorption this would have no effect on the final plug width. However, in the case considered here the plug width, i.e. the total variance over the patch, at the end of each receptor patch has to be multiplied with the ratio of the plug velocities over this receptor patch and the next receptor patch. Furthermore, the dispersion of the analyte plug over sequential receptor patches is additive so that the total FWHM

of the analyte A_k at the end of lane i is given by

$$w_{ik} = 2\sqrt{2\log 2}\sqrt{(\sigma_{i1k}^2 + 2a_{i1}D_{eff})\frac{(1+\xi_{i2})^2}{(1+\xi_{i1})^2} + \cdots + (\sigma_{imk}^2 + 2a_{im}D_{eff})\frac{(1+\xi_{i,m+1})^2}{(1+\xi_{im})^2}} \tag{4.77}$$

where m is the number of receptor patches in lane i. This allows the calculation of the separation S_{ikl} of the two analytes A_k and A_l on lane i.

4.5.3 Results and discussion

The governing equations derived in the last two sections together with fabrication constraints can be used to design microfluidic affinity separation systems for the multiplexed separation of multiple analytes. The separation channel length L and the detection length L_d are limited by the device fabrication technique. On a standard 4 inch wafer the maximal channel length is about 5 cm if the fluidic connections are incorporated on the chip and the design is restricted to straight channels. For longer separation lengths serpentine channels have to be used. The initial plug length L_i is defined by the plug injection method (section 2.4.4). Initial plug lengths down to $L_i = 10^{-4}$ m are achievable with on-chip injectors [106]. The detection method and required efficiency puts constraints on the detection region L_d and the lane width W_l, e.g. the maximal resolution for MSI detection is about 50 μm [120].

The equations 4.49 and 4.50 are used to calculate the smallest possible patch length L_p which depends on the channel height and the analyte-receptor pairs. The ratio of the separation channel length L and the minimal patch length L_p is proportional to the separation range of the separation system which can be calculated from equation 4.55. The receptor patches for a single-patch setup are defined by equation 4.62. A corresponding dual-patch setup for a specific example is shown in figure 4.13. These configurations ensure that all analytes whose channel capacities are in the separation range are detected in the detection region. However, it does not guarantee that all analytes are separated. To ensure this the separation between two analyte plugs can be calculated with equation 4.74. For analytes with known channel capacities the presented equations can be used to design a separation system specific to these analytes.

An example for the separation of a sample plug containing two analytes with different affinities for the receptor molecules is shown in figure 4.16. The concentration profile

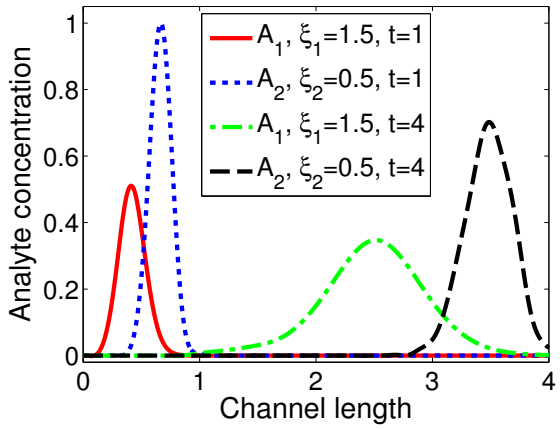

Figure 4.16: Numerical simulation of the concentration distribution of two analytes A_1 and A_2 with different channel capacities $\xi_1 = 1.5$ and $\xi_2 = 0.5$. Parameter: $a_{11} = 1$, Gz $= 0.05$, $\kappa = 250$, $\lambda = 0.05$, $\zeta = 50$

of the two analytes is shown for two different times. The two analytes were introduced at the same time in a mixed sample plug onto a one-patch system with $a_{11} = 1$. The relative error between the peak separation distance predicted by equation 4.54 and the numerical simulation is less than 1%. Furthermore, the relative error between the peak width predicted by equation 4.77 and the peak width from the numerical simulation is below 6%. This error is due to the difference in initial plug width between the analytical and numerical solution. This shows that the derived equations are a good starting point for the design of a separation system.

A limitation of open separation systems is the low sample loading capacity. The maximal load concentration for a typical system, i.e. $H = 5\,\mu$m and $X_0 = 10^{-8}\,\mathrm{mol\,m^{-2}}$, which fulfils $\kappa \geq 200$ is $A_0 = 10\,$nM. This shows that open systems are only feasible for the separation of low copy number analytes. Moving from a monolayer stationary phase to a thick, porous stationary phase can increase the sample loading capacity but adds to the complexity of the device fabrication and modelling [178]. Furthermore, the load volume is restricted by the channel height and width as well as by the required separation efficiency. For a channel height and width of $H = 5\,\mu$m and $W = 200\,\mu$m, respectively, the sample volume has to be in the sub-nanolitre range.

Incorporating multiple receptor patches into one lane has several advantages and disadvantages which have to be assessed depending on the size and diversity of the sample. Single-patch lanes are easier to fabricate and offer the highest achievable peak separation if all analytes can be separated by the same receptor molecule. On the other hand, multi-patch lanes allow the separation of analytes which could not be separated by single-patch lanes because each analyte shares at least on channel capacity with each of the other analytes. A further benefit is the reduction of the required number of lanes. This allows the incorporation of multiple, different receptor patches while keeping the number of lanes low.

4.6 Summary

In this chapter a theoretical model, which describes the behaviour of analyte plugs in microfluidic affinity separation systems, was derived. This model reveals two simple, analytical expressions, which describe the analyte retention and dispersion, and have been used to derive design guidelines for multiplexed, microfluidic separation systems.

The transport-reaction equations for microfluidic affinity systems introduced in section 3.3 were evaluated for fast diffusion across the channel height and high adsorption capacity. Due to the ongoing trend of miniaturisation in microfluidics more and more systems fulfil these requirements [14; 152]. These governing equations were simplified and the simplified system was solved analytically. Analysing the analytical solution in the asymptotic limit of fast binding yielded two simple, analytical expressions for the analyte plug velocity and the dispersion of the analyte plug in open microfluidic affinity separation systems. These expressions depend only on global device parameters and describe the behaviour of a sample plug in the microfluidic affinity separation system. The resulting analytical solution as well as the analytical expressions for the plug velocity and dispersion are in good agreement with numerical simulations performed with the full 2D model. Limiting values for the Graetz number ($\mathrm{Gz} \leq 0.05$), adsorption capacity ($\kappa \geq 200$) and reaction/convection number ($\zeta \geq 20$) for which the simplifications are valid were explored numerically.

The simple analytical expressions agree with the theory for column chromatography. The expression for the analyte plug velocity is similar to the equation for the band velocity while the equation for the dispersion has a similar form than the equation describing the dispersion due to mass transfer in open-tubular systems. Together the two analytical expressions are guidelines for the design of microfluidic affinity separation systems for the efficient separation of target molecules from sample mixtures. Conventionally, such a design would require computationally expensive numerical simulations of the nonlinear governing equations. However, the simple nature of the two analytical expressions allows the design of multiplex separation systems. In these designs more than one receptor molecule and several parallel microfluidic lanes are incorporated into a microfluidic separation device which is capable of separating a wide range of analytes. In the second part of this chapter the theoretical framework for such a design was derived. This includes expressions defining the channel geometry, detection region and distribution of the different receptor molecules as well as the separation of different analyte plugs. This design framework offers step by step instructions for the design of multiplexed separation systems.

Chapter 5

Optimisation of microfluidic devices, with small Graetz number, for integrated biosensors

5.1 Introduction

Microfluidic affinity sensors are receiving much attention for life science and environmental analytical science applications [1; 11]. These affinity sensors typically consists of a microfluidic channel in which one or more walls are functionalised with recognition molecules. The sample containing the target analyte is flowed through these channels. The recognition-binding event, most typically antibody-antigen or DNA hybridisation, immobilises the target analyte at the functionalised surface. The bound analyte-receptor complex is detected, for example by optical means, e.g. fluorescence [112] or surface plasmon resonance [108]. These integrated affinity sensors have two key applications: (i) the evaluation of binding parameters for biomolecular recognition between one immobilised molecule and another in solution (as developed by companies such as Biacore), and (ii) the quantification of low levels of analyte by association with a recognition molecule that is immobilised on the sensor. The fluidic structures and the operation requirements in these two application areas are quite different. For the evaluation of binding parameters it is important to decouple the recognition-binding event from the mass transport of

analyte to the sensor surface, while for the quantification of low levels of analyte it is important to ensure that all analyte molecules have a chance to interact with the sensor surface.

For the evaluation of binding parameters the integrated fluidic structures and operation parameters are chosen so that the biomolecular recognition event is 'binding limited', i.e. the transport of analytes to the sensor surface is faster than the recognition-binding event of the analyte with the surface immobilised receptor [190] (see section 3.4). This ensures that the rate of the recognition-binding event depends solely on the kinetic parameters and is decoupled from the transport of analytes to the sensor surface. The required structures and parameters for these systems have been well considered [130]. However, these systems capture only a small fraction of the analyte molecules and are thus unsuited for the quantification of low levels of analyte from small sample volumes.

For the quantification of low levels of analyte the fluidic structures and operation parameters have to be chosen so that the majority of analyte molecules are transported and uniformly associated to the affinity sensor surface. These two goals of a high yield and uniform association of the analyte over the affinity sensor require the careful design of the microfluidic elements. This is due to the small size of microfluidic sensors which can lead to two distinct depletion effects (section 3.4). The first is due to the slow diffusive transport of analytes to the active sensor surface. When the reaction is faster than the analyte transport to the sensor surface, a boundary layer which is depleted of analyte forms close to the sensor surface. The second effect is due to the limited amount of analyte which can lead to a depletion of the complete analyte plug so that the sensor response is different from the channel entrance to the channel exit. Both depletion effects can have a negative influence on the sensor performance: the formation of a depleted boundary layer results in a low analyte capture fraction, while the depletion of the analyte plug results in non-uniform association of the analyte over the affinity sensor surface.

While there has been much effort focused on the reduction of the size of the microfluidic sensor devices [14] and the improvement of the detection systems [191], far less attention has been placed on the improvement of the design of the microfluidic

elements of the integrated system. However, this is a very important design consideration, especially where the sensor size and/or analyte volume is small and where highly sensitive levels of detection and quantification are needed. Microfluidic strategies which ensure both a high capture fraction as well as uniform mass transfer of analytes to the sensor surface and subsequent association along the sensor length are needed to take full advantage of improved detection systems.

Here new designs for microfluidic channels to be integrated with small scale affinity sensors for analytical applications are presented. These are created with a view to achieve both high yield and uniform association of the analyte over the affinity sensors. Theoretical approaches demonstrate efficient and uniform mass transfer of the analyte from the bulk flow to small scale affinity sensors in the base of fluidic channels by (i) active control of the analyte flow speed over the affinity sensor, (ii) non-uniform distribution of surface immobilised receptor molecules over the active area of the sensor and (iii) non-rectangular channel geometries. The high yield and uniform association of the analyte along the sensor will lead to an improved sensor response. The designs are suitable for use with small sample volumes on small scale sensor devices. This is becoming increasingly important with the requirement for multiplex analysis of small quantities of biological analytes.

5.2 Literature review - optimisation of analyte transport to the active surface

The behaviour of the analyte in an integrated microfluidic device depends on the balance of the convection, diffusion and binding rates, see section 3.3. For the two regimes of the Graetz number different mass transport limitations arise. In the 'entrance region' ($Gz \gg 1$) the transport of the analyte to the receptor molecules is limited by diffusion and a depleted boundary layer results [129]. In the 'fully developed' region ($Gz \ll 1$) the analyte transport is limited by convection and the analyte concentration is depleted along the length of the sensor system [19]. To achieve more efficient mass transfer of analyte to the sensor surface several strategies, which try to compensate these depletion

effects, have been implemented [25; 192; 193; 194; 195]. Most of these strategies are developed for the high Graetz number case where a depleted boundary layer develops. The different strategies are based on four different techniques: (i) mixing of the analyte within the flow cell with micromixers [23], (ii) reduction of the depleted boundary layer through flow based methods, (iii) improved mass transfer through externally applied forces and (iv) optimisation of the device parameters.

Micromixers

One of the simplest methods for effective mass transfer of analyte to the sensor surface is achieved by periodically pulsing the analyte solution in a 'forward-backward' flow in 2D serpentine channels [192]. This oscillatory flow results in an improvement of the mixing between the depleted and non-depleted analyte layers and a subsequent increase in the contact time between the analyte molecules and the receptor sites. Together this provides a reduction in the sample consumption and allows the detection of analytes with low affinities for the receptor molecules. A similar approach integrates 3D serpentine channels, which are chaotic mixers, into a microfluidic sensor [196]. As a result of this chaotic mixing, the mass flux of analyte towards the sensor surface increases which leads to an increase in the rate of detection by a factor of 2. An innovative active mixer strategy has been reported [194], where a bubble in the microfluidic channel is used to create a 'mixing' vortex sheet between a fluid layer close to the sensor surface and the bulk analyte fluid. This simple, but innovative approach resulted in effective mixing and effective transport of the analyte to the sensor surface.

Recently, much attention has been focused on the effect of surface groove induced secondary flow [24] on the adsorption in microfluidic devices. Surface grooves in microfluidic channels produce a helical flow as shown in figure 5.1. This helical flow removes depleted fluid away from the active surface at the bottom of the channel and replaces it with non-depleted fluid from the top of the channel. This effect has been used to increase the yield of bound analyte by 26% [25] and to increase the conversion efficiency of an electrochemical reactor up to a factor of 2 [195]. Numerical and analytical studies provide evidence that an increased ratio of transverse to axial flow and

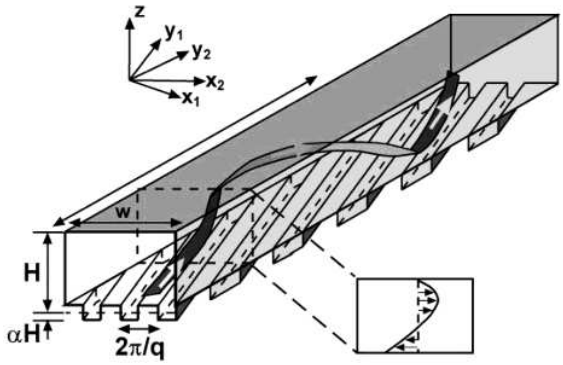

Figure 5.1: Schematic of a microfluidic channel with surface groove induced secondary flow. The ribbon indicates a helical streamline. Reprinted with permission from [197]. Copyright 2002 American Chemical Society.

the homogenisation of the concentration profile are mandatory for an increase in device efficiency [198; 199]. Surface groove induced secondary flows are discussed in detail in chapter 7.

Flow based methods

The thickness of the depleted boundary layer can be decreased by flow based methods. The simplest approach is based on an increase in the shear rate by an increase in the fluid flow velocity [193]. This will decrease the thickness of the depleted boundary layer and therefore reduce the influence of the mass transport. The main drawback of this method is an increased sample consumption. The use of a confinement flow as shown in figure 5.2 achieves an increased shear rate without increasing the sample consumption [200]. It also decreases the diffusion distance. However, this approach might not be suitable for sensor arrays because the confinement is only effective for a short length due to diffusional loss from the sample into the confinement flow. A further approach uses multiple inlets or outlets situated along the sensor surface to add fresh analyte or remove the depleted layer, respectively [195]. The configuration with three inlets as shown in figure 5.3 increases the association compared to a standard system by a factor of 2.

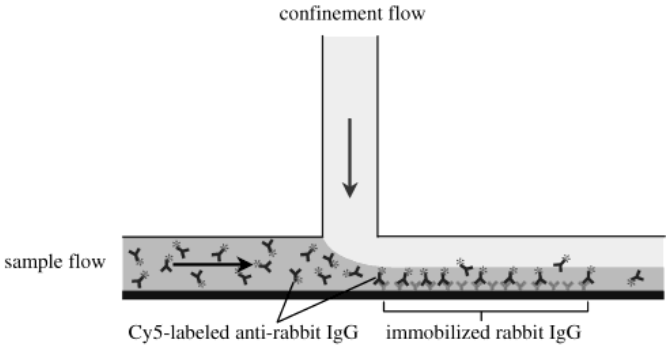

Figure 5.2: Schematic of confinement flow. The sample flow is confined to a thin layer close to the active surface. Reprinted with permission from [200]. Copyright 2002 American Chemical Society.

Externally applied forces

Externally applied forces can be used to increase the analyte transport to the sensor surface [201; 202]. Heating the solution in the depleted boundary layer via self-focused microwave heating enhances the mass transport through its effect on the diffusion coefficient as well as through convection in the direction of the temperature gradient and the formation of a stable steam bubble [202]. An acoustic standing wave can apply a radiation force on small particles and spores which moves them towards the nodal planes of the wave [201]. Designing the system so that the nodal plane is close to the active surface can lead to an improved particle capture and device sensitivity. A similar strategy uses an electrostatic field to induce a flow perpendicular to the main flow direction [203].

Optimisation of device parameters

A full numerical model was used to optimise microfluidic affinity sensors with respect to flow velocity, surface immobilised receptor density, analyte concentration and association rate constant [122]. Optimisation results, which achieve either faster measurements or minimal sample volume requirements, are presented. A further numerical investigation studied the capture fraction of heterogeneous immunoassays under sample and assay time constraints [204]. It was shown that an optimal flow rate exists for which the

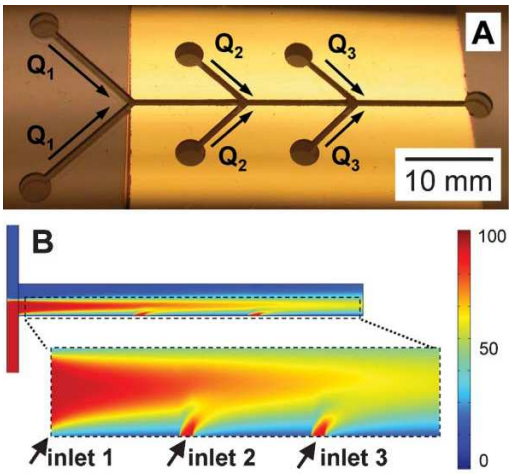

Figure 5.3: (A) Optical micrograph of a flow cell with three inlets along the active surface and (B) simulated concentration profile in the flow cell from [195] - Reproduced by permission of The Royal Society of Chemistry

maximal signal is achieved in the minimal assay time.

While some effort has been focused on improving the transport of the analyte across the depleted boundary layer to the sensor surface, little design consideration has been given to the analyte depletion along the channel. For channel heights in the low micrometre range the depletion of the analyte along the length of the sensor becomes significant [131] so that the resulting analyte association to the active area of the affinity sensor is non-uniform. This can lead to a less robust and sensitive integrated affinity sensor system which is particularly true in the case where there is limited sample volume and the analyte needs to be injected as a short plug.

5.3 Theoretical model

The theoretical model, used both to establish the mass transfer of the analyte to the affinity sensor and to maintain the uniformity of the associated analyte bound to the recognition molecules, for both (i) integrated microfluidic channels conventionally used with affinity sensors and (ii) optimised fluidic - affinity sensor formats, has been introduced in chapter 3. Here only the case of irreversible association or where the rate of

dissociation is so slow that it can be neglected is considered. This case is described by

$$A + X \xrightarrow{k_a} B \tag{5.1}$$

where the analyte A binds to the surface immobilised receptor molecule X to form the recognition molecule-analyte complex B. The constant k_a is the association rate constant for the bimolecular reaction between the analyte and the recognition molecules. It is further assumed that the height of the microfluidic channel is much smaller than the width and length so that the diffusion in the x and z direction can be neglected. With these simplifications the governing equations 3.18-3.20 (chapter 3) are simplified to

$$A_t + \mathbf{u} \cdot \nabla A = \frac{LD}{H^2U} A_{yy} \qquad , x, y \in [0,1] \tag{5.2}$$

$$A_y = \frac{k_a H X_0}{D}\, A(1-B) \qquad , x \in [0,1], y = 0 \tag{5.3}$$

$$B_t = \frac{LD}{H^2U} \frac{A_0 H}{X_0}\, A_y \qquad , x \in [0,1], y = 0 \tag{5.4}$$

where again all variables are nondimensional with the nondimensionalisations: $\bar{x} = Lx$, $\bar{y} = Hy$, $\bar{z} = Wz$, $\bar{A} = A_0 A$, $\bar{X} = X_0 X$, $\bar{B} = X_0 B$ and $\bar{t} = \frac{L}{U} t$, where U is the mean velocity of the flow through the channel and the bar indicates the dimensional variables. All calculations in this chapter are performed with the nondimensional variables and all figures show nondimensional quantities. The remaining boundary conditions include no movement of analyte across non-active channel walls ($A_y = 0$ and $A_z = 0$) and no diffusive movement of analyte across the channel exit ($A_x = 0$).

In contrast to much of the published theoretical work in this field [129; 130], a continuous analyte input is not used. Instead, an analyte plug is injected in a pulse of time λ, so that at the entrance to the channel

$$A(0, y, z, t) = \hat{\mathrm{H}}(t)\, \hat{\mathrm{H}}(\lambda - t) \tag{5.5}$$

where $\hat{\mathrm{H}}$ is the Heaviside step function. It is only considered that analyte is introduced in short pulses into the channel and hence it is assumed that $\lambda \ll 1$. This assumption is valid for an increasing number of microfluidic systems where the sample plug is much shorter than the channel length [106; 107]. The different physical effects in this system

are related by the three nondimensional parameters

$$\mathrm{Gz} = \frac{H^2 U}{LD}$$
$$\mathrm{Da} = \frac{k_a H X_0}{D}$$
$$\kappa = \frac{X_0}{A_0 H}$$

which were introduced in section 3.3. For the sensor applications of interest here, where small samples of low analyte concentration are used, the devices are designed such that a large adsorption capacity value ($\kappa \gg 1$) applies. To achieve this it is assumed that the recognition molecules attached on the sensor surface are at a high concentration and the total available is far in excess of the amount of analyte. The concentration of free surface immobilised receptors will remain almost constant at X_0 throughout the measurement, thus every analyte molecule reaching the sensor surface has the same opportunity to bind to a receptor molecule. It is further assumed that the Graetz number is small ($\mathrm{Gz} \ll 1$) so that every analyte molecule has the chance to reach the active sensor surface.

This model is now used to optimise the behaviour of integrated affinity sensors with respect to two quantities, namely the spatial uniformity of the bound analyte, and the fraction of analyte associated to receptor molecules on the sensor surface.

5.4 Rectangular channel with constant parameters

In the first instance the theoretical performance of the integrated microfluidic, multisensor system of Hua et al. [21; 205; 206] which is shown in figure 5.4 was evaluated. The multisensor is designed to simultaneously monitor 32 different pollutants in river water in an indirect competitive assay, see section 3.5. The system consists of a waveguide chip, shown in figure 5.5, which has 32 sensor windows, and a microfluidic flow cell which is bonded to the top of the waveguide chip and covers all 32 sensor windows. The river water is premixed with a solution containing fluorescently labelled antibodies for the 32 pollutants. After an incubation period the mixed solution is flowed through the multisensor. The unbound antibodies in this solution interact with the surface immobilised receptors in a recognition-binding event. The fluorophores attached to the

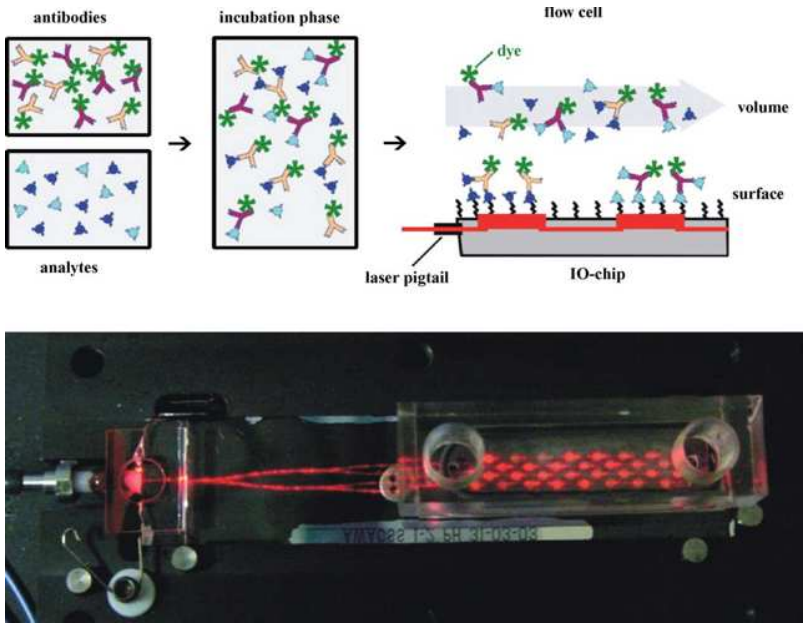

Figure 5.4: (bottom) Picture of the multisensor system and (top) schematic of the indirect competitive assay protocol. Reprinted from [205] with permission from Elsevier.

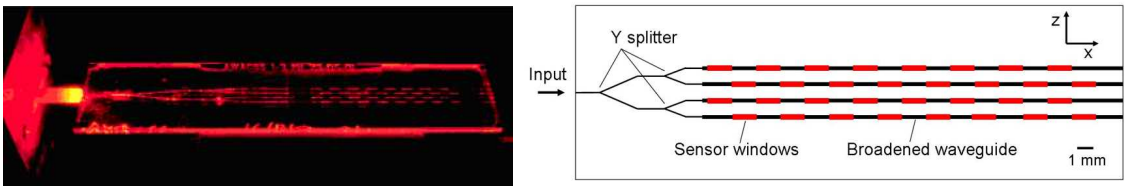

Figure 5.5: Picture and schematic of the waveguide chip showing the 32 sensor windows. Reproduced from [21] with permission from the author and the Optical Society of America.

captured antibodies are excited by the evanescent field of the waveguide and the emitted light is collected by photodetectors. Although this system has an excellent detection limit, below $1\,\mathrm{ng\,l^{-1}}$ for estrone, the design of the microfluidic elements had not been optimised.

For the multisensor flow cell of Hua et al. the width W of the microfluidic channel is about 140 times the height H which means that the flow is uniform over most of the width of the channel. This is again used to reduce the dimension of the theoretical model by assuming that the analyte transport and association on the active area is uniform over the complete width of the device. This reduction of the governing equation 5.2

leads to the following equation,

$$A_t + u(y)A_x = \mathrm{Gz}^{-1}\, A_{yy} \tag{5.6}$$

where the velocity, u is only dependent on the channel height and represents the parabolic flow profile given in equation 4.9.

The flow cell of the multisensor from Hua et al. [21] is 35 μm high and every sensor patch is 1.5 mm long. The average flow velocity is 14 mm s^{-1} which yields a Graetz number of $\sim$ 228 for many small molecules ($D \approx 5 \times 10^{-11}\,\mathrm{m^2\,s^{-1}}$ [126]). The sensor clearly operates in the 'entrance region', see section 3.3, and less than 10% of the analyte molecules reach the affinity sensor surface to bind to receptor molecules. For many antibody-antigen interactions, the association rate constant k_a is between 10^5 to $10^6\,\mathrm{M^{-1}\,s^{-1}}$ [207] and the receptor concentration X_0 ranges between 10^{-8} and $10^{-7}\,\mathrm{mol\,m^{-2}}$ [208; 209]. This yields a Damköhler number between 0.7 and 70. For most systems the Damköhler number is greater than 1 and the system is 'diffusion limited' (see section 3.3). Figure 5.6 illustrates the device behaviour for a continuous analyte input: the majority of the analyte molecules flow through the device without encountering recognition molecules on the sensor surface. The simulations in this section are performed for the full 2D model which is given by equations 3.18-3.20. Details of the implementation are given in appendix B. The magnitude of the concentration gradient at the active surface increases with the Damköhler number. Simulations performed with an analyte pulse of 1 s and a rate constant $k_a = 10^6\,\mathrm{M^{-1}\,s^{-1}}$ show that less than 5% of the analyte will be bound by the receptor molecules on the active surface. On the other hand, the transport of analytes across the depleted boundary layer is almost constant along the length of the channel so that the bound analyte concentration is approximately uniform once the depleted boundary layer is formed. Such a configuration might be appropriate to establish the rate constant for the association between the analyte and the recognition molecule attached to the affinity sensor, for instance in a Biacore sensor [129]. However, where highly sensitive quantification of analytes from limited sample volumes is the aim, an alternative strategy for analyte handling is required.

The first step to improve the system for the quantification from limited sample volumes is to increase the transport from the bulk to the sensor surface where a measure

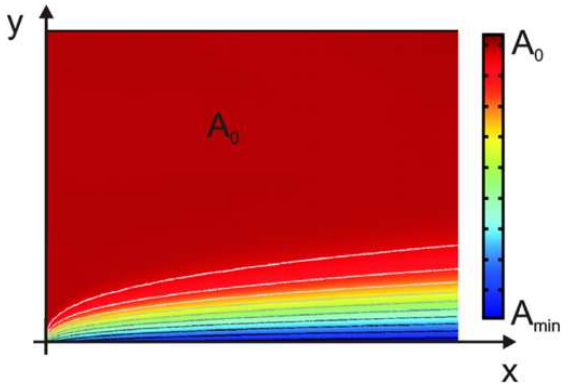

Figure 5.6: Simulated quasi-steady state bulk concentration for one sensor patch of the multisensor for a continuous analyte input. The value of A_{min} depends on the Damköhler number and ranges from $A_{min} = 0.1A_0$ for Da = 70 to $A_{min} = 0.93A_0$ for Da = 0.7. Parameters: Da = 0.7 − 70, Gz = 200, $\kappa = 100$

for this is the Graetz number (see section 3.3). For a Graetz number below 1 every analyte molecule can diffuse to the active surface before it is flowed out of the microfluidic channel. The Graetz number depends on the channel height and length, fluid flow velocity and analyte diffusion coefficient. The diffusion coefficient is almost constant for a given analyte and the sensor length is often defined by the detection system. However, a reduction in channel height and fluid flow velocity are feasible options for the reduction of the Graetz number below 1.

From now on it is assumed that the Graetz number is small (Gz $\ll 1$) and thus the system is operated in the 'fully developed' region, see section 3.3. Briefly, in the 'fully developed' region the diffusion across the height of the microfluidic channel is much faster than the convection and the analyte concentration is almost constant over the height of the channel. In the 'fully developed' region the analyte concentration is given to the first order by

$$A(x,t) = \exp(-\zeta x)\,\hat{\mathrm{H}}(t-x)\,\hat{\mathrm{H}}(x-t+\lambda) \tag{5.7}$$

(Details of the lengthy derivation are given in appendix A.) Thus the capture fraction of the integrated device depends on the reaction/convection number ζ and is given by

$$F = 1 - \frac{|A|}{|A_0|} = 1 - \exp(-\zeta) \tag{5.8}$$

where $|A_0|$ and $|A|$ are the amount of analytes entering and leaving the system, respectively. For analytes with high association rate constants, the capture fraction approaches 1, i.e. almost 100% of the analyte molecules are captured at the active surface. However, due to the depletion of the analyte plug this high capture fraction comes at the expense of the uniformity: large amounts of the analyte bind close to the channel entrance and the bound concentration decreases exponentially along the sensor length. This is shown in figure 5.7. For example, for $\zeta = 2.3$ which corresponds to a capture fraction of 0.9

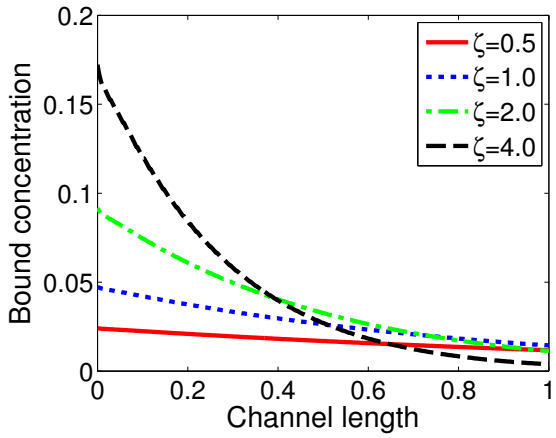

Figure 5.7: Simulated bound analyte concentration for different values of the reaction/convection number. Parameters: $\mathrm{Gz} = 0.05$, $\kappa = 100$, $\lambda = 10$, $t = 5$

more than three quarters of the bound analyte associates in the first half of the sensor patch. For slower reactions less analyte gets associated with the active surface. This results in non-depleted analyte plugs and a more uniform distribution of the bound analyte.

Whilst the model given by equation 5.7 can be used to define the optimal flow rate and channel height to achieve high efficiency of analyte mass transfer to the affinity sensor surface and subsequent association, there is not a straight-forward method to achieve both high and uniform analyte association over the whole sensor patch. The two optimisation goals, high capture fraction and uniform distribution of the bound analyte along the sensor surface, are mutually exclusive in rectangular channels with constant flow rate and constant surface site concentration.

5.5 Design optimisation - rectangular channel

Design concepts and assay protocols for microfluidic affinity sensors are developed such that the analyte mass transfer to the sensor surface and subsequent association is constant along the sensor patch. These design strategies take the depletion of the analyte concentration along the sensor patch into account. Three approaches, which go beyond conventional microfluidic affinity sensors, are considered: (i) the variation of the flow velocity as the analyte plug travels down the channel (section 5.5.1), (ii) the variation of the surface immobilised receptor molecule concentration along the sensor area (section 5.5.2) and (iii) non-rectangular device geometries (section 5.6).

The first two approaches which are presented in this section are based on the modification of the reaction/convection number as the analyte plug is flowed over the sensor area. For integrated affinity sensors which are operated in the 'fully developed' region the analyte mass transfer to the sensor surface and subsequent association is controlled by the analyte concentration A and the reaction/convection number ζ. An increasing reaction/convection number as the analyte plug is flowed over the sensor area will compensate the decreasing analyte concentration and ensure a constant analyte mass transfer to the sensor surface and subsequent association.

From the five parameters which define the reaction/convection number ζ the fluid flow velocity U, the receptor concentration X_0 and the channel height H can be adjusted along the channel. Changing the flow velocity as the analyte plug travels through the sensor or creating a gradient in the surface immobilised receptor concentration along the sensor patch are the most feasible options because changes in the channel height are linked to the fluid flow velocity through the flow rate $Q = UHW$. Changing the channel height introduces the opposite effect in the flow velocity in the case of a constant channel width, i.e. halving the channel height doubles the flow velocity. Without an opposing change in the channel width the reaction/convection number stays constant and the system response is similar to the channel with fixed height. Furthermore, the fabrication of microfluidic devices with non-uniform channel height requires 3D fabrication methods which are slower and more expensive than the planar fabrication methods required for the fabrication of devices with a fixed channel height (section 2.3).

5.5.1 Temporal variation of the fluid flow velocity

The first design concept to be considered was where the flow velocity of the analyte plug in the channel was varied as it passed the sensor patch: reducing the flow velocity as the analyte plug travels over the active surface results in an increase in the reaction/convection number and an enhancement of the fraction of analyte that associates with the immobilised receptors along the channel. Here the optimal flow velocity modification is derived which compensates for the depletion of the analyte plug as it moves along the sensor patch. The flow velocity is given by $u(t)U$ where U is the initial velocity and $u(t)$ is the temporal modification ($u(0) = 1$). Introducing this modifies the governing equations 4.11 and 4.12 (chapter 4) to

$$\frac{\partial A}{\partial t} + u(t)\frac{\partial A}{\partial x} = -\zeta A(1-B) \tag{5.9}$$

$$\frac{\partial B}{\partial t} = \frac{\zeta}{\kappa} A(1-B) \tag{5.10}$$

where A is the analyte concentration and B is the bound analyte concentration. The equation 5.10 for the bound analyte concentration B can be solved with the integrating factor $\exp\left(-\int_0^t \frac{\zeta}{\kappa} A(x,t)dt\right)$. The solution is dependent on the analyte concentration A and given by

$$B(x,t) = 1 - \exp\left(-\int_0^t \frac{\zeta}{\kappa} A(x,t)dt\right) \tag{5.11}$$

For systems with a large adsorption capacity κ, the bound analyte concentration B is small, i.e. the relative change in bound analyte concentration is small ($B \ll 1$), and thus can be ignored in equation 5.9. In these circumstances the analyte concentration A is now independent of the concentration of the surface immobilised receptors. In this case the analyte plug behaviour is described by a travelling wave with speed $u(t)$ which links t and x by

$$\int_0^t u(\tau)d\tau = x \tag{5.12}$$

The height of the wave depends only on the time the analyte spends in the channel before it reaches the point x. This modifies the solution 5.7 for the bulk concentration to

$$A(x,t) = e^{-\zeta(t-t_0)}\,\hat{\mathrm{H}}\left(\int_0^t u(\tau)d\tau - x\right)\hat{\mathrm{H}}\left(x - \int_\lambda^t u(\tau)d\tau\right) \tag{5.13}$$

with $t_0(x,t)$ defined by the equation $\int_{t_0}^{t} u(\tau)d\tau = x$. This means that the analyte which is at position x at time t entered the channel at time t_0 and thus spent $t - t_0$ time in the sensor channel.

The bound analyte concentration B can be established by inserting the solution 5.13 for the analyte concentration A into equation 5.11. Thus the distribution of the bound analyte concentration B along the sensor is dependent on the modification of the flow velocity $u(t)$. The target of a constant value for the bound analyte concentration B over the affinity sensor active area is equivalent to seeking

$$\int_0^T A(x,\tau)d\tau = const \tag{5.14}$$

for all values of x and for T sufficiently large. The upper boundary of the integration has to be large enough so that the analyte plug has left the channel, i.e.

$$\int_\lambda^T u(\tau)d\tau \geq 1 \tag{5.15}$$

The condition 5.14 ensures that at every point of the surface, the same amount of analyte is available. As the analyte concentration A is independent of the input analyte concentration A_0 this condition ensures a uniform binding regardless of the input concentration. However, the optimisation breaks down if A_0 is so high that the condition of a high capacity system is breached.

The temporal variation of the flow speed $u(t)$ that makes equation 5.14 valid is sought. Gradually reducing the flow velocity as the analyte plug passes over the affinity sensor gives the analyte more time to bind as the plug concentration depletes along the active area. A natural and very robust ansatz, to compensate for the exponential decrease of the analyte concentration, is given by

$$u(t) = \exp(-at) \tag{5.16}$$

where a is the flow modification parameter. For this ansatz the requirement 5.15 puts a strong restriction on the allowed plug length λ which can be approximated for large T to be

$$\lambda \leq -\frac{\log(a)}{a} \tag{5.17}$$

From this equation it can be seen that a has to be smaller than 1 because otherwise the allowed plug length is zero.

The ansatz 5.16 depends only on one parameter for which an approximation can be found. For an arbitrary point x_i along the sensor the time for the front and back of the plug to reach x_i is defined by t_i and $t_i + \lambda_i$, respectively. The time λ_i the plug requires to flow past position x_i is defined by

$$\int_{t_i}^{t_i+\lambda_i} e^{-a\tau} d\tau = \int_0^{\lambda} e^{-a\tau} d\tau \tag{5.18}$$

The condition 5.14 can be reformulated into the equivalent form

$$\int_{t_1}^{t_1+\lambda_1} e^{-\zeta(\tau-t_0)} d\tau = \int_{t_2}^{t_2+\lambda_2} e^{-\zeta(\tau-t_0)} d\tau \tag{5.19}$$

for two arbitrary positions x_1 and x_2. For short plugs the parameter $t_0(x,t)$ approaches zero and can be removed from equation 5.19. This approximation is valid because long plugs can be split up into independent small plugs. For each of the small plugs a solution similar to equation 5.13 exists. The only difference is a constant offset which modifies the exponential term. This offset appears on both sides of equation 5.19 and can be removed. With the approximation $t_0 \to 0$ it becomes apparent by comparing equation 5.18 and 5.19 that $a \approx \zeta$. Numerical computations are performed to verify this approximation. The condition 5.14 is transformed into an equation for the square error between the integral of the analyte concentration and a constant c

$$R(a,c) = \sum_{i=0}^{N} \left(\int_0^T A(x_i,\tau) d\tau - c \right)^2 \tag{5.20}$$

where N is the number of sample points and $x_i = \frac{i}{N}$. This error function is minimised over the parameters a and c with the Matlab least-square optimisation routine. The results of this least-square optimisation confirm the approximation $a \approx \zeta$.

Numerical simulations for the reduced 1D problem (equations 5.9 and 5.10) and the full 2D problem (equations 3.18-3.20) including axial diffusion and second order kinetics validate the optimisation as shown in figure 5.8. The numerical simulations are performed with the commercial finite element method (FEM) package COMSOL Multiphysics 3.4 (COMSOL AB, Stockholm, Sweden). For details of the implementation see appendix B. Figure 5.8 shows the comparison of the bound analyte concentration for the case of constant flow speed with the case of the optimised flow speed according to equation 5.16. The slight differences in the bound analyte concentration between the

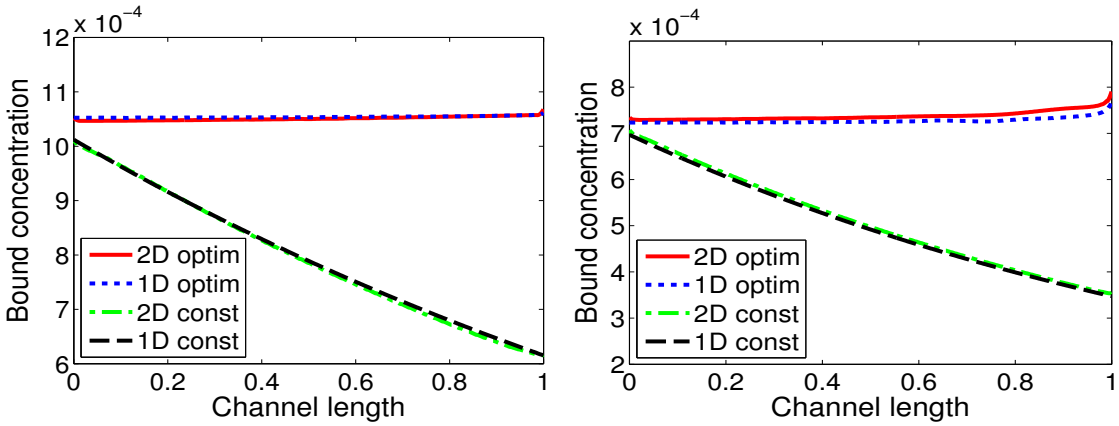

Figure 5.8: Numerical simulation of the bound analyte concentration B for constant flow velocity (const) and for the flow velocity modified by equation 5.16 (optim). Parameters: (left) $a = \zeta = 0.5$, $\mathrm{Gz} = 0.05$, $\kappa = 100$, $\lambda = 0.2$ (right) $a = \zeta = 0.7$, $\mathrm{Gz} = 0.05$, $\kappa = 100$, $\lambda = 0.1$

1D and the 2D simulations depend on the Graetz number and thus approach zero for $\mathrm{Gz} \to 0$. However, the increase in the bound analyte concentration at the end of the sensor patch, as seen in the right-hand side plot of figure 5.8, increases with decreasing Graetz number. This is due to the increasing importance of axial diffusion compared to convection for very small Graetz numbers. The good qualitative and quantitative agreement between the 1D and 2D model shows that the simplifications are reasonable for the case of small Graetz number and high adsorption capacity.

Figure 5.9 shows that the modification of the flow velocity yields a uniform bound analyte concentration which is insensitive to slight variations in the flow parameters. The model is based upon the assumption that any variation in flow velocity starts immediately as the analyte plug reaches the start of the sensor. If the variation in the flow velocity starts before or after the analyte plug reaches the start of the sensor the flow velocity is given by

$$u(t) = \exp\left(-a(t - t_{off})\,\hat{\mathrm{H}}(t - t_{off})\right) \tag{5.21}$$

where t_{off} is the offset between the arrival of the analyte plug and the start of the variation in the flow velocity. A negative offset ($t_{off} < 0$) only has a slight effect on the magnitude of the bound analyte concentration through an increase in the reaction/convection number. On the other hand, for a positive offset the flow velocity is only modified for $t > t_{off}$ so that the bound concentration behaves as in the constant

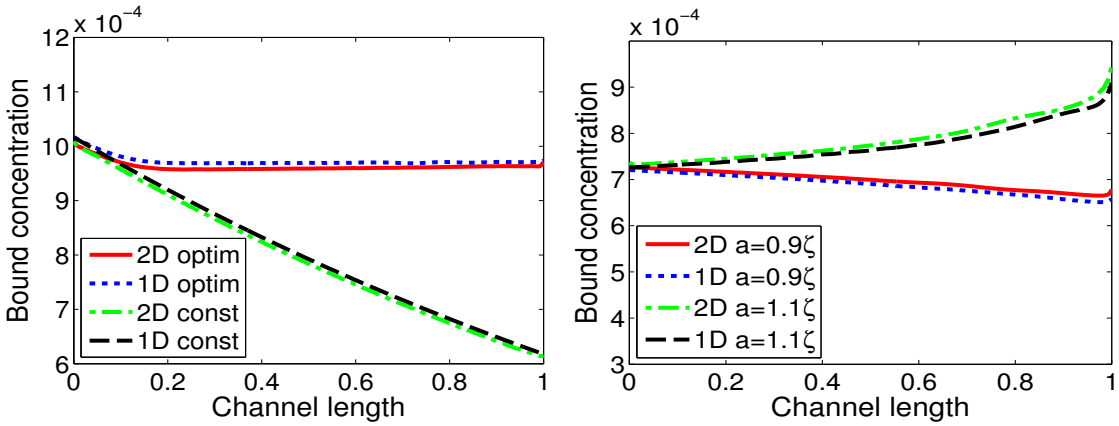

Figure 5.9: Numerical simulation of the bound concentration B for variations in the flow modification. (left) Positive offset in the flow modification, (right) variations in the flow modification parameter a. Parameters: (left) $a = \zeta = 0.5$, Gz $= 0.05$, $\kappa = 100$, $\lambda = 0.2$, $t_{off} = 0.2$ (right) $\zeta = 0.7$, Gz $= 0.05$, $\kappa = 100$, $\lambda = 0.1$

flow velocity case for $t < t_{off}$. This is shown in the left plot of figure 5.9. The right plot in figure 5.9 shows the bound analyte concentration for variations in the flow modification parameter a. The resulting bound concentration profile for a 10% deviation from the optimal flow modification parameter is still much more uniform than the constant flow velocity case. These simulations suggest that a reduction of the flow modification parameter has a less negative effect than an increase.

The modification of the flow velocity is a simple and robust method to increase not only the uniformity of the bound analyte but also the capture fraction defined in equation 5.8. This improvement of the analyte capture fraction of the sensor depends on the reaction/convection number. For $\zeta = 0.7$ about 75% of the analyte is captured at the active surface which is an improvement of about 50% over the constant flow velocity case. For $\zeta = 0.9$ over 90% of the analyte binds to the surface but condition 5.17 allows only short analyte plugs and depending on the value of Gz the uniformity of the bound analyte degrades at the end of the sensor patch. A further benefit of this method is the offered flexibility. The flow modification can be changed dynamically by changing the operational parameters of the pump. This allows the optimisation of the bound analyte concentration for analyte-receptor pairs with different reaction/convection numbers in one system.

The practical implementation of this ansatz requires sophisticated pumps as well as accurate control of the plug position. Many external pumps, e.g. syringe pumps, are computer programmable and allow the modification of the flow rate and thus the flow velocity in the microfluidic channel. However, studies have shown that the change in flow velocity is not instantaneous but lags behind the change in pump rate [210]. In addition, the model is based upon the assumption that the analyte plug reaches the sensor patch at exactly the point where the flow velocity parameters change and is only valid for analyte plugs much shorter than the sensor length. These limitations on the plug length given by equation 5.17 and the required positional accuracy of the plug put strong requirements on the sample introduction scheme (see section 2.4.4). Off-chip sample introduction schemes such as 6-port valves require extensive characterisation before they can be employed in this design. This is due to uncertainties in the sample size and the connection between the valve and the microfluidic chip. On the other hand, on-chip sample introduction schemes have been presented which offer the required accuracy, control and sample size [106; 107].

5.5.2 Spatial variation of the receptor concentration

The second design concept considers the spatial distribution of surface immobilised receptor molecules over the active area of the sensor. More specifically, how an increase in the density of the surface immobilised receptor molecules along the active surface can enhance the analyte mass transfer and subsequent association along the length of the channel. For instance, if the density of surface immobilised receptor molecules along the sensor surface is increased it may be possible to compensate for the depletion of the analyte plug. In effect by tailoring the receptor concentration on the sensor surface it will be possible to achieve a uniform density of associated analyte.

The total receptor concentration is taken to be $X_s(x)X_0$ where X_0 is the concentration at the outlet and $X_s(x)$ describes the variation in the receptor concentration along the active area of the sensor ($X_s(1) = 1$). For these studies the flow velocity of the analyte is constant. Introduction of a variable receptor concentration along the sensor

length modifies the governing equations 4.11 and 4.12 (chapter 4) to

$$\frac{\partial A}{\partial t} + \frac{\partial A}{\partial x} = -\zeta A(X_s(x) - B) \tag{5.22}$$

$$\frac{\partial B}{\partial t} = \frac{\zeta}{\kappa} A(X_s(x) - B) \tag{5.23}$$

A similar analysis, as in section 5.5.1, results in equations describing the analyte concentration A and the bound analyte concentration B, as a function of distance along the channel x and time t.

$$A(x,t) = \exp\left(-\zeta \int_0^x X_s(x)dx\right) \hat{\mathrm{H}}\left(t - x\right) \hat{\mathrm{H}}\left(x - t + \lambda\right) \tag{5.24}$$

$$B(x,t) = X_s(x)\left(1 - \exp\left(-\lambda \frac{\zeta}{\kappa} A(x,t)\right)\right) \tag{5.25}$$

The distribution of the bound analyte concentration is dependent on the variation of the surface immobilised receptor concentration $X_s(x)$. A model is developed here to provide the optimal spatial distribution of the receptor concentration $X_s(x)$ on the sensor patch so that the bound analyte concentration B is constant over the sensor patch which is equivalent to

$$B(x,t) = const \tag{5.26}$$

for all x and for t sufficiently large. By analogy with the variation of the flow velocity (section 5.5.1) the following ansatz is made

$$X_s(x) = \exp(-a(1-x)) \tag{5.27}$$

where a is the concentration variation parameter. This is a natural and robust ansatz which compensates the exponential decreasing analyte concentration with an exponential increase in the receptor concentration. Furthermore, it ensures that the maximal receptor concentration is limited because there is a practical limit to the achievable concentration of surface immobilised receptors. A least-squares optimisation is performed in Matlab to find the value of a for a range of reaction/convection numbers. Briefly, the condition 5.26 is transformed into an equation for the square error between the bound analyte concentration and a constant c

$$R(a,c) = \sum_{i=0}^{N} \left(B(x_i,t) - c\right)^2 \tag{5.28}$$

ζ	a	Capture fraction
0.5	0.409	0.344
1.0	0.701	0.522
1.5	0.950	0.630
2.0	1.155	0.705
2.5	1.333	0.759
3.0	1.492	0.799
3.5	1.636	0.831
4.0	1.767	0.856
4.5	1.887	0.877
5.0	1.999	0.894
5.5	2.103	0.908

Table 5.1: Results of the least-squares optimisation over equation 5.28 for the concentration variation parameter a and for different values of the reaction/convection number ζ. Parameters: $\kappa = 100$, $\lambda = 0.1$

where N is the number of sample points, $x_i = \frac{i}{N}$ and t is sufficiently large. This error function is minimised over the parameters a and c with the Matlab least-square optimisation routine. The results, including the capture fraction, are shown in table 5.1. The capture fraction is lower than for the case of uniform receptor concentration. This is expected because the ansatz 5.27 leads to a reduction in the number of available binding sites compared to the uniform receptor concentration case. A further decrease in the flow speed or a higher maximal receptor concentration X_0 can increase the reaction/convection number and accordingly the capture fraction.

Numerical simulations comparing the constant with the modified receptor concentration case are shown in figure 5.10. The numerical simulations are performed with the commercial FEM package COMSOL Multiphysics 3.4 (COMSOL AB, Stockholm, Sweden). For details of the implementation see appendix B. The numerical simulations are performed for the reduced 1D model as well as for the full 2D model including axial diffusion and second order kinetics. The numerical simulations show that the bound analyte concentration is almost constant along the length of the sensor for small reac-

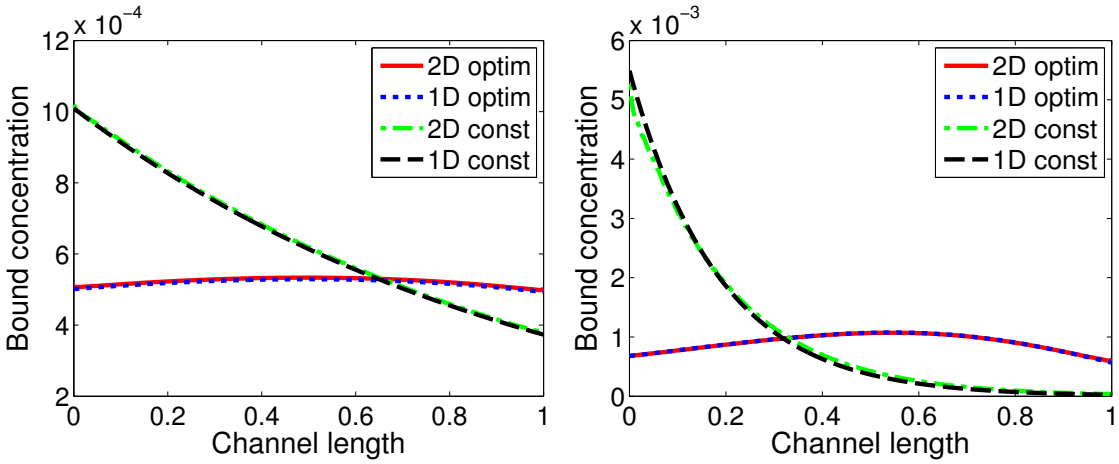

Figure 5.10: Numerical simulation of the bound concentration B for constant receptor concentration and for the receptor concentration modified by equation 5.27. Parameters: (left) $a = 0.701$, $\mathrm{Gz} = 0.05$, $\kappa = 100$, $\lambda = 0.1$, $\zeta = 1$, (right) $a = 2.103$, $\mathrm{Gz} = 0.05$, $\kappa = 100$, $\lambda = 0.1$, $\zeta = 5.5$

tion/convection numbers ($\zeta \leq 1$) but that a 'hump' in the middle of the sensor length develops for larger reaction/convection numbers ($\zeta > 1$). The relative deviation from the mean bound analyte concentration increases with the reaction/convection number but even for an analyte capture fraction of 0.9 stays below 20%. This means that the ansatz 5.27 is not sufficient to completely compensate for the depletion of the analyte concentration along the channel but still gives a large improvement compared to the case with constant receptor concentration which was described in section 5.4.

A more flexible approach than ansatz 5.27 is needed to achieve a constant bound concentration along the sensor. The ansatz

$$X_a(x) = 1 + \sum_{i=1}^{n} b_i (x-1)^i \tag{5.29}$$

offers more flexibility but depends on more parameters. Furthermore, care has to be taken to ensure that the resulting modification of the receptor concentration is viable, i.e. $0 \leq X_a \leq 1$. Figure 5.11 shows a comparison between the ansatz 5.27 and ansatz 5.29 for $n = 3$. The deviation from the mean bound concentration is greatly reduced while maintaining the high capture fraction.

Figure 5.12 shows the bound concentration for variations in the concentration vari-

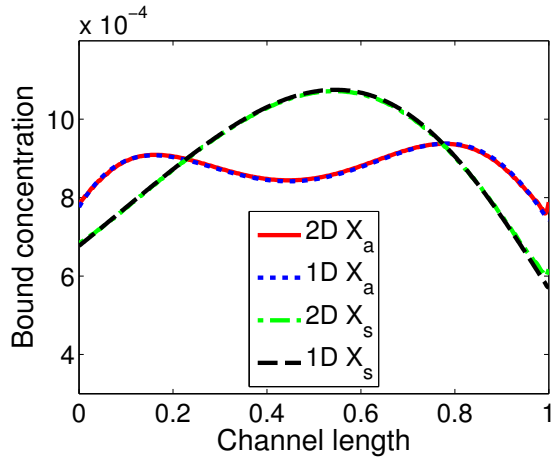

Figure 5.11: Numerical simulation of the bound analyte concentration B comparing ansatz 5.27 with ansatz 5.29. Parameters: $a = 2.103$, $b = [2.89, 3.67, 1.64]$, Gz $= 0.05$, $\kappa = 100$, $\lambda = 0.1$, $\zeta = 5.5$

ation parameters a from ansatz 5.27 and b from ansatz 5.29. If it is not practically possible to achieve the desired spatial distribution of receptors on the sensor patch, the results from this study demonstrate that this still yields increased uniformity of the analyte associated to the sensor patch. Furthermore, the optimisation seems to be independent to variations in the adsorption capacity κ and the plug length λ as long as the requirements of the simplification are fulfilled.

By varying the spatial concentration of the receptor on the sensor surface it is possible to create a robust method for achieving uniformity of the bound analyte. In contrast to the system described in section 5.5.1, where the flow velocity of the analyte plug over the sensor is varied, this method is insensitive to the position of the analyte plug and is also suitable for arbitrary long analyte plugs. On the other hand, this method is less flexible because, once the gradient of the receptor concentration on the sensor surface is fabricated, the system is fixed for one value of the reaction/convection number. The difficulties in the practical implementation of this method lay in the creation of the gradient in the surface immobilised receptor concentration (see section 2.4.1). However, several potential methods for the creation of surface gradients exist [19; 90; 211]; a relatively simple method exploits the fact that the profile of the optimal surface immobilised receptor concentration is similar to the bound concentration for constant parameters. By using microfluidic patterning (section 2.4.1) and flowing the solution containing the

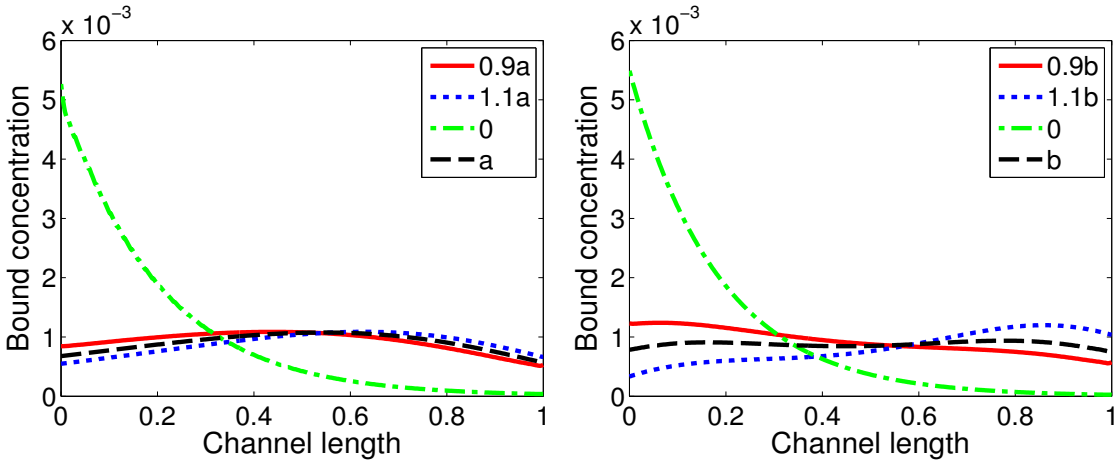

Figure 5.12: Numerical simulation of the bound analyte concentration B for variations in the concentration variation parameters. (left) Variation of the concentration variation parameter a of ansatz 5.27, (right) variation of the concentration variation parameter b of ansatz 5.29. Parameters: (left) $a = 2.103$, $\mathrm{Gz} = 0.05$, $\kappa = 100$, $\lambda = 0.1$, $\zeta = 5.5$ (right) $b = [2.89, 3.67, 1.64]$, $\mathrm{Gz} = 0.05$, $\kappa = 100$, $\lambda = 0.1$, $\zeta = 5.5$

receptor molecules in the opposite direction the depletion of the receptor plug is transferred to the surface and thus a surface gradient is created [19; 212]. A further flow based method applies microfluidic gradient generators [211] (see chapter 7). The gradient generator creates a concentration gradient in the bulk of the microfluidic channel which is transferred to the surface of the receptor patch. In a modification of microcontact printing [83] where the receptor molecules are incubated on an elastomeric stamp and stamped onto the sensor surface, the receptor molecules are only applied to one side of the stamp and are allowed to diffuse to the other side, thus creating a concentration gradient [213]. A further method is based on photoimmobilisation [90]; the immobilisation yield is proportional to the exposure dose, thus by varying the exposure with different laser scan speeds or grey-scale masks it is possible to fabricate receptor patches with different spatial densities of receptors. The combination of a microfluidic gradient generator and microfluidic photomasks offer the possibility of inexpensive grey-scale masks [26].

5.6 Non-rectangular channel shape and active area

The next design approach is based on non-rectangular device geometries. This approach presents a more practical solution compared to the approaches presented in section 5.5 where a constant analyte mass transfer to the sensor surface and subsequent association was achieved by variations of the flow velocity or surface immobilised receptor concentration as the analyte plug is flowed over the sensor. In the approach presented here the flow velocity and concentration of surface immobilised receptor molecules are kept constant. Instead, a non-rectangular microfluidic channel and sensor patch, are utilised; the channel geometry is varied in the plane of the active sensor area and the shape of the receptor patch is varied independently. This approach takes the depletion of the analyte plug along the sensor length into account and yields a more uniform bound analyte concentration over the sensor patch compared to conventional systems which were described in section 5.4.

5.6.1 Modelling of non-rectangular device geometry

In a tapered channel of constant height, as shown in a top view representation in figure 5.13, streamlines are crossing from the inactive into the active region over the whole length of the sensor area. These streamlines represent the transport of analyte molecules

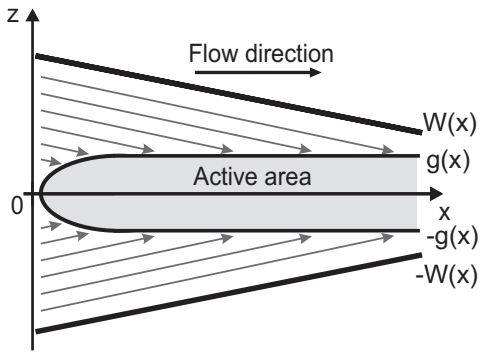

Figure 5.13: Top view diagram of a tapering channel. Streamlines reach the active/inactive interface along the whole sensor length.

into the active area and thus by variation of the channel/sensor geometry replenishment

of the analyte concentration over the sensor patch results. This continuous replenishment of analytes in the active area along the channel results in a reduction of the effects of depletion of the analyte concentration in the bulk as seen in section 5.4. The lower surface of the device is divided into a region with no receptor molecules (shown in white) and a region with a uniform concentration of receptor molecules attached to the active area (shown in grey). Different geometries of the channel wall $W(x)$ and the active/inactive boundary $g(x)$ on the base of the channel are considered.

The system shown in figure 5.13, compared to the previous ones (section 5.5), has the added complexity that the fluid velocity in both the x and z directions must be considered and that the affinity reaction takes place only in parts of the channel. Incorporating this modifies the governing equations 4.11 and 4.12 to

$$A_t + uA_x + wA_z = -\chi(x,z)\zeta A(1-B) \tag{5.30}$$

$$B_t = \chi(x,z)\frac{\zeta}{\kappa}A(1-B) \tag{5.31}$$

with the active region described by $\chi(x,z) = 1$ for $0 \leq z \leq g(x)$ and zero otherwise. The system is assumed to be symmetric with respect to the x axis and hence only the region $0 \leq z \leq W(x)$ has to be considered. In contrast to the rectangular device geometry considered in section 5.5, no analytical solution for the flow velocity exists. However, the governing equations for the flow in microfluidic channels where the height of the channel is much smaller than the width and the length can be significantly simplified. Neglecting the side wall effects and using thin film theory [123] it can be seen that the streamlines are only dependent on the gradient of the pressure. Thin film theory which is valid for

$$\frac{UL}{\nu}\left(\frac{H}{L}\right)^2 \ll 1 \tag{5.32}$$

gives the following approximation of the flow speed

$$u(x,y,z) = -\frac{1}{2\mu}p_x y(H-y) \tag{5.33}$$

$$w(x,y,z) = -\frac{1}{2\mu}p_z y(H-y) \tag{5.34}$$

The calculation of the flow speed is thus reduced to the calculation of the pressure field in the microfluidic channel. Inserting equation 5.33 and 5.34 into the mass conservation

equation 3.2 leads to the Laplace equation

$$\Delta p = 0 \tag{5.35}$$

for the pressure field. The boundary conditions are $p = c_1$, $p = c_2$ and $p_n = 0$ at the channel entrance, channel exit and the channel wall, respectively. Here only cases with uniform analyte concentration over the height of the microfluidic channel are considered and thus the equations 5.33 and 5.34 for the flow velocity can be reduced to (see section 4.3.1)

$$u(x, y, z) = -\frac{1}{2\mu} p_x \tag{5.36}$$

$$w(x, y, z) = -\frac{1}{2\mu} p_z \tag{5.37}$$

The numerical solution of the Laplace equation is more stable and much faster than the numerical solution of the full Navier-Stokes equations. Nevertheless, it would be beneficial to have analytical solutions of the Laplace equation which describe the flow in tapering microfluidic channels. Two analytical solutions of the Laplace equation define tapering regions. The first solution is given through $p_1 = z^2 - x^2$ which defines a 2D pressure field with a saddle point at the origin. The streamlines for p_1 are given by $zx = c$ where c is a constant. The second solution is $p_2 = \log(x^2 + z^2)/2$ which defines a pressure field with a source or sink at the origin. The streamlines for p_2 are given by $z = cx$ where c is constant. To fulfil the boundary conditions, the channel side walls are defined by a streamline for a specific constant c, and this thus defines the dimensions of the channel entrance and exit. The inlet-to-outlet ratio of these tapering channels varies for different values of c. The shape of the channel entrance and exit is given by the pressure isobars. The pressure p_1 defines a channel with an algebraic decrease in width, while p_2 defines a channel with a linear decrease in width, as shown schematically in figure 5.14. The only differences between these two channel structures, as compared with the originally proposed channel (figure 5.13), are that the shapes of the channel entrance and exit are different and are no longer straight lines. However, the deviations resulting from a difference in a vertical inlet and outlet, compared to the shaped ones in figure 5.14, will only have a small effect on the resulting flow velocity. These two

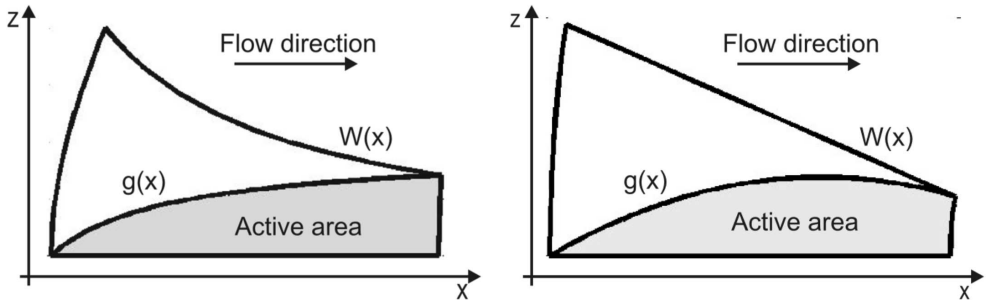

Figure 5.14: Narrowing channel defined through the streamlines and lines of equal pressure of the solution to the Laplace equation 5.35. (left) Channel design and optimal sensing area (grey) for $p_1 = z^2 - x^2$ and (right) channel design and optimal sensing area (grey) for $p_2 = \log(x^2 + z^2)/2$. Reprinted from [214] with permission from Elsevier.

channel designs, for which an example is given in figure 5.14, provide sufficient flexibility to evaluate the replenishment of the analyte concentration along the length of the active sensor area due to a tapering channel.

To a first approximation, the objective of a uniform distribution of bound analyte along the sensor surface is equivalent to a uniform flux of analyte across the active/inactive interface along the channel. To achieve a uniform flux of analyte across the active/inactive interface the shape of the tapering and of the active/inactive boundary have to be considered simultaneously. However, an optimisation over both the channel and active area shape would require a full numerical approach. This would be computationally expensive and is not likely to provide sufficient insight to be valuable. Thus a simplified approach was taken. Rather than optimising both, the shape of the channel $W(x)$ is fixed and only the optimal shape of the active area $g(x)$ is established numerically. The objective of uniform flux of analyte across the active/inactive interface is equivalent to

$$\mathbf{u} \cdot \mathbf{n}_g = const \tag{5.38}$$

where $\mathbf{u}$ is the flow velocity at the interface and $\mathbf{n}_g = (g', -1)((g')^2 + 1)^{-1/2}$ is the normal to the interface g. With the analytic equations of the flow speed 5.33 and 5.34 determined from the pressure fields, this leads to an ordinary differential equation for

$g(x)$ for each of the two pressure fields

$$\mathbf{u} \cdot \mathbf{n}_g = \frac{g'x + g}{\sqrt{(g')^2 + 1}} = const \qquad \text{for } p_1 \tag{5.39}$$

$$\mathbf{u} \cdot \mathbf{n}_g = \frac{-g'x + g}{(x^2 + g^2)\sqrt{(g')^2 + 1}} = const \qquad \text{for } p_2 \tag{5.40}$$

with the boundary conditions $g(0) = 0$ and $g(1) = W(1)$. The boundary conditions ensure that the active area extends across the entire channel at the exit. The nonlinear boundary value problem is solved numerically using an inbuilt Matlab solver. The solutions for two tapering channels, i.e. for the pressure fields $p_1 = z^2 - x^2$ and $p_2 = \log(x^2 + z^2)/2$, define 'boat-shaped' sensor patches which are given in figure 5.14.

5.6.2 Comparison with rectangular channels

The tapering channel and 'boat-shaped' sensor patch are embedded into a sensor element to facilitate better comparability between the two different designs and different inlet-to-outlet ratios. This sensor element consists of a channel where the width increases, a transition region and the tapering channels designed in section 5.6.1. The

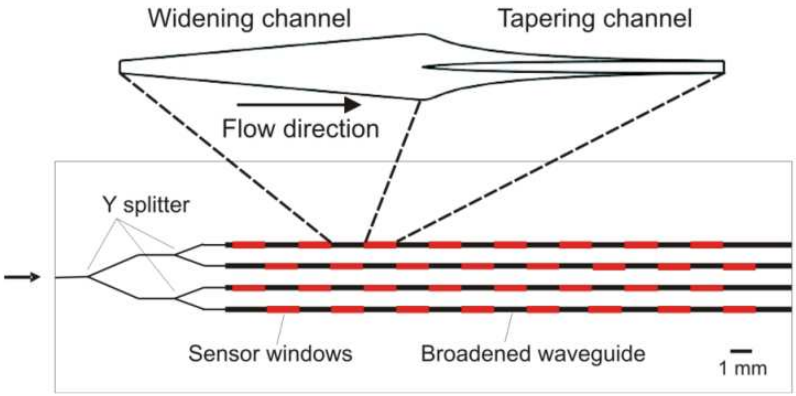

Figure 5.15: Diagram of the sensor element for the algebraic channel with inlet-to-outlet ratio 6 and the relation to the waveguide chip from the multisensor [21].

sensor elements are designed to fit over the waveguide and sensor windows of the multisensor [21] as indicated in figure 5.15. The inlet and outlet have the same width of 60 μm to enable the sequential configuration of several sensor elements. The length of both the widening and tapering region is 1.5 mm. The sensor element is designed such

that the widening channel occupies the whole space between two sensor windows; this configuration gives the lowest possible distortion of the analyte plug due to the radial flow profile in the widening channel. The tapering region spans not the whole length of the sensor patch. This would lead to a low capture fraction because analyte molecules close to the walls of the channel would only flow over the sensor patch for a very short amount of time. To increase the capture fraction a short straight channel is added at the end of the sensor element. The length of this region is a trade-off between improved capture fraction and reduced uniformity. Here the length is chosen to be $100\,\mu$m. For a system with $\zeta = 10$ this length of the straight region ensures that $\sim 50\%$ of the analyte molecules close to the channel wall are associated at the receptor patch.

To assess the uniformity of the bound analyte concentration the following integral is used

$$\upsilon = \frac{\int_S (B(x,z) - B_{avg})^2 \, dz \, dx}{B_{avg}^2 \int_S dz \, dx} \tag{5.41}$$

where S is the active surface and B_{avg} is the average bound analyte concentration. This measure gives an indication of the deviation of the bound analyte concentration from the average bound analyte concentration so that a uniformity of $\upsilon = 0$ indicates optimal uniformity and the uniformity decreases with increasing υ. From equations 5.30 and 5.31 it is clear that beside the channel shape only the reaction/convection number ζ and the adsorption capacity κ have an influence on the amount and uniformity of the bound analyte concentration. In the following analysis the adsorption capacity is kept much larger than the analyte plug length ($\kappa \gg \lambda$) which ensures that the free receptor concentration stays almost constant.

To establish whether the simplifications made in the reduction to a 2D model are reasonable, simulations using the 2D model are compared to full 3D simulations. The critical issue in this comparison is the effect of the flow velocity. The 2D model neglects the effects of the side walls on the flow which is a reasonable simplification for systems where the sensor patch is far away from the side walls. However, in the tapering channel design the sensor patch goes up to the side wall so that the reduced flow near the side walls might have an effect on the association of the analyte. The complex shape of the device, combined with the low channel height, poses significant challenges for the numerical simulation of the 3D problem. To achieve the numerical simulation the

complexity of the geometry was reduced; the complex sensor element is replaced by a simple, linear tapering channel and a triangular sensor patch. The comparison of the 2D and 3D simulations showed that both models have a qualitatively similar bound concentration profile. However, the 2D model predicts a higher average bound concentration and better uniformity. This can be explained by the simplified flow profile which improves the association of analyte in the narrower region of the tapering channel. In addition, the uniformity of the bound analyte concentration for both the 2D and 3D simulations increases about sevenfold from the straight to the tapered channel. Together this shows that the 2D model is not a 100% accurate representation of the full 3D system but a reasonable approximation which provides qualitative information on the uniformity of the bound analyte concentration profile.

Figure 5.16 and 5.17 show the capture fraction and the uniformity against the reaction/convection number for the two channel designs and various inlet-to-outlet ratios. Here 'algebraic$_n$' and 'linear$_n$' refer to the algebraic and linear channel design with

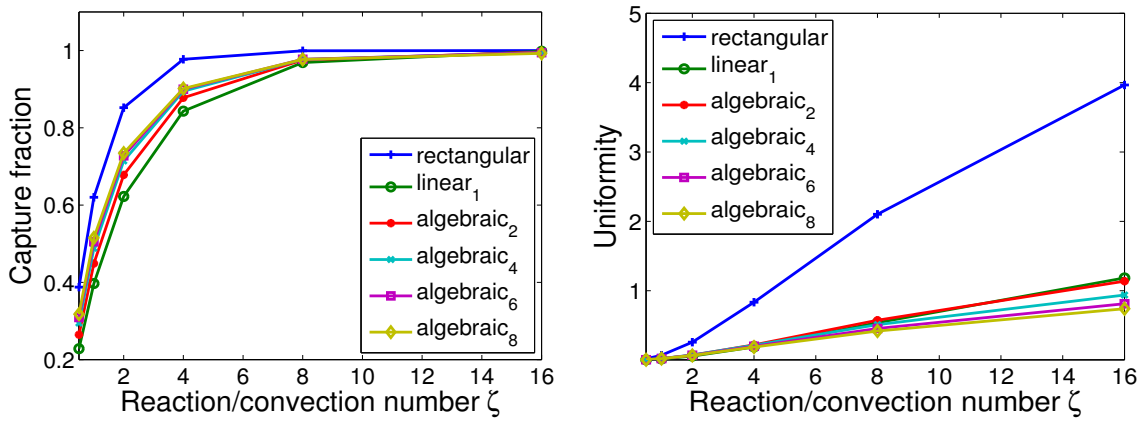

Figure 5.16: Comparison of the performance of the sensor elements with various inlet-to-outlet ratios of the algebraic channel design. (left) Capture fraction against the reaction/convection number ζ, (right) uniformity measure υ against the reaction/convection number ζ. The uniformity measure υ is calculated with equation 5.41 and increases with decreasing uniformity. Parameters: $\kappa = 100$, $\lambda = 10$, $t = 20$

inlet-to-outlet ratio n, respectively, while 'rectangular' refers to the straight channel with rectangular sensor patch. Figures of the sensor elements are shown in appendix C.

The design 'linear$_1$' is a straight channel whose active area is defined through equation 5.38. It can be seen in both figures that for small reaction/convection numbers the capture fraction is dependent on the geometry of the channel and the sensor patch. For

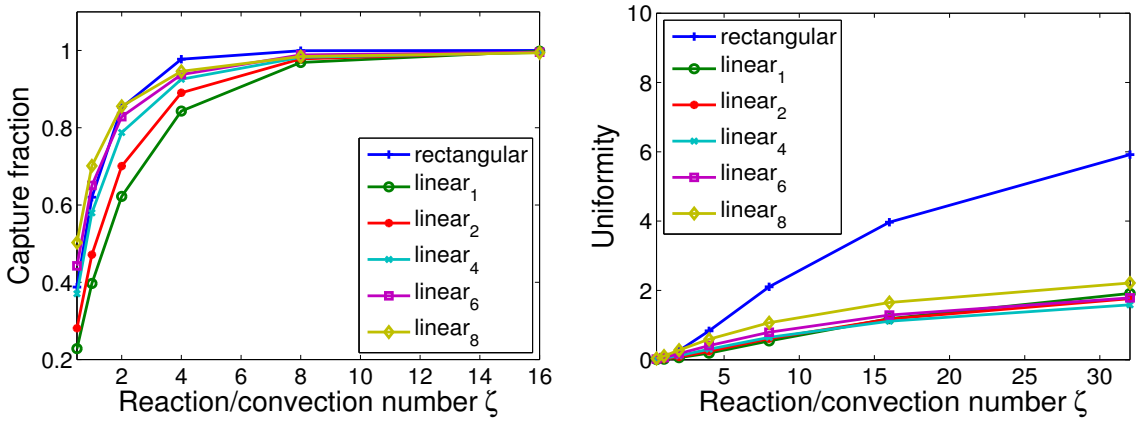

Figure 5.17: Comparison of the performance of the sensor elements with various inlet-to-outlet ratios of the linear channel design. (left) Fraction bound against the reaction/convection number ζ, (right) uniformity measure υ against the reaction/convection number ζ. The uniformity measure υ is calculated with equation 5.41 and increases with decreasing uniformity. Parameters: $\kappa = 100$, $\lambda = 10$, $t = 20$

the smallest simulated reaction/convection number $\zeta = 0.5$ about 1.5 times as much of the analyte associates in the straight channel with a rectangular sensor patch compared to tapering channels with inlet-to-outlet ratio 2. The reason for this is that the time where the bulk solution is not above the active area is 'lost time for binding'. It is therefore not surprising that a large fraction of the analyte is not captured by the receptor molecules over the active area. This loss is particularly high at the edges of the tapered channels. This difference in capture fraction, between straight and tapered channels, decreases with increasing reaction/convection number ζ and becomes negligible for $\zeta > 10$. The difference in capture fraction for sensor elements with different inlet-to-outlet ratios is due to the different average velocities in the tapering region. The average velocity decreases with an increase in the inlet-to-outlet ratio and this also results in an increase in the capture fraction.

The uniformity of associated analyte at the sensor surface, as defined by equation 5.41, is generally much better for the tapering channels than for the rectangu-

lar channel. However, the two different channel shapes behave differently. The right plot of figure 5.16 shows that the uniformity of associated analyte for the algebraic tapering channels increases for all values of the reaction/convection number ζ with the inlet-to-outlet ratio; thus the sensor element 'algebraic$_8$' has the highest uniformity of associated analyte at the sensor surface. The same is not true for the linear tapering channels as shown in figure 5.17. Here the channel with the highest uniformity of associated analyte at the sensor surface is dependent on both the reaction/convection number and the adsorption capacity. For low values of ζ the uniformity increases with decreasing inlet-to-outlet ratios so that 'linear$_1$' has the highest uniformity. However, for $\zeta > 15$ the design 'linear$_4$' has the highest uniformity of associated analyte at the sensor surface. Further simulations with larger values of the adsorption capacity and reaction/convection number have shown that the order of the uniformity of analyte bound to the sensor patch approaches the order of the algebraic channels, i.e. the uniformity of analyte bound to the sensor patch increases with the inlet-to-outlet ratio, for large values of κ and ζ. Simulations for longer analyte plugs show the same behaviour as long as the number of receptor molecules is much larger than the number of analyte molecules ($\kappa \gg \lambda$), see figure 5.18. For short analyte plugs the bound analyte concentration is

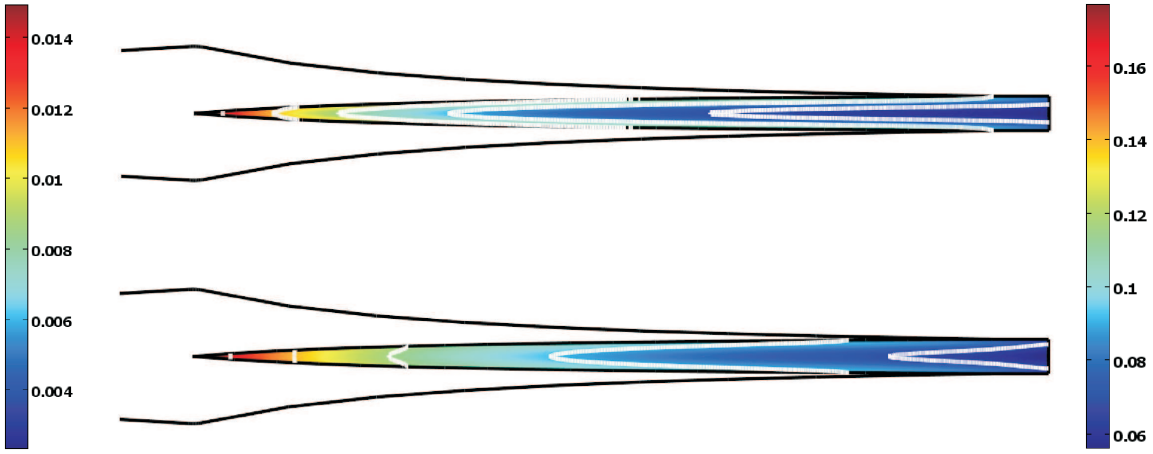

Figure 5.18: Surface and contour plots of the bound analyte concentration of the sensor element 'algebraic$_4$' for different times. (top) $t = 10$, (bottom) $t = 110$. The left colourbar is for the top plot and the right colourbar is for the bottom plot. The contour lines (white) are equally spaced through the concentration range. Parameters: $\kappa = 1000$, $\lambda = 100$, $\zeta = 2$

uniform along the active/inactive boundary and along lines which are quasi-parallel to

the boundary. For longer plugs the system approaches equilibrium and the taper has less impact on the capture fraction or the uniformity of analyte associated on the sensor patch.

Thus the improvement, in the uniformity of the bound analyte concentration, is mainly dependent on the channel shape and the reaction/convection number. The largest influence is given by the reaction/convection number ζ. The improvement of the uniformity of analyte associated on the sensor patch for tapered channels compared to rectangular channels increases with ζ while the uniformity decreases. This is due to the faster depletion of the bulk concentration so that the analyte replenishment is more effective while the gradients in the bound concentration become larger. The figures 5.16 and 5.17 show that there is a trade-off between capture fraction and uniformity of the bound analytes: the capture fraction increases with the reaction/convection number ζ while the uniformity decreases. The left plots of the figures 5.16 and 5.17 show that a value of $\zeta = 10$ is sufficient to achieve a capture fraction of 0.95. A further increase of ζ would only decrease the uniformity without significant improvements in the capture fraction. Compared to the reaction/convection number ζ, the different inlet-to-outlet ratios of the tapering channels have a much smaller effect on the uniformity of analyte bound to the sensor patch. For $\zeta < 4$ the highest uniformity of analyte bound to the sensor patch is achieved by channel design 'linear$_1$'. For larger values of ζ the algebraic channel with inlet-to-outlet ratio 8 has the highest uniformity of analyte bound to the sensor patch.

The comparison of the tapered channels with 'boat-shaped' sensor patches with rectangular systems shows that non-rectangular devices have the potential to increase the uniformity of the bound analyte while retaining a high capture fraction. As found for the two approaches described in section 5.5 this design is only of value for analyte plugs which are short compared to the sensor length. The utilisation of tapered channels requires only a simple flow control and a sensor patch with a uniform distribution of receptor molecules. However, the matched shape of the channel and sensor patch require the careful alignment of the immobilisation of the receptors and the assembly of the microfluidic channel to the waveguide chip.

A further advantage for integrating tapered channels in affinity sensors in a serial configuration is that tapers with different inlet-to-outlet ratio can be used. As was seen in figures 5.16 and 5.17, tapers with different inlet-to-outlet ratios have different capture fractions for a fixed reaction/convection number ζ. This opens the possibility to change the inlet-to-outlet ratio in subsequent sensor elements according to the reaction/convection number of the analyte-receptor pair; ensuring the same capture fraction in each sensor element. Thus for a series of sensors for the detection of multiple analytes, the channels can be tailored to suit the binding properties of the analyte-receptor pair in each sensor element.

5.7 Summary

Novel design guidelines for the improved transport of analytes in microfluidic affinity sensors were presented. These design guidelines take the depletion of the analyte plug along the sensor surface into account and generate a constant analyte mass transfer to the active sensor surface and subsequent association while retaining a high capture fraction.

The simple device designs and assay protocols, which reduce the effect of the analyte plug depletion on the bound analyte concentration, were developed based on the analysis of conventional biosensors, i.e. rectangular device geometry and constant device parameters. It was shown that these conventional biosensors can achieve either a high capture fraction or a uniform distribution of bound analyte along the sensor surface but not both; this is due to the depletion of the analyte plug along the sensor surface. This showed that there is a need for new design strategies which compensate for this analyte depletion.

In this chapter three design strategies have been evaluated. The first two theoretical design strategies (section 5.5) evolved from an analysis of the governing equations 5.2-5.4 of the microfluidic affinity system. The local binding of the analyte to the receptor molecules depends on the analyte concentration A and the reaction/convection number ζ so that an increasing reaction/convection number can compensate the decreasing analyte

concentration. The most practical way to increase the reaction/convection number is (i) a reduction of the flow velocity or (ii) an increase in the surface immobilised receptor concentration as the analyte travels down the channel. Both methods achieve a constant bound analyte concentration along the sensor length as well as a high capture fraction. The former method has the added benefit that the flow velocity can be adjusted dynamically while the latter is fixed after the immobilisation of the receptors. However, the latter method is feasible for arbitrary long analyte plugs while the former has strong restrictions on the allowed sample plug length. A drawback of both methods is the increased complexity of the device operation in the form of complex flow control and non-uniform surface immobilised receptor concentration, respectively.

The third design strategy (section 5.6) is based on a non-rectangular device geometry where the shape of the microfluidic channel and the shape of the sensor patch are modified. By changing the flow cell from a rectangular geometry to a tapering geometry, streamlines are crossing the active/inactive boundary along the whole length of the sensor patch. This continuously replenishes the analyte in the active area and thus improves the uniformity of the bound analytes. However, this replenishment is not uniform along the length of the sensor for rectangular sensor patches. For two different shapes of the taper, linear and algebraic, the shape of the active/inactive boundary is optimised so that the analyte flux across this boundary is uniform over the length of the sensor. The resulting non-rectangular device, i.e tapering channel and 'boat-shaped' sensor patch, has increased uniformity of the distribution of bound analyte at the sensor patch compared to the standard, rectangular sensors. Furthermore, this approach requires only simple flow control and a uniform distribution of receptor molecules which makes it more practical than the approaches considered in section 5.5. The application of the non-rectangular device geometry for a microfluidic biosensor for the detection of low cytokine levels is presented in chapter 6.

Conventional microfluidic affinity sensors with rectangular geometries and constant device parameters can either achieve a high capture fraction or a high uniformity of the associated analyte along the sensor surface. The design strategies presented here overcome this limitation and allow the design of integrated microfluidic affinity sensors which achieve a high capture fraction while retaining a high uniformity of the associated

analyte along the sensor surface.

Chapter 6

Adaptation of integrated microfluidic biosensors for the detection of low cytokine levels

6.1 Introduction

The detection, quantification and monitoring of proteins from small sample volumes requires sophisticated and sensitive immunoassays (section 2.2). In this chapter the results from chapter 5 are applied to the design of a microfluidic affinity sensor system for the sensitive detection and quantification of low levels of cytokines from serum. Cytokines are signaling molecules which are important for intercellular communication and especially for the immune response following infection through a pathogen, i.e. fungus, virus, bacteria or chemical agent [215]. This physiological, metabolic and behavioural immune response can be triggered by pro-inflammatory cytokines [216].

Elevated cytokine levels have an impact on the brain and it has been suggested that even low-grade inflammations and the resulting slightly elevated cytokine levels may contribute to the progression of chronic neurodegenerative diseases like Alzheimer's and Multiple Sclerosis [6]. For example, Holmes et al. [217] linked systemic infection and raised levels of the cytokine IL-1β to impaired cognitive function in Alzheimer's patients.

Extensive clinical studies of the cytokine concentration and accompanying behavioural changes will lead to a better understanding of immune-to-brain communication and may lead to the development of therapeutic intervention approaches for neurodegenerative diseases. In addition, cytokine concentrations might also be used as an early indicator for inflammatory injury [218]. Continuous or repeated measurement of the concentration of the cytokine IL-6 in serum can help in the monitoring and treating of inflammatory injury. Furthermore, it has been suggested that the cytokines IL-6 and IL-10 can be used as biomarkers for Systemic Lupus Erythematosus [9]. However, the monitoring of several cytokines poses significant challenges due to the low physiological concentration levels and the large concentration variations. The concentration of some cytokines, e.g. IL-6, are normally in the sub-picomolar range but can increase by 3 orders of magnitude as a result of infection [219; 220]. Furthermore, the required sample and reagent volumes should be kept as low as possible because the available sample volume is often limited [8]. This is especially important for the analysis of blood from neonates and animal models, e.g. mouse models, where the sample volume is limited to the low microlitre range, or for the analysis of difficult to obtain samples such as cerebrospinal fluid [22]. The available detection systems are either not sensitive enough to detect these low cytokine concentrations or require large sample volumes ($> 100\,\mu$l) so that continuous monitoring is not feasible. Furthermore, the simultaneous measurement of many different cytokines from small sample volumes would greatly increase the reliability and robustness of the diagnosis because cytokines can have overlapping functions [221].

To address these issues the multisensor from Hua et al. [21] is combined with the optimised microfluidic design from section 5.6. The multisensor consists of a waveguide chip onto which a microfluidic flow cell is bonded and uses an indirect competitive assay which was described in section 3.5. Briefly, the target analyte is pre-incubated with a matching capture antibody which is fluorescently labelled. After the mixture reaches the equilibrium it is flowed through the microfluidic flow cell where the unbound capture antibodies interact with the surface immobilised receptors. Finally, the evanescent field of the waveguide which extends about 100 nm into the flow cell excites the fluorescent labels of the surface bound capture antibodies and the emitted light from the fluorophores is detected by a CCD camera (section 2.5). The multisensor

has 32 sensor windows which can be functionalised with different receptors so that the system can simultaneously detect 32 different analytes. The multisensor has achieved a limit of detection of $1\,\mathrm{ng\,l^{-1}}$ for estrone which is an environmental contaminant in freshwater reservoirs. Estrone has a molecular weight of 270.4 Da so that this detection limit corresponds to a bulk concentration of 3.7 fM. This limit of detection would enable the multisensor to detect physiological levels of cytokines without preconcentration or amplification steps. However, drawbacks of the system are the relatively large sample consumption of 1 ml and the low capture fraction of less than 0.01 (see section 5.4). Here the flow cell is redesigned according to the design guidelines from section 5.6. The new design reduces the sample consumption to the low microlitre range which makes more frequent monitoring of the cytokine level feasible.

The combination of the waveguide sensor with the improved fluidics poses a variety of challenges ranging from the detection system over the device fabrication to the modelling and data analysis. The contributions here are in the design, modelling and analysis of the system. However, to present a complete picture of the proposed device a brief description of the other aspects is provided. The combination of all research elements will yield a highly sensitive and easy to use device for the simultaneous detection of multiple analytes at physiological levels.

6.2 Literature review - immunoassays for cytokine detection

Immunoassays which are based on the affinity interaction of antibodies with antigens, chemicals, viruses or cells are used to detect the presence and quantity of target analytes (section 2.2). Immunoassays for the detection and quantification of multiple cytokines from small sample volumes have to fulfil many requirements to be of great value. The main requirement is a low limit of detection so that the physiological concentration levels which are in the picomolar range [219; 220] can be reliably monitored. Furthermore, assay formats which allow for the detection of multiple analytes simultaneously are beneficial because it has been shown that different cytokines have overlapping func-

tions and can regulate the expression levels of other cytokines. For these reasons it is beneficial to monitor several cytokines simultaneously to get a more complete picture of the biological system [221]. Finally the device should be easy to use, fast, cost-effective and amenable for automation. Integrating immunoassays into microfluidic lab-on-a-chip systems has the potential to fulfil many of these requirements [8] (chapter 2). Besides the obvious advantages of reduced sample consumption and decreased analysis time microfluidic systems offer improved repeatability and sensitivity as well as the potential for automation and multiplexing.

One of the most widely used immunoassays is the enzyme-linked immunosorbent assay (ELISA) which is shown schematically in figure 6.1. Commercial ELISA kits containing all required reagents are available from a range of suppliers, e.g. BD Biosciences (San Jose, USA) and R&D Systems (Minneapolis,USA). In an ELISA the target analyte is captured via a capture antibody to the surface of the well plate. After the

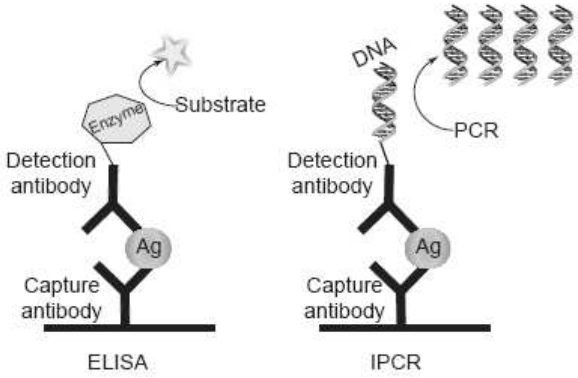

Figure 6.1: (left) ELISA and (right) immuno-PCR detection. Reprinted from [222] with permission from Elsevier.

immobilisation a detection antibody which binds to the target is added. Finally, an enzyme which is linked to this detection antibody transforms a suitable substrate into chromogenic or fluorogenic product. This transformation of the substrate into product is an amplification step which allows the sensitive detection down to physiological levels. ELISA's have been used to detect different cytokines with a limit of detection below $10\,\mathrm{pg\,ml^{-1}}$ [223]. However, the high sensitivity comes at the price of high sample consumption ($\sim 100\,\mu\mathrm{l}$), long assay times (hours) and a labour-intensive protocol with multiple pipetting steps. The high sample consumption and the lack of multiplexing can

be partially overcome by an array-based ELISA [224]. Here the patterning of an array of capture antibodies in one sample well allows the simultaneous detection of multiple cytokines. These microarray assays which have been implemented for most assay types allow the detection of the coordinated levels of multiple cytokines while keeping the sample consumption and assay times low [16]. Commercially available microarray systems (Randox Laboratories Ltd., Crumlin, UK) which use chemiluminescence imaging achieve a detection limit between $0.12\,\mathrm{pg\,ml^{-1}}$ and $2.12\,\mathrm{pg\,ml^{-1}}$ for 12 human cytokines in serum [225].

A further commercially available system which achieves almost the same sensitivity as an ELISA but with much reduced sample consumption is the Bio-Plex system from Bio-Rad (Bio-Rad Laboratories Ltd., Hemel Hempstead, UK). This system consists of 100 color-coded beads which can be conjugated with different capture antibodies so that 100 different analytes can be analysed simultaneously. The system employs a sandwich assay where the target analytes are first captured on the beads by the capture antibodies and then labelled through a detector antibody. The color-coded beads are then flowed through a flow cytometer. In the flow cytometer the color-coded beads with the captured analytes are interrogated by two laser beams: a green laser excites the fluorophores attached to the detector antibodies which allows the quantification of the captured analyte, a red laser excites the fluorophores in the beads which allows the identification of the bead and therefore the analyte. A comparative study of 15 human cytokines showed that the Bio-Plex systems achieves a dynamic range between 4 and $5000\,\mathrm{pg\,ml^{-1}}$ for many cytokines [226]. The Bio-Plex system has a slightly lower sensitivity but higher dynamic range than an ELISA.

An approach which uses the polymerase chain reaction (PCR) for the amplification of the signal is immuno-PCR which is shown schematically in figure 6.1. Here the analyte of interest is usually captured by a surface immobilised capture antibody and a second detection antibody, which is tagged with a DNA marker, is used to sandwich the analyte [222]. Once the detection antibody is bound to the target analyte the DNA marker is amplified by PCR. This approach can be multiplexed by providing a distinct DNA marker for every analyte of interest [227]. This method is often called the 'bio-barcode assay' and has been used to detect the cytokine IL-2 with 30 aM

sensitivity [228]. A similar approach of DNA amplification is called rolling-circle amplification (RCA) [229]. This approach is shown schematically in figure 6.2. Here a DNA

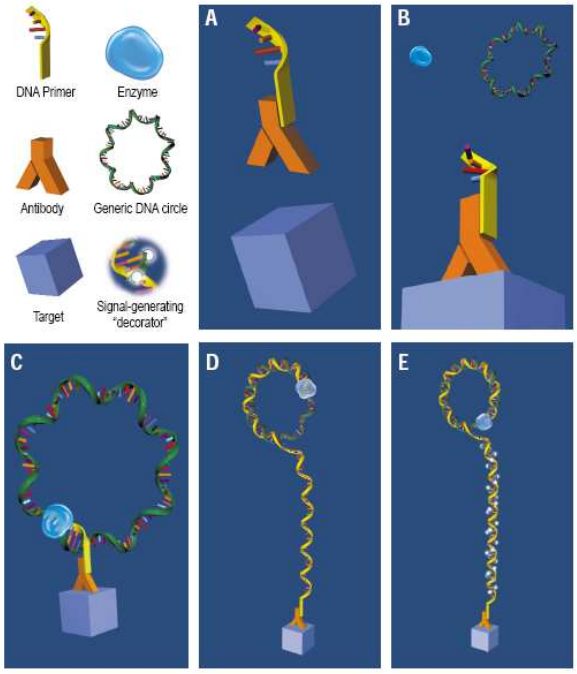

Figure 6.2: Cytokine detection by rolling-circle amplification. Reprinted by permission from Macmillan Publishers Ltd: Nature Biotechnology [229], copyright 2002.

primer which is attached to the detection antibody hybridises to a circular DNA strand which gets multiplied by PCR. This results in a long DNA strand to which complementary fluorescent oligonucleotides can be hybridised. This technique is compatible with DNA microarray equipment and analysis methods. RCA has been used on multiplexed protein microarrays to enhance the measurement of 75 cytokines expressed by human dendritic cells. For 60 % of the cytokines they achieve a sensitivity $\leq 10\,\mathrm{pg\,ml^{-1}}$ and a dynamic range over 3 orders of magnitude. This high sensitivity is achieved from complex analyte mixtures and simultaneously for 38 cytokines in each subarray. Recent reviews show that immuno-PCR technologies are very sensitive, quantitative and reproducible [222; 230]. However, the long assay times as well as the complex instrumentation and assay protocol prevent its wide spread clinical use.

A further technique which uses PCR amplification is the proximity ligation assay [231]. Here two proximity probes, e.g. antibodies, bind pairwise to the target analyte. Attached to these proximity probes are oligonucleotide sequences which can

hybridise through an added connector oligonucleotide. The proximity of the two oligonucleotides increases their local concentration by a factor of 10^6 and accordingly their ligation. The ligated oligonucleotides are amplified by PCR while unbound oligonucleotides are not amplified. A proximity ligation assay was used to detect cytokines with femtomolar sensitivity ($10\,\mathrm{fg\,ml^{-1}}$) in $1\,\mu$l samples [232]. The assay is very sensitive due to the dual binding and very robust because no wash or separation steps are needed. However, it has the same drawbacks as the other PCR-type methods including the requirement for complex instrumentation and long assay times.

The commercial Biacore system, where surface plasmon resonance (SPR) (see section 2.5) is the physical sensing approach used, has been applied to the detection of IL-8 in human saliva down to a concentration of 0.25 nM or $2.1\,\mathrm{ng\,ml^{-1}}$ [233]. The system was stable for 150 cycles and each assay time is as low as 13 minutes. A sensor based on fiber-optic SPR, where the surface plasmons propagate along a metal coated fibre, was shown to have a detection limit for IL-1, IL-6 and TNF-α in buffered saline solution and in cell culture medium down to $1\,\mathrm{ng\,ml^{-1}}$ which allows the quantification of the cytokine levels in nonhealing wounds [234]. While the sensitivity of SPR systems is $2-3$ orders of magnitude lower than the sensitivity for some of the labelled methods, such as immuno-PCR or fluorescence based methods, SPR systems have the advantage of simple, label-free operation and short analysis times.

An approach based on a commercially available waveguide chip was previously reported for the detection of 8 different human cytokines [42]. In this approach a microarray was spotted onto the waveguide chip. After the receptor immobilisation a microfluidic structure is bonded onto this waveguide chip. The microfluidic structure contains 6 flow cells and is compatible with the fluid handling for 96 well plates so that the sample solution and the other reagents can be pipetted either manually or by an automated fluid handling robot. The system uses a sandwich assay where the target analyte is sandwiched between a capture antibody and a fluorescently labelled detection antibody. The fluorophores attached to the detection antibodies are excited by the evanescent field of the waveguide. The resulting fluorescence is detected by a fluorescence reader. This system achieved a detection limit of $15\,\mathrm{pg\,ml^{-1}}$ for all tested cytokines from $20\,\mu$l of sample. However, the assay took several hours to complete and

requires complex instrumentation, i.e. a fluid handling robot.

A different approach for the detection and quantification of cytokines is based on the separation of the analytes by chip-based electrophoresis. In chip-based electrophoresis multiple analytes from a small sample are separated based on their mass-to-charge ratio [22] (section 4.2). The combination of electrophoresis with immunoaffinity capture and laser-induced fluorescence detection allowed the detection of 6 cytokines from less than $1\,\mu$l of sample with a detection limit of $2\,\mathrm{pg\,ml^{-1}}$ in less than 2 minutes. The immunoaffinity capture step which is performed before the electrophoresis step separates the target cytokines from the rest of the sample. This reduces the complexity of the sample and enhances the sensitivity of the detection. Advantages of this approach are the fast analysis times, low sample consumption and inherent multi-analyte detection. However, electrokinetic methods require large voltages which increase the complexity of the instrumentation and can lead to adverse effects such as water electrolysis, metallic ion injection and bubble formation [3].

Table 6.1 summaries the different methods for the detection and quantification of cytokines. While a low limit of detection (LOD) and a small sample size of the assay

	LOD	Sample size	Multiplexing	Complexity	Time	Reference
ELISA	$10\,\mathrm{pg\,ml^{-1}}$	$100\,\mu$l	microarray	medium	hours	[223]
Bio-Plex	$5\,\mathrm{pg\,ml^{-1}}$	$70\,\mu$l	inherent	medium	hour	[226]
Immuno-PCR	$10\,\mathrm{pg\,ml^{-1}}$	$10\,\mu$l	microarray	high	hours	[229]
Barcode	$1\,\mathrm{fg\,ml^{-1}}$	$< 20\,\mu$l	inherent	high	hours	[228]
Proximity	$10\,\mathrm{fg\,ml^{-1}}$	$1\,\mu$l	inherent	high	hours	[232]
SPR	$2\,\mathrm{ng\,ml^{-1}}$	$100\,\mu$l	microarray	low	minutes	[233]
Waveguide	$15\,\mathrm{pg\,ml^{-1}}$	$15\,\mu$l	microarray	medium	hours	[42]
Separation	$2\,\mathrm{pg\,ml^{-1}}$	$< 1\,\mu$l	inherent	medium	minutes	[22]

Table 6.1: Comparison of the characteristics of various techniques for cytokine detection.

are necessary for the quantification of low levels of cytokines, the other three properties are important for the wide spread applicability of the assay. Methods with 'inherent' multiplexing can detect multiple cytokines simultaneously without further instrumentation, i.e. the barcode assay has a different marker for every analyte of interest, while

the other methods rely on microarray approaches for multiplex detection of different cytokines. The column 'Complexity' refers to the complexity of the assay instrumentation and protocol. The method relying on electrophoretic separation fulfils the requirements on sensitivity, sample size, assay time and complexity of the assay instrumentation and protocol but the applied large voltages can make it unsuitable for some applications. None of the remaining methods fulfil all the desired characteristics. All the PCR-type methods have sufficient sensitivity but require complex systems and have long assay times. On the other hand, the widely used ELISA and SPR methods require sample sizes that are larger than practically feasible. The presented waveguide system has a sufficiently low LOD but uses only a simple flow cell so that the sample requirements and assay times are too large. However, the application of the design guidelines from chapter 5 to the flow cell of the waveguide system has the potential to lead to an efficient and sensitive system.

6.3 Device design and modelling

6.3.1 Design of the microfluidic channel

For the sensitive detection of cytokines the microfluidic flow cell has to be designed with the aim of high capture fraction and uniform analyte mass transfer to the sensor surface and subsequent association along the length of the sensor (section 5.4). In this section the results from chapter 5 are applied to the design of the microfluidic flow cell, the corresponding sensor patches and the operating parameters. The aim of this design is the reduction of the sample consumption to the low microlitre level while retaining the excellent sensitivity, ease of use and the short assay time of the original multisensor.

The design of the microfluidic system is constrained by the design of the existing waveguide chip whose schematic is shown in figure 6.3. A single 2.5 μm wide waveguide is split into four branches by three Y splitters and then broadened to a 30 μm or 60 μm wide waveguide. The broadening increases the usable sensor patch area and reduces the optical density which reduces the rate of photobleaching. The separate waveguide branches are 1 mm apart. The whole surface of the waveguide chip except the sensor

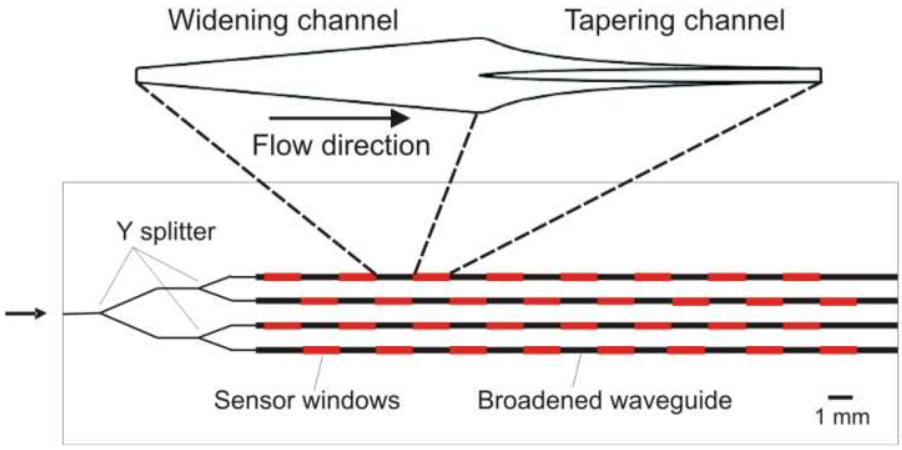

Figure 6.3: Schematic of the waveguide chip adapted from [21] and of one sensor element which consists of a widening channel region and a tapering channel region.

windows is covered by a 1 μm thick silica isolation layer which prevents the light from leaking out of the waveguide. The sensor windows are 1.5 mm long, 0.3 mm wide and 1.5 mm separated. A microfluidic flow cell is placed on top of the waveguide chip as shown in figure 5.4.

The original flow cell which covered all four waveguides simultaneously was 5 mm wide and was about 35 μm high. In this setup only about 5% of the analyte molecules are flowed over the sensor patches while the rest passes between the four waveguide branches. One measurement (with the original flow cell) required about 1 ml of sample and less than 1% of the available analyte molecules can theoretically bind at the sensor patches, see section 5.4 for details. The proposed, redesigned flow cell which mimics the underlaying waveguides is shown in figure 6.4. From a single inlet the flow channel is split up into four separate channels by three Y splitters. The inset of figure 6.4 shows a zoomed in view of the inlet which clearly shows the Y splitters and the first sensor elements. The rounded corners in the Y splitters ensure a more uniform flow compared to channels with sharp turns where the flow velocity goes to zero in the outer corners. After the Y splitters each channel has 8 sensor elements which were described in section 5.6.2. Briefly, each sensor element is 3 mm long and designed to fit over the waveguide and the sensor windows (see figure 6.3). The sensor elements consist of a 1.5 mm long widening region and a 1.5 mm long tapering region. The width of both the inlet and outlet is 60 μm which enables the sequential configuration of several sensor

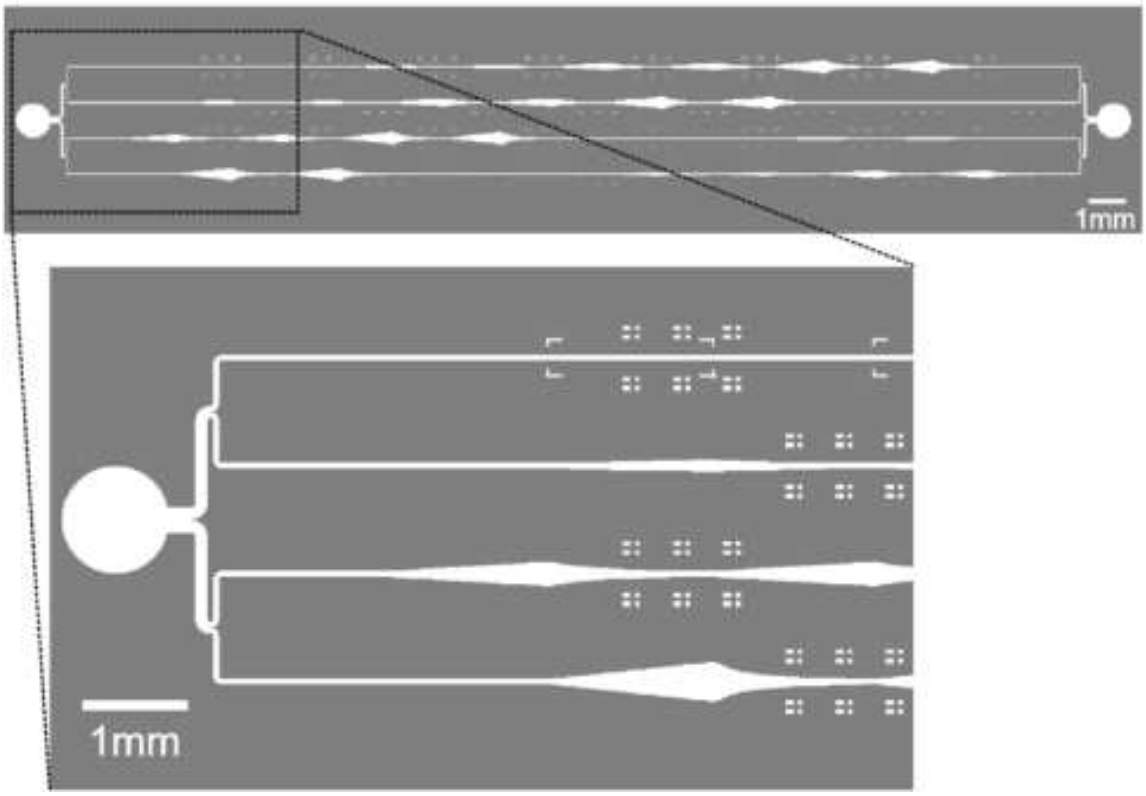

Figure 6.4: Schematic of the photomask for the microfluidic flow cell. The inset shows a zoomed in view of the channel inlet.

elements. Each channel in this photomask has 2 sensor elements each with inlet-to-outlet ratios, which are the ratios between the width at the widest part of the sensor element and the exit of the sensor element, of 1, 2, 4 and 6, respectively. The order of the different sensor elements varies between the 4 channels. The proposed channel width of 60 μm means that the channels fit exactly over the widest waveguide. In this configuration every analyte molecule is flowed over the sensor patches which increases the capture fraction of the device. After the 8 sensor elements in each channel the four channels are combined to a single outlet channel. Using a single inlet and outlet simplifies the connection between the macro and the micro world. To achieve the same flow rate in each of the four parallel channels the flow resistances in the four channels have to be equal. The easiest way to achieve this is by having sensor elements with the same inlet-to-outlet ratios in each of the four channels, e.g. each channel has two sensor elements with inlet-to-outlet ratio 4 and six sensor elements with inlet-to-outlet ratio 8. However, the sensor elements can be in an arbitrary order because the total

flow resistance of each channel is the sum of the flow resistances of the sensor elements.

Following the redesign of the planar layout of the flow cell, the height of the flow cell and the flow velocity are considered. This redesign of the channel height and flow velocity is based on the Graetz number and the reaction/convection number which were introduced in chapter 3 and are repeated here

$$\mathrm{Gz} = \frac{H^2 U}{LD} \tag{6.1}$$

$$\zeta = \frac{k_a L X_0}{HU} \tag{6.2}$$

The original flow cell was about $35\,\mu$m high and the sample was pumped through the system with an average flow velocity of $14\,\mathrm{mm\,s^{-1}}$. The resulting system was mass-transfer limited. For an association rate constant $k_a = 5 \times 10^5\,\mathrm{M\,s^{-1}}$ less than 5% of the analyte which is flowed over the sensor patch will be captured. The main problem of the original design is the high Graetz number ($\mathrm{Gz} \approx 200$) which prevents the majority of the analytes from reaching the sensor surface, see figure 5.6. To increase the fraction of analytes that can reach the sensor surface the Graetz number has to be reduced (see section 5.4). The most feasible way to reduce the Graetz number is by decreasing the channel height or the average flow velocity. The results of chapter 5 show that for an efficient system the Graetz number should ideally be below 1 which would allow each analyte molecule to reach the active sensor surface. The second problem is a low value of the reaction/convection number which is related to the capture fraction by equation 5.8. The capture fraction increases with the reaction/convection number and for $\zeta = 1$ approximately 60% of the analyte molecules bind to the active sensor surface. The reaction/convection number can be increased by a reduction of the channel height and the average flow velocity. The feasible range of channel heights and flow speeds which guarantee $\mathrm{Gz} < 1$ and $\zeta > 1$ is shown in the left plot of figure 6.5 for one set of the other parameters. The two lines define the boundary at which $\mathrm{Gz} = 1$ and $\zeta = 1$, respectively. A combination of channel height and flow velocity to the left of both lines creates a system where $\mathrm{Gz} < 1$ and $\zeta > 1$.

Figure 6.5 shows that a further reduction of the channel height and flow velocity creates a system with a small Graetz number and high reaction/convection number so that a capture fraction of 1 can be achieved. However, this further reduction would

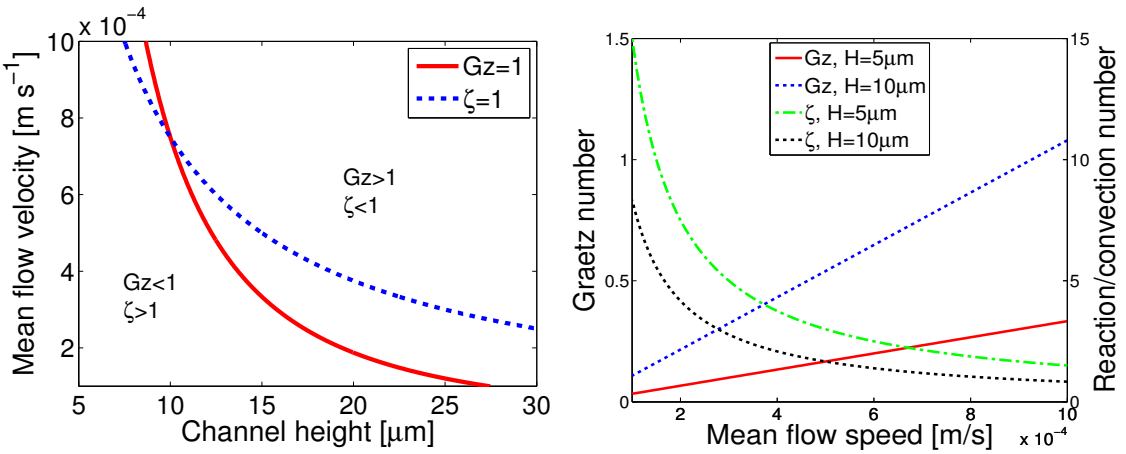

Figure 6.5: (left) Feasible range of channel heights and flow speeds. The region to the left of both lines guarantees sufficiently fast diffusion to the surface and a large capture fraction. (right) Graetz number and reaction/convection number for various flow rates and channel heights. Parameters: $D = 5 \times 10^{-11}\,\mathrm{m^2\,s^{-1}}$, $k_a = 5 \times 10^5\,\mathrm{M^{-1}\,s^{-1}}$, $L = 1.5 \times 10^{-3}\,\mathrm{m}$, $X_0 = 10^{-8}\,\mathrm{mol\,m^{-2}}$

increase the assay time considerably. For example, for the smallest shown channel height of $5\,\mu$m and the smallest average flow velocity of $10^{-4}\,\mathrm{m\,s^{-1}}$ it takes about 5 hours for a sample plug of $2\,\mu$l to be pumped through the microfluidic channel. It is therefore not practical to further reduce the channel height or flow velocity. Because the Graetz number is proportional (i) to the square of the channel height and (ii) to the flow velocity, it is better to reduce the channel height to achieve a smaller Graetz number. Thus the Graetz number is reduced and the assay time is as short as possible. However, there are practical limits for the channel height; the probability of blockage in microfluidic channels increases with decreasing channel height. Here channel heights below $5\,\mu$m were not considered.

The right plot in figure 6.5 takes a closer look at the Graetz number and the reaction/convection number for fixed channel heights of $5\,\mu$m and $10\,\mu$m and flow velocities between 10^{-4} and $10^{-3}\,\mathrm{m\,s^{-1}}$. A channel height of $10\,\mu$m allows the use of a flow velocity up to $7.5 \times 10^{-4}\,\mathrm{m\,s^{-1}}$ which would decrease the assay time to about 20 min. The reaction/convection number for this setup is 1. Depending on the actual values of k_a and X the flow velocity could be reduced further to achieve a sufficiently high reaction/convection number though this would increase the assay time.

6.3.2 Assay design

The assay format in the original multisensor is an indirect competitive assay, see section 3.5, which will also be used in the detection and quantification of cytokines. Briefly, the target cytokines (analyte) are mixed with their antibodies (receptor) which are labelled with the fluorophore Cy5.5. The mixture is given time to reach equilibrium. In the second step the mixture is flowed through the integrated microfluidic affinity sensor where the unbound antibodies can bind to the matching cytokines which are immobilised at the sensor surface. The interactions are represented by the following equations

$$A + X \underset{k'_d}{\overset{k'_a}{\rightleftharpoons}} X_b \tag{6.3}$$

$$X + A_i \underset{k_d}{\overset{k_a}{\rightleftharpoons}} B \tag{6.4}$$

where A, X, X_b, A_i and B are the concentrations of the cytokine molecules, antibody molecules, cytokine-antibody complex, surface immobilised cytokine molecules and the surface immobilised cytokine-antibody complex, respectively. The association and dissociation rate constants between the antibody molecules and the surface immobilised cytokines are given by k_a and k_d, respectively, while the association and dissociation rate constants between the antibody molecules and the free cytokines are given by k'_a and k'_d, respectively.

The interaction between the cytokines and the antibodies described by equation 6.3 takes place in a closed system without flow and can thus be described by the equations for the stagnant and well-mixed systems from section 3.4.1. Equation 6.3 is translated into a differential equation for the concentrations

$$\frac{\partial X_b}{\partial t} = k'_a A X - k'_d X_b \tag{6.5}$$

In a closed system the concentrations of the cytokine and antibody molecules are linked to the concentration of the bound cytokine-antibody complex X_b by $A = A_0 - X_b$ and $X = X_0 - X_b$. This allows the analytical calculation of the equilibrium solution of equation 6.5

$$X_b = \frac{1}{2}(\mathrm{K_d}' + A_0 + X_0) - \sqrt{\frac{1}{4}(\mathrm{K_d}' + A_0 + X_0)^2 - A_0 X_0} \tag{6.6}$$

with the dissociation constant $\mathrm{K_d}' = k_d'/k_a'$. The interaction between the free antibodies and the surface immobilised cytokines described by equation 6.4 depends on the transport of the antibodies in the bulk of the channel and on the antibody-cytokine interaction at the active surface. The transport in the bulk of the channel can be described by the convection-diffusion equation 4.1 and the association at the active surface can be described by the differential equation 4.3. In this case the governing equations are given by

$$\frac{\partial X}{\partial t} + (\mathbf{u} \cdot \bigtriangledown) X = D \bigtriangledown^2 X \tag{6.7}$$

$$\frac{\partial B}{\partial t} = k_a A_i X - k_d B \tag{6.8}$$

Here it is assumed that X only changes due to interactions with the surface immobilised cytokines and that the concentration of the cytokine-antibody complex X_b stays constant. This is a reasonable assumption because the timescale for the dissociation of the cytokine-antibody complex is much larger than the residence time of the cytokine-antibody complex over the sensor patch.

In contrast to the systems considered in chapter 4 and 5 the sample plug in this system is much larger than the sensor length. For a $2\,\mu$l sample volume in the above described geometry ($H = 10\,\mu$m, $W = 60\,\mu$m, $L = 1.5\,$mm) the sample plug is about $L_{plug} = 0.83\,$m long. The sample plug is much longer than the sensor area so that even for a high value of the adsorption constant κ the number of immobilised cytokine molecules might be on the same order as the number of antibody molecules. In this case the concentration of the free surface immobilised cytokines can not be assumed to be constant. In fact, depending on the antibody concentration and the dissociation constant a large percentage of the surface immobilised cytokine molecules can be occupied. Due to this, the asymptotic solutions presented in section 3.4, which are only valid for systems with a constant concentration of surface immobilised receptors, are not applicable here and the analysis requires full numerical simulations.

The numerical simulations are computationally expensive and give only information about one set of parameter values and thus it is beneficial to calculate the equilibrium solution of equation 6.8 which acts as a boundary case. The system is modelled as a stagnant and well-mixed system where the entire sample plug is above the sensor

surface so that every antibody molecules can associate with the surface immobilised cytokines. In this model the antibody concentration X and the concentration of the surface immobilised cytokine-antibody complex are linked by

$$X = X_0 - X_b - \frac{BL}{HL_{plug}} \tag{6.9}$$

where X_0 is the initial antibody concentration and X_b the concentration of the bulk cytokine-antibody complex. Here the concentration of surface immobilised cytokine-antibody complex B had to be transformed into a bulk concentration and scaled by the ratio of the sensor patch length and the plug length. In this situation, where the entire sample plug is above the sensor surface, this scaling corresponds to a transformation of the channel height H into an effective channel height

$$H_e = H\frac{L_{plug}}{L} \tag{6.10}$$

For a sample volume of $2\,\mu$l and a channel height of $10\,\mu$m the effective channel height is $H_e = 5.6\,$mm. This adjustment is rather crude and might underestimate the actual surface immobilised cytokine-antibody complex concentration. This is because, in the dynamic case, the antibody solution is continuously replenished at the channel inlet and this will lead to a higher bound concentration at the channel inlet. Despite these shortcomings the equilibrium solution for this effective channel height model gives valuable information about the system behaviour and can be used to find suitable starting parameters for full numerical simulations.

The surface concentration of free, surface immobilised cytokines is given by $A_i = A_{i0} - B$ where A_{i0} is the total surface concentration of surface immobilised cytokines. In this case the equilibrium solution of equation 6.8 is given by

$$B = \frac{1}{2}(H_e(\mathrm{K_d} + X_0 - X_b) + A_{i0}) - \sqrt{\frac{1}{4}(H_e(\mathrm{K_d} + X_0 - X_b) + A_{i0})^2 - H_e A_{i0}(X_0 - X_b)} \tag{6.11}$$

with the dissociation constant $\mathrm{K_d} = k_d/k_a$. This equation together with equation 6.6 can be used to calculate the sensor response for different antibody and cytokine concentrations. The dose-response curve, which depends on the surface immobilised cytokine concentration as well as on the antibody concentration, is shown in figure 6.6. Physiological cytokine concentrations (see section 6.1) are in the left, almost constant

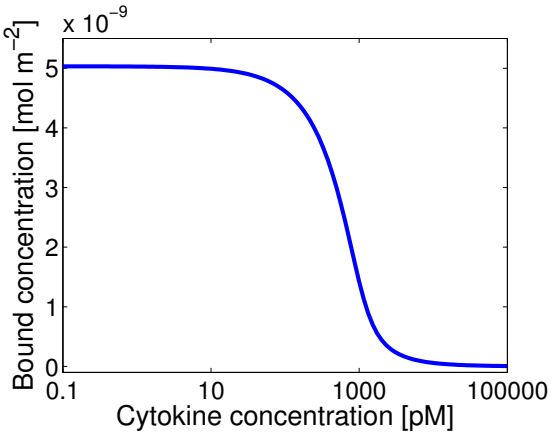

Figure 6.6: Concentration of surface immobilised cytokine-antibody complex B for cytokine concentrations A_0 between 0.1 pM and 100 nM. The surface immobilised cytokine-antibody complex B is calculated in two steps: first, X_b is calculated from equation 6.6; second, B is calculated from equation 6.11. Parameters: $A_{i0} = 10^{-8}\,\mathrm{mol\,m^{-2}}$, $H_e = 5.6\,\mathrm{mm}$, $\mathrm{K_d} = \mathrm{K_d}' = 0.1\,\mathrm{nM}$, $X = 1\,\mathrm{nM}$

part of the curve which shows only a small change in the bound concentration compared to the blank sample.

From now on it is assumed that the dissociation constants for the interaction between the cytokine and antibody molecules are the same for free and surface immobilised cytokines. Thus the dissociation constant for both reactions is $\mathrm{K_d}$. This assumption simplifies the presentation of the results. Figure 6.7 shows the difference in the surface immobilised cytokine-antibody complex concentration between a blank sample and various cytokine concentrations calculated with equations 6.6 and 6.11 over the antibody concentration X. The different plots of figure 6.7 are for three values of the dissociation constant $\mathrm{K_d}$ which cover the range of reported dissociation constants for various cytokines with cytokine antibodies [234]. The figure indicates that the optimal antibody concentration, i.e. the antibody concentration which gives the largest change in bound concentration, is independent of the cytokine concentration. On the other hand, the magnitude of the difference between the blank and the various cytokine concentrations depends on the dissociation constant and the cytokine concentration. Furthermore, the optimal antibody concentration depends on the dissociation constant as can be seen in the middle and right plots where the maximal change in bound concentration is given for

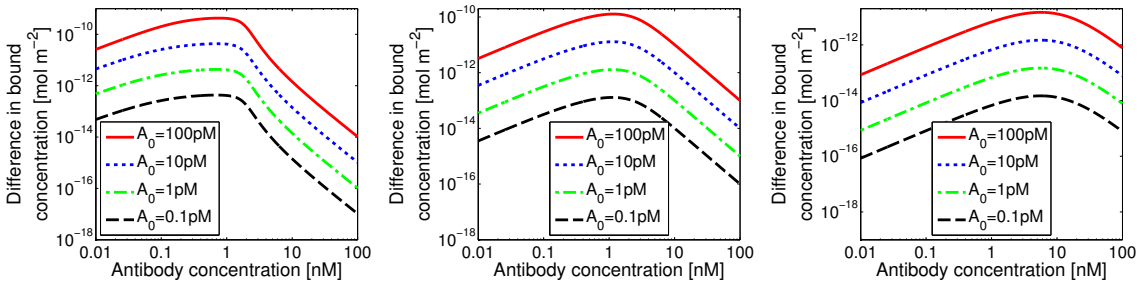

Figure 6.7: Difference in the surface immobilised cytokine-antibody complex concentration between blank and various cytokine concentrations for three different dissociation constants: (left) $K_d = 0.1\,nM$, (middle) $K_d = 1\,nM$, (right) $K_d = 10\,nM$. Parameters: $H_e = 5.6\,mm$, $A_{i0} = 10^{-8}\,mol\,m^{-2}$

$X_0 \approx K_d$. This relationship breaks down for $K_d = 0.1\,nM$ due to depletion of the antibody concentration, see the left plot of figure 6.7. A further decrease of the dissociation constant or an increase in the surface immobilised cytokine concentration has almost no effect on the change of surface immobilised cytokine-antibody complex concentration.

In contrast to label-free detection methods such as SPR where the absolute change in bound concentration is the most important parameter, the relative change in bound concentration is at least as important in fluorescence based assays as discussed in section 2.5. Here the number of fluorophores per antibody molecule can be increased to amplify the signal. Figure 6.8 shows the relative change in immobilised cytokine-antibody complex concentration calculated with the simplified model. It can be seen in figure 6.8 that the

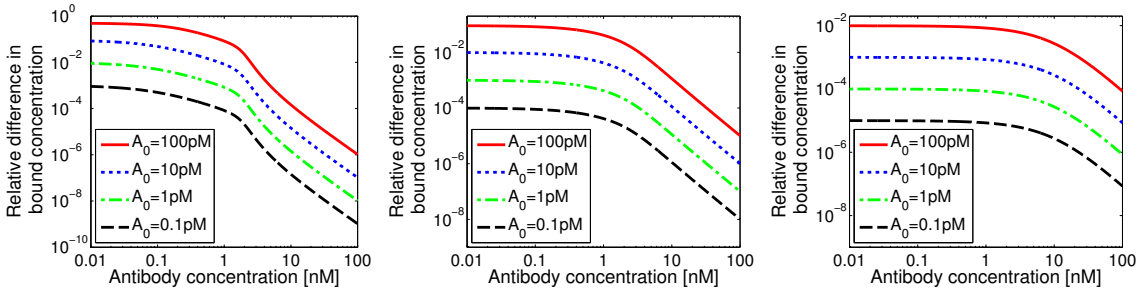

Figure 6.8: Difference in the surface immobilised cytokine-antibody complex concentration between blank and various cytokine concentrations relative to the surface immobilised cytokine-antibody complex concentration for the blank. The plots show the relative difference for different dissociation constants: (left) $K_d = 0.1\,nM$, (middle) $K_d = 1\,nM$, (right) $K_d = 10\,nM$. Parameters: $H_e = 5.6\,mm$, $A_{i0} = 10^{-8}\,mol\,m^{-2}$

relative difference in immobilised cytokine-antibody complex concentration decreases with the antibody concentration and thus a low antibody concentration provides the largest relative change in bound concentration. However, the decrease in the relative difference in the bound concentration is negligible for antibody concentrations below the dissociation constant. In practical applications the antibody concentration should be chosen just below the dissociation constant. This guarantees a large relative and absolute change in bound cytokine-antibody complex concentration. The latter reduces the required number of fluorophores per antibody molecule which decreases the influence of the potentially noisy amplification, i.e. the number N of fluorophores per antibody molecule is not deterministic but rather given by a statistical distribution with a mean of N.

The simplified analytical solution given by equations 6.6 and 6.11 is used to pick the antibody concentration with the maximal change in bound cytokine-antibody complex concentration. For example, for $\mathrm{K_d} = 0.1\,\mathrm{nM}$ an antibody concentration of $\sim 0.7\,\mathrm{nM}$ gives the largest change in the bound concentration, i.e. $4.3 \times 10^{-12}\,\mathrm{mol\,m^{-2}}$ for a cytokine concentration of $A_0 = 1\,\mathrm{pM}$. This is compared with FEM simulations for the rectangular and the tapering channels. These simulations are performed with the top view model which is described in appendix B.2. The difference in bound concentration for a range of antibody concentrations is shown in table 6.2. The difference in the bound concentration for these numerical simulations corresponds very well with the simplified model. However, the antibody concentration which gives the maximal difference in the immobilised cytokine-antibody complex concentration between a blank sample and a 1 pM cytokine concentration is slightly lower than for the simplified model. This is due to the simplifying assumptions of a stagnant and well-mixed system in equilibrium. Nevertheless, the comparison shows that the simplified model gives valuable information about the optimal antibody concentration for the detection of a given cytokine-antibody system.

A further result of the numerical simulations is that the difference in the bound concentration in the tapering channel geometry is about 5 % higher than for the rectangular channel. This result was not expected because the tapering channel geometry was originally (see chapter 5) designed for short sample plugs. This shows that the

Antibody concentration [nM]	Rectangular channel $(B_{0pM} - B_{1pM})\,[\mathrm{mol\,m^{-2}}]$	Tapering channel $(B_{0pM} - B_{1pM})\,[\mathrm{mol\,m^{-2}}]$
0.3	3.77×10^{-12}	4.09×10^{-12}
0.5	4.02×10^{-12}	4.25×10^{-12}
0.6	4.08×10^{-12}	4.25×10^{-12}
0.7	3.88×10^{-12}	4.14×10^{-12}
0.9	3.44×10^{-12}	3.92×10^{-12}
1.1	3.13×10^{-12}	3.53×10^{-12}

Table 6.2: Comparison of the difference in the bound concentration between a blank sample B_{0pM} and a sample with a 1 pM cytokine concentration B_{1pM} for the rectangular and the tapering channel geometry. The tapering geometry is given by the sensor element 'algebraic$_4$' as defined in section 5.6.2 and given in figure C.2. Parameters: $A_{i0} = 10^{-8}\,\mathrm{mol\,m^{-2}}$, Gz = 0.67, $H = 10\,\mu\mathrm{m}$, $k_a = 10^6\,\mathrm{M^{-1}\,s^{-1}}$, $k_d = 10^{-4}\,\mathrm{s^{-1}}$, $\mathrm{K_d} = 0.1\,\mathrm{nM}$, $\lambda = 1667\,\mathrm{s}$, $t = 1700\,\mathrm{s}$, $U = 5 \times 10^{-4}\,\mathrm{m\,s^{-1}}$

improved transport of analytes to the sensor patch increases the average bound concentration compared to a rectangular channel as long as the equilibrium is not reached. At equilibrium the average bound concentrations in the rectangular and tapering channels are the same.

6.3.3 Design example

While the flow cell given by figure 6.4 and the design of the device parameters is motivated by the multisensor [21], the results presented in this section can be applied to different sensor systems which employ the indirect competitive assay. For different assay types, e.g. direct competitive assay or sandwich assay, the results from section 6.3.2 have to be adapted while the results from section 6.3.1 are still valid. Here a step by step design example is presented.

It is assumed that the sensor shape and the analyte-receptor pair are fixed so that the sensor length $L = 1\,\mathrm{mm}$, sensor width $W = 200\,\mu\mathrm{m}$, the association rate constant $k_a = 5 \times 10^5\,\mathrm{M^{-1}\,s^{-1}}$, the dissociation rate constant $k_d = 5 \times 10^{-4}\,\mathrm{s^{-1}}$, the concentration

of surface immobilised analyte $A_i = 10^{-8}\,\mathrm{mol\,m^{-2}}$ and the diffusion coefficient $D = 2 \times 10^{-11}\,\mathrm{m^2\,s^{-1}}$ are given. The design is split into two steps: (i) determination of the necessary flow velocity and channel height and (ii) determination of the required antibody concentration X_0.

In the first step the flow velocity U and channel height H are chosen so that the Graetz number which is given by equation 6.1 is below 1 and the reaction/convection number which is given by equation 6.2 is above 1. These requirements can be translated into the following inequalities

$$H^2 U < LD \tag{6.12}$$

$$HU < k_a L X_0 \tag{6.13}$$

For a channel height of $5\,\mu$m which is a feasible channel height with current microfabrication methods the flow velocity in the example considered here has to be below $8 \times 10^{-4}\,\mathrm{m\,s^{-1}}$ where the Graetz number is $\mathrm{Gz} = 1$ and the reaction/convection number is $\zeta = 1.25$. A lower flow velocity will increase the capture fraction of the system but it will also increase the assay time, i.e. the time required for the sample plug to be flowed through the flow cell, which is given by

$$t_{assay} = \frac{Q}{UHW} \tag{6.14}$$

where Q is the sample volume. For a $1\,\mu$l sample plug and a flow velocity of $U = 8 \times 10^{-4}\,\mathrm{m\,s^{-1}}$ the assay time is $t_{assay} \approx 20\,\mathrm{min}$.

In the second step the antibody concentration X_0 is determined from equations 6.6 and 6.11. In this example the dissociation constant is $\mathrm{K_d} = 1\,\mathrm{nM}$ so that the optimal antibody concentration can be determined from the middle plots of the figures 6.7 and 6.8. Here the optimal antibody concentration is given by $X_0 \approx 1\,\mathrm{nM}$.

6.4 Device fabrication and assembly

The proposed device consists of two parts: the waveguide chip and the microfluidic flow cell. These two parts are fabricated separately and only combined at the end of

the fabrication process. The reductions in the channel and sensor patch size compared to the original system increase the requirements on the fabrication of the microfluidic affinity sensor and on the assembly of the device. Especially the alignment of the active sensor patch and the flow channel with the waveguide chip are crucial.

The waveguide chip is taken from the multisensor [21] and is shown schematically in figure 6.3. The cytokine molecules for the active sensor patch have to be attached to the waveguide chip before the waveguide chip and the microfluidic flow cell are combined. This surface functionalisation is performed in-house by Dr. Lucy Braddick and Dr. Patrick Garland. The cytokine molecules are attached to the waveguide surface by microcontact printing, see section 2.4.1. Briefly, an elastomeric stamp is incubated with a solution containing streptavidin molecules. The incubated stamp is then pressed against the substrate to transfer the streptavidin molecules to the substrate. In the next step the substrate is incubated with biotinylated cytokine molecules, i.e. cytokine molecules with an attached biotin molecule. Biotin has very high affinity ($K_d = 10^{-15}\,M$) for streptavidin and thus the cytokine molecules are immobilised at the substrate surface by the biotin-streptavidin interaction. The elastomeric stamp is fabricated by casting of PDMS on a SU-8 master (section 2.3). The master was fabricated in SU-8 10 (MicroChem Corp., Newton, USA) on glass according to the instructions from the manufacturer. The SU-8 is hardbaked to increase the mechanical stability. Sylgard 184 PDMS (Dow Corning Co., Midland, USA) in the usual mixture, 10 parts base elastomer to 1 part curing agent, is poured onto the SU-8 master, degased and cured at 150 °C for 15 min. The PDMS can be peeled of the master straight after the curing. Microcontact printing offers the flexibility for the shape and size of the receptor patch required by the design of the active sensor patches (see figure 5.14).

In contrast to the original system, the sensor patches are smaller than the underlying waveguide and thus have to be aligned to the waveguide. This alignment of the receptor patch as well as the alignment of the microfluidic channel to the waveguide chip are crucial for the efficient and sensitive detection of cytokines. A misalignment in either of the two steps will reduce the capture fraction as well as the uniformity of the association of the antibodies with the surface immobilised cytokine molecules. Here numerical simulations are performed to quantify the effect of misalignment between the receptor

patch and the microfluidic channel.

The misalignment can be a translation along the flow direction, a translation across the flow direction, a rotation or a combination of the three. Table 6.3 and figure 6.9 show simulation results for a perfectly aligned channel and misaligned channels under the assumption that the receptor patch is perfectly aligned to the waveguide chip. A

Alignment	Amount bound [mol]	uniformity
perfect	3.4077×10^{-19}	0.0367
$+10\,\mu$m x-axis	3.4133×10^{-19}	0.0365
$-10\,\mu$m x-axis	3.4016×10^{-19}	0.0370
$+10\,\mu$m z-axis	3.2081×10^{-19}	0.0392
1° rotation	3.2468×10^{-19}	0.0391

Table 6.3: Comparison of the amount of bound antibody molecules and the uniformity of the distribution of associated antibodies at the receptor patch for different alignments. Parameters: $A_{i0} = 10^{-8}\,\mathrm{mol\,m^{-2}}$, $H = 10\,\mu$m, $k_a = 2.4 \times 10^5\,\mathrm{M^{-1}\,s^{-1}}$, $\lambda = 60\,$s, $t = 100\,$s, $U = 4 \times 10^{-4}\,\mathrm{m\,s^{-1}}$, $X_0 = 0.1\,$nM, inlet-to-outlet ratio 3.5.

translation below $10\,\mu$m and a rotation below 1° is well within the achievable alignment accuracy so that the results present a worst-case scenario. From the presented data it is clear that a misalignment across the flow direction or a rotation is worse than a translation along the flow direction. In these cases a part of the receptor patch is not covered by the microfluidic channel which reduces the number as well as the uniformity of the associated antibody molecules. Even in this worst-case scenario the reduction of uniformity and number of associated antibodies is well below 10%.

First the stamp has to be aligned to the waveguide. Figure 6.10 shows a schematic of one PDMS stamp aligned to the waveguide. The alignment marks on the waveguide chip, i.e. the green crosses in the figure, are etched into the glass substrate by ion beam etching, see section 2.3. The alignment marks on the stamp are made from PDMS and thus have the same height as the main part of the stamp. These alignment marks in the PDMS stamp stabilise the stamping onto the glass substrate. This stabilising is important because the stamping has to be performed with uniform force across the

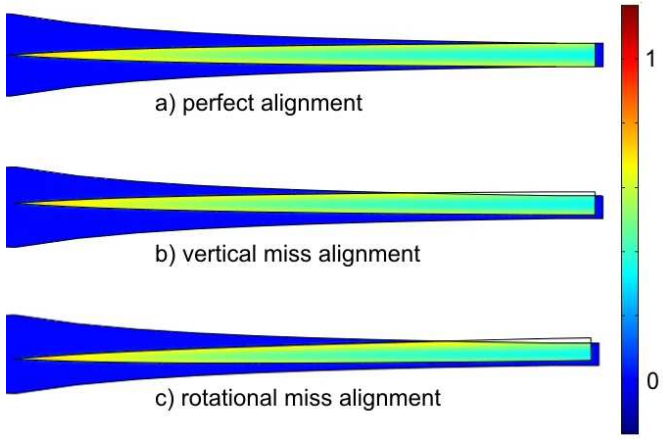

Figure 6.9: Top view of the microfluidic system showing the bound concentration of the antibody on the 'boat-shaped' receptor patch. Comparison of (a) a perfect aligned receptor patch, (b) a 10 μm misalignment across the flow direction and (c) a 1° misalignment around the midpoint of the receptor patch. Parameters: $A_{i0} = 10^{-8}\,\mathrm{mol\,m^{-2}}$, $H = 10\,\mu\mathrm{m}$, $k_a = 2.4 \times 10^5\,\mathrm{M^{-1}\,s^{-1}}$, $\lambda = 60\,\mathrm{s}$, $t = 100\,\mathrm{s}$, $U = 4 \times 10^{-4}\,\mathrm{m\,s^{-1}}$, $X_0 = 0.1\,\mathrm{nM}$, inlet-to-outlet ratio 3.5.

stamp and a parallel alignment of the stamp surface and the waveguide chip. Two pillars at the front of the stamp are added to stabilise the front of the stamp because there are no alignment marks at the front of the stamp. The alignment of the stamp and the waveguide chip is performed in a homemade alignment system, see figure 6.11. The alignment system which was build in-house by Dr. Matt Praeger consists of motorised stages for the $x - z$ direction, a rotational stage and a goniometer to compensate the rotation around the x and z axis. The $x - z$ and rotational alignment is monitored by a microscope. The rotational alignment around the x and z axis is monitored by

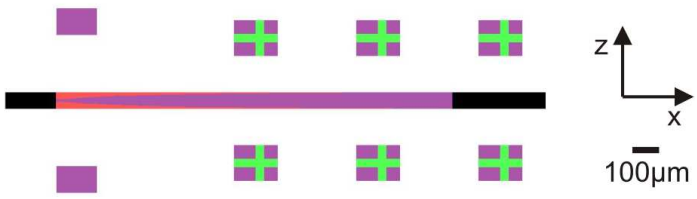

Figure 6.10: Schematic plot of one PDMS stamp (purple) aligned to the alignment marks (green) on the waveguide chip. The waveguide without the silica isolation layer is shown in red, while the silica isolation layer is shown in black.

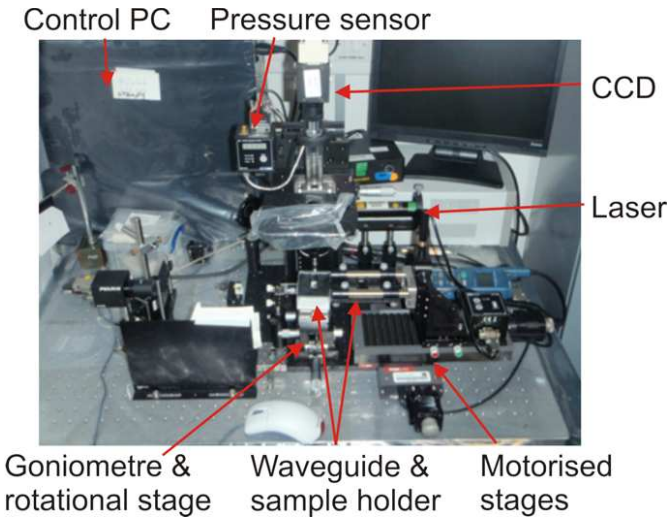

Figure 6.11: Picture of the alignment system.

diffraction patterns; the stamp and substrate are parallel when a circular and centred diffraction pattern appears. After the aligning step the stamp and the waveguide chip are pressed together to transferred the streptavidin molecules from the stamp to the waveguide chip.

The required accuracy for the fabrication of the proposed flow cell is much higher compared to the fabrication of the flow cell for the original multisensor. To achieve the required accuracy the microfluidic flow cell was fabricated by the same method as the PDMS stamp. The photomask shown schematically in figure 6.4 was drawn in L-Edit (Tanner Research, Monrovia, USA) and fabricated by Compugraphics (Compugraphics International Ltd, Glenrothes, Scotland). Microfabrication in PDMS has several advantages compared to other microfabrication methods, see sections 2.3 and 2.4. First, the fabrication is faster and less expensive than traditional silicon or glass fabrication. Second, the sticking properties of PDMS simplify the bonding of the flow cell to the waveguide chip and the fluidic connection to the macro world. The microfabrication produces microfluidic channels with channel dimensions accurate to 1 μm. The channel height can be tuned by a change in the fabrication parameters of the SU-8 master but is very consistent for constant fabrication parameters.

At the inlet and outlet of the channel a hole is punched through the PDMS with a syringe needle, see section 2.4. A capillary is placed in the hole to establish a connection

between the microfluidic channel and the external pump. The punched hole has a diameter roughly equal to the inner diameter of the syringe needle. To achieve a good seal the diameter of the hole should be smaller than the outer diameter of the capillary. A 26 gauge needle which has a nominal inner diameter of 241 μm and a nominal outer diameter of 457 μm is used to punch the holes for the connection of capillaries with outer diameters of 360 μm. Figure 6.12 shows typical microscope images of the entrance and exit of the punched hole. The diameters of the holes are about 250 μm which is in

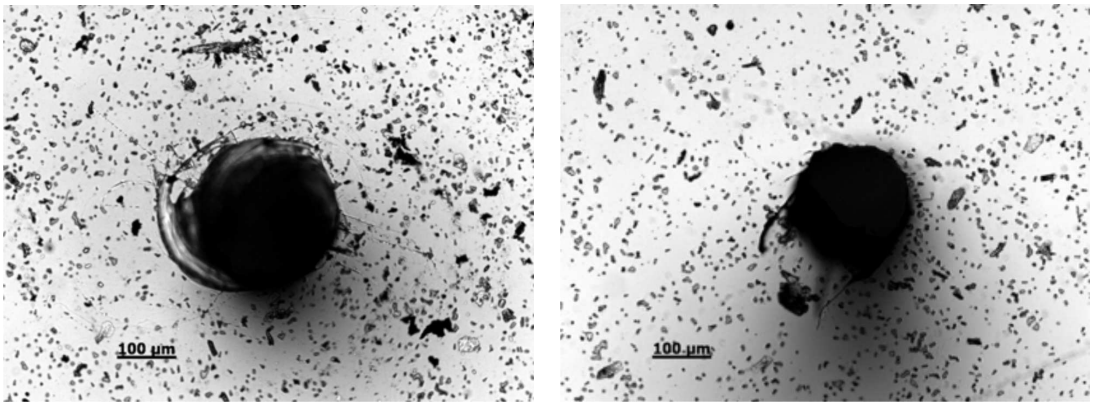

Figure 6.12: Microscope images of the connection hole in the PDMS. The punched hole shown from (left) the side the needle is pushed in and (right) the exit side. Images taken with 10x magnification.

agreement with the inner diameter of the syringe needle. The entrance of the punched hole is almost circular and shows no tears, i.e. small rips. The exit of the punched hole on the other side shows tears which might reduce the quality of the seal. To ensure a good seal, the holes are punched from the channel side which minimises the impact of the tears.

Once the connection holes are punched through the PDMS, the microfluidic channel has to be aligned to the waveguide chip. This alignment of the flow cell and waveguide chip is also performed with the alignment system shown in figure 6.11. The alignment marks shown in figure 6.4 are aligned to the etched alignment marks on the waveguide chip. Figure 6.13 shows the first trial of aligning a microfluidic flow cell to the alignment marks on a waveguide chip. Once the flow cell and the waveguide chip are aligned the two parts are pressed together. The PDMS of the flow cell will stick to the glass waveguide chip and thus form a reversible bond. During the alignment special attention was given

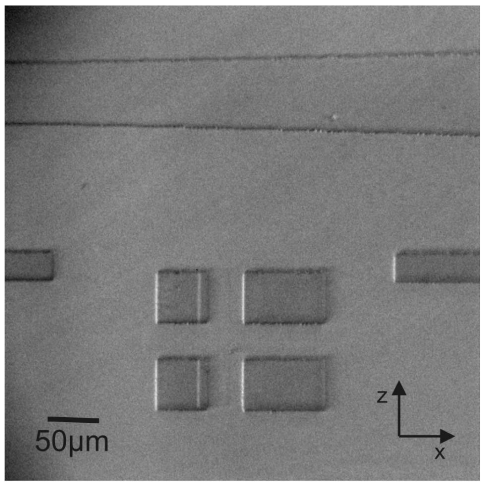

Figure 6.13: Microscope image of a part of the microfluidic channel aligned to the alignment marks on the waveguide chip. Image taken with 10x magnification.

to the alignment along the z axis where a miss alignment has the largest influence on the device performance. The resulting alignment accuracy is very good along the z axis ($< 5\,\mu$m) while the alignment along the x axis is on the order of $10\,\mu$m.

When the microfluidic channel and the waveguide chip are combined, capillaries with an outer diameter of $360\,\mu$m and an inner diameter of $50\,\mu$m are connected to the microfluidic flow cell. The choice of capillaries with a small inner diameter reduces the dead volume as well as the time require for the sample to be flowed from the 6-port valve to the flow cell.

6.5 Experimental setup and calibration

6.5.1 Experimental setup

The combined flow cell-waveguide chip is mounted in a holder which fixes the position of the device and holds it in front of the CCD camera. A picture and a schematic of the setup is shown in figure 6.14. The inlet capillary of the flow cell is connected to a 6-port valve (Rheodyne, Rohnert Park, USA) which allows the introduction of small sample volumes down to $2\,\mu$l, while the outlet capillary is connected to a waste

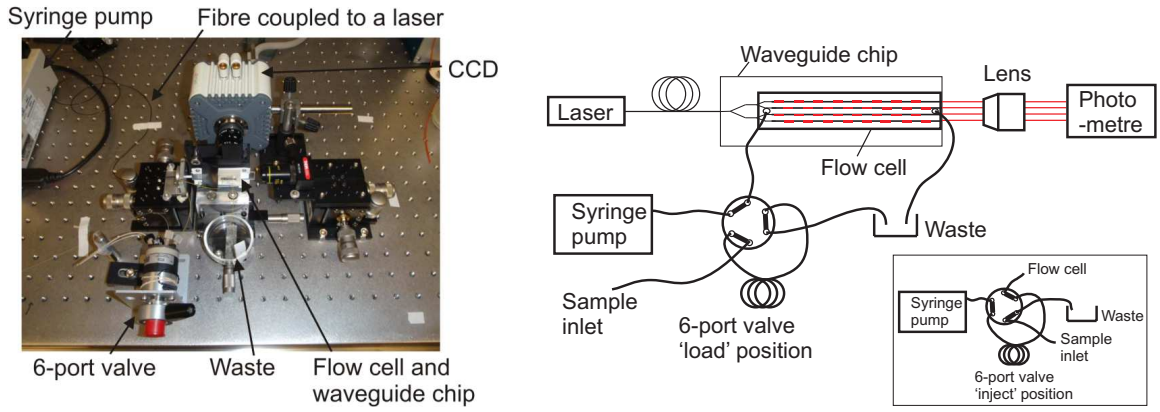

Figure 6.14: Setup of the fluorescence experiments. (left) Picture of the setup, (right) schematic of the optical and fluidic connections. The inset in the right part shows the 'inject' position of the 6-port valve.

reservoir. The 6-port valve is connected to a syringe pump (KDS200, KD Scientific Inc., Holliston, USA) which provides the buffer flow. This syringe pump is capable of flow rates down to $1\,\mathrm{nl\,hr^{-1}}$ which translates to a minimum average flow velocity of about $1.16 \times 10^{-7}\,\mathrm{m\,s^{-1}}$ in the proposed flow cell, i.e. 4 channels each $10\,\mu$m high and $60\,\mu$m wide. In the 'load' position of the 6-port valve the buffer flows straight through the valve and into the microfluidic flow cell. In this position the sample loop is filled with the sample. Switching the valve to the 'inject' position reroutes the buffer flow through the sample loop so that the sample is transported by the buffer stream through the microfluidic flow cell.

The fibre which is connected to a 637 nm diode laser (iFLEX-1000, Point Source, Hamble, UK) is butt-coupled to the waveguide chip. The alignment of the fibre and the waveguide chip is achieved by a $x - y - z$ stage for the fibre and a $x - y$ stage for the waveguide chip. The lens focuses the light exiting the waveguide chip onto a photometre which is used to monitor the output power of the waveguide. The output power which is a measure of how much light is coupled into the waveguide is used in the alignment of the fibre with the waveguide chip and for the calibration of the experiments. Behind the waveguide chip is a CCD camera (ORCA-R^2, HAMAMATSU Photonics K.K., Hamamatsu City, Japan) which is used to capture the light emitted from the fluorophores. The complete system is enclosed to reduce the influence of the ambient light on the experiments.

During the loading of the sample onto the chip, i.e. while the sample plug is in the flow cell, the laser is switched off to prevent the onset of photobleaching [21]. After the sample plug has left the flow cell the laser is switched on and the emitted fluorescence is detected by the CCD camera. Once the laser is switched on the surface immobilised fluorophores are bleached within about 10 seconds. This photobleaching puts constraints on the sample detection and especially the maximal exposure length. After the detection of the signal, the sensor surface can be regenerated by flowing sodium dodecyl sulphate through the flow cell to remove the associated antibodies [21].

6.5.2 Limit of detection

Bulk dye experiments are performed to calibrate the assembled device and to establish the limit of detection (LOD). Here a solution containing dye molecules is flowed through the device. The dye molecules which are close to the sensor surface are excited by the evanescent field of the waveguide and the emitted signal is recorded. These experiments have the advantages that no surface functionalisation and subsequent recognition-binding event is necessary and that the fluorophores are continuously replenished which prevents photobleaching. The concentration of dye in the sample can be related to a surface concentration because the evanescent field which is used to excite the fluorophores penetrates only about 100 nm into the flow cell. The surface concentration is calculated by multiplying the dye concentration with the height of the evanescent field. For example, for an evanescent field, which penetrates about 100 nm into the flow cell, a bulk concentration of 10^{-7} M is approximately equal to a surface concentration of $10^{-11}\,\mathrm{mol\,m^{-2}}$.

In the bulk dye experiments a $2\,\mu$l sample plug containing fluorophores is flowed through the flow cell with an average flow speed $U \approx 5\,\mathrm{mm\,s^{-1}}$. The CCD camera captures the emitted light before, during and after the dye plug is in the microfluidic flow cell. Figure 6.15 shows the CCD image of one sensor window while the dye Cy5.5 is flowed through the channel. The yellow colour in the sensor window, which is bounded by the white rectangle, indicates a high pixel count compared to the blue colour in the rest of the frame. The pixel count is a measure for the amount of light which falls onto

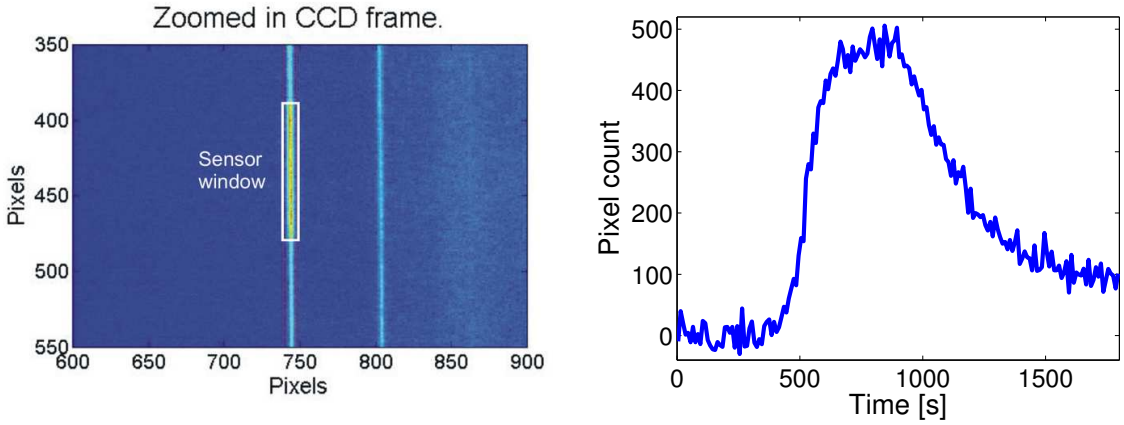

Figure 6.15: (left) Zoomed in view of a CCD frame showing two branches of the waveguide chip and one sensor window. The pixel count is indicated by the colour, i.e. the pixel count increases from blue to yellow. (right) Average pixel count in the sensor window over time. Parameters: $C_{dye} = 1\,\mu$M, $t_{ex} = 10\,$s

a single pixel in the CCD camera. The images are stored and subsequently analysed in Matlab. First, the background noise is subtracted from the pixel count. Second, the average pixel count in the sensor windows is calculated for each detection frame. The mean pixel count and the standard deviation of the pixel count for the buffer and the dye sample are given in table 6.4. The temporal mean and standard deviation is calculated

	Buffer		Dye sample		
Concentration	Mean	Std	Mean	Std	SNR
$1\,\mu$M	1.5	18.7	468.2	20.3	25
$0.1\,\mu$M	0.9	15.2	52.9	14.8	3.5

Table 6.4: Temporal mean and standard deviation (Std) for the buffer and the sample in the detection window. Parameters: $t_{ex} = 10\,$s

over several subsequent frames. The values for the buffer are calculated over 40 frames, while the values for the sample are calculated over 23 frames. The output power for these experiments which is monitored by the photometre was $16\,\mu$W. The pixel count for the dye sample is decreased if the laser power is decreased. The signal-to-noise ratio (SNR) is calculated as the ratio of the signal for the sample divided by the standard deviation of the buffer signal.

From the bulk dye experiments the limit of detection (LOD), which is the smallest analyte concentration which can be distinguished from a blank sample, is calculated through the following formula

$$LOD = \frac{3C_{dye}}{SNR} \tag{6.15}$$

With the results from table 6.4 this gives a $LOD = 85.7\,\mathrm{nM}$. With a 100 nm high evanescent field this bulk concentration corresponds to a surface concentration of $8.57 \times 10^{-12}\,\mathrm{mol\,m^{-2}}$. This value is about twice the maximal change in bound concentration for a cytokine concentration of 1 pM. To achieve the required sensitivity for the detection of cytokine molecules from serum each antibody molecule has to be labelled with at least two fluorophores. The achieved LOD agrees with the LOD of the original multisensor where depending on the target analyte the number of fluorophores per antibody molecule varied between 2 and 6.

6.6 Proof of concept experiment

The proof of concept experiments for the presented designs have to establish whether the system with the redesigned flow cell is capable of detecting and quantifying low levels of cytokine from limited sample volumes. A second objective is the verification of the mathematical models and simplifications employed in the design of the tapering channels. The design of the proof of concept experiment has to be as simple and robust as possible but still offer some flexibility to fulfil the objectives.

The analysis of the tapering channels and 'boat-shaped' patches in chapter 5 showed that the behaviour of the system depends only on the reaction/convection number ζ, the adsorption capacity κ and the inlet-to-outlet ratio of the channel designs. Most of the parameters, which define ζ and κ, are given by the cytokine-antibody pair and the device geometry. The only free parameters are (i) the antibody concentration X_0 and (ii) the flow velocity U. The antibody concentration can be used to tune the adsorption capacity and thus indirectly the concentration of the surface bound cytokine-antibody complex. However, the antibody concentration has to be low enough so that $\kappa \gg 1$ and high enough so that the interaction is detectable. The flow velocity can be used

to change the reaction/convection number and therefore the capture fraction of the system. The only limitations are given by the capabilities of the syringe pump and the requirement of $\mathrm{Gz} \ll 1$. These two parameters can be used to vary the experimental conditions and allow the verification of many different system configurations without changing the device geometry or the cytokine-antibody pair.

Numerical simulations for sensor elements with different inlet-to-outlet ratios showed that the largest difference in the uniformity of the associated analyte along the sensor is given between the standard, rectangular channel and the algebraic channel with the largest inlet-to-outlet ratio (section 5.6.2). Therefore, the comparison between the rectangular channel and an algebraic channel with a high inlet-to-outlet ratio offers the best chance to detect the difference in uniformity of the associated analyte along the sensor for the two channel geometries.

In the proof of concept experiments the flow velocity and antibody concentration are used to change the values of the reaction/convection number and the adsorption capacity. A first experiment has to be performed to approximate the unknown surface immobilised cytokine concentration and the dissociation constant. In this experiment a low flow velocity ($U = 10^{-4}\,\mathrm{m\,s^{-1}}$) and an antibody concentration close to a typical dissociation constant ($X_0 = 1\,\mathrm{nM}$) are chosen. This choice has the greatest chance to fulfil the prerequisite on the reaction/convection number ($\zeta > 1$) regardless of the surface immobilised cytokine concentration and the dissociation constant. For this flow speed and the available sample loop the assay time is about 3 hours. Once the surface immobilised cytokine concentration and the dissociation constant are estimated, the results from section 6.3.2 are used to optimise the immunoassay. This means the flow velocity and antibody concentration are adjusted to increase the difference in surface immobilised cytokine-antibody complex concentration and to reduce the assay time while still fulfiling the requirements on the adsorption capacity κ and the reaction/convection number ζ.

6.7 Summary

For the quantification of low levels of cytokines from small quantities of sample it is important to ensure that all analyte molecules can reach the active surface of the affinity sensor and subsequently associate to the surface immobilised receptor molecules. In this chapter the flow cell of the sensitive waveguide sensor from Hua et al. [21] was redesigned according to the design strategies for the optimisation of microfluidic affinity sensors from chapter 5. The resulting microfluidic affinity sensor is theoretically capable of detecting low concentrations (1 pM) of cytokines from small quantities of sample (2 μl).

While the quantification of cytokines offers many possibilities for the monitoring of neurodegenerative diseases [6], no currently available affinity sensor fulfils the requirements on sensitivity, sample size and assay complexity. However, the waveguide sensor, which was originally developed for river water monitoring and achieved a limit of detection of $1\,\mathrm{ng\,l^{-1}}$ for estrone, has the potential to fulfil these requirements. Here the fluidic structures and operation parameters are redesigned with the aim of low sample consumption and efficient analyte transport to the active sensor surface. This is achieved in a two step process: (i) variation of the flow cell shape and the flow velocity and (ii) optimisation of the antibody concentration for a given cytokine-antibody pair.

First the flow cell shape and the flow velocity were redesigned according to the design guidelines derived in chapter 5. The low capture fraction of the original system was increased by splitting the flow cell which covered all four waveguides in the original setup into four parallel branches which mimic the design of the waveguide chip and reduce the dead volume of the microfluidic flow cell. This has the effect that every analyte molecule is flowed directly over the sensor patches which increases the capture fraction. Furthermore, the channel height and flow velocity were adjusted with the aim that every analyte molecule can reach the active surface, i.e. $\mathrm{Gz} < 1$, and that a large percentage of the analyte molecules associates to the surface immobilised receptors, i.e. $\zeta > 1$. Together these three measures increase the capture fraction from about 0.01 to at least 0.6. However, with this setup the distribution of bound analyte along the sensor surface is not uniform. To increase the uniformity of the associated analyte the non-rectangular device geometry derived in section 5.6.1 is incorporated into the individual

flow cell branches. These tapering channels will increase the uniformity of the associated antibodies along the active sensor surface.

In the second step a simple analytical model and numerical simulations were used to analyse the device performance and to evaluate the optimal operating parameters. The simple, equilibrium model which agrees with full, numerical simulations gives guidelines for the choice of the optimal antibody concentration to achieve the maximal difference in the bound cytokine-antibody complex concentration between a blank sample and a sample with a low cytokine concentration. Furthermore, the numerical simulations showed that the tapering channels from section 5.6.1 have a 5% higher difference in the bound cytokine-antibody complex concentration compared to the standard, rectangular device geometry.

The theoretical investigations suggest that the new flow cell design will reduce the required amount of analyte from about 1 ml to the low microlitre regime while retaining the excellent limit of detection of the waveguide sensor. To validate these theoretical results the proposed flow cell was designed, fabricated and combined with the waveguide chip. Compared to the original flow cell this required higher accuracy in the fabrication and especially in the alignment of the flow cell to the waveguide chip. This accuracy was achieved by microfabrication in PDMS and the incorporation of alignment marks in both the waveguide chip and in the flow cell. Unfortunately, the immobilisation of cytokine molecules to the waveguide chip by microcontact printing was not completed within the timescale of this thesis. For this reason only bulk dye experiments could be performed with the assembled flow cell-waveguide system. However, the bulk dye experiments suggest that a LOD which is sufficient for the detection of low concentrations (1 pM) of cytokines from small sample volumes (2 μl) can be achieved.

Chapter 7

Design of a grooved gradient generator for the delivery of concentration gradients across microfluidic channels

7.1 Introduction

Microfluidic concentration gradient generators are receiving much attention for lab-on-a-chip applications [27; 235]. These concentration gradient generators yield a well-defined gradient in analyte concentration across one or more device dimensions, e.g. the analyte concentration decreases in a controlled manner across the width of a microfluidic channel. The resulting concentration gradients have important applications for the study of cell proliferation, differentiation and migration [236; 237]; for example, chemotaxis, i.e. the directed movement of cells along concentration gradients of signalling molecules such as cytokines (see chapter 6), plays an important role in wound healing [237] and the immune response following inflammatory infection [238]. The study of these gradient signalling processes requires devices for the generation of concentration gradients which are well-defined over physiological relevant length scales, i.e. tens to hundreds of micrometres [27], and stable for extended periods of time, i.e. hours to days [239].

Further requirements for gradient generators are the generation of concentration gradients which are controllable and quantifiable; this allows the reliable and repeatable performance of lab-on-a-chip devices for the study of gradient signalling processes. In addition, the concentration gradient generator design should be flexible enough to be adaptable for different predefined concentration gradients, e.g. linear or exponential concentration gradients. Exponential concentration gradients which span $3-5$ orders of magnitude are especially important for bioanalysis applications because they offer a wider range of concentrations compared to the linear concentration gradient. Furthermore, for the integration of several functions into multiplexed microfluidic lab-on-a-chip systems (chapter 2) it is increasingly important that the concentration gradient generator has a small footprint and requires only a small number of connecting channels, e.g. the ideal concentration gradient generator will require only two inlets, an analyte and a buffer inlet.

In recent years the generation of concentration gradients has moved from macro-scale systems, i.e. Boyden and Zigmund chamber, to microfluidic systems (see chapters 2 and 3) which offer improved spatial and temporal control of the soluble microenvironment as well as potential for high levels of automation and integration [240]. The increased control of the soluble microenvironment facilitates repeatable and quantitative studies of gradient signalling processes. The improved long term stability of the concentration gradient is especially important for studies of the proliferation and differentiation of cells [239] where the concentration gradient has to be stable for several days. For these applications the 'split and recombine' gradient generator [30] is the most widely used device [239; 241]. This device generates a concentration gradient perpendicular to the direction of the flow in the microfluidic channel. Due to the slow diffusive transport microfluidic channels for the 'split and recombine' gradient generators have to be several millimetres long and thus use much space on lab-on-a-chip devices [242].

Here a gradient generator, which is based on surface groove induced secondary flow [24] to transport analyte from the source stream to the sink stream in a controlled manner, is presented. A schematic of the proposed design is shown in figure 7.1. Several studies showed that the size of the surface groove has a significant influence on the secondary flow profile [28; 29]. This is employed in the grooved gradient generator

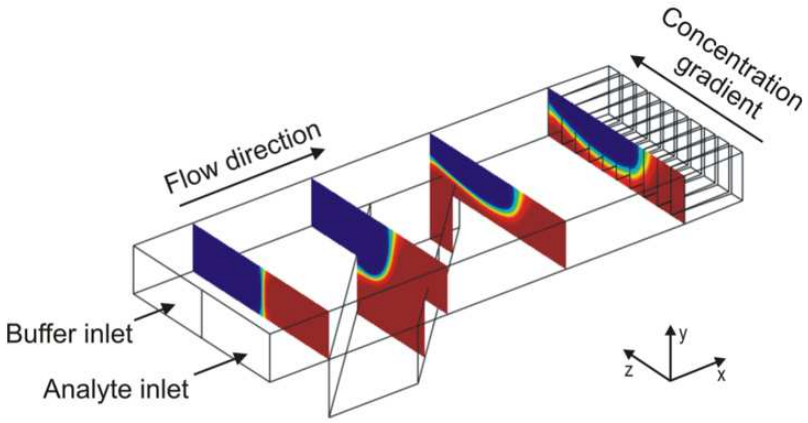

Figure 7.1: Schematic of the proposed grooved gradient generator. The analyte stream (red) and the buffer stream (blue) are flowed in continuously from the left. The analyte molecules are transported by the secondary flow across the width of the channel. In the outlet channels the analyte concentration is homogenised over the height and width of the outlet channels.

where the shape and size of the surface groove is modified so that the analyte molecules are transported from a source stream across the width of the channel in a controlled manner. Here it is proposed that a linear or exponential concentration gradient across the width of the channel can be created by numerical optimisations over the size and ,for the first time, shape of the surface groove with the aim of matching the output concentration profile with a predefined concentration profile. This has the potential to reduce the required length of the concentration gradient generator compared to approaches which rely on diffusion alone.

7.2 Literature review

7.2.1 Microfluidic concentration gradient generators

In traditional, macro-scale gradient generators, like the Boyden and Zigmond chamber, the concentration gradient is created by diffusion of analyte molecules from a source reservoir to a sink reservoir across a porous membrane or through a small connection

channel, respectively [240]. The resulting concentration gradients are almost stable for a short period of time but are averaged out through diffusion in a few hours. A further conventional method is micropipette gradient generation. Here the tip of a micropipette is positioned in the sink reservoir and the source solution is pneumatically ejected out of the pipette [240]. This yields a radial concentration gradient around the pipette tip. These traditional systems are easy to configure but lack the spatial control and temporal stability required for quantitative assays [239]. In recent years, the stable and controllable flow profile in microfluidic systems (section 3.2) has led to the development of microfluidic concentration gradient generators which give much better spatial and temporal control and are thus important for repeatable and quantitative studies. These microfluidic concentration gradient generators can be divided into two types. The first type creates concentration gradients in stagnant solutions, i.e. without convective flow, while the second type employs flowing solutions.

Gradient generators in stagnant solutions

Most of the microfluidic devices which utilise diffusion in stagnant solutions can be seen as miniaturisations of the traditional systems, i.e. Boyden and Zigmond chamber and micropipette-generated gradients. In a miniaturisation of the Zigmund chamber the source and sink reservoir are replaced by two parallel microfluidic channels which are connected through much smaller perpendicular channels [27] as shown in figure 7.2. The analyte molecules are transported through the connecting channels by diffusion only because the flow resistance in these channels is much higher than in the source and sink channel. Miniaturisation provides the potential for exact control of the flow resistance in the channels so that the solution in the source and sink channel can be continuously replenished while the solution in the connecting channel stays stagnant. This continuous replenishment to the source and sink channel is the reason why the concentration gradient in the microfluidic version of the Zigmund chamber is temporally stable. A further benefit is the improved control over the shape and length of the connecting channels which allows the creation of various different concentration profiles [243; 244], e.g. the connecting channel in figure 7.2 (C) generates a concave, nonlinear concentration profile, while the connecting channel in figure 7.2 (D) generates a linear concentration

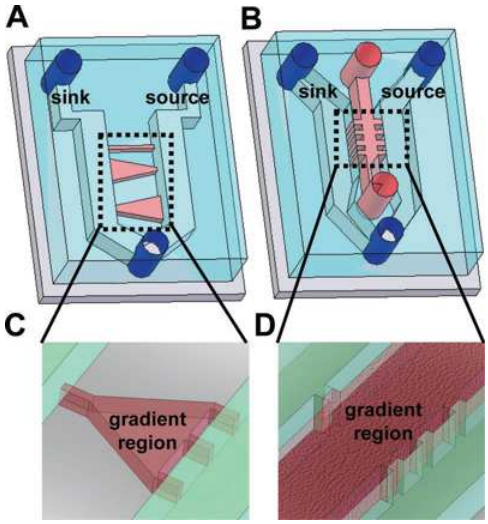

Figure 7.2: Diagram of a miniaturisation of the Zigmund chamber. Reprinted with permission from [243]. Copyright 2007 American Chemical Society.

profile. Micropipette gradient generation is miniaturised by integrating an injection nozzle into a microfluidic channel [245]. The pulsatile injection of minute amounts of analyte can create a stable concentration gradient with minimal convective flow. This steady state results from the superposition of the concentration profiles of the individual injections. The integration into a microfluidic system allows the precise fabrication and positioning of the injection nozzle which significantly increases the reproducibility and controllability of the concentration gradients.

An interesting approach which utilises diffusion through a hydrogel layer allows the generation of arbitrary, stable concentration gradients [246]. A schematic of this design is shown in figure 7.3. The system consists of a microfluidic channel which is capped by a hydrogel layer. The sides of the hydrogel layer are connected to source and sink reservoirs which are periodically replenished so that a stable concentration gradient is created across the hydrogel. The analytes diffuse from the hydrogel into the much smaller microfluidic channel below and thus eventually create a concentration gradient in the microfluidic channel that is at equilibrium between the hydrogel and the microfluidic channel. The equilibrium concentration between the microfluidic channel and the hydrogel depends on the distance between the source and sink reservoir, i.e. the equilibrium concentration decreases from the source to the sink reservoir. By changing the path of the microfluidic channel under the hydrogel different concentration profiles

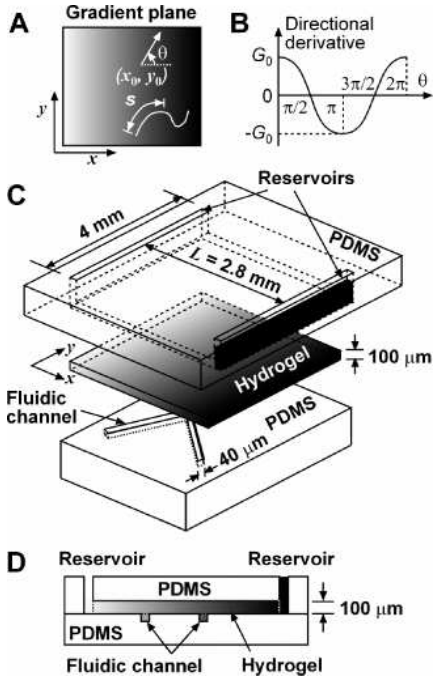

Figure 7.3: Diagram of a microfluidic gradient generator which utilises diffusion through a hydrogel layer. Reprinted with permission from [246]. Copyright 2006 American Chemical Society.

(linear, exponential, alternating) along the channel can be created, e.g. a channel perpendicular, i.e. running along the x axis in figure 7.3, to the source and sink reservoir has a linear concentration gradient.

All the approaches developed so far to generate concentration gradients in stagnant solutions rely solely on diffusion. This has the advantage that cells, which are often the subject of concentration gradient studies [27], are not exposed to shear forces. However, some applications, such as microfluidic affinity sensors [247] or cell culture [239], benefit from the continuous replenishment of the analyte molecules which requires non-stagnant solutions.

Gradient generators in non-stagnant solutions

For the second type of concentration gradient generators the concentration gradient is created by balancing the effects of diffusion and convection. This type of concentration gradient generators is only feasible in microfluidic systems which offer very stable and

highly controllable flows (see section 3.2). An example is where the effects of diffusion and convection are exploited in a counter-flow configuration [248]. In this configuration

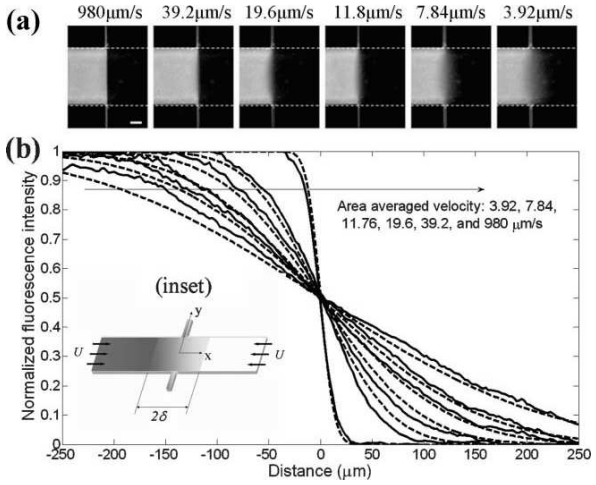

Figure 7.4: Microfluidic gradient generator with a counter-flow configuration from [248] - Reproduced by permission of The Royal Society of Chemistry. Inset in (b): the source stream is flowing in from the left and the sink stream from the right.

shown in figure 7.4 the slow flowing streams from the source and sink channel meet at a channel crossing with two small, perpendicular outlet channels. At this interface the two streams mix by diffusion and create a stable concentration gradient. The slope of this concentration gradient depends on the relative magnitude of diffusion and convection. This provides a way to dynamically control the concentration gradient by a change in the flow velocities of the source and sink stream, i.e. the slope increases with increasing flow velocities.

A widely used and flexible method for the generation of concentration gradients utilises the diffusion of analytes across parallel flowing source and sink streams. In the simplest setup the analytes from two inlet streams diffuse unhindered across the width of a single microfluidic channel [249]. The resulting concentration profile has a sigmoidal shape whose slope depends on the relative magnitude of diffusion and convection. For a fixed flow rate the concentration gradient across the width of the microfluidic channel at a fixed position along the channel is temporally stable. A more powerful approach is the widely used 'split and recombine' gradient generator [30]. These devices consist of a network of microfluidic channels with several branches and stages as shown in fig-

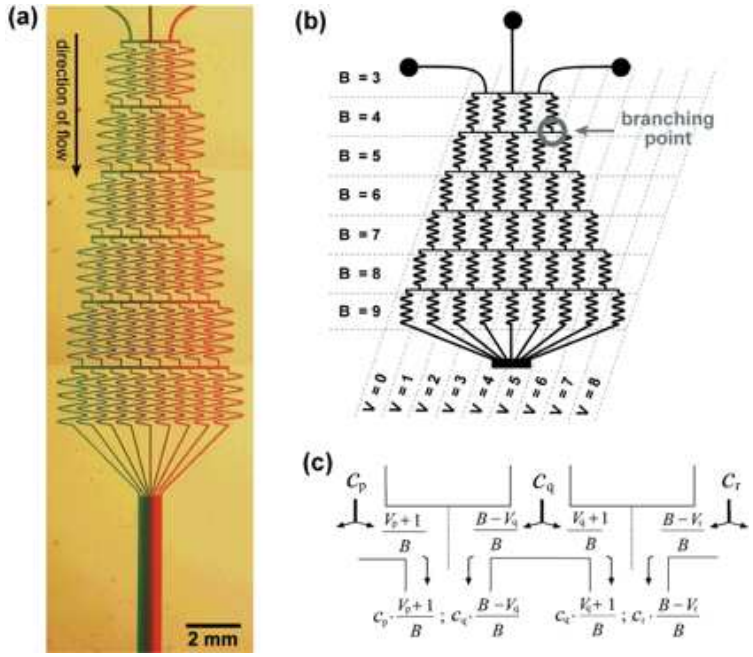

Figure 7.5: Microfluidic 'split and recombine' gradient generator. Reprinted with permission from [242]. Copyright 2001 American Chemical Society.

ure 7.5. Different solutions are pumped simultaneously into different inlet branches. In each stage of the network the branches are split, combined with a neighbouring branch and the fluid streams from the two branches are mixed. As a result of this splitting and recombining the solution in the branches in stage n is different from the branches in stage $n-1$. Recombining the branches into one, wide channel establishes a concentration gradient across the width of the channel. The gradient in this combined channel has a step profile which gets smoothed out by diffusion. The generated gradients can extend over channels a few millimetres wide and are spatially and temporally constant. Channel cross section concentrations of different shapes (linear, exponential, parabolic, periodic) can be achieved by changing the microfluidic channel network and the flow velocity of the individual inlet branches [242; 250]. It has been shown that a logarithmically small number of stages, i.e. $\log_2(N-1)$, is required to generate a complex concentration gradient across N outlet branches [251]. For a similar approach where dividing walls restrict cross channel diffusion it has been shown that any monotonic concentration gradient can be created [252]. A further advantage is the potential to create overlapping concentration gradients of different analytes by pumping different analytes into different inlet branches. However, a drawback of these systems is the re-

quired length of the channels to achieve complete mixing between subsequent stages. Most mixing channels [239; 242] are several millimeters long so that the system requires a large device and thus large sample volumes.

Microfluidic concentration gradient generators, especially the 'split and recombine' concentration gradient generators, are widely used in bioanalytical applications, for example, for high content screening of cellular responses to several drugs [241] and for the analysis of stem cell growth and differentiation [235; 239]. Furthermore, stable concentration gradients can be exploited in the microfabrication of lab-on-a-chip systems (see section 2.3); concentration gradients can be utilised in the patterning of gradients of surface immobilised receptors [211] (see section 2.4.1). Wet etching with a concentration gradient in the etchant results in spatially controlled etch rates [30]. A direct use is the utilisation of a crosslinker concentration gradient and subsequent photopolymerisation for the generation of gradients in the mechanical properties of hydrogels [253]. However, the large size and large sample volumes of the 'split and recombine' concentration gradient generators offer much room for improvement.

7.2.2 Surface groove induced secondary flow

The flow in straight microfluidic channels is one dimensional along the length of the channel so that the transport of analytes across the width and height of the channel is diffusion dominated (see section 3.2). The slow diffusion of analytes in a direction perpendicular to the direction of the flow is the reason why the large sizes of the 'split and recombine' concentration gradient generators are necessary. One possible approach to increase the transport of analytes across the width of the microfluidic channel is by surface groove induced secondary flow as shown in figure 7.6. The surface grooves induce a secondary flow because in shallow channels the flow resistance is inversely proportional to the cube of the channel height (see section 3.2) so that flow parallel to the grooves is easier than across the grooves [24]. The main axial flow and the transverse secondary flow combine to a helical flow profile along the channel which was shown in figure 5.1. These structures were originally developed to improve the mixing in microfluidic systems; the staggered herringbone mixer (SHM) which is shown

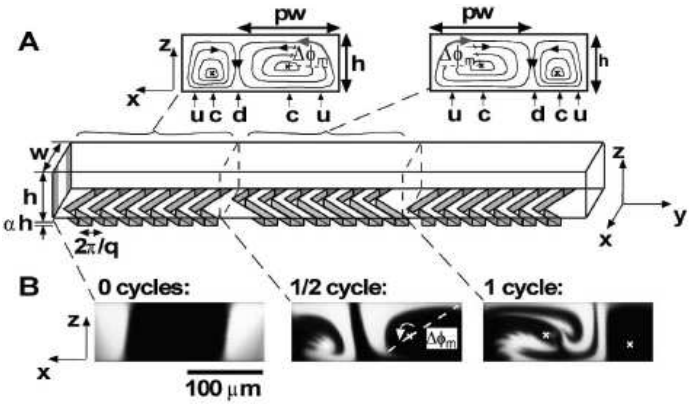

Figure 7.6: Diagram of the staggered herringbone mixer and the induced secondary flow from [24]. Reprinted with permission from AAAS.

in figure 7.6 reduces the mixing length to the order of log(Pe) compared to straight microfluidic channels where the mixing length scales linearly with the Péclet number Pe. The SHM performs effectively for devices with a Reynolds numbers Re $<$ 100. Furthermore, these mixers have relatively simple structures, a low pressure drop and achieve good mixing. Further improvements in the magnitude of the secondary flow and the mixing efficiency have been achieved by incorporating grooves on more than one channel wall which removes the dead mixing zones, i.e. zones with no secondary flow, in the top corners [254; 255].

Analytical studies of the 3D flow profile in microfluidic channels with surface grooves showed that the angle of the helical trajectories depends on the depth and spacing of the surface grooves [197; 256]. Several numerical studies which investigated the effect of various geometric parameters, such as groove angle, groove length and groove depth, on the secondary flow profile showed that the groove depth has the largest impact on the magnitude of the secondary flow [28; 257; 258]. Furthermore, these studies showed that the number of grooves has only a small effect on the magnitude of the secondary flow [258]. A systematic study over the channel width and height as well as the groove depth, width and spacing showed that a 50% increase of the transverse velocity compared to the original SHM is possible [29]. The results of this study allow the optimisation of the groove shape for a given channel aspect ratio W/H.

Surface groove induced secondary flow has been used to remove depleted fluid layers

away from the active surface in integrated microfluidic affinity sensors [25]. In a further application the secondary flow is used to hydrodynamically focus a sample stream in the middle of a microfluidic channel surrounded by buffer [259]. This design, shown

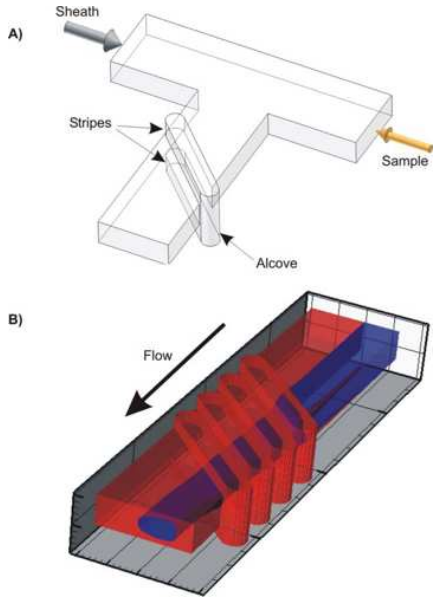

Figure 7.7: Hydrodynamic focusing by surface groove induced secondary flow from [259] - Reproduced by permission of The Royal Society of Chemistry

in figure 7.7, requires only one buffer inlet while conventional designs require multiple buffer inlets whose flow rates have to be balanced. This application demonstrates that surface groove induced secondary flows can be applied to manipulate sample streams in a microfluidic system in a controlled manner.

All studies performed so far, use either the slanted groove design shown in figure 5.1 or the herringbone design shown in figure 7.6. The only deviations from these designs include a change in the asymmetry ratio, i.e. the ratio between the long and short arms of the herringbone groove, along the channel from the fixed ratio of the SHM to a varying ratio [260; 261]. However, the secondary flow profile is directly dependent on the shape and size of the surface grooves. Thus a more flexible approach, which changes the shape of the grooves, might have the potential to tailor the secondary flow for the improved mixing of analytes or for the generation of concentration gradients.

7.3 Design of the grooved gradient generator

The design of the proposed grooved gradient generator is based on parallel flowing source and sink streams and controlled analyte transport across the width of the microfluidic channel by surface groove induced secondary flow. This transverse flow generated by the surface grooves offers the possibility to transport the analyte across the width of the channel much faster than by diffusion alone and thus reduces the size of the device. However, conventional grooves, i.e. uniform depth and parallel side walls, create non-monotonous concentration gradients so that more flexible groove shapes are required. In the first groove design, called the simple groove design, described in this section the requirement of parallel side walls is removed, i.e. the groove can get shorter or longer across the width of the channel. Previous studies [262] as well as preliminary simulations with a single groove in the bottom of the channel (the simulated channel and groove geometry as well as the concentration profile are shown in figure 7.1) showed that a single groove is sufficient to transport the analyte from one side of the channel to the other side; this suggests that optimisation over the size and shape of a single groove is sufficient for the generation of a concentration gradient across the width of a microfluidic channel.

A schematic for the proposed concentration gradient generator is shown in figure 7.8. The microfluidic channel consists of two inlet streams, a groove in the bottom of the channel and 10 outlet channels. The two inlet streams, analyte inlet stream and buffer inlet stream, are modelled as a concentration profile across the width of the channel: the concentration is one for the analyte inlet stream and zero for the buffer inlet stream. The analyte inlet stream has width W_i while the buffer inlet stream has width $W - W_i$. These widths correspond to the flow rates of the analyte and buffer inlet streams. The ratio of the width of the two inlet streams has to be adjusted depending on the required cross sectional concentration profile, i.e. the width of the analyte inlet stream has to be reduced with increasing slope of the concentration gradient. The outlet channels are equivalent to the branches in the 'split and recombine' concentration gradient generator and are required to homogenise the analyte concentration over the height of the microfluidic channel. This is necessary because at the end of the channel the analyte

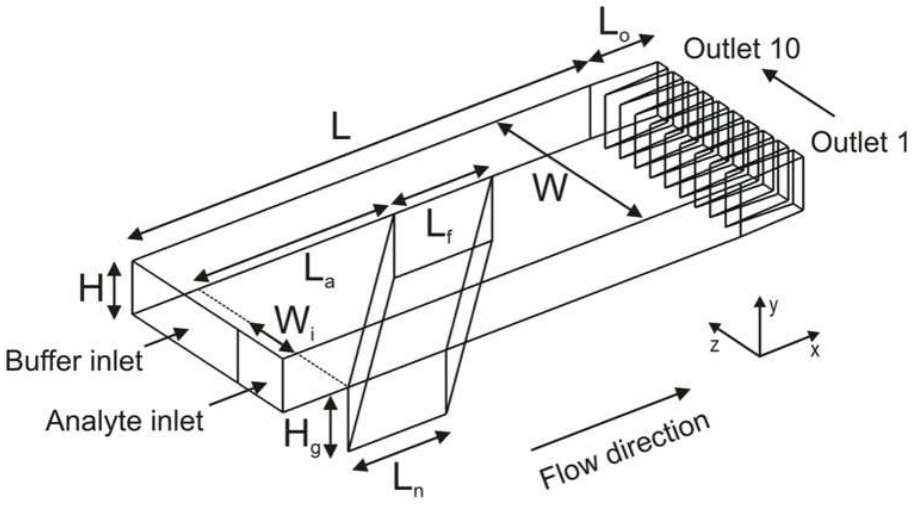

Figure 7.8: Diagram of the proposed 3D channel structure of the grooved gradient generator for the creation of concentration gradients across the width of a microfluidic channel. The width W_i indicates the width of the analyte inlet stream. The dotted line is a guide to the eye.

molecules are mainly located in the bottom of the channel as shown in figure 7.1. The length of the outlet channels which has to be long enough to allow for the thorough mixing of the analytes could be reduced by incorporating a micromixer into the design [23]. However, the mixing in the outlet channels is not included in the numerical simulations. Once the outlet channels are homogenised they are combined to establish a defined concentration gradient spatially across the width of a microfluidic channel. Initially, i.e. at the beginning of the wide channel, this concentration gradient has a step profile which gets smoothed out to a continuous concentration gradient by diffusion along the length of the wide channel. The surface groove in the bottom of the channel is defined by four parameters: groove depth H_g, groove length near side L_n, groove length far side L_f and groove offset L_a which is proportional to the angle between the groove and the microfluidic channel. The numerical optimisations are performed over the parameters defining the surface groove in the bottom of the channel while the general channel shape stays constant and is given by the design in figure 7.8.

The numerical optimisations over the parameters defining the groove are performed separately for two target concentration gradients: (i) a linear concentration gradient from the input concentration to zero and (ii) an exponential concentration gradient, i.e. the concentration decreases exponentially across the width of the microfluidic channel. The numerical optimisations are performed with the aim of fitting the concentration profile at the channel exit with one of the two target concentration profiles, i.e. linear or exponential. The quality of the fit is defined as the square error between the target concentration profile and the simulated concentration profile through

$$E_l = \sum_{i=1}^{n} \left(\frac{n-i}{n-1} - c_i \right)^2 \tag{7.1}$$

for the linear concentration profile and

$$E_e = \sum_{i=1}^{n} \left(1 - \frac{c_i}{\omega^{1-i}} \right)^2 \tag{7.2}$$

for the exponential concentration profile where n is the number of outlet channels, ω the coefficient for the exponential decay and c_i is the simulated average outlet concentration in outlet i. The average outlet concentration c_i in outlet i is calculated by the velocity-weighted area integral of the analyte concentration at the exit of the outlet and normalised with the area of the exit of the outlet channel. The square error E_e for the exponential concentration gradient is given by the relative error, i.e. the error is scaled with the target concentration profile, while the square error E_l for the linear concentration gradient is given by the absolute error. This scaling of the square error for the exponential concentration gradient gives every outlet channel the same weight in the error function regardless of the magnitude of the target concentration. This is important for the exponential concentration gradient where the concentration in the outlet channels varies by 3 orders of magnitude. However, for the linear concentration gradient the absolute error function was chosen because it provided better optimisation results than the relative error function.

The flow profile in the microfluidic channel shown in figure 7.8 is described by the Navier-Stokes equations 3.1 and 3.2 (see section 3.2). At the channel entrance and exit the pressure is set to a constant value, i.e. p_1 and p_2, respectively, and it is required that the viscous stress is zero. This leads to a pressure driven flow. At the channel side walls

no-slip boundary conditions are applied. This condition implies that the fluid velocity at the side walls is zero. The channel height and flow velocity in systems employing gradient generators, are typically up to $100\,\mu$m and $1\,\mathrm{mm\,s^{-1}}$ [235; 239], respectively. However, the Reynolds numbers for these examples are still below 1: the devices operate in the stable, laminar flow regime and the flow can be described by the linear Stokes equations 3.4 and 3.5. A consequence of this is that the flow profile depends only on the ratios of the channel and groove geometry, i.e. the flow profile for one set of channel and groove geometry ratios is independent of the actual size of the channel. The transport of the analyte through the microfluidic channel is described by the convection-diffusion equation 3.12. The generated concentration profile at the channel outlet depends on the relative magnitude of the convective and diffusive terms which is indicated by the Graetz number Gz (section 3.3). Ideally the Graetz number is kept large so that diffusion plays only a small role compared to convection. In the proof-of-concept simulations the Graetz number is fixed at $\mathrm{Gz} = 50$ which corresponds to a flow velocity of $\sim 3 \times 10^{-4}\,\mathrm{m\,s^{-1}}$ for analytes with a diffusion coefficient of $D = 5 \times 10^{-11}\,\mathrm{m^2\,s^{-1}}$.

The proof-of-concept simulations are performed with the microfluidic channel shown in figure 7.8. In these simulations the microfluidic channel has a channel height of $H = 75\,\mu$m, a channel width of $W = 300\,\mu$m and a channel length of $L = 700\,\mu$m. This setup corresponds to the ratios $H = \frac{1}{4}W = \frac{3}{28}L$. The height is chosen to be in accordance with typical microfluidic gradient generators [30], while the width is chosen so that the channel has an aspect ratio well above one which is required to achieve a sufficiently strong transverse flow [29]. The starting groove geometry for the following numerical optimisation is chosen so that the transverse flow is maximal for this channel height and width. The strongest transverse flow, according to the work of Lynn and Dandy [29], is given for a groove length of $L_n = L_f = 150\,\mu$m and a groove depth of $H_g = 90\,\mu$m. The groove offset is chosen to be $L_a = 300\,\mu$m, which is equivalent to an angle of 45° between the upstream groove edge and the channel side wall, and the groove is anchored $100\,\mu$m away from the inlet. This ensures that the parabolic flow profile is fully developed before it reaches the groove. This choice of groove requires a channel length of at least $550\,\mu$m. The chosen channel length of $L = 700\,\mu$m allows room for an increase in the groove angle and groove length. The length of the outlet

channels is $L_o = 100\,\mu$m and their exit width is $26\,\mu$m.

7.4 Optimisation over the groove parameters

Numerical optimisations over the parameters defining the groove shape are performed with the aim of matching the simulated concentration profile across the exit of the microfluidic channel with a predefined concentration profile. These numerical optimisations are performed in a two stage process: (i) a random search over the complete parameter range and (ii) a local optimisation starting from the resulting parameter set of the random search.

In the random search stage of the optimisation the groove parameters are chosen randomly from the allowed parameter range which is given in table 7.1 for the simple groove design [263]. For this randomly chosen groove the numerical simulation is performed. The error between the target concentration profile and the simulated concentration profile is calculated and stored. The random search over the complete parameter range is used to identify the most promising parameter sets, i.e. parameter sets where the error given by equation 7.1 or 7.2 is below a certain threshold. The random search is a global optimisation routine which makes the complete optimisation more robust by sampling the error over the whole parameter range. However, the random search is not very efficient: at least 100 times the number of parameters, e.g. 500 for the simple groove design with five parameters, parameter sets have to be evaluated to identify promising parameter sets for the subsequent local optimisation routine. This is feasible in the problem studied here where each function evaluation requires about 8 minutes. Furthermore the random search compared favourably against the more sophisticated simulated annealing routine [264] inbuilt in Matlab. An example script for the random search routine is given in appendix D.1.

In the second stage the Nelder-Mead algorithm [265] is used to find the local optimum starting from the most promising parameter sets identified by the random search. The Nelder-Mead algorithm is a direct optimisation routine which uses only the error values in the attempt to minimise this error. In the first step of the Nelder-Mead algorithm the

error values for $n+1$ parameter sets, where n is the number of parameters, is calculated and stored. These $n+1$ parameter sets generate a nondegenerate simplex in the n dimensional parameter space, e.g. for $n = 2$ the 3 parameter sets define a triangle. In subsequent iteration steps of the algorithm, the error value for a new parameter set is calculated. This parameter set is generated from the original simplex; for example, the parameter set with the largest error can be replaced by its reflection through the centroid of the remaining n parameter sets. Once a parameter set with a lower error is identified the original simplex is updated with this parameter set and the next iteration step starts. The Nelder-Mead algorithm is a local optimisation routine which is very robust and effective. The combination of the global random search with the local Nelder-Mead algorithm results in a robust optimisation routine. Both stages are performed in the Matlab environment which has an inbuilt Nelder-Mead algorithm. Sample scripts for the optimisation routine are given in appendix D.1.

The optimisation routine calls a COMSOL script which solves the fluid dynamics and transport problem (see section 7.3) and returns an error value. This script takes the groove parameters, i.e. H_g, L_n, L_f and L_a, and the analyte inlet stream width W_i as input variables while the channel size is specified in the script. The inclusion of the analyte inlet stream width into the numerical optimisation increases the flexibility of the design; a variable analyte inlet stream width can improve the quality of the fit if the groove shape is not flexible enough to guarantee an exact fit of the simulated outlet concentration with the target concentration. However, the analyte inlet stream width is defined by the target concentration gradient for an exact fit of the simulated outlet concentration with the target concentration. The partial differential equations are solved on the defined geometry (figure 7.8) and the script calculates the square error between the target concentration profile and the simulated concentration profile; this error is calculated according to equation 7.1 for the linear concentration profile or equation 7.2 for the exponential concentration profile. More details about the numerical implementation and a sample script can be found in appendix D.2.

In the first optimisation the simple groove design with a constant depth and straight sides is considered. Here only the depth, the angle and the length at the near and far side are the free parameters of the groove. Together with the variable inlet width

Description	Parameter	Lower limit	Upper limit
Analyte inlet width	W_i	$20\,\mu$m	$200\,\mu$m
Groove depth	H_g	$20\,\mu$m	$100\,\mu$m
Groove length far side	L_f	$10\,\mu$m	$220\,\mu$m
Groove length near side	L_n	$100\,\mu$m	$450\,\mu$m
Groove offset	L_a	$100\,\mu$m	$370\,\mu$m

Table 7.1: Lower and upper limit of the parameters for the random search for the simple groove design.

this gives five parameters. In the first stage of the optimisation 1000 iterations of the random search are performed. The lower and upper limit for the five parameters used in the random search are given in table 7.1. This range of parameters encompasses the groove with the maximal transverse flow and provides room for variation from this case. The three parameter sets of the random search with the lowest error are used as the starting points for Nelder-Mead optimisations with 400 iterations. Following this, the three resulting parameter sets of the Nelder-Mead optimisations are compared and the parameter set with the lowest error is used as a starting parameter set for another Nelder-Mead optimisation with 500 iterations. In the case of the exponential concentration gradient a further Nelder-Mead optimisation has to be performed with a finer mesh because the accuracy of the simulations with the coarse mesh, see appendix D.2.3, is not sufficient to resolve the small concentrations at the far side of the channel, i.e. the low concentrations in the outlets 9 and 10. Each simulation with the finer mesh requires about 15 minutes so that it is not feasible to use the fine mesh for the whole optimisation. However, the optimisation results with the coarse mesh provide very good initial values for the optimisation with the fine mesh so that the optimisation converges in less than 150 iterations.

The best simulated concentration gradients both for the linear concentration gradient and the exponential concentration gradient with $\omega = 2$ are shown in figure 7.9. The simulated concentration gradient is defined by the velocity-averaged outlet concentrations c_i. It can be seen that the simulated concentration gradient deviates significantly from the target concentration gradient. This suggests that the groove shape is not

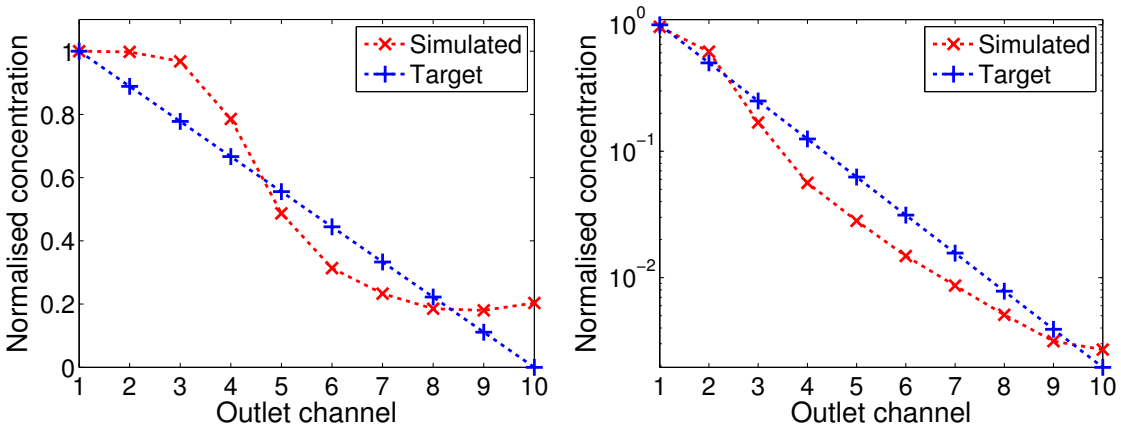

Figure 7.9: Comparison of the target concentration gradient and the simulated concentration gradient for the simple groove design. (left) Linear concentration gradient, (right) semi-log plot for the exponential concentration gradient. The dotted lines are a guide for the eye. Parameters: Gz = 50, $\omega = 2$

flexible enough to create the desired concentration gradient.

Two approaches for a more complex groove shape were considered: (i) a groove with non-uniform groove depth and (ii) a groove with a non-straight groove edge. The first approach (i) considers a linear gradient in the groove depth, i.e. the groove depth changes linearly across the width of the microfluidic channel. Preliminary numerical optimisations with this complex groove shape showed an improved fit as shown in figure 7.10 for the exponential concentration gradient. However, the fabrication of a surface groove with non-uniform depth requires 3D fabrication methods which are considerably more complex and expensive than 2D fabrication methods (see section 2.3). The second approach (ii) considers grooves with uniform depth where the downstream side of the groove is non-straight, see figure 7.11. This complex groove shape can be fabricated with the same methods as the simple groove which makes it more feasible compared to the groove design with non-uniform depth. In addition to the parameters defining the simple groove, this complex groove shape has two additional parameters: width of the midpoint W_m and groove length at the midpoint L_m.

In the first stage of the optimisation for the complex groove design (ii) with uniform depth the number of iterations was increased to 1400 to account for the increase in parameters from 5 to 7. The lower and upper limit for the seven parameters used

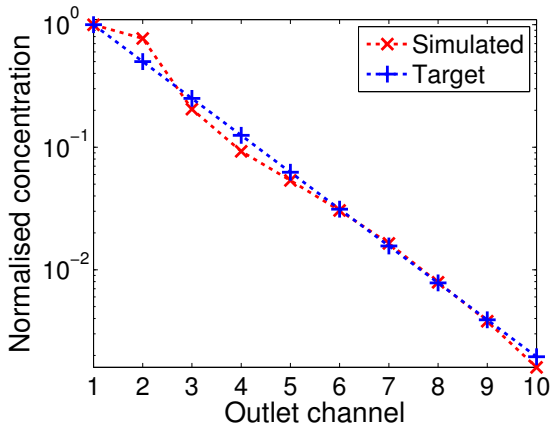

Figure 7.10: Comparison of the target concentration gradient and the simulated concentration gradient for the complex groove design (i) with a variable depth. The dotted lines are a guide to the eye. Parameters: Gz = 50, $\omega = 2$

in the random search are given in table 7.2. The three parameter sets of the random search with the lowest error are used as the starting parameter sets for Nelder-Mead optimisations with 400 iterations. Following this, the three resulting parameter sets are compared and the parameter set with the lowest error is used as the starting parameter set for another Nelder-Mead optimisation with 500 iterations. For the exponential concentration gradient a further Nelder-Mead optimisation with a finer mesh is performed, see appendix D.2.3. The resulting concentration gradients for the linear and exponential case are shown in figure 7.12. The simulated concentration profiles agree in both cases much better with the target concentration profiles than the simulated concentration profiles of the simple groove shape which were shown in figure 7.9. The remaining deviation from the target concentration profile is below 10% for most outlets for the linear concentration gradient and below 20% for most outlets for the exponential concentration gradient. The resulting parameter values of the optimisation as well as the errors are shown in table 7.3. The resulting errors for the linear and exponential concentration gradients are not directly comparable because the numerical optimisation for the exponential concentration gradient uses the relative error, while the numerical optimisation for the linear concentration gradient uses the absolute error.

Description	Parameter	Lower limit	Upper limit
Analyte inlet width	W_i	20 μm	200 μm
Groove depth	H_g	20 μm	110 μm
Groove length far side	L_f	10 μm	200 μm
Groove length near side	L_n	100 μm	450 μm
Groove offset	L_a	150 μm	340 μm
Groove midpoint	W_m	50 μm	210 μm
Groove length at the midpoint	L_m	50 μm	360 μm

Table 7.2: Lower and upper limit of the parameters for the random search for the complex groove design (ii) with uniform depth.

Parameter	Simple Linear	Simple Exponential	Complex Linear	Complex Exponential
W_i	152.9 μm	65.6 μm	143.9 μm	66.9 μm
H_g	71.6 μm	32.4 μm	98.5 μm	51.7 μm
L_f	217.7 μm	168.0 μm	195.0 μm	38.8 μm
L_n	394.5 μm	268.0 μm	149.5 μm	371.2 μm
L_a	360.4 μm	302.0 μm	249.8 μm	301.2 μm
W_m	na	na	141.2 μm	142.8 μm
L_m	na	na	377.8 μm	322.8 μm
$Error$	0.142	1.544	0.014	0.296

Table 7.3: Results of the optimisation for the simple and complex groove shape (ii) with uniform depth and for the linear and exponential concentration gradient. Parameters: Gz = 50, $\omega = 2$

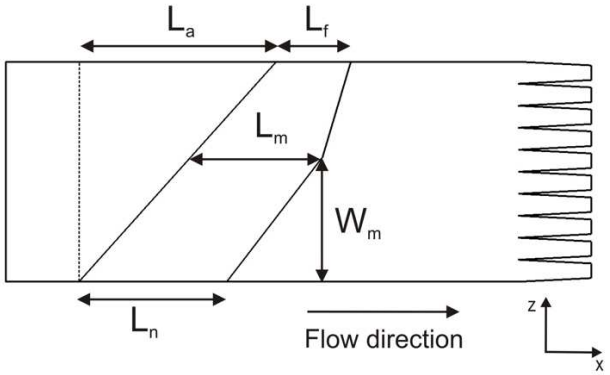

Figure 7.11: Top view schematic of the groove and channel shape for the complex groove design (ii) with uniform depth. The groove design is extruded in the y direction, i.e. perpendicular to the plane of the paper. The dotted line is a guide to the eye.

7.5 Results and discussion

The optimisation results from section 7.4 show that a microfluidic channel with one surface groove can create linear and exponential concentration gradients across the width of the microfluidic channel. However, the optimisation produces groove geometries with sub-micrometre precision and is only valid for a fixed value of the Graetz number. It is therefore important to check how robust the generated concentration gradients are to variations in the groove geometry and Graetz number.

The optimisation results from the last section are achieved with sub-micrometre precision groove geometries while the fabrication of the grooved gradient generator is limited by the accuracy of present day fabrication methods which is in the low micrometre range (see section 2.3). It is therefore necessary to check how robust the grooved gradient generator is to variations in the groove geometry. Here a simple sensitivity analysis where every groove parameter is either rounded up or down to the nearest micrometre is performed. All combinations where the 7 groove parameters given in table 7.3 are either rounded up or down result in $2^7 = 128$ combinations. For each of these 128 parameter sets the concentration profile is calculated; the resulting error is compared with the error generated by the groove which is defined by the exact optimisation result. The left plot of figure 7.13 shows the concentration profiles for the parameter sets with the smallest and the largest error as well as the concentration profile calcu-

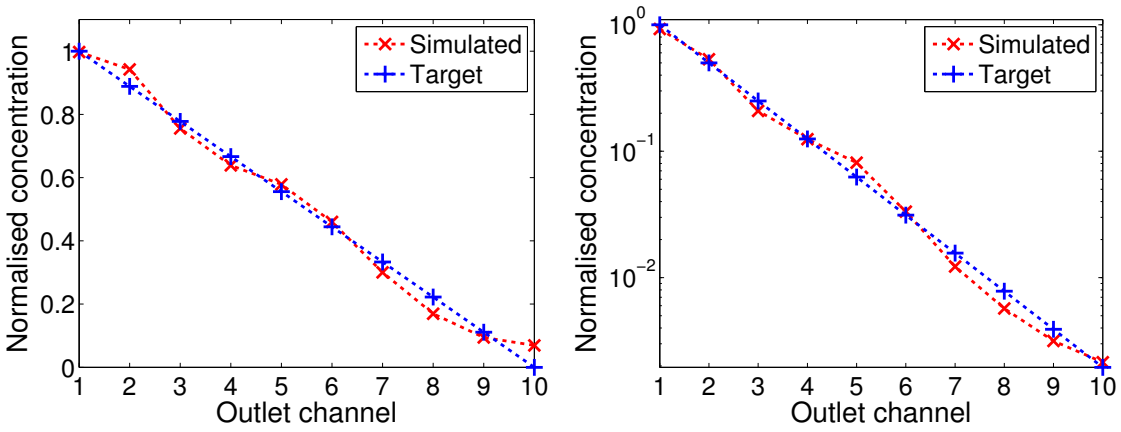

Figure 7.12: Comparison of the target concentration gradient and the simulated concentration gradient for the complex groove design (ii) with uniform depth. (left) Linear concentration gradient, (right) semi-log plot for the exponential concentration gradient. The dotted lines are a guide to the eye. Parameters: Gz = 50, $\omega = 2$

lated from the exact optimisation results. It can be seen that the three concentration profiles almost coincide and indeed the minimal and maximal error are 0.304 and 0.362, respectively, which is close to the optimal value of 0.296. This suggests that the gradient generator design is robust enough to provide a well-defined concentration gradient in a microfluidic system fabricated with current microfabrication technologies (section 2.3).

The right plot of figure 7.13 shows the simulated concentration gradient for different values of the Graetz number. While the optimisation was performed with Gz = 50, the right plot of figure 7.13 shows that the concentration profile stays almost constant for $25 \leq \text{Gz} \leq 100$. For smaller values of the Graetz number the effect of diffusion increases and the generated concentration profile becomes uniform across the width of the channel for Gz < 1. For larger values of the Graetz number (Gz > 100) the concentration at the far side of the channel, i.e. at the outlets 8, 9 and 10, decreases which is due to negligible diffusive transport in this case.

The literature about surface groove micromixers [28; 29] and the above sensitivity analysis suggested that not all groove parameters have the same influence on the secondary flow profile: the values of the groove offset L_a and of the midpoint W_m stayed close to the initial values in all performed optimisations. Furthermore, slight variations in these two parameters had a negligible effect on the concentration profile. This sug-

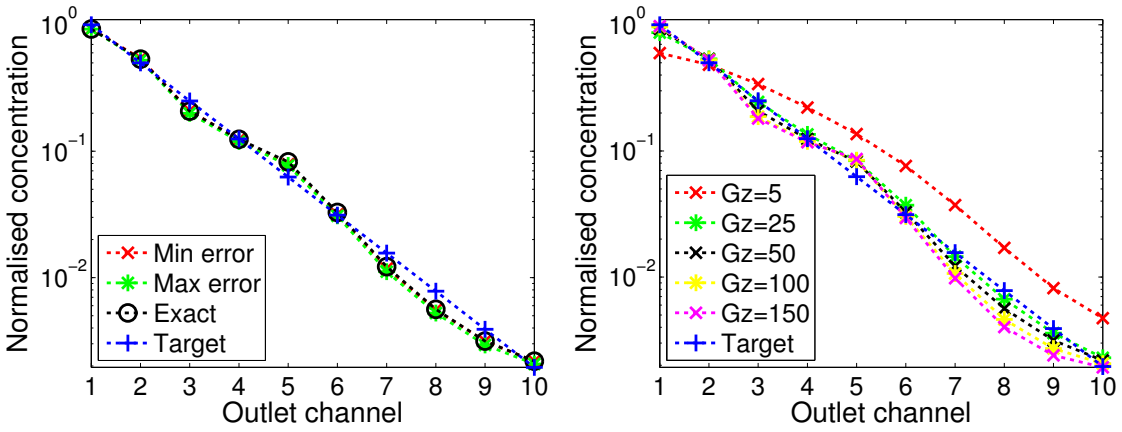

Figure 7.13: (left) Concentration profiles for varied groove geometries: the concentration profiles for the groove geometries which produce the smallest and largest deviation from the minimal error are shown. (right) Simulated concentration gradients for different values of the Graetz number Gz. The dotted lines are a guide to the eye. Parameters: (left) Gz = 50, $\omega = 2$, (right) $\omega = 2$

gests that the complexity of the design (ii) could be reduced with little impact on the outlet concentration profile. Here the groove offset and the midpoint are set to fixed values: the groove offset is set to $L_a = 300\,\mu$m and the midpoint to exactly the middle of the channel ($W_m = 150\,\mu$m). Thus the number of parameters is reduced from seven to five. This reduction in the number of parameters simplifies the model which reduces the complexity and computational cost of the numerical optimisation. Figure 7.14 shows the concentration profile resulting from the numerical optimisation. The error $E_e = 0.394$ compares well with the error $E_e = 0.296$ for the full complex model. This suggests that the simplified groove design can generate the target concentration profile with similar accuracy compared to the full complex groove design (ii) with uniform depth.

The flow profile in the microfluidic channel depends only on the ratios of the channel and groove geometries so that the results from section 7.4 can be applied to smaller or larger channels as long as the flow is stable, laminar flow, all aspect ratios stay the same and the Graetz number is Gz ≈ 50. This scaled grooved gradient generator produces the same concentration profile if all three prerequisites are fulfilled and the groove parameters are scaled by the same factor as the channel parameters. This means that the optimisation results from section 7.4 can be directly applied to channels with different

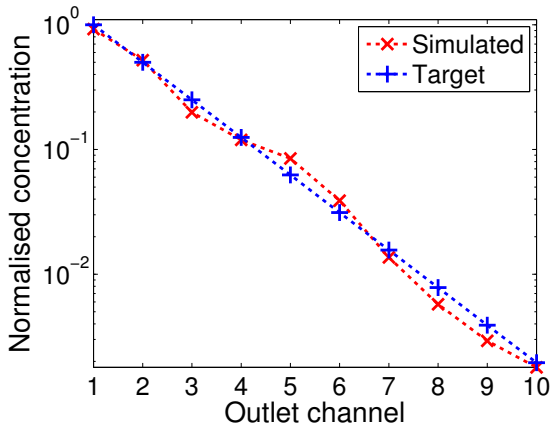

Figure 7.14: Optimisation result with the simplified groove geometry for the exponential concentration gradient. The dotted lines are a guide to the eye. Parameters: Gz = 50, $L_a = 300\,\mu$m, $\omega = 2$, $W_m = 150\,\mu$m

channel heights and are thus useful for applications which require different microfluidic channel heights. On the other hand, the optimisation results are not applicable for channels with different aspect ratios. While all numerical optimisation results shown here are for the channel geometry introduced in section 7.3, preliminary simulations for channels with a different aspect ratio showed the same behaviour (data not shown).

The generation of the concentration gradient is dependent on the number and size of the outlet channels and each optimisation is tailored to one channel design. Figure 7.15 shows the analyte concentration profile in the $y-z$ plane inside the 10 outlet channels. The height of the interface between the analyte (red) and the buffer (blue), i.e. the

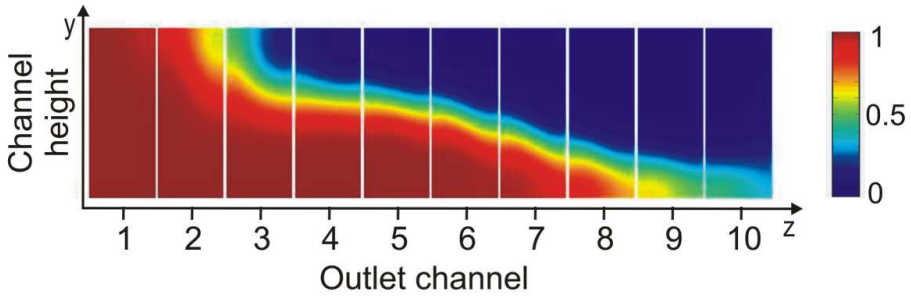

Figure 7.15: Plot of the analyte concentration in the outlet channels of a gradient generator generating a linear concentration gradient. The analyte concentration decreases from red to blue. Parameters: Gz = 50

green area in figure 7.15 where the analyte concentration is 0.5, is a good indicator for the concentration gradient across the width of the microfluidic channel. It can be seen that the interface between the analyte and buffer decreases nonlinearly across the width of the microfluidic channel. This shows that the splitting of the main channel into a finite number of outlet channels averages the analyte concentration in the outlet channels and is thus vital for the generation of the concentration gradient. Thus the numerical optimisations are only valid for one channel design and have to be repeated if the number of outlet channels is changed.

Microfluidic channels with surface grooves with uniform depth have been fabricated in a number of different ways. In the most widely used process a channel master is fabricated by two-step photolithography in SU-8 [24; 266] (section 2.3). Microfluidic channels with grooves in more than one surface can be fabricated by multi-directional 3D inclined photolithography in SU-8 [255] or by bonding of two substrates which each have surface grooves [259]. Alternative methods such as milling or laser ablation have been used to fabricate channels with surface grooves with uniform depth [259]. All these methods can be applied to the simple geometry and to the complex geometry (ii) with a non-straight groove edge. The fabrication for the complex geometry (i) with non-uniform groove depth requires full 3D fabrication methods. However, these methods are more time consuming and expensive compared to the wafer scale fabrication methods for the geometries with uniform groove depth (section 2.3).

7.6 Summary

A novel design strategy for the generation of concentration gradients across microfluidic channels based on surface groove induced secondary flow was presented. This chapter contains the design concept and numerical optimisations which show that the new design strategy can generate linear or exponential concentration gradients.

The proposed gradient generator is based on the surface groove induced secondary flow which was originally developed for the mixing of analyte streams. Here the transverse flow is utilised to transport analyte molecules from the source to the sink stream

with the aim of generating a predefined concentration gradient at the exit of the microfluidic channel. While it is well known that the secondary flow profile is dependent on the size of the surface groove, here, for the first time, the size of the surface groove is modified to achieve a controlled transport of analyte molecules across the width of the microfluidic channel. Numerical optimisations over the size of a conventional surface groove, i.e. a groove with uniform depth and straight side walls (figure 7.8), with the aim of matching the concentration profile at the exit of the microfluidic channel with a predefined concentration profile, i.e. a linear or exponential concentration gradient, across the width of the microfluidic channel suggested that this groove shape is not flexible enough to generate a predefined concentration gradient. This motivated the move to more complex groove shapes: (i) a groove with non-uniform groove depth and (ii) a groove with a non-straight groove edge but uniform depth which is shown in figure 7.11.

Numerical optimisations over the size of these complex groove shapes, with the aim of matching the concentration profile at the exit of the microfluidic channel with a predefined concentration profile showed that these two shapes, are flexible enough to generate predefined concentration gradients with sufficient accuracy. This is especially true for complex design (ii) with the non-straight groove edge but uniform depth. This design is promising because it can be fabricated with the same methods as the conventional surface grooves (see section 2.3). A simple sensitivity analysis suggested that the design is insensitive against slight variations in the device geometry that may result during the device fabrication. Furthermore, the device is also insensitive to slight variations in the device operation parameters such as flow rate and diffusion coefficient of the analytes. While the numerical models and simulations were compared to results from the literature, only a practical implementation of the proposed design can validate its applicability in lab-on-a-chip devices.

The presented design has a few drawbacks compared to the 'split and recombine' gradient generator [30]. First, the fabrication tolerances for the grooved gradient generator are lower because the shape and size of the grooves are crucial for the generation of the concentration gradient. Second, each optimisation is only valid for one Graetz number which is defined by the channel geometry, flow rate and diffusion coefficient of the analyte. However, the results from section 7.5 show that a variation of the Graetz

number by a factor of 2 produces results which are close to the results for the original Graetz number. Furthermore, the fabrication of the grooved gradient generator requires two-step photolithography which makes it slightly more complex than the fabrication of the 'split and recombine' gradient generator. On the other hand, this fabrication allows the direct integration of surface grooves into the mixing channels without any further costs. This would reduce the required mixing length and has already been applied to the 'split and recombine' gradient generator [211].

The presented design strategy for microfluidic gradient generators offers an interesting alternative to the widely used 'split and recombine' gradient generators. The grooved gradient generator requires only one mixing stage, while the 'split and recombine' gradient generator [30] requires at least $\log_2(n-1)$ mixing stages to create n different outlet channels. Thus the resulting gradient generator is much shorter and consequently requires less chip real-estate. Furthermore, the numerical optimisation depends only on the ratios of the channel and groove geometries so that the results can be applied to microfluidic system which are scaled versions of the presented device.

Chapter 8

Conclusion and suggestions for future work

8.1 Thesis conclusion

The aim of this thesis was to optimise the transport of analytes in integrated microfluidic systems and to generate guidelines for the design of more efficient microfluidic systems. The efficient transport of analytes, through the bulk of the microfluidic channel and to active components of the system, i.e. surface immobilised receptors, is becoming more important and challenging with the ever-decreasing size of integrated microfluidic systems. This thesis presents novel, theoretical approaches and design guidelines for three distinct but overlapping projects. First, the modelling and design of microfluidic affinity separation systems for the separation of proteins in chapter 4, second, the optimisation of the transport of analytes to the active surface in affinity biosensors in chapters 5 and 6, and third, the design of a microfluidic grooved gradient generator in chapter 7.

Modelling approach

The modelling in all three projects is based on the governing equations introduced in chapter 3. In the first step of the analysis these governing equations are nondimensionalised. This reveals five nondimensional parameters, i.e. the Reynolds number Re, the

Graetz number Gz, the Damköhler number Da, the nondimensional dissociation constant $\bar{K}_d$ and the adsorption capacity κ; these link the physical effects and characterise the behaviour of the microfluidic affinity system. Especially the values of the Graetz number and the Damköhler number have a large influence on the device behaviour. This work is mainly concerned with microfluidic affinity systems for the separation and detection of low copy number analytes which leads to small values of the Reynolds number ($Re < 1$) and large values of the nondimensional dissociation constant ($\bar{K}_d > 1$) and adsorption capacity ($\kappa \gg 1$). However, the Graetz and Damköhler numbers can vary considerably between different systems. In the asymptotic limits of the Graetz and Damköhler number, i.e. each of the two numbers goes to zero or infinity, the governing equations can be simplified and analysed to derive analytical solutions. These analytical solutions provide insights into the relationship between different parameters and the behaviour of the device without the need for extensive and computationally expensive numerical simulations. Furthermore, the asymptotic solutions represent the boundary for the device behaviour and are thus important for the analysis and optimisation of microfluidic affinity systems. However, the majority of these solution are for the case of continuous analyte input ($\lambda \gg 1$), see section 3.4, while this work is mainly concerned with short analyte plugs.

In the second step the solutions in the asymptotic limits are supported by numerical simulations. In contrast to the analytical solutions which provide guidelines for the device behaviour, numerical simulations provide solutions for a specific device configuration. The combination of analytical and numerical methods, which is employed in this work, brings together the respective strength of both methods: the insight into the device behaviour of the analytical solutions and the specific solution of the numerical simulations. The numerical simulations in this work are performed with the commercial FEM package COMSOL Multiphysics 3.4 (COMSOL AB, Stockholm, Sweden).

Separation of proteins

In the first project of this research an investigation was carried out on the modelling of microfluidic affinity separation systems for the separation of proteins from complex

samples, see chapter 4. The idea is that analyte molecules which specifically interact with surface immobilised receptor molecules are 'slowed down' and thus separated from non-interacting analytes. This concept is viable for systems with fast diffusion across the height of the channel ($\mathrm{Gz} \gg 1$) and high adsorption capacity ($\kappa \gg 1$) so that every analyte molecule has the same opportunity to interact with the receptor molecules immobilised at the channel wall. Under these assumptions the governing transport-reaction equations for microfluidic affinity systems, which were introduced in chapter 3, are simplified to a linear problem. This simplified, linear problem is solved analytically with the Laplace transform method.

For an efficient separation system the rate of association of the analyte molecules with the surface immobilised receptors has to be sufficiently fast, i.e. the reaction/convection number $\zeta = \mathrm{Da} \,/\, \mathrm{Gz}$ has to be large. Analysing the analytical solution for large values of the reaction/convection number revealed two simple, analytical expressions for the analyte plug velocity and dispersion in microfluidic affinity chromatography systems. Numerical simulations with the full model, i.e. 2D model with diffusion and second order kinetics, are in good agreement with the analytical solution and the analytical expressions for the plug velocity 4.36 and the plug dispersion 4.44. Furthermore, the analytical expressions agree with the established theory for column chromatography and can thus be seamlessly integrated into the design process for microfluidic affinity separation systems.

In the second part of chapter 4 the two analytical expressions which only depend on global device parameters are used to design microfluidic affinity separation systems for the efficient separation of target analytes from sample mixtures. The simple nature of the expressions allows the design of complex, multiplexed separation systems which consist of several parallel microfluidic channels which each have multiple, different receptor patches. Conventionally the design of such multiplexed separation systems requires computationally expensive numerical simulations. Here a complete, theoretical framework, which requires no computationally expensive simulations, for such a design is created. This framework consists of analytical expressions defining the channel and detection region as well as expressions specifying the separation between different analyte plugs. Microfluidic affinity separation devices designed according to this framework

have the potential to separate low-abundance proteins ($A_0 < 1\,\mathrm{nM}$) from small sample volumes ($V < 1\,\mu\mathrm{l}$).

Optimisation of biosensors

In the second project the transport of analytes to the active surface of microfluidic affinity sensors was investigated, see chapter 5. The continuous reduction of the size of microfluidic affinity sensors pushes these systems into the 'convection limited' regime where the diffusion of the analytes to the active surface and the interaction of the analytes with the surface immobilised receptors is faster than the convection of the analytes through the microfluidic channel. This leads to a depletion of the analyte plug as it moves along the sensor; thus in conventional microfluidic systems, i.e. rectangular channel geometry and constant device parameters, a high capture fraction and a uniform association of the analyte along the active sensor surface are mutually exclusive. Here three design strategies, which go beyond the design of conventional microfluidic systems and can achieve a high capture fraction of the analyte as well as a high uniformity of the bound analyte-receptor complex, were developed.

The first two design strategies depend on the modification of one device parameter while the analyte plug is flowed through the microfluidic channel. These designs which evolved from an analysis of the governing equations are based on the idea that an increasing reaction/convection number can compensate the decreasing analyte concentration and ensure a constant analyte mass transfer to the active surface and subsequent association. A reduction of the flow velocity as the analyte plug travels down the channel or an increase in the receptor concentration along the length of the active surface are the most practical approaches to increase the reaction/convection number as the analyte plug travels down the channel. Both approaches can achieve a uniform concentration of associated analyte along the sensor as well as a capture fraction up to 0.9. Each of the two approaches has its strengths and weaknesses. The variation of the flow velocity is more flexible because it can be adjusted dynamically by changing the operational parameters of the pump. On the other hand, this approach puts strong limitations on the allowed sample plug length. The variation of the receptor concentration is fixed

at the time of the device fabrication but it has the benefit of allowing arbitrarily long analyte plugs. Both approaches can improve the sensitivity of the microfluidic affinity sensor at the cost of a more complex device operation.

The third design strategy is based on a non-rectangular device geometry but constant device parameters. Here the rectangular microfluidic channel is replaced with a tapering channel. This tapering of the channel changes the flow profile so that streamlines are crossing the active/inactive boundary along the whole length of the sensor patch; this replenishes the analyte concentration over the active sensor patch of the device. In the next step, the shape of the active/inactive boundary is optimised so that the replenishment of the analyte is uniform over the length of the sensor patch. This optimisation was performed for two different shapes of the taper: linear and algebraic tapering. The resulting, optimised non-rectangular device geometry increases the uniformity of the bound analyte-receptor complex compared to the conventional systems while retaining the high capture fraction. While the resulting uniformity of the bound analyte-receptor complex along the sensor surface is lower than for the first two strategies, this strategy presents a more practical approach which requires only simple flow control and a uniform distribution of surface immobilised receptor molecules.

Adaptation of the multisensor

The design guidelines for the optimisation of analyte transport in microfluidic biosensors were applied to the redesign of the flow cell of the multisensor [21] for the sensitive detection and quantification of low levels ($A_0 \leq 1\,\mathrm{nM}$) of cytokines from small sample volumes ($V = 2\,\mu\mathrm{l}$), see chapter 6. The original multisensor has an excellent limit of detection of $1\,\mathrm{ng\,l^{-1}}$ but the sensor requires relatively large sample volumes (1 ml) and the capture fraction is below 0.01. Here the flow cell was redesigned with the aim of a reduction of the sample volume to the low microlitre range while retaining the excellent limit of detection.

The redesign is based on two steps. First, the Graetz number of the device is reduced below 1 by a decrease in the channel height and the flow velocity. This allows every analyte molecule to diffuse to the active surface and thus increases the capture fraction

of the device. In the second step the shape of the flow cell is changed from one wide channel where only 5% of the analytes are flowed directly over the sensor windows to 4 narrow channels. The shape of these narrow channels mimics the underlying waveguide so that every analyte molecule is flowed directly over the sensor windows. Together the two steps increase the capture fraction from less than 0.01 up to 0.9. However, the high capture fraction comes at the price of non-uniform association of the analyte along the sensor surface. The tapering channels which were introduced in chapter 5 were employed to increase the uniformity along the sensor surface, while retaining the high capture fraction, and thus increase the sensitivity of the detection. While the improvement in the uniformity for this approach, i.e. tapering channel geometry, is lower than for the other two approaches presented in chapter 5, the tapering channels are much easier to integrate into the device and do not require additional instrumentation.

For an optimal sensor response not only the flow cell but also the assay parameters have to be optimised. While the dissociation constant and the concentration of surface immobilised receptor molecules are defined by the cytokine-antibody pair, the antibody concentration and the number of fluorophores per antibody molecule can be varied. A simple, analytical model which describes the surface immobilised cytokine-antibody complex concentration depending on the antibody concentration was derived. This model which agrees with numerical simulations can be used to optimise the device parameters to achieve a maximal change in the concentration of the surface immobilised cytokine-antibody complex concentration for a given cytokine-antibody pair, i.e. the optimum depends on the concentration of surface immobilised cytokines and the dissociation constant. Furthermore, the numerical simulations showed that the change in the surface immobilised cytokine-antibody complex concentration is about 5% larger for the tapering channel geometry compared to a rectangular channel which is due to the improved transport of analytes to the active sensor surface.

The redesigned flow cell was fabricated in PDMS and combined with the waveguide chip. Due to the fact that the immobilisation of the cytokines to the sensor surface was incomplete before the end of the thesis, only bulk dye experiments could be performed. However, these suggest that the limit of detection of the redesigned system is sufficient for the detection of low concentrations (1 pM) of cytokines from small sample volumes

($2\,\mu$l). A drawback of the proposed design is the increased complexity of the fabrication and assembly compared to the original system.

Grooved gradient generator

In the last project a microfluidic gradient generator which has a smaller size than the available systems was designed, see chapter 7. The proposed design is based on the convection of analyte molecules across the width of the microfluidic channel by surface groove induced secondary flow. This is in contrast to the available systems which rely on diffusion to transport the analytes across the microfluidic channel.

Conventionally surface groove induced secondary flow has been employed in micromixers to improve the mixing between a source and sink stream [24]. In this application regular grooves with uniform depth and parallel side walls are used. However, the secondary flow depends directly on the shape of the surface groove and thus a modification of the groove shape will modify the secondary flow profile. In the proposed design the shape and size of the surface groove is modified with the aim to transport analyte molecules across the width of the microfluidic channel in a controlled manner; thus generating a predefined concentration gradient. Numerical optimisations over the groove size were performed for various target concentration profiles and groove designs. These optimisations showed that the conventional groove shape, i.e. uniform depth and straight side walls, is not flexible enough to create the desired concentration profiles. However, a groove design where the downstream edge consists of two straight section is flexible enough to generate a linear as well as an exponential concentration gradient.

The presented design strategy for microfluidic gradient generators offers an interesting alternative to the widely used 'split and recombine' gradient generators. Compared to these conventional gradient generators this design requires only one mixing stage which significantly reduces the requirements on size. This advantage is balanced by a slightly more complex fabrication process which requires two-step photolithography. A further drawback is the dependence on specific operational parameters, i.e. each groove shape is only valid for one Graetz number which is defined by the channel geometry, flow rate and diffusion coefficient of the analyte.

Summary

In summary, in the three projects mathematical modelling and optimisation, both analytically and numerically, were used to evaluate and improve the transport of analytes in microfluidic channels. The derived guidelines and designs can be used to understand and improve the transport of analytes in integrated microfluidic systems for bioanalysis applications.

8.2 Future work

While there has been significant progress in the development of lab-on-a-chip systems for the automated and fast analysis of proteins from small samples, significant challenges spanning many disciplines remain. One of the main challenges is the integration of working subsystems, such as pumps, separation channels and detectors, into a highly integrated and automated lab-on-a-chip system. This integration requires the concerted effort of experimentalists and theoreticians; with the latter modelling and designing these integrated systems.

While the theoretical models and design guidelines presented in this thesis were compared to existing systems, an experimental verification is missing. Ideally the experimental verification of the analytical expressions for the separation of analytes in microfluidic affinity separation systems (chapter 4) and of the optimisation of microfluidic biosensors (chapter 5) will verify the mathematical models, the simplifications and the derived design guidelines. However, even if the theoretical work is not immediately verified the experiments will give valuable insight into the device behaviour and might allow the improvement and extension of the theoretical models. For example, the theoretical models could be extended for different reaction kinetics, e.g. Michaelis-Menten kinetics [267], or by incorporating more physical effects such as steric hindrance [268] between bound analyte molecules, rough sensor surfaces [269] or the incorporation of multiple, different surface immobilised receptors in one receptor patch [141].

Beside the experimental verification there are other areas where the presented work

can be improved or extended. So far the design of the flow cell for the sensitive detection of low levels of cytokines (chapter 6) consists of 8 arbitrary sensor elements, i.e. sensor elements with arbitrary inlet-to-outlet ratios, in each of the 4 flow channels. After the proof of concept experiment, which should verify the theory developed in section 5.6 and establish the limit of detection of the system, the flow cell can be adjusted to accommodate different cytokines. If the association rate constants and surface immobilised receptor concentrations for the different cytokines are known the inlet-to-outlet ratios of the sensor elements can be chosen so that each sensor element produces a signal of similar strength, see section 5.6.2. Furthermore, the design of the waveguide chip could be revised to incorporate more sensor windows in the same space. This would allow the monitoring of more different analytes without an increase in the footprint of the device.

Further room for improvement of the multisensor (chapter 6) lays in the analysis of the CCD images. At the moment the analysis of the cytokine experiments uses the average immobilised cytokine-antibody complex concentration over the whole sensor window. However, the CCD camera provides spatial resolved information of the immobilised cytokine-antibody complex concentration. Improved image analysis which incorporates this spatially resolved information has the potential to increase the dynamic range of the sensor as well as to increase the reliability of the sensor response [247; 270]. Furthermore, the additional information in the spatially resolved information could be used to reduce the number of experiments required for the determination of rate constants from biosensor data. While current systems for the determination of rate constants, e.g. Biacore, average over the whole sensor area and require the binding data at different time steps, spatially resolved binding data can be analysed with analytical and numerical methods to potentially derive binding rate constants as well as surface immobilised receptor concentrations and diffusion coefficients from one measurement. This could prove beneficial for the analysis of fluorescence data, where only a limited number of frames can be recorded due to photobleaching.

The optimisation of biosensors in chapter 5 neglected ways to increase the analyte mass transport either through mechanical, electrical or acoustical means. One of the most interesting ways to improve the analyte mass transfer to the active surface and subsequent association is based on the effect of surface groove induced secondary flow [25;

198]. However, the existing models and systems all work in the 'entrance region' ($Gz \gg 1$) and thus the capture fraction is low. Operating these systems closer to $Gz = 1$ and modifying the surface grooves along the length of the sensor has the potential to achieve a high capture fraction and uniform distribution of associated analyte along the sensor surface. However, the evaluation and design of such systems most likely has to rely on large-scale numerical simulations.

While the presented design strategy for the generation of concentration gradients (chapter 7) is flexible enough to generate linear or exponential concentration gradients, it has not been employed for the generation of more complex, non-monotonous concentration gradients. Such more complex concentration gradients might require groove shapes with more degrees of freedom or the serial combination of several grooves. The numerical simulations for the latter, i.e. multiple grooves, would benefit from an approach similar to the microfluidic toolbox from Mott et al. [262]. This microfluidic toolbox is based on advection maps, i.e. a map which links each point of the inlet to the corresponding point at the outlet. The microfluidic toolbox has already been applied to improve the mixing by surface groove induced secondary flow [271]. An approach similar to the microfluidic toolbox would allow the fast calculation of the resulting concentration profile for serial combinations of surface grooves. Furthermore, in this work the number of outlet channels was limited to 10 but similar optimisations can be performed for a larger number of outlet channels. However, these optimisations might also require more complex groove shapes because in the current setup the outlet channels play an important role in the gradient formation, as shown in figure 7.15. Grooved gradient generators with more degrees of freedom for the shape of the groove might offer the possibility of a better fit between the target concentration gradient and the simulated concentration gradient but increase the complexity of the optimisation.

Appendix A

Asymptotic expansion

The left and ride side of the convection-diffusion equation 4.1 are linked by the nondimensional Graetz number Gz. In the asymptotic limit $\mathrm{Gz} \ll 1$ the following ansatz is made

$$A = A^{(0)} + \mathrm{Gz}\, A^{(1)} + \mathrm{Gz}^2\, A^{(2)} + \dots \tag{A.1}$$

$$X = X^{(0)} + \mathrm{Gz}\, X^{(1)} + \mathrm{Gz}^2\, X^{(2)} + \dots \tag{A.2}$$

These asymptotic expansions are inserted into the simplified equation 4.10 in the bulk of the channel

$$\begin{aligned} &\mathrm{Gz}\left(\frac{\partial A^{(0)}}{\partial t} + \mathrm{Gz}\,\frac{\partial A^{(1)}}{\partial t} + \mathrm{Gz}^2\,\frac{\partial A^{(2)}}{\partial t} + \dots\right) \\ &+ \mathrm{Gz}\left(\frac{\partial}{\partial x}(6y(1-y)A^{(0)}) + \mathrm{Gz}\,\frac{\partial}{\partial x}(6y(1-y)A^{(1)}) + \mathrm{Gz}^2\,\frac{\partial}{\partial x}(6y(1-y)A^{(2)}) + \dots\right) \\ &= \frac{\partial^2 A^{(0)}}{\partial y^2} + \mathrm{Gz}\,\frac{\partial^2 A^{(1)}}{\partial y^2} + \mathrm{Gz}^2\,\frac{\partial^2 A^{(2)}}{\partial y^2} + \dots \end{aligned} \tag{A.3}$$

and the boundary conditions 4.2 and 4.3

$$\frac{\partial A^{(0)}}{\partial y} + \mathrm{Gz}\,\frac{\partial A^{(1)}}{\partial y} + \mathrm{Gz}^2\,\frac{\partial A^{(2)}}{\partial y} + \dots = \zeta\,\mathrm{Gz}\sum_{i=0}^{\infty}\mathrm{Gz}^i\left(\sum_{j=0}^{i} A^{(j)}X^{(i-j)} - \bar{\mathrm{K}}_\mathrm{d}\,B^{(i)}\right) \tag{A.4}$$

$$\frac{\partial X^{(0)}}{\partial t} + \mathrm{Gz}\,\frac{\partial X^{(1)}}{\partial t} + \mathrm{Gz}^2\,\frac{\partial X^{(2)}}{\partial t} + \dots = -\frac{1}{\mathrm{Gz}\,\kappa}\left(\frac{\partial A^{(0)}}{\partial y} + \mathrm{Gz}\,\frac{\partial A^{(1)}}{\partial y} + \mathrm{Gz}^2\,\frac{\partial A^{(2)}}{\partial y} + \dots\right) \tag{A.5}$$

Comparing the coefficients in equation A.3 results in

$$\mathrm{Gz}^0: \qquad 0 = \frac{\partial^2 A^{(0)}}{\partial y^2} \tag{A.6}$$

$$\mathrm{Gz}^1: \qquad \frac{\partial A^{(0)}}{\partial t} + \frac{\partial}{\partial x}\left(6y(1-y)A^{(0)}\right) = \frac{\partial^2 A^{(1)}}{\partial y^2} \tag{A.7}$$

$$\mathrm{Gz}^2: \qquad \frac{\partial A^{(1)}}{\partial t} + \frac{\partial}{\partial x}\left(6y(1-y)A^{(1)}\right) = \frac{\partial^2 A^{(2)}}{\partial y^2} \tag{A.8}$$

and so on

The solution for equation A.6 can be calculated by integrating twice with respect to y and is given by

$$A^{(0)}(x,y,t) = f^{(0)}(x,t) + g^{(0)}(x,t)y \tag{A.9}$$

The upper boundary condition $A_y^{(0)} = 0$ implies that $g^{(0)}(x,t) = 0$. From this it follows that $A^{(0)}(x,t) = f^{(0)}(x,t)$ depends only on x and t and is independent of y. With this $A^{(0)}$ the solution of equation A.7 can be found by direct integration with respect to y

$$A^{(1)}(x,y,t) = f^{(1)}(x,t) + g^{(1)}(x,t)y + f_t^{(0)}\frac{y^2}{2} + A_x^{(0)}y^3 - A_x^{(0)}\frac{y^4}{2} \tag{A.10}$$

With the convention $B^{(i)} = 1 - X^{(i)}$ the boundary condition at the active surface is given by

$$\left.\frac{\partial A^{(1)}}{\partial y}\right|_{y=0} = g^{(1)} = \zeta\left(A^{(0)}X^{(0)} - \bar{\mathrm{K}}_\mathrm{d}(1 - X^{(0)})\right) \tag{A.11}$$

and the boundary condition at $y = 1$ is given by

$$\left.\frac{\partial A^{(1)}}{\partial y}\right|_{y=1} = g^{(1)} + A_t^{(0)} + A_x^{(0)} = 0 \tag{A.12}$$

Combining these two boundary conditions gives an equation for $A^{(0)}$

$$A_t^{(0)} + A_x^{(0)} = -\zeta\left(A^{(0)}X^{(0)} - \bar{\mathrm{K}}_\mathrm{d}(1 - X^{(0)})\right) \tag{A.13}$$

which describes a travelling wave with speed 1 and varying amplitude.

The reaction equation A.5 for the first order of Gz is given by

$$\frac{\partial X^{(0)}}{\partial t} = X^{(0)}\left(-\frac{\zeta}{\kappa}A^{(0)}(x,t) - \frac{\bar{\mathrm{K}}_\mathrm{d}\,\zeta}{\kappa}\right) + \frac{\bar{\mathrm{K}}_\mathrm{d}\,\zeta}{\kappa} \tag{A.14}$$

With the integrating factor $h(t) = e^k e^{\int(-\frac{\zeta}{\kappa}A^{(0)}(x,t) - \frac{\bar{\mathrm{K}}_\mathrm{d}\,\zeta}{\kappa})dt}$ the solution is given by

$$X^{(0)}(x,t) = \frac{1}{e^{\int_0^t\left(-\frac{\zeta}{\kappa}A^{(0)}(x,t) - \frac{\bar{\mathrm{K}}_\mathrm{d}\,\zeta}{\kappa}\right)dt}}\left(\int_0^t \frac{\bar{\mathrm{K}}_\mathrm{d}\,\zeta}{\kappa}e^{\int_0^t(-\frac{\zeta}{\kappa}A^{(0)}(x,t) - \frac{\bar{\mathrm{K}}_\mathrm{d}\,\zeta}{\kappa})dt}dt + K\right) \tag{A.15}$$

For the simple case with no detachment this reduces to

$$X^{(0)}(x,t) = e^{-\int_0^t \frac{\zeta}{\kappa} A^{(0)}(x,t)dt} \tag{A.16}$$

For $\kappa \gg 1$ the receptor concentration $X^{(0)}$ stays almost constant. With this and the boundary condition

$$A^{(0)}(0,t) = \hat{\mathrm{H}}(t)\,\hat{\mathrm{H}}(\lambda - t) \tag{A.17}$$

equation A.13 can be solved

$$A^{(0)}(x,t) = \exp(-\zeta x)\,\hat{\mathrm{H}}(t-x)\,\hat{\mathrm{H}}(x - t + \lambda) \tag{A.18}$$

This is a travelling wave with speed 1 where the amplitude is damped by the factor $\exp(-\zeta x)$.

Appendix B

Implementation of the transport-reaction model

The numerical simulations of the transport-reaction problems were performed with the commercial finite element package COMSOL Multiphysics 3.4 (COMSOL AB, Stockholm, Sweden). This software package allows the combined simulation of various physical effects in a uniform environment which is beneficial in the here studied case of a combined fluid dynamics, transport and reaction problem. Furthermore, COMSOL Multiphysics is seamlessly integrated into the Matlab environment (The Mathworks, Natick, MA, USA). This facilitates the use of the extensive Matlab library of analysis and plotting tools.

During the course of this thesis numerical simulations were performed for the full 3D problem as well as for simplified problems. Here the implementation of these models is presented. The implementation follows a two step process. In the first step the flow profile is calculated. In the second step which requires the solution of the first step the concentrations of the analyte and the surface immobilised receptor are simulated. All numerical simulations are performed with the nondimensionalised system unless otherwise stated. All simulations are performed on a computer with a Dual Core AMD Opteron Processor 880 2.4 GHz and 8 GB of main memory.

B.1 Side view model

In the side view model the analyte concentration is assumed to be uniform over the width of the microfluidic channel so that it is sufficient to simulate the solution in the $x - y$ plane. This assumption is used in chapter 4 and for the design optimisation in rectangular channels in chapter 5. The geometry and the system of equations are setup in the graphical user interface (GUI) of COMSOL and then exported to Matlab. This allows the control of the numerical simulations from Matlab which is beneficial for the subsequent analysis.

The nondimensional channel geometry is given by a rectangle with height 1 and length 1.2. The active area of the affinity system is at the bottom of the channel between $x = 0.1$ and $x = 1.1$. The increase of the channel length removes the edges of the active area from the channel inlet and outlet which reduces potential adverse effects on the numerical simulation and allows the formation of the analyte plug before it reaches the active area. The flow profile in this geometry is parabolic over the height of the channel and given by equation 3.7.

The convection-diffusion equation 3.18 in the bulk of the microfluidic channel is defined through the transient 'Convection and Diffusion' model. In the 'Subdomain Settings' dialog box the x-velocity is defined as the parabolic flow profile. The diffusion coefficient for the x coordinate is given by $D_x = \frac{D}{UL}$ and the diffusion coefficient for the y coordinate is given by $D_y = \frac{LD}{H^2U}$. The boundary conditions are given by 'Concentration' at the channel inlet, 'Convective flux' at the channel outlet, 'Insulation/Symmetry' at non-active channel walls and 'Flux' at the active channel wall. This flux which is defined through a boundary expression links the model for the bulk analyte concentration and the bound analyte concentration. The concentration at the channel inlet is defined by a step function which is 1 for $t < \lambda$ and zero otherwise. The differential equation 3.20 for the bound analyte expression at the active interface, i.e. between $x = 0.1$ and $x = 1.1$, is defined through the transient 'Weak Form, Boundary' model. See the example script in section B.1.1 for details about the implementation of the 'Weak Form, Boundary' model and the 'Flux' at the active channel wall.

In the first instance the geometry is meshed with the default values. The two coupled differential equations are then solved with the transient 'Spooles' solver.

B.1.1 Example script

```
% ------------------------------------------------------------------
% Variables
tu=5;           % upper timelimit for the solver
H = 10e-6;      % height [m]
L = 0.2e-2;     % length [m]
Umean = 1e-4;   % mean velocity [m s^{-1}]
D = 1e-10;      % Diffusion coefficient [ m^2 s^{-1}]
A0 = 1e-5;      % initial analyte concentration [mol m^{-3}]
X0 = 1e-8;      % surface receptor concentration [mol m^{-2}]
ka = 250;       % on rate constant [m^3 mol^{-1} s^{-1}]
kd =0.1;        % off rate constant [s^{-1}]

% ------------------------------------------------------------------
% Nondimensional numbers
Zeta = ka*L*X0/(Umean*H);   % reaction/convection number
Kd = kd/(A0*ka);            % nondimensional dissociation constant
Kappa = X0/(A0*H);          % adsorption capacity
Gz = H^2*Umean/(L*D);       % Graetz number
Alpha = L/H;                % channel aspect ratio
Lambda = 1;                 % nondimensional plug length

% ------------------------------------------------------------------
% COMSOL version
flclear fem
clear vrsn
vrsn.name = 'COMSOL 3.4';
vrsn.ext = 'a';
vrsn.major = 0;
vrsn.build = 603;
vrsn.rcs = '$Name:  $';
vrsn.date = '$Date: 2008/12/03 17:02:19 $';
fem.version = vrsn;

% ------------------------------------------------------------------
% Geometry
g1=rect2(1.2,1,'base','corner','pos',[-0.1,0]);
parr={point2(0,0)};
g2=geomcoerce('point',parr);
parr={point2(1,0)};
g3=geomcoerce('point',parr);

% Analyzed geometry
clear p s
```

```
p.objs={g2,g3};
p.name={'PT1','PT2'};
p.tags={'g2','g3'};

s.objs={g1};
s.name={'R1'};
s.tags={'g1'};

fem.draw=struct('p',p,'s',s);
fem.geom=geomcsg(fem);

% ------------------------------------------------------------------
% Constants
fem.const = {'zeta',Zeta, ...
  'kd',Kd, ...
  'kappa',Kappa, ...
  'Dx',1/(Gz*Alpha^2), ...
  'Dy',1/Gz, ...
  'lambda',Lambda};

scaling = sqrt(Alpha);

% ------------------------------------------------------------------
% Initialize mesh
fem.mesh=meshinit(fem, ...
                  'hauto',3, ...
                  'xscale',scaling);

% ------------------------------------------------------------------
%% initialize the equations
% (Default values are not included)

% Application mode 1
% Convection/Diffusion problem
clear appl
appl.mode.class = 'FlConvDiff';
appl.sshape = 2;
appl.assignsuffix = '_cd';
clear bnd
bnd.c0 = {0,'(t<lambda)',0,0};
bnd.N = {0,0,'-react_surf',0};
bnd.type = {'N0','C','N','Nc'};
bnd.ind = [2,1,1,3,1,4];
appl.bnd = bnd;
clear equ
equ.dtensor = {{{'Dx';'Dy'}}};
equ.u = 'y*(1-y)*6';
equ.dtype = 'aniso';
equ.ind = [1];
appl.equ = equ;
```

```
fem.appl{1} = appl;

% Application mode 2
% Reaction at the active boundary
clear appl
appl.mode.class = 'FlPDEWBoundary';
appl.dim = {'cs','cs_t'};
appl.sshape = 2;
appl.assignsuffix = '_wb';
clear prop
clear weakconstr
weakconstr.value = 'off';
weakconstr.dim = {'lm2','lm3'};
prop.weakconstr = weakconstr;
appl.prop = prop;
clear bnd
bnd.dweak = {0,'cs_test*cs_time'};
bnd.usage = {0,1};
bnd.weak = {0,'cs_test*react_surf_cs'};
bnd.ind = [1,1,1,2,1,1];
appl.bnd = bnd;
fem.appl{2} = appl;
fem.frame = {'ref'};
fem.border = 1;
fem.outform = 'general';
clear units;
units.basesystem = 'SI';
fem.units = units;

% Boundary settings
clear bnd
bnd.ind = [1,1,1,2,1,1];
bnd.dim = {'c','cs'};

% Boundary expressions
bnd.expr = {'react_surf',{'','zeta*(c*(1-cs)-kd*cs)'}, ...
  'react_surf_cs',{'','zeta*(c*(1-cs)-kd*cs)/kappa'}};
fem.bnd = bnd;

% ODE Settings
clear ode
clear units;
units.basesystem = 'SI';
ode.units = units;
fem.ode=ode;

% ------------------------------------------------------------------
% Solve the system of equations
% Multiphysics
fem=multiphysics(fem);
```

```
% Extend mesh
fem.xmesh=meshextend(fem);

% Solve problem
fem.sol=femtime(fem, ...
                'solcomp',{'c','cs'}, ...
                'outcomp',{'c','cs'}, ...
                'blocksize','auto', ...
                'tlist',[colon(0,0.05,tu)], ...
                'tout','tlist', ...
                'linsolver','spooles');
```

B.2 Top view model

In the top view model the analyte concentration is assumed to be constant over the height of the channel so that it is sufficient to simulate the device in the $x - z$ plane. This assumption is used for the non-rectangular channel designs in chapter 5 and 6.

The nondimensionalisation in this case is performed with $L = W = H$ so that the sensor element, see figure 5.15, can be directly imported into COMSOL. The flow profile in this geometry is calculated through the Laplace equation which is defined by the 'Laplace's Equation' model with a pressure drop between the inlet and outlet. The flow profile in the channel is related to the pressure field p by $\mathbf{u} = (-p_x, -p_z)$. The pressure drop between the inlet and outlet is chosen so that $-p_x = 1$ at the channel outlet.

The governing equations including diffusion are given by

$$A_t + uA_x + wA_z = -\chi(x,z)\zeta(A(1-B) - \bar{\mathrm{K}}_\mathrm{d}\, B) + \frac{D}{LU} \bigtriangledown^2 A \tag{B.1}$$

$$B_t = \chi(x,z)\frac{\zeta}{\kappa}(A(1-B) - \bar{\mathrm{K}}_\mathrm{d}\, B) \tag{B.2}$$

where $\chi(x,z) = 1$ if (x,z) is in the active area and zero otherwise. Equation B.1 is defined as a 'Convection and Diffusion' model. The boundary conditions are given by 'Concentration' at the channel inlet, 'Convective flux' at the channel outlet and 'Insulation/Symmetry' at the channel walls. The concentration at the channel inlet is defined by a step function which is 1 for $t < \lambda$ and zero otherwise. In the 'Subdomain

Settings' dialog box the diffusion coefficient is set to $\frac{D}{LU}$, the flow velocity in the x direction to $-p_x$ and the flow velocity in the z direction to $-p_z$. In the active area of the channel the 'Reaction rate' is defined by the flux

$$flux = \zeta(A(1-B) - \bar{\mathrm{K}}_{\mathrm{d}}\, B) \tag{B.3}$$

which links equation B.1 with equation B.2 and is defined as a 'Subdomain Expressions'. The equation B.2 for the bound analyte is defined through the 'Diffusion' model. Here all boundary conditions are set to 'Insulation/Symmetry'. In the 'Subdomain Settings' dialog box the diffusion coefficient is set to zero and the 'Reaction rate' is defined by the flux B.3 divided by κ.

The first simulation is performed with the default mesh. The simulation is performed in a two step process. First, the stationary 'Spooles' solver is used to calculate the pressure field p. Second, the transient 'Spooles' solver is used to calculate the unbound analyte concentration A and the bound analyte concentration B.

B.3 3D model

The full 3D model of the transport-reaction problem is given by the Navier-Stokes equations 3.1-3.2 and the nondimensional convection-reaction equations 3.18-3.20 with suitable boundary conditions. The nondimensionalisation in this case is performed with $L = W = H$.

The main difference between the side view model and the 3D model is the calculation of the flow profile. In the 3D model the flow profile is calculated from the complete Navier-Stokes equations. The fluid properties are defined by choosing the 'Library material: Water, liquid'. The boundary conditions are a defined pressure and no viscous stress at the inlet and outlet, and the no slip boundary condition at the channel walls.

The convection-diffusion equation 3.18 in the bulk of the microfluidic channel is defined through the transient 'Convection and Diffusion' model. In the 'Subdomain Settings' dialog box the flow velocity is defined as the solution of the Navier-Stokes equations. The diffusion coefficient is given by $\frac{D}{UL}$. The boundary conditions are given

by 'Concentration' at the channel inlet, 'Convective flux' at the channel outlet, 'Insulation/Symmetry' at non active channel walls and 'Flux' at the active channel wall. The concentration at the channel inlet is defined by a step function which is 1 for $t < \lambda$ and zero otherwise. The boundary flux which is defined through a boundary expression links the model for the bulk analyte concentration and the bound analyte concentration. The differential equation 3.20 for the bound analyte concentration at the active interface is defined through the transient 'Weak Form, Boundary' model. See the implementation of the side view model in section B.1 for details.

In the first instance the geometry is meshed with the default values. The simulation is performed in a two step process. First, the Navier-Stokes equations are solved with the default static solver ('gmres') and then the coupled convection-diffusion-reaction problem is solved with the transient 'spooles' solver.

B.4 Meshing and validation of the implementation

The default mesh generated by COMSOL is a good starting point for the simulations but it is often too coarse to achieve sufficiently accurate solutions. A mesh convergence study was performed to deduce the necessary mesh size. First, the numerical simulation was performed on a coarse mesh. Second, the mesh is refined and the simulation is repeated on the finer mesh. The two simulation results are compared. If the two simulations agree with sufficient accuracy the coarse mesh is chosen for the simulations. If the two simulation results are different the process is repeated with the finer mesh as the new coarse mesh. Figure B.1 shows the results for the side view model.

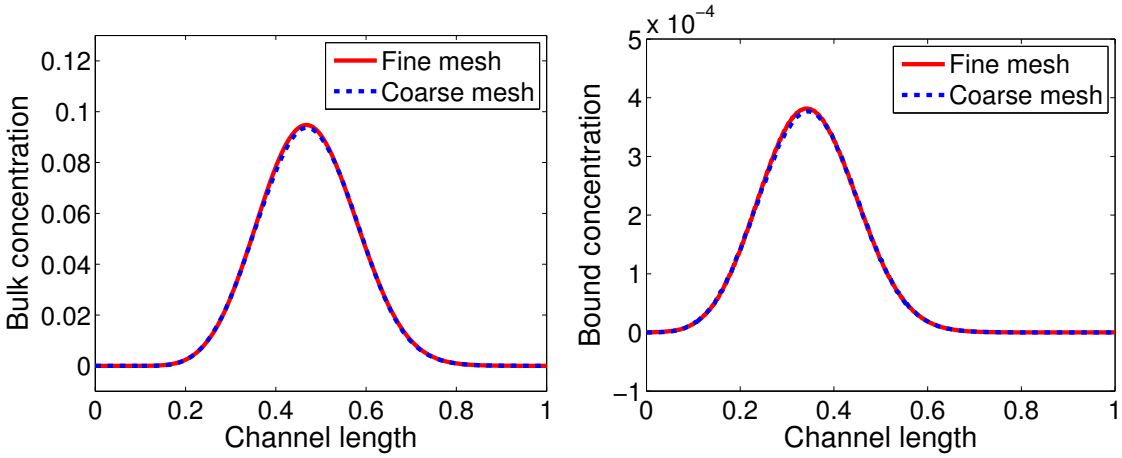

Figure B.1: Plot comparing the numerical simulations for a coarse and fine mesh. (left) Bulk analyte concentration A and (left) bound analyte concentration B. Parameters: $\mathrm{Gz} = 0.05$, $\kappa = 250$, $\bar{\mathrm{K}}_\mathrm{d} = 250$, $\lambda = 0.05$, $t = 0.8$, $\zeta = 25$

Appendix C

Sensor elements

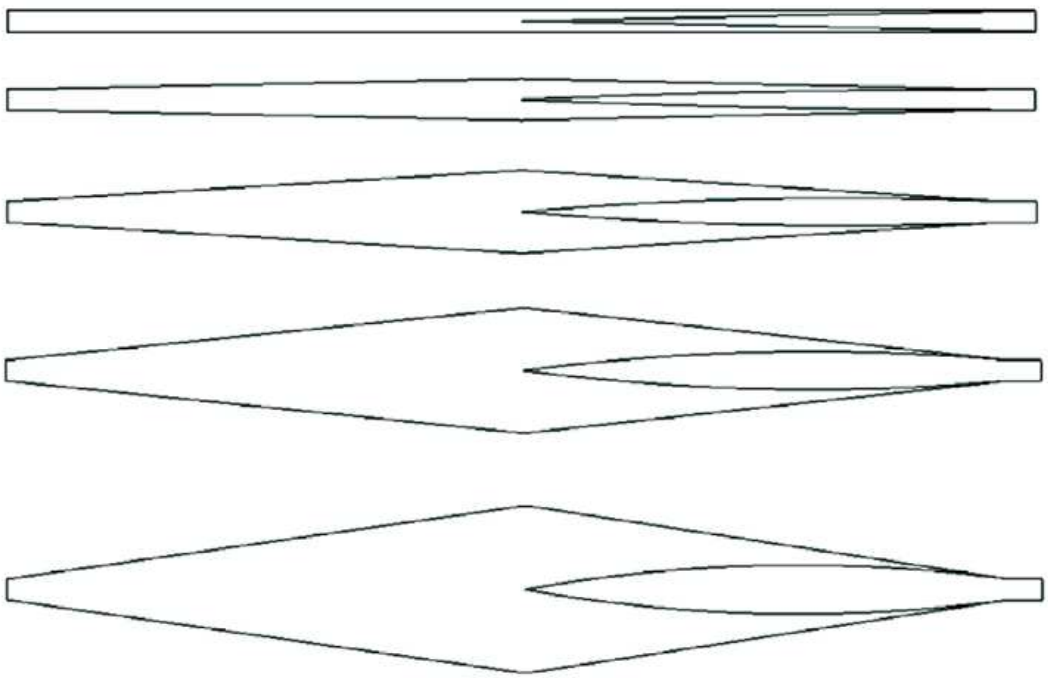

Figure C.1: Top view of the sensor elements for the linear tapering from section 5.6. The sensor elements are designed to fit over the waveguide chip from the multisensor as shown in figure 5.15. Each sensor element consists of a widening section, a tapering section and the active area. From top to bottom: 'linear$_1$', 'linear$_2$', 'linear$_4$', 'linear$_6$', 'linear$_8$'

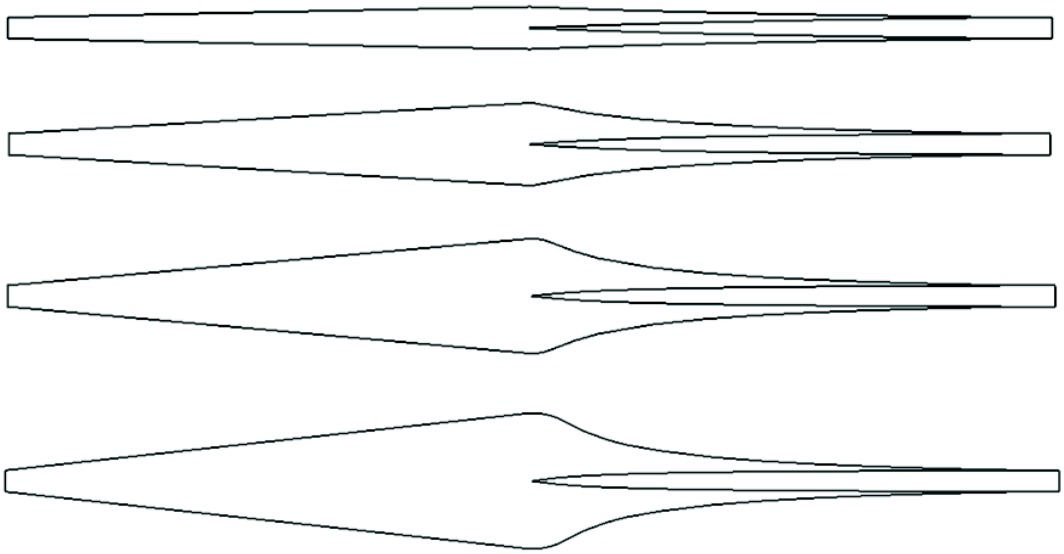

Figure C.2: Top view of the sensor elements for the algebraic tapering from section 5.6. The sensor elements are designed to fit over the waveguide chip from the multisensor as shown in figure 5.15. Each sensor element consists of a widening section, a tapering section and the active area. From top to bottom: 'algebraic$_2$', 'algebraic$_4$', 'algebraic$_6$', 'algebraic$_8$'

Appendix D

Numerical optimisation for the grooved gradient generator

D.1 Optimisation routine

In this section the Matlab scripts for the random search and the Nelder-Mead optimisation are presented. All simulations are performed on a computer with a Dual Core AMD Opteron Processor 880 2.4 GHz and 8 GB of main memory.

D.1.1 Random search

```
% Grooved gradient generator
% Random search of the parameter space
clear;

%% initialize lower and upper bounds of the parameters
% a=[inlet_width g_depth g_length_far g_length_near g_angle
% m_width m_length];
lb=[40  20   10  100  150 50    50];
ub=[200 110  200 450  340 210   360];

%% loop to call random points
for indux = 1:1400,
    % generate random groove shape
    a = lb + (ub-lb).*rand(1,7);
```

```
    % calculate the square error between target and simulated
    % concentration
    tic;
    error = comsol_complex_lin(a);
    zeit=toc;
    % save the parameters, error and computation time
    Asave_lin(indux,:) = [a error zeit];
    save('random_lin_31072009.mat','Asave_lin','-ascii');
end;
```

D.1.2 Nelder-Mead optimisation

```
% Grooved gradient generator
% Nelder-Mead optimisation starting from the best points of the
% random search of the parameter space
clear;

%% initialise starting points from the random search
data_lin=load('random_start_lin_31072009.mat','-ascii')

%% First Nelder-Mead optimisation
for ii=1:3,
a1=data_lin(ii,1:7)
options = struct('Display','iter','MaxFunEvals',400);
[x,fval,exitflag,output]=fminsearch('comsol_complex_lin',a1,options)
x_pre(ii,:)=x;
fval_pre(ii)=fval;
end;
save('best_lin.mat','x_pre','fval_pre','-ascii');

%% Second Nelder-Mead starting from the best point of the first
[val, indix]=min(fval_pre);
opt = struct('Display','iter','MaxFunEvals',500);
[x,fval,exitflag,output]=fminsearch('comsol_complex_lin',x_pre(indix,:),opt)

save('winner_lin.mat','x','fval','-ascii');
```

D.2 COMSOL model

The COMSOL script which is called by the optimisation routine, e.g. the script 'comsol_complex_lin' in the example in section D.1, is created in a two stage process. In the first stage the GUI of COMSOL is used to create the geometry, physics model, mesh and solver setup. This COMSOL model is then exported as a Matlab script which is

modified by hand in the second stage. The main steps in this second stage are the insertion of variables defining the device geometry and the calculation of the square error between the target concentration profile and the simulated concentration profile.

D.2.1 GUI model

The COMSOL GUI provides a simple and easy to learn interface for the setup of complex multiphysics problems in a step by step manner. First, the 3D geometry is defined through a simple computer-aided design tool. For the system considered here, see figure 7.8, the geometry is uniform in the y direction. Using this the outline of the device in the $x - z$ plane is drawn (see figure 7.11) and extruded in the y direction.

In the second step, the physics models for the incompressible Navier-Stokes equations 3.1 and 3.2 and the convection-diffusion equation 3.12 are defined. Both are available from the 'Model Navigator' in the basic COMSOL module. The simulations are performed for aqueous solutions at room temperature ($T = 25^\circ$ C) so the density and dynamic viscosity of water are given by: $\rho = 997.13\,\mathrm{kg\,m^{-3}}$, $\mu = 0.891 \times 10^{-3}\,\mathrm{kg\,m^{-1}\,s^{-1}}$. The boundary conditions are set to a constant pressure at the inlet ('Pressure, no viscous stress'), atmospheric pressure at the outlet ('Pressure, no viscous stress') and the no-slip condition at the channel walls. The solution of the Navier-Stokes equations is used as the velocity vector in the convection-diffusion equation. The boundary conditions for the convection-diffusion equation are set to 'Insulation/Symmetry' at the channel walls, 'Convective flux' at the outlets and 'Concentration' at the channel inlet. The concentration profile at the channel inlet defines the width of the analyte and buffer stream, i.e. the concentration in the analyte stream is set to 1 while the concentration in the buffer stream is set to 0. The step in the inlet concentration boundary condition poses problems for the numerical solution of the convection-diffusion equation. By replacing the discontinuous step function with a smooth step function the numerical properties of the system are improved. The resulting system is more stable and the convergence properties are enhanced. Furthermore, in the physical system the discontinuous step in the input concentration is smoothed to a continuous step immediately after the two streams merge. Here the inbuilt function 'flc1hs' which is a smoothed Heaviside function

Variable	Description
c_width	Channel width W
c_height	Channel height H
c_length	Channel length L
g_start	Groove start
inlet_width	Analyte stream width W_i
g_depth	Groove depth H_g
f_length	Groove length far side L_f
n_length	Groove length near side L_n
angle	Groove offset L_a
m_width	Groove midpoint W_m
m_length	Groove length at midpoint L_m

Table D.1: Groove parameters in the COMSOL script

without overshoot is used. The distance over which the smoothing occurs is set to $3\,\mu$m. This is a reasonable choice because for a diffusion coefficient $D = 5 \times 10^{-11}\,\mathrm{m^2\,s^{-1}}$ the analytes diffuse this distance in less than 0.2 s.

The meshing of the geometry is performed with the default values provided by COMSOL. Later, this default mesh is analysed and improved to achieve the desired accuracy in the solution. The last step, the solving of the physics model is performed sequentially. First, the Navier-Stokes equations are solved with the default static solver ('gmres') and then the convection-diffusion equation is solved with the static 'spooles' solver. The completed GUI model is then exported as a Matlab script.

D.2.2 Modification of the GUI model

The Matlab script containing the GUI model is modified by hand. The numerical values defining the channel and groove geometry are replaced by the variables given in table D.1. This simplifies the modification of the channel and groove dimensions and allows the optimisation over the groove parameters. The additional variables 'inlet_mesh',

'wall_mesh_fine' and 'wall_mesh' which define the maximal mesh size at the channel inlet, the channel outlets and the channel wall, respectively, are introduced.

Furthermore, the area integral of the velocity weighted analyte concentration at the channel outlets is calculated and normalised with the size of the channel outlets. In the last step, the square error between the target concentration profile and the simulated concentration profile is calculated and returned to the optimisation routine.

D.2.3 Meshing and model validation

Meshing is very important for the accuracy and convergence of FEM simulations. This is especially true for 3D simulations. However, the problem considered here is numerically more stable than the problems considered in chapters 4 and 5 because the only concentration gradient is across streamlines and not along streamlines.

Here two strategies for the mesh generation are used to ensure an accurate solution of the problem. First, the maximal size of the mesh elements at the boundaries of the microfluidic channel, especially at the inlet and the outlet channels, is restricted. This is necessary because the flow velocity changes considerably close to the channel walls and the interface between the analyte and buffer is most important at the inlet and outlets. The second strategy uses the adaptive mesh refinement from COMSOL. Using this in the calculation of the convection-diffusion problem refines the mesh at the interface between the two input streams where the largest gradient in the concentration occurs.

A mesh convergence study which compares the simulated concentration gradient for different mesh sizes was performed. A preliminary mesh convergence study was performed with a non-optimised surface groove. This study suggested that 1.3×10^5 mesh elements are sufficient for an accuracy of 10^{-3} in the normalised outlet concentration c_i. The optimisations for the linear and exponential concentration gradients were performed with this mesh. A further mesh convergence study was performed for the optimised surface grooves. Here, the mesh size was increased from about 10^5 elements to 6×10^5 elements which increases the simulation time from about 6 minutes to almost 4

Mesh size	Mean error	Standard deviation	Computation time
10^5	3.8×10^{-3}	2.6×10^{-3}	6 min
1.3×10^5	2.3×10^{-3}	1.5×10^{-3}	8 min
2×10^5	2.0×10^{-3}	1.7×10^{-3}	13 min
3×10^5	1.1×10^{-3}	1.2×10^{-3}	29 min

Table D.2: Comparison of the simulation results for the coarse meshes with the fine mesh for the linear concentration gradient.

hours. The solution at the finest mesh is assumed to be the most accurate solution against which the solutions from the coarser meshes are compared. The mean error and standard deviation of the solutions of the coarse mesh simulations compared to the fine mesh simulation are shown in table D.2. This mesh convergence study shows that for the linear concentration gradient a mesh with 1.3×10^5 elements produces a result with sufficient accuracy. However, for the exponential concentration gradient which requires an accuracy to 3 significant figures a finer mesh is required. The results from table D.2 suggest that a mesh with about 2×10^5 elements is sufficient for the exponential concentration gradient. Thus for the exponential concentration gradient a further Nelder-Mead optimisation with this finer mesh and the results of the first optimisation as initial values is performed. This optimisation converges in less than 150 iterations. The results of this optimisation were compared to the results of the finest mesh with 6×10^5 elements. The mean error over the 10 outlet channels is 4.3×10^{-4} with a standard deviation of 4.3×10^{-4} so that the mesh with 2×10^5 elements is sufficient for this exponential concentration gradient.

The calculated flow profile corresponds qualitatively with the flow profile presented in previous publications [272]. Furthermore, the magnitude of the transverse flow matches the magnitude of the transverse flow calculated by Lynn and Dandy [29]. This suggests that the simulation results are a valid representation of the actual device behaviour.

D.2.4 Example COMSOL script

```
% COMSOL Multiphysics Model M-file
```

```
% Generated by COMSOL 3.5a (COMSOL 3.5.0.606, $Date: 2009/04/29 09:11:29 $)

% generates the channel and groove geometry, solves the two partial
% differential equations and calculates the error between the target and
% simulated concentration profile

function error_I = comsol_complex_lin(b)

% scaling parameter
scal = 1;

%b=[45.6467    48.7000    42.4467   222.9467   130.3333 ]

% scale the geometry
a=1e-6*b*scal;
flclear fem

%% constants
wall_mesh = 30e-6;
wall_mesh_fine = 17e-6;
inlet_mesh = 15e-6;

%% initialise the geometry parameters
c_width = 300e-6*scal;
c_height = 75e-6*scal;
c_length = 700e-6*scal;
g_start = c_length/7;

inlet_width = a(1);
g_depth = a(2);
f_length = a(3);
n_length = a(4);
angle = a(5);
m_width = a(6);
m_length = a(7);

%% Initialise COMSOL version 3.4
clear vrsn
vrsn.name = 'COMSOL 3.4';
vrsn.ext = '';
vrsn.major = 0;
vrsn.build = 248;
vrsn.rcs = '$Name:  $';
vrsn.date = '$Date: 2007/10/10 16:07:51 $';
fem.version = vrsn;

% Geometry 2
% bulk of the channel
carr={curve2([0,c_length],[0,0],[1,1]), ...
  curve2([c_length,c_length],[0,c_width],[1,1]), ...
```

```
  curve2([c_length,0],[c_width,c_width],[1,1]), ...
  curve2([0,0],[c_width,0],[1,1])};
g1=geomcoerce('solid',carr);

% outlet channels
carr={curve2([c_length,c_length+c_length/7],[c_width,c_width-c_width/100],...
    [1,1]),curve2([c_length+c_length/7,c_length+c_length/7], ...
    [c_width-c_width/100,c_width-c_width*9/100],[1,1]), ...
    curve2([c_length+c_length/7,c_length],...
    [c_width-c_width*9/100,c_width-c_width/10],[1,1]), ...
    curve2([c_length,c_length],[c_width-c_width/10,c_width],[1,1])};
g2=geomcoerce('solid',carr);
garr=geomarrayr(g2,0,-c_width/10,1,10);
[g3,g4,g5,g6,g7,g8,g9,g10,g11,g12]=deal(garr{:});
g13=geomcomp({g1,g2,g4,g5,g6,g7,g8,g9,g10,g11,g12},'ns',{'g1','g2','g4', ...
'g5','g6','g7','g8','g9','g10','g11','g12'},'sf', ...
'g1+g2+g4+g5+g6+g7+g8+g9+g10+g11+g12','edge','none');
g14=geomdel(g13);

% extrude to channel height
g15=extrude(g14,'distance',[c_height],'scale',[1;1],'displ',[0;0], ...
'twist',[0],'face','none','wrkpln',[0 1 0;0 0 1;0 0 0]);

% groove geometry
carr={curve2([g_start,g_start+angle],[0,c_width],[1,1]), ...
  curve2([g_start+angle,g_start+angle+f_length],[c_width,c_width],[1,1]),...
  curve2([g_start+angle+f_length,g_start+m_width/c_width*angle+m_length],...
  [c_width,m_width],[1,1]), ...
  curve2([g_start+m_width/c_width*angle+m_length,g_start+n_length], ...
  [m_width,0],[1,1]), curve2([g_start+n_length,g_start],[0,0],[1,1])};
g16=geomcoerce('solid',carr);
g17=extrude(g16,'distance',[-g_depth],'scale',[1;1],'displ',[0;0], ...
'twist',[0],'face','none','wrkpln',[0 1 0;0 0 1;0 0 0]);

% Geometry 3
carr={curve2([inlet_width,inlet_width],[0,c_height],[1,1])};
g20=geomcoerce('curve',carr);
g21=embed(g20,'Wrkpln',[0 0 0;0 1 0;0 0 1]);

% Geometry 1
flclear fem

% Analyzed geometry
clear c s
c.objs={g21};
c.name={'EMB1'};
c.tags={'g21'};

s.objs={g15,g17};
s.name={'EXT1','EXT2'};
```

```
s.tags={'g15','g17'};

fem.draw=struct('c',c,'s',s);
fem.geom=geomcsg(fem);

% Constants
D_help=1e-10*scal*scal;
fem.const = {'T','298', ...
  'D',D_help};

% Scalar expressions
fem.expr = {'inlet_width',a(1)};

% Initialize mesh
fem.mesh=meshinit(fem, ...
                  'hauto',2, ...
                  'hmaxfac',[1,inlet_mesh,35,inlet_mesh,36,inlet_mesh, ...
                  37,inlet_mesh,38,inlet_mesh,39,inlet_mesh,40, ...
                  inlet_mesh,41,inlet_mesh,42,inlet_mesh, ...
                  43,inlet_mesh,44,inlet_mesh,2,wall_mesh, ...
                  3,wall_mesh,4,wall_mesh,6,wall_mesh, ...
                  7,15e-6,8,wall_mesh,9,wall_mesh,10,wall_mesh, ...
                  11,wall_mesh,12,wall_mesh,13,wall_mesh,14, ...
                  wall_mesh,15,wall_mesh_fine,16,wall_mesh_fine, ...
                  17,wall_mesh_fine,18,wall_mesh_fine,19, ...
                  wall_mesh_fine,20,wall_mesh_fine,21, ...
                  wall_mesh_fine,22,wall_mesh_fine,23, ...
                  wall_mesh_fine,24,wall_mesh_fine,25, ...
                  wall_mesh_fine,26,wall_mesh_fine,27, ...
                  wall_mesh_fine,28,wall_mesh_fine, ...
                  29,wall_mesh_fine,30,wall_mesh_fine, ...
                  31,wall_mesh_fine,32,wall_mesh_fine, ...
                  33,wall_mesh_fine,34,wall_mesh_fine]);

% Application mode 1
clear appl
appl.mode.class = 'FlNavierStokes';
appl.gporder = {4,2};
appl.cporder = {2,1};
appl.assignsuffix = '_ns';
clear prop
prop.analysis='static';
appl.prop = prop;
clear bnd
bnd.type = {'walltype','int','inlet','outlet'};
bnd.p0 = {0,0,2,0};
bnd.intype = {'uv','uv','p','uv'};
bnd.ind = [3,1,1,1,3,1,1,1,1,2,1,1,1,1,1,1,1,1,1,1,1,1,1,1,1,1, ...
    1,1,1,1,1,1,1,4,4,4,4,4,4,4,4,4];
appl.bnd = bnd;
```

```
clear equ
equ.rho = 'mat1_rho(T[1/K])[kg/m^3]';
equ.eta = 'mat1_eta(T[1/K])[Pa*s]';
equ.cporder = {{1;1;1;2}};
equ.gporder = {{1;1;1;2}};
equ.sdon = 0;
equ.ind = [1,1];
appl.equ = equ;
fem.appl{1} = appl;

% Application mode 2
clear appl
appl.mode.class = 'FlConvDiff';
appl.assignsuffix = '_cd';
clear prop
prop.analysis='static';
clear weakconstr
weakconstr.value = 'off';
weakconstr.dim = {'lm5'};
prop.weakconstr = weakconstr;
appl.prop = prop;
clear bnd
bnd.type = {'N0','cont','Nc','C'};
bnd.c0 = {0,0,0,'1*flc1hs(inlet_width-y,4e-6)'};
bnd.ind = [4,1,1,1,4,1,1,1,1,2,1,1,1,1,1,1,1,1,1,1,1,1,1,1,1, ...
    1,1,1,1,1,1,1,1,3,3,3,3,3,3,3,3,3];
appl.bnd = bnd;
clear equ
equ.D = 'D';
equ.w = 'w';
equ.v = 'v';
equ.u = 'u';
equ.ind = [1,1];
appl.equ = equ;
fem.appl{2} = appl;
fem.border = 1;

% Library materials
clear lib
lib.mat{1}.name='Water, liquid';
lib.mat{1}.varname='mat1';
lib.mat{1}.variables.sigma='5.5e-6[S/m]';
lib.mat{1}.variables.nu0='nu0(T[1/K])[m^2/s]';
lib.mat{1}.variables.k='k(T[1/K])[W/(m*K)]';
lib.mat{1}.variables.gamma='1.0';
lib.mat{1}.variables.rho='rho(T[1/K])[kg/m^3]';
lib.mat{1}.variables.cs='cs(T[1/K])[m/s]';
lib.mat{1}.variables.C='Cp(T[1/K])[J/(kg*K)]';
lib.mat{1}.variables.eta='eta(T[1/K])[Pa*s]';
clear fcns
```

```
fcns{1}.type='inline';
fcns{1}.name='k(T)';
fcns{1}.expr='0.0015*T+0.1689';
fcns{1}.dexpr={'diff(0.0015*T+0.1689,T)'};
fcns{2}.type='inline';
fcns{2}.name='Cp(T)';
fcns{2}.expr='4200';
fcns{2}.dexpr={'diff(4200,T)'};
fcns{3}.type='interp';
fcns{3}.name='rho';
fcns{3}.method='cubic';
fcns{3}.extmethod='const';
fcns{3}.x={'273.15','275.15','277.15','279.15','281.15','283.15', ...
  '293.15','313.15','353.15','373.15'};
fcns{3}.data={'999.841','999.941','999.973','999.941','999.85','999.7', ...
  '998.2','992.3','971.8','958.4'};
fcns{4}.type='interp';
fcns{4}.name='nu0';
fcns{4}.method='cubic';
fcns{4}.extmethod='const';
fcns{4}.x={'273','275','293','300','320','325','340','360','375'};
fcns{4}.data={'1.79E-06','1.67E-06','1.01E-06','8.57E-07','5.84E-07', ...
  '5.38E-07','4.32E-07','3.39E-07','2.91E-07'};
fcns{5}.type='interp';
fcns{5}.name='eta';
fcns{5}.method='cubic';
fcns{5}.extmethod='const';
fcns{5}.x={'273','275','293','300','320','325','340','360','375'};
fcns{5}.data={'1.79E-03','1.67E-03','1.00E-03','8.54E-04','5.78E-04', ...
  '5.31E-04','4.23E-04','3.28E-04','2.78E-04'};
fcns{6}.type='interp';
fcns{6}.name='cs';
fcns{6}.method='cubic';
fcns{6}.extmethod='const';
fcns{6}.x={'273','278','283','293','303','313','323','333','343','353', ...
  '363','373'};
fcns{6}.data={'1403','1427','1447','1481','1507','1526','1541','1552', ...
  '1555','1555','1550','1543'};
lib.mat{1}.functions = fcns;

fem.lib = lib;

% Multiphysics
fem=multiphysics(fem);

% Extend mesh
fem.xmesh=meshextend(fem);

% Solve problem
fem.sol=femstatic(fem, ...
```

```
                    'u',0, ...
                    'solcomp',{'w','u','p','v'}, ...
                    'outcomp',{'w','c','u','p','v'}, ...
                    'ntol',1.0E-7, ...
                    'linsolver','gmres');

% Save current fem structure for restart purposes
fem0=fem;

% Calculate the average flow velocity
area1=postint(fem,'1', ...
            'unit','mol/m', ...
            'dl',1, ...
            'edim',2);

area5=postint(fem,'1', ...
            'unit','mol/m', ...
            'dl',5, ...
            'edim',2);

flow1=postint(fem,'u', ...
            'unit','mol/m', ...
            'dl',1, ...
            'edim',2);

flow5=postint(fem,'u', ...
            'unit','mol/m', ...
            'dl',5, ...
            'edim',2);

flow_speed=(flow1+flow5)/(area1+area5);

% Modify the diffusion coefficient to have a constant Graetz number
graetz=50;

% Constants
D_help=c_height*c_height*flow_speed/c_length/graetz;
fem.const = {'T','298', ...
  'D',D_help};

% (Default values are not included)

% Application mode 1
clear appl
appl.mode.class = 'FlNavierStokes';
appl.gporder = {4,2};
appl.cporder = {2,1};
appl.assignsuffix = '_ns';
clear prop
prop.analysis='static';
```

```
appl.prop = prop;
clear bnd
bnd.type = {'inlet','walltype','int','outlet'};
bnd.p0 = {2,0,0,0};
bnd.intype = {'p','uv','uv','uv'};
bnd.ind = [1,2,2,2,1,2,2,2,2,3,2,2,2,2,2,2,2,2,2,2,2,2,2,2,2,2,2,2,2, ...
  2,2,2,2,4,4,4,4,4,4,4,4,4,4];
appl.bnd = bnd;
clear equ
equ.rho = 'mat1_rho(T[1/K])[kg/m^3]';
equ.eta = 'mat1_eta(T[1/K])[Pa*s]';
equ.cporder = {{1;1;1;2}};
equ.gporder = {{1;1;1;2}};
equ.sdon = 0;
equ.ind = [1,1];
appl.equ = equ;
fem.appl{1} = appl;

% Application mode 2
clear appl
appl.mode.class = 'FlConvDiff';
appl.assignsuffix = '_cd';
clear prop
prop.analysis='static';
clear weakconstr
weakconstr.value = 'off';
weakconstr.dim = {'lm5'};
prop.weakconstr = weakconstr;
appl.prop = prop;
clear bnd
bnd.type = {'N0','cont','Nc','C'};
bnd.c0 = {0,0,0,'1*flc1hs(inlet_width-y,4e-6)'};
bnd.ind = [4,1,1,1,4,1,1,1,1,2,1,1,1,1,1,1,1,1,1,1,1,1,1,1,1,1,1,1,1, ...
  1,1,1,1,3,3,3,3,3,3,3,3,3,3];
appl.bnd = bnd;
clear equ
equ.D = 'D';
equ.w = 'w';
equ.v = 'v';
equ.u = 'u';
equ.ind = [1,1];
appl.equ = equ;
fem.appl{2} = appl;
fem.border = 1;

% Library materials
clear lib
lib.mat{1}.name='Water, liquid';
lib.mat{1}.varname='mat1';
lib.mat{1}.variables.sigma='5.5e-6[S/m]';
```

```
lib.mat{1}.variables.nu0='nu0(T[1/K])[m^2/s]';
lib.mat{1}.variables.k='k(T[1/K])[W/(m*K)]';
lib.mat{1}.variables.gamma='1.0';
lib.mat{1}.variables.rho='rho(T[1/K])[kg/m^3]';
lib.mat{1}.variables.cs='cs(T[1/K])[m/s]';
lib.mat{1}.variables.C='Cp(T[1/K])[J/(kg*K)]';
lib.mat{1}.variables.eta='eta(T[1/K])[Pa*s]';
clear fcns
fcns{1}.type='inline';
fcns{1}.name='k(T)';
fcns{1}.expr='0.0015*T+0.1689';
fcns{1}.dexpr={'diff(0.0015*T+0.1689,T)'};
fcns{2}.type='inline';
fcns{2}.name='Cp(T)';
fcns{2}.expr='4200';
fcns{2}.dexpr={'diff(4200,T)'};
fcns{3}.type='interp';
fcns{3}.name='rho';
fcns{3}.method='cubic';
fcns{3}.extmethod='const';
fcns{3}.x={'273.15','275.15','277.15','279.15','281.15','283.15', ...
  '293.15','313.15','353.15','373.15'};
fcns{3}.data={'999.841','999.941','999.973','999.941','999.85','999.7', ...
  '998.2','992.3','971.8','958.4'};
fcns{4}.type='interp';
fcns{4}.name='nu0';
fcns{4}.method='cubic';
fcns{4}.extmethod='const';
fcns{4}.x={'273','275','293','300','320','325','340','360','375'};
fcns{4}.data={'1.79E-06','1.67E-06','1.01E-06','8.57E-07','5.84E-07', ...
  '5.38E-07','4.32E-07','3.39E-07','2.91E-07'};
fcns{5}.type='interp';
fcns{5}.name='eta';
fcns{5}.method='cubic';
fcns{5}.extmethod='const';
fcns{5}.x={'273','275','293','300','320','325','340','360','375'};
fcns{5}.data={'1.79E-03','1.67E-03','1.00E-03','8.54E-04','5.78E-04', ...
  '5.31E-04','4.23E-04','3.28E-04','2.78E-04'};
fcns{6}.type='interp';
fcns{6}.name='cs';
fcns{6}.method='cubic';
fcns{6}.extmethod='const';
fcns{6}.x={'273','278','283','293','303','313','323','333','343','353', ...
  '363','373'};
fcns{6}.data={'1403','1427','1447','1481','1507','1526','1541','1552', ...
  '1555','1555','1550','1543'};
lib.mat{1}.functions = fcns;

fem.lib = lib;
```

```
% Multiphysics
fem=multiphysics(fem);

% Extend mesh
fem.xmesh=meshextend(fem);

% Mapping current solution to current extended mesh
u = asseminit(fem,'init',fem0.sol,'xmesh',fem0.xmesh);

% Solve problem
fem=adaption(fem, ...
             'u',u, ...
             'solcomp',{'c'}, ...
             'outcomp',{'w','c','u','p','v'}, ...
             'ntol',1.0E-7, ...
             'solver','stationary', ...
             'l2scale',[1], ...
             'l2staborder',[2], ...
             'eigselect',[1], ...
             'maxt',10000000, ...
             'ngen',1, ...
             'resorder',[0], ...
             'rmethod','longest', ...
             'tppar',1.15, ...
             'linsolver','spooles', ...
             'geomnum',1);

% Save current fem structure for restart purposes
fem0=fem;

%% Calculate the outlet concentrations
for indix=35:44,
    % velocity averaged concentration
    I1(indix-34) = postint(fem,'c*u', ...
           'unit','mol/m', ...
           'dl',indix, ...
           'edim',2);
    % outlet area
    exit_area(indix-34) =  postint(fem,'u', ...
           'unit','mol/m', ...
           'dl',indix, ...
           'edim',2);
end;
% normalise the outlet concentration
I1_norm=I1./exit_area;

%% Calculate the error
% number of outlet channels
xdata=1:10;
```

```
% exponential (1) or linear (0) gradient
expo_lin = 0;

if (expo_lin == 1)
    % exponential gradient
    c = 2;  % coefficient of the exponential
    % error function
    error_I=sum((1-(c.^(xdata-1).*I1_norm)).^2)
else
    % linear gradient
    c=0.0; % coefficient linear gradient
    % error function
    error_I=sum(((1 + (xdata-1)./(size(xdata,2)-1)*(c-1))-I1_norm).^2)
end;
```

Appendix E

Publications

1. D.Friedrich, C.Please, T.Melvin. Optimisation of analyte transport in integrated microfluidic affinity sensors for the quantification of low levels of analyte. *Sensors and Actuators B*, 131(1):323-332, 2008.

Bibliography

[1] S. Rodriguez-Mozaz, M. J. L. de Alda, and D. Barcelo. Biosensors as useful tools for environmental analysis and monitoring. *Analytical and Bioanalytical Chemistry*, 386(4):1025–1041, 2006.

[2] J. Atencia and D. J. Beebe. Controlled microfluidic interfaces. *Nature*, 437(7059): 648–655, 2005.

[3] T. M. Squires and S. R. Quake. Microfluidics: Fluid physics at the nanoliter scale. *Reviews of Modern Physics*, 77(3):977–1026, 2005.

[4] R. B. Schasfoort. Proteomics-on-a-chip: the challenge to couple lab-on-a-chip unit operations. *Expert Review of Proteomics*, 1(1):123–132, 2004.

[5] R. M. Twyman. *Principles of proteomics*. Advanced text. BIOS Scientific, Abingdon, 2004.

[6] V. H. Perry. The influence of systemic inflammation on inflammation in the brain: implications for chronic neurodegenerative disease. *Brain Behavior and Immunity*, 18(5):407–413, 2004.

[7] G. L. Corthals, V. C. Wasinger, D. F. Hochstrasser, and J. C. Sanchez. The dynamic range of protein expression: a challenge for proteomic research. *Electrophoresis*, 21(6):1104–1115, 2000.

[8] A. Bange, H. B. Halsall, and W. R. Heineman. Microfluidic immunosensor systems. *Biosensors and Bioelectronics*, 20(12):2488–2503, 2005.

[9] H. Chun, J. Chung, H. Kim, J. Yun, J. Jeon, Y. Ye, S. Kim, H. Park, and C. Suh. Cytokine IL-6 and IL-10 as biomarkers in systemic lupus erythematosus. *Journal of Clinical Immunology*, 27(5):461–466, 2007.

[10] F. Okanda and Z. El Rassi. Biospecific interaction (affinity) CEC and affinity nano-LC. *Electrophoresis*, 28(1-2):89–98, 2007.

[11] U. Bilitewski. Protein-sensing assay formats and devices. *Analytica Chimica Acta*, 568(1-2):232–247, 2006.

[12] W. Lee and K. Lee. Applications of affinity chromatography in proteomics. *Analytical Biochemistry*, 324(1):1–10, 2004.

[13] M. Mann and O. N. Jensen. Proteomic analysis of post-translational modifications. *Nature Biotechnology*, 21(3):255–261, 2003.

[14] J. C. T. Eijkel and A. van den Berg. Nanofluidics: what is it and what can we expect from it? *Microfluidics and Nanofluidics*, 1(3):249–267, 2005.

[15] R. E. Kunz and K. Cottier. Optimizing integrated optical chips for label-free (bio-)chemical sensing. *Analytical and Bioanalytical Chemistry*, 384(1):180–190, 2006.

[16] B. B. Haab. Applications of antibody array platforms. *Current Opinion in Biotechnology*, 17(4):415–421, 2006.

[17] C. Situma, M. Hashimoto, and S. A. Soper. Merging microfluidics with microarray-based bioassays. *Biomolecular Engineering*, 23(5):213–231, 2006.

[18] B. Goldstein, D. Coombs, X. Y. He, A. R. Pineda, and C. Wofsy. The influence of transport on the kinetics of binding to surface receptors: application to cells and biacore. *Journal of Molecular Recognition*, 12(5):293–299, 1999.

[19] I. Caelen, A. Bernard, D. Juncker, B. Michel, H. Heinzelmann, and E. Delamarche. Formation of gradients of proteins on surfaces with microfluidic networks. *Langmuir*, 16(24):9125–9130, 2000.

[20] G. E. Yue, M. G. Roper, C. Balchunas, A. Pulsipher, J. J. Coon, J. Shabanowitz, D. F. Hunt, J. P. Landers, and J. P. Ferrance. Protein digestion and phosphopeptide enrichment on a glass microchip. *Analytica Chimica Acta*, 564(1):116–122, 2006.

[21] P. Hua, J. P. Hole, J. S. Wilkinson, G. Proll, J. Tschmelak, G. Gauglitz, M. A. Jackson, R. Nudd, H. M. T. Griffith, R. A. Abuknesha, J. Kaiser, and P. Kraemmer. Integrated optical fluorescence multisensor for water pollution. *Optics Express*, 13(4):1124–1130, 2005.

[22] T. M. Phillips. Rapid analysis of inflammatory cytokines in cerebrospinal fluid using chip-based immunoaffinity electrophoresis. *Electrophoresis*, 25(10-11):1652–1659, 2004.

[23] N. T. Nguyen and Z. G. Wu. Micromixers - a review. *Journal of Micromechanics and Microengineering*, 15(2):R1–R16, 2005.

[24] A. D. Stroock, S. K. W. Dertinger, A. Ajdari, I. Mezic, H. A. Stone, and G. M. Whitesides. Chaotic mixer for microchannels. *Science*, 295(5555):647–651, 2002.

[25] J. P. Golden, T. M. Floyd-Smith, D. R. Mott, and F. S. Ligler. Target delivery in a microfluidic immunosensor. *Biosensors and Bioelectronics*, 22(11):2763–2767, 2007.

[26] C. C. Chen, D. Hirdes, and A. Folch. Gray-scale photolithography using microfluidic photomasks. *Proceedings of the National Academy of Sciences of the United States of America*, 100(4):1499–1504, 2003.

[27] W. Saadi, S. W. Rhee, F. Lin, B. Vahidi, B. G. Chung, and N. L. Jeon. Generation of stable concentration gradients in 2D and 3D environments using a microfluidic ladder chamber. *Biomedical Microdevices*, 9(5):627–635, 2007.

[28] M. A. Ansari and K. Y. Kim. Shape optimization of a micromixer with staggered herringbone groove. *Chemical Engineering Science*, 62(23):6687–6695, 2007.

[29] N. S. Lynn and D. S. Dandy. Geometrical optimization of helical flow in grooved micromixers. *Lab on a Chip*, 7(5):580–587, 2007.

[30] N. L. Jeon, S. K. W. Dertinger, D. T. Chiu, I. S. Choi, A. D. Stroock, and G. M. Whitesides. Generation of solution and surface gradients using microfluidic systems. *Langmuir*, 16(22):8311–8316, 2000.

[31] A. Manz, N. Graber, and H. M. Widmer. Miniaturized total chemical-analysis systems - a novel concept for chemical sensing. *Sensors and Actuators B-Chemical*, 1(1-6):244–248, 1990.

[32] D. R. Reyes, D. Iossifidis, P. A. Auroux, and A. Manz. Micro total analysis systems. 1. introduction, theory, and technology. *Analytical Chemistry*, 74(12): 2623–2636, 2002.

[33] M. Toner and D. Irimia. Blood-on-a-chip. *Annual Review of Biomedical Engineering*, 7:77–103, 2005.

[34] S. Chien. Mechanotransduction and endothelial cell homeostasis: the wisdom of the cell. *American Journal of Physiology-Heart and Circulatory Physiology*, 292 (3):H1209–H1224, 2007.

[35] J. El-Ali, P. K. Sorger, and K. F. Jensen. Cells on chips. *Nature*, 442(7101): 403–411, 2006.

[36] D. Wild. *The Immunoassay handbook*. Elsevier, Amsterdam, 3rd edition, 2005.

[37] A. Pandey and M. Mann. Proteomics to study genes and genomes. *Nature*, 405 (6788):837–846, 2000.

[38] B. Weigl, G. Domingo, P. LaBarre, and J. Gerlach. Towards non- and minimally instrumented, microfluidics-based diagnostic devices. *Lab on a Chip*, 8(12):1999–2014, 2008.

[39] S. P. Gygi, Y. Rochon, B. R. Franza, and R. Aebersold. Correlation between protein and mRNA abundance in yeast. *Molecular and Cellular Biology*, 19(3): 1720–1730, 1999.

[40] W. P. Blackstock and M. P. Weir. Proteomics: quantitative and physical mapping of cellular proteins. *Trends in Biotechnology*, 17(3):121–127, 1999.

[41] L. Bousse, S. Mouradian, A. Minalla, H. Yee, K. Williams, and R. Dubrow. Protein sizing on a microchip. *Analytical Chemistry*, 73(6):1207–1212, 2001.

[42] M. Pawlak, E. Schick, M. A. Bopp, M. J. Schneider, P. Oroszlan, and M. Ehrat. Zeptosens' protein microarrays: A novel high performance microarray platform for low abundance protein analysis. *Proteomics*, 2(4):383–393, 2002.

[43] M. J. Madou. *Fundamentals of microfabrication: the science of miniaturization*. CRC Press, Boca Raton, 2nd ed. edition, 2002.

[44] P. Abgrall and A. M. Gue. Lab-on-chip technologies: making a microfluidic network and coupling it into a complete microsystem - a review. *Journal of Micromechanics and Microengineering*, 17(5):R15–R49, 2007.

[45] H. Becker and C. Gartner. Polymer microfabrication technologies for microfluidic systems. *Analytical and Bioanalytical Chemistry*, 390(1):89–111, 2008.

[46] J. Haneveld, H. Jansen, E. Berenschot, N. Tas, and M. Elwenspoek. Wet anisotropic etching for fluidic 1D nanochannels. *Journal of Micromechanics and Microengineering*, 13(4):S62–S66, 2003.

[47] F. Marty, L. Rousseau, B. Saadany, B. Mercier, O. Francais, Y. Mita, and T. Bourouina. Advanced etching of silicon based on deep reactive ion etching for silicon high aspect ratio microstructures and three-dimensional micro- and nanostructures. *Microelectronics Journal*, 36(7):673–677, 2005.

[48] M. Bu, T. Melvin, G. Ensell, J. Wilkinson, and A. Evans. A new masking technology for deep glass etching and its microfluidic application. *Sensors and Actuators A-Physical*, 115(2-3):476–482, 2004.

[49] J. Park, N. Lee, J. Lee, J. Park, and H. Park. Continuous and cyclic deep reactive ion etching of borosilicate glass by using SF_6 and SF_6/Ar inductively coupled plasmas. *Journal of the Korean Physical Society*, 47:S422–S428, 2005.

[50] E. Metwalli and C. Pantano. Reactive ion etching of glasses: Composition dependence. *Nuclear Instruments and Methods in Physics Research Section B-Beam Interactions with Materials and Atoms*, 207(1):21–27, 2003.

[51] H. Becker and L. Locascio. Polymer microfluidic devices. *Talanta*, 56(2):267–287, 2002.

[52] S. Tuomikoski. *Fabrication of SU-8 Microstructures for Analytical Microfluidic Applications*. PhD thesis, 2007.

[53] J. Mark. *Physical properties of polymer handbook*. Springer, 2nd ed. edition, 2006.

[54] H. Shadpour, H. Musyimi, J. Chen, and S. Soper. Physiochemical properties of various polymer substrates and their effects on microchip electrophoresis performance. *Journal of Chromatography A*, 1111(2):238–251, 2006.

[55] A. del Campo and C. Greiner. SU-8: a photoresist for high-aspect-ratio and 3D submicron lithography. *Journal of Micromechanics and Microengineering*, 17(6): R81–R95, 2007.

[56] J. O'Brien, P. Hughes, M. Brunet, B. O'Neill, J. Alderman, B. Lane, A. O'Riordan, and C. O'Driscoll. Advanced photoresist technologies for microsystems. *Journal of Micromechanics and Microengineering*, 11(4):353–358, 2001.

[57] T. Anhoj, A. Jorgensen, D. Zauner, and J. Hubner. The effect of soft bake temperature on the polymerization of SU-8 photoresist. *Journal of Micromechanics and Microengineering*, 16(9):1819–1824, 2006.

[58] M. Gaudet, J. Camart, L. Buchaillot, and S. Arscott. Variation of absorption coefficient and determination of critical dose of SU-8 at 365 nm. *Applied Physics Letters*, 88(2):–, 2006.

[59] J. Hsieh, C. Weng, H. Yin, H. Lin, and H. Chou. Realization and characterization of SU-8 micro cylindrical lenses for in-plane micro optical systems. *Microsystem Technologies-Micro-and Nanosystems-Information Storage and Processing Systems*, 11(6):429–437, 2005.

[60] G. Kotzar, M. Freas, P. Abel, A. Fleischman, S. Roy, C. Zorman, J. Moran, and J. Melzak. Evaluation of MEMS materials of construction for implantable medical devices. *Biomaterials*, 23(13):2737–2750, 2002.

[61] G. Voskerician, M. Shive, R. Shawgo, H. von Recum, J. Anderson, M. Cima, and R. Langer. Biocompatibility and biofouling of MEMS drug delivery devices. *Biomaterials*, 24(11):1959–1967, 2003.

[62] M. Nordström, R. Marie, M. Calleja, and A. Boisen. Rendering SU-8 hydrophilic to facilitate use in micro channel fabrication. *Journal of Micromechanics and Microengineering*, 14(12):1614–1617, 2004.

[63] F. Walther, P. Davydovskaya, S. Zucher, M. Kaiser, H. Herberg, A. Gigler, and R. Stark. Stability of the hydrophilic behavior of oxygen plasma activated SU-8. *Journal of Micromechanics and Microengineering*, 17(3):524–531, 2007.

[64] R. Liska, M. Schuster, R. Infuhr, C. Tureeek, C. Fritscher, B. Seidl, V. Schmidt, L. Kuna, A. Haase, F. Varga, H. Lichtenegger, and J. Stampfl. Photopolymers for rapid prototyping. *Journal of Coatings Technology and Research*, 4(4):505–510, 2007.

[65] C. Malek. Laser processing for bio-microfluidics applications (part i). *Analytical and Bioanalytical Chemistry*, 385(8):1351–1361, 2006.

[66] C. Malek. Laser processing for bio-microfluidics applications (part ii). *Analytical and Bioanalytical Chemistry*, 385(8):1362–1369, 2006.

[67] M. Roberts, J. Rossier, P. Bercier, and H. Girault. UV laser machined polymer substrates for the development of microdiagnostic systems. *Analytical Chemistry*, 69(11):2035–2042, 1997.

[68] D. Duffy, J. McDonald, O. Schueller, and G. Whitesides. Rapid prototyping of microfluidic systems in poly(dimethylsiloxane). *Analytical Chemistry*, 70(23): 4974–4984, 1998.

[69] D. Duffy, O. Schueller, S. Brittain, and G. Whitesides. Rapid prototyping of microfluidic switches in poly(dimethyl siloxane) and their actuation by electro-osmotic flow. *Journal of Micromechanics and Microengineering*, 9(3):211–217, 1999.

[70] J. McDonald, D. Duffy, J. Anderson, D. Chiu, H. Wu, O. Schueller, and G. Whitesides. Fabrication of microfluidic systems in poly(dimethylsiloxane). *Electrophoresis*, 21(1):27–40, 2000.

[71] J. C. McDonald and G. M. Whitesides. Poly(dimethylsiloxane) as a material for fabricating microfluidic devices. *Accounts of Chemical Research*, 35(7):491–499, 2002.

[72] S. Cesaro-Tadic, G. Dernick, D. Juncker, G. Buurman, H. Kropshofer, B. Michel, C. Fattinger, and E. Delamarche. High-sensitivity miniaturized immunoassays for tumor necrosis factor α using microfluidic systems. *Lab on a Chip*, 4(6):563–569, 2004.

[73] C. Effenhauser, G. Bruin, A. Paulus, and M. Ehrat. Integrated capillary electrophoresis on flexible silicone microdevices: Analysis of DNA restriction fragments and detection of single dna molecules on microchips. *Analytical Chemistry*, 69(17):3451–3457, 1997.

[74] M. Holden, S. Kumar, A. Beskok, and P. Cremer. Microfluidic diffusion diluter: bulging of PDMS microchannels under pressure-driven flow. *Journal of Micromechanics and Microengineering*, 13(3):412–418, 2003.

[75] D. Bodas and C. Khan-Malek. Formation of more stable hydrophilic surfaces of PDMS by plasma and chemical treatments. *Microelectronic Engineering*, 83(4-9): 1277–1279, 2006.

[76] M. Ebara, J. Hoffman, P. Stayton, and A. Hoffman. Surface modification of microfluidic channels by UV-mediated graft polymerization of non-fouling and 'smart' polymers. *Radiation Physics and Chemistry*, 76(8-9):1409–1413, 2007.

[77] S. W. Lee and S. S. Lee. Shrinkage ratio of PDMS and its alignment method for the wafer level process. *Microsystem Technologies-Micro-and Nanosystems-Information Storage and Processing Systems*, 14(2):205–208, 2008.

[78] M. Heckele and W. Schomburg. Review on micro molding of thermoplastic polymers. *Journal of Micromechanics and Microengineering*, 14(3):R1–R14, 2004.

[79] E. W. Becker, W. Ehrfield, P. Hagmann, A. Maner, and D. Münchmeyer. Fabrication of microstructures with high aspect ratios and great structural heights by synchrotron radiation lithography, galvanoforming, and plastic moulding (LIGA process). *Microelectronic Engineering*, 4(1):35–56, 1986.

[80] Y. Luo, X. Wang, C. Liu, Z. Lou, D. Chu, and D. Yu. Swelling of SU-8 structure in Ni mold fabrication by UV-LIGA technique. *Microsystem Technologies-Micro- and Nanosystems-Information Storage and Processing Systems*, 11(12):1272–1275, 2005.

[81] J. Arnold, U. Dasbach, W. Ehrfeld, K. Hesch, and H. Lowe. Combination of excimer-laser micromachining and replication processes suited for large-scale production. *Applied Surface Science*, 86(1-4):251–258, 1995.

[82] M. Jensen, J. McCormack, B. Helbo, L. Christensen, T. Christensen, and O. Geschke. Rapid prototyping of polymer microsystems via excimer laser ablation of polymeric moulds. *Lab on a Chip*, 4(4):391–395, 2004.

[83] D. Falconnet, G. Csucs, H. M. Grandin, and M. Textor. Surface engineering approaches to micropattern surfaces for cell-based assays. *Biomaterials*, 27(16): 3044–3063, 2006.

[84] M. S. Hasenbank, T. Edwards, E. Fu, R. Garzon, T. F. Kosar, M. Look, A. Mashadi-Hossein, and P. Yager. Demonstration of multi-analyte patterning using piezoelectric inkjet printing of multiple layers. *Analytica Chimica Acta*, 611 (1):80–88, 2008.

[85] E. Delamarche, A. Bernard, H. Schmid, A. Bietsch, B. Michel, and H. Biebuyck. Microfluidic networks for chemical patterning of substrate: Design and application to bioassays. *Journal of the American Chemical Society*, 120(3):500–508, 1998.

[86] J. Renault, A. Bernard, A. Bietsch, B. Michel, H. Bosshard, E. Delamarche, M. Kreiter, B. Hecht, and U. Wild. Fabricating arrays of single protein molecules on glass using microcontact printing. *Journal of Physical Chemistry B*, 107(3): 703–711, 2003.

[87] L. Lauer, S. Ingebrandt, M. Scholl, and A. Offenhausser. Aligned microcontact printing of biomolecules on microelectronic device surfaces. *IEEE Transactions on Biomedical Engineering*, 48(7):838–842, 2001.

[88] B. C. Wheeler, J. M. Corey, G. J. Brewer, and D. W. Branch. Microcontact printing for precise control of nerve cell growth in culture. *Journal of Biomechanical Engineering-Transactions of the Asme*, 121(1):73–78, 1999.

[89] A. Bernard, J. Renault, B. Michel, H. Bosshard, and E. Delamarche. Microcontact printing of proteins. *Advanced Materials*, 12(14):1067–1070, 2000.

[90] C. L. Hypolite, T. L. McLernon, D. N. Adams, K. E. Chapman, C. B. Herbert, C. C. Huang, M. D. Distefano, and W. S. Hu. Formation of microscale gradients of protein using heterobifunctional photolinkers. *Bioconjugate Chemistry*, 8(5): 658–663, 1997.

[91] F. Niklaus, G. Stemme, J. Q. Lu, and R. J. Gutmann. Adhesive wafer bonding. *Journal of Applied Physics*, 99(3):–, 2006.

[92] S. Bhattacharya, A. Datta, J. M. Berg, and S. Gangopadhyay. Studies on surface wettability of poly(dimethyl) siloxane (PDMS) and glass under oxygen-plasma treatment and correlation with bond strength. *Journal of Microelectromechanical Systems*, 14(3):590–597, 2005.

[93] L. Brown, T. Koerner, J. Horton, and R. Oleschuk. Fabrication and characterization of poly(methylmethacrylate) microfluidic devices bonded using surface modifications and solvents. *Lab on a Chip*, 6(1):66–73, 2006.

[94] Y. Sun, Y. Kwok, and N. Nguyen. Low-pressure, high-temperature thermal bonding of polymeric microfluidic devices and their applications for electrophoretic separation. *Journal of Micromechanics and Microengineering*, 16(8):1681–1688, 2006.

[95] R. Truckenmüller, Y. Cheng, R. Ahrens, H. Bahrs, G. Fischer, and J. Lehmann. Micro ultrasonic welding: joining of chemically inert polymer microparts for single material fluidic components and systems. *Microsystem Technologies-Micro-and Nanosystems-Information Storage and Processing Systems*, 12(10-11):1027–1029, 2006.

[96] T. Ussing, L. Petersen, C. Nielsen, B. Helbo, and L. Hojslet. Micro laser welding of polymer microstructures using low power laser diodes. *International Journal of Advanced Manufacturing Technology*, 33(1-2):198–205, 2007.

[97] J. H. Tsai and L. W. Lin. Micro-to-macro fluidic interconnectors with an integrated polymer sealant. *Journal of Micromechanics and Microengineering*, 11(5): 577–581, 2001.

[98] A. Christensen, D. Chang-Yen, and B. Gale. Characterization of interconnects used in PDMS microfluidic systems. *Journal of Micromechanics and Microengineering*, 15(5):928–934, 2005.

[99] F. U. Gast, P. Dittrich, P. Schwille, M. Weigel, M. Mertig, J. Opitz, U. Queitsch, S. Diez, B. Lincoln, F. Wottawah, S. Schinkinger, J. Guck, J. Kas, J. Smolinski, K. Salchert, C. Werner, C. Duschl, M. Jager, K. Uhlig, P. Geggier, and S. Howitz. The microscopy cell (MicCell), a versatile modular flowthrough system for cell biology, biomaterial research, and nanotechnology. *Microfluidics and Nanofluidics*, 2(1):21–36, 2006.

[100] V. Saarela, S. Franssila, S. Tuomikoski, S. Marttila, P. Ostman, T. Sikanen, T. Kotiaho, and R. Kostiainen. Re-usable multi-inlet PDMS fluidic connector. *Sensors and Actuators B-Chemical*, 114(1):552–557, 2006.

[101] G. Perozziello, F. Bundgaard, and O. Geschke. Fluidic interconnections for microfluidic systems: A new integrated fluidic interconnection allowing plug 'n' play functionality. *Sensors and Actuators B-Chemical*, 130(2):947–953, 2008.

[102] C. H. Chiou and G. B. Lee. Minimal dead-volume connectors for microfluidics using PDMS casting techniques. *Journal of Micromechanics and Microengineering*, 14(11):1484–1490, 2004.

[103] N. H. Bings, C. Wang, C. D. Skinner, C. L. Colyer, P. Thibault, and D. J. Harrison. Microfluidic devises connected to fused-silica capillaries with minimal dead volume. *Analytical Chemistry*, 71(15):3292–3296, 1999.

[104] B. Wenclawiak and R. Puschl. Sample injection for capillary electrophoresis on a micro fabricated device/on chip CE injection. *Analytical Letters*, 39(1):3–16, 2006.

[105] J. M. Karlinsey, J. Monahan, D. J. Marchiarullo, J. P. Ferrance, and J. P. Landers. Pressure injection on a valved microdevice for electrophoretic analysis of submicroliter samples. *Analytical Chemistry*, 77(11):3637–3643, 2005.

[106] X. X. Bai, H. J. Lee, J. S. Rossier, F. Reymond, H. Schafer, M. Wossner, and H. H. Girault. Pressure pinched injection of nanolitre volumes in planar micro-analytical devices. *Lab on a Chip*, 2(1):45–49, 2002.

[107] A. O'Neill, P. O'Brien, J. Alderman, D. Hoffman, M. McEnery, J. Murrihy, and J. Glennon. On-chip definition of picolitre sample injection plugs for miniaturised liquid chromatography. *Journal of Chromatography A*, 924(1-2):259–263, 2001.

[108] C. T. Campbell and G. Kim. SPR microscopy and its applications to high-throughput analyses of biomolecular binding events and their kinetics. *Biomaterials*, 28(15):2380–2392, 2007.

[109] K. W. Ro, K. Lim, B. C. Shim, and J. H. Hahn. Integrated light collimating system for extended optical-path-length absorbance detection in microchip-based capillary electrophoresis. *Analytical Chemistry*, 77(16):5160–5166, 2005.

[110] C. Taitt, G. Anderson, and F. Ligler. Evanescent wave fluorescence biosensors. *Biosensors and Bioelectronics*, 20(12):2470–2487, 2005.

[111] S. Gotz and U. Karst. Recent developments in optical detection methods for microchip separations. *Analytical and Bioanalytical Chemistry*, 387(1):183–192, 2007.

[112] B. Kuswandi, Nuriman, J. Huskens, and W. Verboom. Optical sensing systems for microfluidic devices: A review. *Analytica Chimica Acta*, 601(2):141–155, 2007.

[113] M. E. Johnson and J. P. Landers. Fundamentals and practice for ultrasensitive laser-induced fluorescence detection in microanalytical systems. *Electrophoresis*, 25(21-22):3513–3527, 2004.

[114] H. Grandin, B. Stadler, M. Textor, and J. Voros. Waveguide excitation fluorescence microscopy: A new tool for sensing and imaging the biointerface. *Biosensors and Bioelectronics*, 21(8):1476–1482, 2006.

[115] X. Hoa, A. Kirk, and M. Tabrizian. Towards integrated and sensitive surface plasmon resonance biosensors: A review of recent progress. *Biosensors and Bioelectronics*, 23(2):151–160, 2007.

[116] R. Aebersold and M. Mann. Mass spectrometry-based proteomics. *Nature*, 422 (6928):198–207, 2003.

[117] K. Mogensen, H. Klank, and J. Kutter. Recent developments in detection for microfluidic systems. *Electrophoresis*, 25(21-22):3498–3512, 2004.

[118] G. A. Schultz, T. N. Corso, S. J. Prosser, and S. Zhang. A fully integrated monolithic microchip electrospray device for mass spectrometry. *Analytical Chemistry*, 72(17):4058–4063, 2000.

[119] K. Jo, M. Heien, L. Thompson, M. Zhong, R. Nuzzo, and J. Sweedler. Mass spectrometric imaging of peptide release from neuronal cells within microfluidic devices. *Lab on a Chip*, 7(11):1454–1460, 2007.

[120] P. Chaurand, S. Schwartz, and R. Caprioli. Imaging mass spectrometry: a new tool to investigate the spatial organization of peptides and proteins in mammalian tissue sections. *Current Opinion in Chemical Biology*, 6(5):676–681, 2002.

[121] D. G. Myszka, T. A. Morton, M. L. Doyle, and I. M. Chaiken. Kinetic analysis of a protein antigen-antibody interaction limited by mass transport on an optical biosensor. *Biophysical Chemistry*, 64:127–137, 1997.

[122] M. Zimmermann, E. Delamarche, M. Wolf, and P. Hunziker. Modeling and optimization of high-sensitivity, low-volume microfluidic-based surface immunoassays. *Biomedical Microdevices*, 7(2):99–110, 2005.

[123] D. J. Acheson. *Elementary Fluid Dynamics*. Oxford University Press, Oxford, 1990.

[124] J. Berthier and P. Silberzan. *Microfluidics for biotechnology*. Artech House, Boston, Mass. ; London, 2006.

[125] R. F. Probstein. *Physicochemical hydrodynamics: an introduction*. Butterworth Publishers, Boston, 1989.

[126] M. K. Liu, P. Li, and J. C. Giddings. Rapid protein separation and diffusion-coefficient measurement by frit inlet flow field-flow fractionation. *Protein Science*, 2(9):1520–1531, 1993.

[127] D. G. Myszka, X. He, M. Dembo, T. A. Morton, and B. Goldstein. Extending the range of rate constants available from BIACORE: Interpreting mass transport-influenced binding data. *Biophysical Journal*, 75(2):583–594, 1998.

[128] D. A. Lauffenburger and J. J. Linderman. *Receptors : models for binding, trafficking, and signalling*. Oxford University Press, New York ; Oxford, 1993.

[129] L. L. H. Christensen. Theoretical analysis of protein concentration determination using biosensor technology under conditions of partial mass transport limitation. *Analytical Biochemistry*, 249(2):153–164, 1997.

[130] A. Onell and K. Andersson. Kinetic determinations of molecular interactions using Biacore - minimum data requirements for efficient experimental design. *Journal of Molecular Recognition*, 18(4):307–317, 2005.

[131] T. Gervais and K. F. Jensen. Mass transport and surface reactions in microfluidic systems. *Chemical Engineering Science*, 61:1102–1121, 2006.

[132] D. A. Edwards, B. Goldstein, and D. S. Cohen. Transport effects on surface-volume biological reactions. *Journal of Mathematical Biology*, 39(6):533–561, 1999.

[133] T. M. Squires, R. J. Messinger, and S. R. Manalis. Making it stick: convection, reaction and diffusion in surface-based biosensors. *Nature Biotechnology*, 26(4): 417–426, 2008.

[134] E. Papoutsakis and D. Ramkrishna. Conjugated graetz problems. 1. general formalism and a class of solid-fluid problems. *Chemical Engineering Science*, 36(8): 1381–1391, 1981.

[135] T. A. Morton, D. G. Myszka, and I. M. Chaiken. Interpreting complex binding-kinetics from optical biosensors - a comparison of analysis by linearization, the integrated rate-equation, and numerical-integration. *Analytical Biochemistry*, 227 (1):176–185, 1995.

[136] P. Schuck and A. P. Minton. Analysis of mass transport-limited binding kinetics in evanescent wave biosensors. *Analytical Biochemistry*, 240(2):262–272, 1996.

[137] K. Sigmundsson, G. Masson, R. H. Rice, N. Beauchemin, and B. Obrink. Determination of active concentrations and association and dissociation rate constants of interacting biomolecules: An analytical solution to the theory for kinetic and mass transport limitations in biosensor technology and its experimental verification. *Biochemistry*, 41(26):8263–8276, 2002.

[138] D. A. Edwards. Estimating rate constants in a convection-diffusion system with a boundary reaction. *IMA Journal of Applied Mathematics*, 63(1):89–112, 1999.

[139] T. Mason, A. R. Pineda, C. Wofsy, and B. Goldstein. Effective rate models for the analysis of transport-dependent biosensor data. *Mathematical Biosciences*, 159(2):123–144, 1999.

[140] J. Jenkins, B. Prabhakarpandian, K. Lenghaus, J. Hickman, and S. Sundaram. Fluidics-resolved estimation of protein adsorption kinetics in a biomicrofluidic system. *Analytical Biochemistry*, 331(2):207–215, 2004.

[141] J. Svitel, H. Boukari, D. Van Ryk, R. C. Willson, and P. Schuck. Probing the functional heterogeneity of surface binding sites by analysis of experimental binding traces and the effect of mass transport limitation. *Biophysical Journal*, 92(5): 1742–1758, 2007.

[142] K. Lebedev, S. Mafe, and P. Stroeve. Convection, diffusion and reaction in a surface-based biosensor: Modeling of cooperativity and binding site competition on the surface and in the hydrogel. *Journal of Colloid and Interface Science*, 296 (2):527–537, 2006.

[143] K. E. Sapsford, P. T. Charles, C. H. Patterson, and F. S. Ligler. Demonstration of four immunoassay formats using the array biosensor. *Analytical Chemistry*, 74 (5):1061–1068, 2002.

[144] M. Hartmann, M. Schrenk, A. Dottinger, S. Nagel, J. Roeraade, T. Joos, and M. Templin. Expanding assay dynamics: A combined competitive and direct assay system for the quantification of proteins in multiplexed immunoassays. *Clinical Chemistry*, 54(6):956–963, 2008.

[145] M. Pelzing and C. Neusüß. Separation techniques hyphenated to electrospray-tandem mass spectrometry in proteomics: Capillary electrophoresis versus nano-liquid chromatography. *Electrophoresis*, 26(14):2717–2728, 2005.

[146] H. J. Issaq. The role of separation science in proteomics research. *Electrophoresis*, 22(17):3629–3638, 2001.

[147] B. E. Slentz, N. A. Penner, and F. E. Regnier. Protein proteolysis and the multi-dimensional electrochromatographic separation of histidine-containing peptide fragments on a chip. *Journal of Chromatography A*, 984(1):97–107, 2003.

[148] M. McEnery, A. M. Tan, J. Alderman, J. Patterson, S. C. O'Mathuna, and J. D. Glennon. Liquid chromatography on-chip: progression towards a μ-total analysis system. *Analyst*, 125(1):25–27, 1999.

[149] H. Tsai, F. Hsu, Y. Lin, and C. Fuh. Separation method based on affinity reaction between magnetic and nonmagnetic particles for the analysis of particles and biomolecules. *Journal of Chromatography A*, 1130(2):227–231, 2006.

[150] W. C. Yang, X. H. Sun, T. Pan, and A. T. Woolley. Affinity monolith preconcentrators for polymer microchip capillary electrophoresis. *Electrophoresis*, 29(16): 3429–3435, 2008.

[151] G. Guiochon, D. G. Shirazi, A. Felinger, and A. M. Katti. *Fundamentals of preparative and nonlinear chromatography*. Academic Press, Boston, 2nd ed. edition, 2006.

[152] T. P. Burg, M. Godin, S. M. Knudsen, W. Shen, G. Carlson, J. S. Foster, K. Babcock, and S. R. Manalis. Weighing of biomolecules, single cells and single nanoparticles in fluid. *Nature*, 446(7139):1066–1069, 2007.

[153] R. L. Cunico, K. M. Gooding, and T. Wehr. *Basic HPLC and CE of biomolecules*. Bay Bioanalytical Laboratory, Richmond, CA, 1998.

[154] M. G. Khaledi. *High-performance capillary electrophoresis : theory, techniques, and applications*. Chemical analysis. Wiley, New York ; Chichester, 1998.

[155] T. Rabilloud. *Proteome research: two-dimensional gel electrophoresis and identification methods*. Principles and practice. Springer, Berlin ; London, 2000.

[156] D. Figeys, S. Gygi, G. McKinnon, and R. Aebersold. An integrated microfluidics tandem mass spectrometry system for automated protein analysis. *Analytical Chemistry*, 70(18):3728–3734, 1998.

[157] S. P. Gygi, G. L. Corthals, Y. Zhang, Y. Rochon, and R. Aebersold. Evaluation of two-dimensional gel electrophoresis-based proteome analysis technology. *Proceedings of the National Academy of Sciences of the United States of America*, 97 (17):9390–9395, 2000.

[158] H. Issaq and T. Veenstra. Two-dimensional polyacrylamide gel electrophoresis (2D-PAGE): advances and perspectives. *Biotechniques*, 44(5):697–698, 700, 2008.

[159] M. Unlu, M. E. Morgan, and J. S. Minden. Difference gel electrophoresis: A single gel method for detecting changes in protein extracts. *Electrophoresis*, 18 (11):2071–2077, 1997.

[160] K. K. Yeung and C. A. Lucy. Ultrahigh-resolution capillary electrophoretic separation with indirect ultraviolet detection: isotopic separation of [14N]- and [15N]ammonium. *Electrophoresis*, 20(12):2554–2559, 1999.

[161] Y. Saito, K. Jinno, and T. Greibrokk. Capillary-columns in liquid chromatography: between conventional columns and microchips. *Journal of Separation Science*, 27(17-18):1379–1390, 2004.

[162] Y. Shen, N. Tolic, C. Masselon, L. Pasa-Tolic, D. G. Camp, K. K. Hixson, R. Zhao, G. A. Anderson, and R. D. Smith. Ultrasensitive proteomics using high-efficiency on-line micro-SPE-NanoLC-NanoESI MS and MS/MS. *Analytical Chemistry*, 76 (1):144–154, 2004.

[163] D. S. Hage. Affinity chromatography: A review of clinical applications. *Clinical Chemistry*, 45(5):593–615, 1999.

[164] N. H. H. Heegaard, S. Nilsson, and N. A. Guzman. Affinity capillary electrophoresis: important application areas and some recent developments. *Journal of Chromatography B*, 715(1):29–54, 1998.

[165] K. Mondal and M. N. Gupta. The affinity concept in bioseparation: Evolving paradigms and expanding range of applications. *Biomolecular Engineering*, 23 (2-3):59–76, 2006.

[166] N. Zolotarjova, J. Martosella, G. Nicol, J. Bailey, B. E. Boyes, and W. C. Barrett. Differences among techniques for high-abundant protein depletion. *Proteomics*, 5 (13):3304–3313, 2005.

[167] S. Ohlson, M. Bergstrom, P. Pahlsson, and A. Lundblad. Use of monoclonal antibodies for weak affinity chromatography. *Journal of Chromatography A*, 758 (2):199–208, 1997.

[168] W. J. Chung, M. S. Kim, S. Cho, S. S. Park, J. H. Kim, Y. K. Kim, B. G. Kim, and Y. S. Lee. Microaffinity purification of proteins based on photolytic elution: Toward an efficient microbead affinity chromatography on a chip. *Electrophoresis*, 26(3):694–702, 2005.

[169] L. Mu, Y. Liu, S. Y. Cai, and J. L. Kong. A smart surface in a microfluidic chip for controlled protein separation. *Chemistry-A European Journal*, 13(18):5113–5120, 2007.

[170] N. Malmstadt, P. Yager, A. S. Hoffman, and P. S. Stayton. A smart microfluidic affinity chromatography matrix composed of poly(N-isopropylacrylamide)-coated beads. *Analytical Chemistry*, 75(13):2943–2949, 2003.

[171] N. A. Guzman and R. J. Stubbs. The use of selective adsorbents in capillary electrophoresis-mass spectrometry for analyte preconcentration and microreactions: A powerful three-dimensional tool for multiple chemical and biological applications. *Electrophoresis*, 22(17):3602–3628, 2001.

[172] M. F. Lopez, B. S. Kristal, E. Chernokalskaya, A. Lazarev, A. I. Shestopalov, A. Bogdanova, and M. Robinson. High-throughput profiling of the mitochondrial proteome using affinity fractionation and automation. *Electrophoresis*, 21(16): 3427–3440, 2000.

[173] A. Dodge, K. Fluri, E. Verpoorte, and N. F. de Rooij. Electrokinetically driven microfluidic chips with surface-modified chambers for heterogeneous immunoassays. *Analytical Chemistry*, 73(14):3400–3409, 2001.

[174] D. Figeys and D. Pinto. Proteomics on a chip: Promising developments. *Electrophoresis*, 22(2):208–216, 2001.

[175] A. Ishida, T. Yoshikawa, M. Natsume, and T. Kamidate. Reversed-phase liquid chromatography on a microchip with sample injector and monolithic silica column. *Journal of Chromatography A*, 1132(1-2):90–98, 2006.

[176] E. Doherty, R. Meagher, M. Albarghouthi, and A. Barron. Microchannel wall coatings for protein separations by capillary and chip electrophoresis. *Electrophoresis*, 24(1-2):34–54, 2003.

[177] M. Peoples and H. Karnes. Microfluidic immunoaffinity separations for bioanalysis. *Journal of Chromatography B*, 866(1-2):14–25, 2008.

[178] R. Swart, J. C. Kraak, and H. Poppe. Recent progress in open tubular liquid chromatography. *Trends in Analytical Chemistry*, 16(6):332–342, 1997.

[179] A. Sin, S. Murthy, A. Revzin, R. Tompkins, and M. Toner. Enrichment using antibody-coated microfluidic chambers in shear flow: Model mixtures of human lymphocytes. *Biotechnology and Bioengineering*, 91(7):816–826, 2005.

[180] G. I. Taylor. Dispersion of soluble matter in solvent flowing slowly through a tube. *Proceedings of the Royal Society A*, 219:186–203, 1953.

[181] J. L. Schiff. *The Laplace transform: theory and applications*. Undergraduate texts in mathematics. Springer, New York, 1999.

[182] J. Orszaghova. Mathematical modelling of protein reactions within microfluidic devices. *Unpublished report*, pages 1–24, 2005.

[183] M. Abramowitz. *Handbook of Mathematical Functions with Formulas, Graphs, and Mathematical Tables*. John Wiley and Sons, 1972.

[184] J. J. VanDeemter, F. J. Zuiderweg, and A. Klinkenberg. Longitudinal diffusion and resistance to mass transfer as causes of nonideality in chromatography (reprinted from chem engng sci, vol 5, pg 271-289, 1956). *Chemical Engineering Science*, 50 (24):3869–3882, 1995.

[185] H. Poppe. Mass transfer in rectangular chromatographic channels. *Journal of Chromatography A*, 948(1-2):3–17, 2002.

[186] H. Eghbali and G. Desmet. Optimum kinetic performance of open-tubular separations in microfluidic devices. *Journal of Separation Science*, 30(10):1377–1397, 2007.

[187] H. Poppe. Some reflections on speed and efficiency of modern chromatographic methods. *Journal of Chromatography A*, 778(1-2):3–21, 1997.

[188] J. H. Knox and M. T. Gilbert. Kinetic optimization of straight open-tubular liquid-chromatography. *Journal of Chromatography*, 186(Dec):405–418, 1979.

[189] D. Dutta and D. Leighton. Dispersion reduction in pressure driven flow through microetched channels. *Analytical Chemistry*, 73(3):504–513, 2001.

[190] V. Sikavitsas, J. M. Nitsche, and T. J. Mountziaris. Transport and kinetic processes underlying biomolecular interactions in the biacore optical biosensor. *Biotechnology Progress*, 18(4):885–897, 2002.

[191] P. Dittrich and A. Manz. Single-molecule fluorescence detection in microfluidic channels - the Holy Grail in μtas? *Analytical and Bioanalytical Chemistry*, 382 (8):1771–1782, 2005.

[192] M. Abrantes, M. Magone, L. Boyd, and P. Schuck. Adaptation of a surface plasmon resonance biosensor with miorofluidics for use with small sample volumes and long contact times. *Analytical Chemistry*, 73(13):2828–2835, 2001.

[193] H. P. Jennissen, A. Sanders, H. J. Schnittler, and V. Hlady. TIRF-rheometer for measuring protein adsorption under high shear rates: Constructional and fluid dynamic aspects. *Materialwissenschaft und Werkstofftechnik*, 30(12):850–861, 1999.

[194] H. P. Jennissen and T. Zumbrink. A novel nanolayer biosensor principle. *Biosensors and Bioelectronics*, 19(9):987–997, 2004.

[195] S. K. Yoon, G. W. Fichtl, and P. J. A. Kenis. Active control of the depletion boundary layers in microfluidic electrochemical reactors. *Lab on a Chip*, 6(12): 1516–1524, 2006.

[196] R. A. Vijayendran, K. M. Motsegood, D. J. Beebe, and D. E. Leckband. Evaluation of a three-dimensional micromixer in a surface-based biosensor. *Langmuir*, 19(5): 1824–1828, 2003.

[197] A. D. Stroock, S. K. Dertinger, G. M. Whitesides, and A. Ajdari. Patterning flows using grooved surfaces. *Analytical Chemistry*, 74(20):5306–5312, 2002.

[198] J. D. Kirtland, G. J. McGraw, and A. D. Stroock. Mass transfer to reactive boundaries from steady three-dimensional flows in microchannels. *Physics of Fluids*, 18 (7):–, 2006.

[199] M. Lopez and M. D. Graham. Enhancement of mixing and adsorption in microfluidic devices by shear-induced diffusion and topography-induced secondary flow. *Physics of Fluids*, 20(5):–, 2008.

[200] O. Hofmann, G. Voirin, P. Niedermann, and A. Manz. Three-dimensional microfluidic confinement for efficient sample delivery to biosensor surfaces. Application to immunoassays on planar optical waveguides. *Analytical Chemistry*, 74(20): 5243–5250, 2002.

[201] S. Martin, R. Townsend, L. Kuznetsova, K. Borthwick, M. Hill, M. McDonnell, and W. Coakley. Spore and micro-particle capture on an immunosensor surface in an ultrasound standing wave system. *Biosensors and Bioelectronics*, 21(5): 758–767, 2005.

[202] U. K. Sur, F. Marken, N. Rees, B. A. Coles, R. G. Compton, and R. Seager. Microwave enhanced electrochemistry: mass transport effects and steady state voltammetry in the sub-millisecond time domain. *Journal of Electroanalytical Chemistry*, 573(1):175–182, 2004.

[203] N. Scuor, P. Gallina, O. Sbaizero, and R. Mahajan. Modeling of a microfluidic channel in the presence of an electrostatic induced cross-flow. *Biomedical Microdevices*, 7(3):231–242, 2005.

[204] H. Parsa, C. D. Chin, P. Mongkolwisetwara, B. W. Lee, J. J. Wang, and S. K. Sia. Effect of volume- and time-based constraints on capture of analytes in microfluidic heterogeneous immunoassays. *Lab on a Chip*, 8(12):2062–2070, 2008.

[205] J. Tschmelak, G. Proll, J. Riedt, J. Kaiser, P. Kraemmer, L. Barzaga, J. S. Wilkinson, P. Hua, J. P. Hole, R. Nudd, M. Jackson, R. Abuknesha, D. Barcelo, S. Rodriguez-Mozaz, M. J. L. de Alda, F. Sacher, J. Stien, J. Slobodnik, P. Oswald, H. Kozmenko, E. Korenkova, L. Tothova, Z. Krascsenits, and G. Gauglitz. Automated water analyser computer supported system (AWACSS) Part I: project objectives, basic technology, immunoassay development, software design and networking. *Biosensors and Bioelectronics*, 20(8):1499–1508, 2005.

[206] J. Tschmelak, G. Proll, J. Riedt, J. Kaiser, P. Kraemmer, L. Barzaga, J. S. Wilkinson, P. Hua, J. P. Hole, R. Nudd, M. Jackson, R. Abuknesha, D. Barcelo, S. Rodriguez-Mozaz, M. J. L. de Alda, F. Sacher, J. Stien, J. Slobodnik, P. Oswald, H. Kozmenko, E. Korenkova, L. Tothova, Z. Krascsenits, and G. Gauglitz. Automated water analyser computer supported system (AWACSS) Part II: intelligent, remote-controlled, cost-effective, on-line, water-monitoring measurement system. *Biosensors and Bioelectronics*, 20(8):1509–1519, 2005.

[207] N. G. Housden, S. Harrison, H. R. Housden, K. A. Thomas, J. A. Beckingham, S. E. Roberts, S. P. Bottomley, M. Graille, E. Stura, and M. G. Gore. Observation and characterization of the interaction between a single immunoglobulin binding domain of protein L and two equivalents of human kappa light chains. *Journal of Biological Chemistry*, 279(10):9370–9378, 2004.

[208] B. Catimel, M. Nerrie, F. T. Lee, A. M. Scott, G. Ritter, S. Welt, L. J. Old, A. W. Burgess, and E. C. Nice. Kinetic analysis of the interaction between the monoclonal antibody A33 and its colonic epithelial antigen by the use of an optical biosensor. A comparison of immobilisation strategies. *Journal of Chromatography A*, 776(1):15–30, 1997.

[209] L. S. Jung and C. T. Campbell. Sticking probabilities in adsorption of alkanethiols from liquid ethanol solution onto gold. *Journal of Physical Chemistry B*, 104(47): 11168–11178, 2000.

[210] X. L. Zhang, P. Coupland, P. D. I. Fletcher, and S. J. Haswell. Monitoring of liquid flow through microtubes using a micropressure sensor. *Chemical Engineering Research and Design*, 87(1A):19–24, 2009.

[211] X. Jiang, Q. Xu, S. K. Dertinger, A. D. Stroock, T. M. Fu, and G. M. Whitesides. A general method for patterning gradients of biomolecules on surfaces using microfluidic networks. *Analytical Chemistry*, 77(8):2338–2347, 2005.

[212] K. A. Fosser and R. G. Nuzzo. Fabrication of patterned multicomponent protein gradients and gradient arrays using microfluidic depletion. *Analytical Chemistry*, 75(21):5775–5782, 2003.

[213] M. Mayer, J. Yang, I. Gitlin, D. H. Gracias, and G. M. Whitesides. Micropatterned agarose gels for stamping arrays of proteins and gradients of proteins. *Proteomics*, 4(8):2366–2376, 2004.

[214] D. Friedrich, C. Please, and T. Melvin. Optimisation of analyte transport in integrated microfluidic affinity sensors for the quantification of low levels of analyte. *Sensors and Actuators B-Chemical*, 131:323–332, 2008.

[215] F. Belardelli. Role of interferons and other cytokines in the regulation of the immune-response. *APMIS*, 103(3):161–179, 1995.

[216] R. Medzhitov. Origin and physiological roles of inflammation. *Nature*, 454(7203): 428–435, 2008.

[217] C. Holmes, M. El-Okl, A. L. Williams, C. Cunningham, D. Wilcockson, and V. H. Perry. Systemic infection, interleukin 1β, and cognitive decline in alzheimer's disease. *Journal of Neurology Neurosurgery and Psychiatry*, 74(6):788–789, 2003.

[218] A. Kaplin, D. Deshpande, E. Scott, C. Krishnan, J. Carmen, I. Shats, T. Martinez, J. Drummond, S. Dike, M. Pletnikov, S. Keswani, T. Moran, C. Pardo, P. Calabresi, and D. Kerr. IL-6 induces regionally selective spinal cord injury in patients with the neuroinflammatory disorder transverse myelitis. *Journal of Clinical Investigation*, 115(10):2731–2741, 2005.

[219] C. Di Campli, M. A. Zocco, R. Gaspari, M. Novi, M. Candelli, A. Santoliquido, R. Flore, P. Tondi, R. Proietti, G. Gasbarrini, P. Pola, and A. Gasbarrini. The decrease in cytokine concentration during albumin dialysis correlates with the prognosis of patients with acute on chronic liver failure. *Transplantation Proceedings*, 37(6):2551–2553, 2005.

[220] M. Hammadeh, C. Fischer-Hammadeh, T. Georg, P. Rosenbaum, and W. Schmidt. Comparison between cytokine concentration in follicular fluid of poor and high responder patients and their influence of ICSI-outcome. *American Journal of Reproductive Immunology*, 50(2):131–136, 2003.

[221] A. O'Garra and K. Murphy. Role of cytokines in determining T-lymphocyte function. *Current Opinion in Immunology*, 6(3):458–466, 1994.

[222] C. M. Niemeyer, M. Adler, and R. Wacker. Immuno-PCR: high sensitivity detection of proteins by nucleic acid amplification. *Trends in Biotechnology*, 23(4): 208–216, 2005.

[223] L. Borg, J. Kristiansen, J. M. Christensen, K. F. Jepsen, and L. K. Poulsen. Evaluation of accuracy and uncertainty of ELISA assays for the determination of interleukin-4, interleukin-5, interferon-gamma and tumor necrosis factor-alpha. *Clinical Chemistry and Laboratory Medicine*, 40(5):509–519, 2002.

[224] M. D. Moody, S. W. Van Arsdell, K. P. Murphy, S. F. Orencole, and C. Burns. Array-based ELISAs for high-throughput analysis of human cytokines. *Biotechniques*, 31(1):186–194, 2001.

[225] S. FitzGerald, R. McConnell, and A. Huxley. Simultaneous analysis of circulating human cytokines using a high-sensitivity cytokine biochip array. *Journal of Proteome Research*, 7(1):450–455, 2008.

[226] W. de Jager, H. te Velthuis, B. Prakken, W. Kuis, and G. Rijkers. Simultaneous detection of 15 human cytokines in a single sample of stimulated peripheral blood mononuclear cells. *Clinical and Diagnostic Laboratory Immunology*, 10(1):133–139, 2003.

[227] J. M. Nam, C. S. Thaxton, and C. A. Mirkin. Nanoparticle-based Bio-Bar codes for the ultrasensitive detection of proteins. *Science*, 301(5641):1884–1886, 2003.

[228] J. M. Nam, A. R. Wise, and J. T. Groves. Colorimetric Bio-Barcode amplification assay for cytokines. *Analytical Chemistry*, 77(21):6985–6988, 2005.

[229] B. Schweitzer, S. Roberts, B. Grimwade, W. Shao, M. Wang, Q. Fu, Q. Shu, I. Laroche, Z. Zhou, V. Tchernev, J. Christiansen, M. Velleca, and S. Kingsmore. Multiplexed protein profiling on microarrays by rolling-circle amplification. *Nature Biotechnology*, 20(4):359–365, 2002.

[230] M. Adler, R. Wacker, and C. Niemeyer. Sensitivity by combination: immuno-PCR and related technologies. *Analyst*, 133(6):702–718, 2008.

[231] S. Fredriksson, M. Gullberg, J. Jarvius, C. Olsson, K. Pietras, S. M. Gustafsdottir, A. Ostman, and U. Landegren. Protein detection using proximity-dependent DNA ligation assays. *Nature Biotechnology*, 20(5):473–477, 2002.

[232] M. Gullberg, S. Gustafsdottir, E. Schallmeiner, J. Jarvius, M. Bjarnegard, C. Betsholtz, U. Landegren, and S. Fredriksson. Cytokine detection by antibody-based proximity ligation. *Proceedings of the National Academy of Sciences of the United States of America*, 101(22):8420–8424, 2004.

[233] C. Y. Yang, E. Brooks, Y. Li, P. Denny, C. M. Ho, F. X. Qi, W. Y. Shi, L. Wolinsky, B. Wu, D. T. W. Wong, and C. D. Montemagno. Detection of picomolar levels of interleukin-8 in human saliva by SPR. *Lab on a Chip*, 5(10):1017–1023, 2005.

[234] T. M. Battaglia, J. F. Masson, M. R. Sierks, S. P. Beaudoin, J. Rogers, K. N. Foster, G. A. Holloway, and K. S. Booksh. Quantification of cytokines involved in wound healing using surface plasmon resonance. *Analytical Chemistry*, 77(21): 7016–7023, 2005.

[235] L. Kim, M. D. Vahey, H. Y. Lee, and J. Voldman. Microfluidic arrays for logarithmically perfused embryonic stem cell culture. *Lab on a Chip*, 6(3):394–406, 2006.

[236] H. L. Ashe and J. Briscoe. The interpretation of morphogen gradients. *Development*, 133(3):385–394, 2006.

[237] R. A. Firtel and C. Y. Chung. The molecular genetics of chemotaxis: sensing and responding to chemoattractant gradients. *Bioessays*, 22(7):603–615, 2000.

[238] X. D. Yang, J. R. F. Corvalan, P. Wang, C. M. N. Roy, and C. G. Davis. Fully human anti-interleukin-8 monoclonal antibodies: potential therapeutics for the treatment of inflammatory disease states. *Journal of Leukocyte Biology*, 66(3): 401–410, 1999.

[239] B. G. Chung, L. A. Flanagan, S. W. Rhee, P. H. Schwartz, A. P. Lee, E. S. Monuki, and N. L. Jeon. Human neural stem cell growth and differentiation in a gradient-generating microfluidic device. *Lab on a Chip*, 5(4):401–406, 2005.

[240] T. M. Keenan and A. Folch. Biomolecular gradients in cell culture systems. *Lab on a Chip*, 8(1):34–57, 2008.

[241] N. N. Ye, J. H. Qin, W. W. Shi, X. Liu, and B. C. Lin. Cell-based high content screening using an integrated microfluidic device. *Lab on a Chip*, 7(12):1696–1704, 2007.

[242] S. K. W. Dertinger, D. T. Chiu, N. L. Jeon, and G. M. Whitesides. Generation of gradients having complex shapes using microfluidic networks. *Analytical Chemistry*, 73(6):1240–1246, 2001.

[243] B. Mosadegh, C. Huang, J. W. Park, H. S. Shin, B. G. Chung, S. K. Hwang, K. H. Lee, H. J. Kim, J. Brody, and N. L. Jeon. Generation of stable complex gradients across two-dimensional surfaces and three-dimensional gels. *Langmuir*, 23(22):10910–10912, 2007.

[244] C. W. Li, R. S. Chen, and M. S. Yang. Generation of linear and non-linear concentration gradients along microfluidic channel by microtunnel controlled stepwise addition of sample solution. *Lab on a Chip*, 7(10):1371–1373, 2007.

[245] B. G. Chung, F. Lin, and N. L. Jeon. A microfluidic multi-injector for gradient generation. *Lab on a Chip*, 6(6):764–768, 2006.

[246] H. K. Wu, B. Huang, and R. N. Zare. Generation of complex, static solution gradients in microfluidic channels. *Journal of the American Chemical Society*, 128 (13):4194–4195, 2006.

[247] K. E. Nelson, J. O. Foley, and P. Yager. Concentration gradient immunoassay. 1. an immunoassay based on interdiffusion and surface binding in a microchannel. *Analytical Chemistry*, 79(10):3542–3548, 2007.

[248] T. Kang, J. Han, and K. S. Lee. Concentration gradient generator using a convective-diffusive balance. *Lab on a Chip*, 8(7):1220–1222, 2008.

[249] M. Holden, S. Kumar, E. Castellana, A. Beskok, and P. Cremer. Generating fixed concentration arrays in a microfluidic device. *Sensors and Actuators B-Chemical*, 92(1-2):199–207, 2003.

[250] F. Lin, W. Saadi, S. W. Rhee, S. J. Wang, S. Mittal, and N. L. Jeon. Generation of dynamic temporal and spatial concentration gradients using microfluidic devices. *Lab on a Chip*, 4(3):164–167, 2004.

[251] K. Campbell and A. Groisman. Generation of complex concentration profiles in microchannels in a logarithmically small number of steps. *Lab on a Chip*, 7(2): 264–272, 2007.

[252] D. Irimia, D. A. Geba, and M. Toner. Universal microfluidic gradient generator. *Analytical Chemistry*, 78(10):3472–3477, 2006.

[253] N. Zaari, P. Rajagopalan, S. K. Kim, A. J. Engler, and J. Y. Wong. Photopolymerization in microfluidic gradient generators: Microscale control of substrate compliance to manipulate cell response. *Advanced Materials*, 16(23-24):2133–2137, 2004.

[254] W. Lin. A passive grooved micromixer generating enhanced transverse rotations for microfluids. *Chemical Engineering and Technology*, 31(8):1210–1215, 2008.

[255] H. Sato, S. Ito, K. Tajima, N. Orimoto, and S. Shoji. PDMS microchannels with slanted grooves embedded in three walls to realize efficient spiral flow. *Sensors and Actuators A-Physical*, 119(2):365–371, 2005.

[256] A. Ajdari. Transverse electrokinetic and microfluidic effects in micropatterned channels: Lubrication analysis for slab geometries. *Physical Review E*, 65(1):–, 2002.

[257] J. T. Yang, K. J. Huang, and Y. C. Lin. Geometric effects on fluid mixing in passive grooved micromixers. *Lab on a Chip*, 5(10):1140–1147, 2005.

[258] J. Aubin, D. F. Fletcher, and C. Xuereb. Design of micromixers using CFD modelling. *Chemical Engineering Science*, 60(8-9):2503–2516, 2005.

[259] P. B. Howell, J. P. Golden, L. R. Hilliard, J. S. Erickson, D. R. Mott, and F. S. Ligler. Two simple and rugged designs for creating microfluidic sheath flow. *Lab on a Chip*, 8(7):1097–1103, 2008.

[260] M. Camesasca, M. Kaufman, and I. Manas-Zloczower. Staggered passive micromixers with fractal surface patterning. *Journal of Micromechanics and Microengineering*, 16(11):2298–2311, 2006.

[261] H. J. Song, X. Z. Yin, and D. J. Bennett. Optimization analysis of the staggered herringbone micromixer based on the slip-driven method. *Chemical Engineering Research and Design*, 86(8A):883–891, 2008.

[262] D. R. Mott, P. B. Howell, J. P. Golden, C. R. Kaplan, F. S. Ligler, and E. S. Oran. Toolbox for the design of optimized microfluidic components. *Lab on a Chip*, 6 (4):540–549, 2006.

[263] M. Aoki. *Introduction to optimization techniques: fundamentals and applications of nonlinear programming.* Macmillan series in applied computer science. Macmillan (N.Y.); London: Collier-Macmillan, New York, 1971.

[264] S. Kirkpatrick, C. D. Gelatt, and M. P. Vecchi. Optimization by simulated annealing. *Science*, 220(4598):671–680, 1983.

[265] J. C. Lagarias, J. A. Reeds, M. H. Wright, and P. E. Wright. Convergence properties of the Nelder-Mead simplex method in low dimensions. *Siam Journal on Optimization*, 9(1):112–147, 1998.

[266] H. Y. Lee and J. Voldman. Optimizing micromixer design for enhancing dielectrophoretic microconcentrator performance. *Analytical Chemistry*, 79(5):1833–1839, 2007.

[267] A. W. Tilles, H. Baskaran, P. Roy, M. L. Yarmush, and M. Toner. Effects of oxygenation and flow on the viability and function of rat hepatocytes cocultured in a microchannel flat-plate bioreactor. *Biotechnology and Bioengineering*, 73(5): 379–389, 2001.

[268] D. A. Edwards. Steric hindrance effects on surface reactions: applications to BIAcore. *Journal of Mathematical Biology*, 55(4):517–539, 2007.

[269] Y. Zheng and A. Rundell. Biosensor immunosurface engineering inspired by B-cell membrane-bound antibodies: Modeling and analysis of multivalent antigen capture by immobilized antibodies. *IEEE Transactions on Nanobioscience*, 2(1): 14–25, 2003.

[270] J. O. Foley, K. E. Nelson, A. Mashadi-Hossein, B. A. Finlayson, and P. Yager. Concentration gradient immunoassay. 2. computational modeling for analysis and optimization. *Analytical Chemistry*, 79(10):3549–3553, 2007.

[271] P. B. Howell, D. R. Mott, F. S. Ligler, J. P. Golden, C. R. Kaplan, and E. S. Oran. A combinatorial approach to microfluidic mixing. *Journal of Micromechanics and Microengineering*, 18(11):–, 2008.

[272] Y. Y. Tsui, C. S. Yang, and C. M. Hsieh. Evaluation of the mixing performance of the micromixers with grooved or obstructed channels. *Journal of Fluids Engineering-Transactions of the Asme*, 130(7):–, 2008.